1982

The Base Balance Measurement Technique And Applications To Dynamic Wind Loading To Structures

Tony Tschanz

CANADIAN THESES ON MICROFICHE

I.S.B.N.

THESES CANADIENNES SUR MICROFICHE

National Library of Canada
Collections Development Branch

Canadian Theses on
Microfiche Service

Ottawa, Canada
K1A 0N4

Bibliothèque nationale du Canada
Direction du développement des collections

Service des thèses canadiennes
sur microfiche

NOTICE

The quality of this microfiche is heavily dependent upon the quality of the original thesis submitted for microfilming. Every effort has been made to ensure the highest quality of reproduction possible.

If pages are missing, contact the university which granted the degree.

Some pages may have indistinct print especially if the original pages were typed with a poor typewriter ribbon or if the university sent us a poor photocopy.

Previously copyrighted materials (journal articles, published tests, etc.) are not filmed.

Reproduction in full or in part of this film is governed by the Canadian Copyright Act, R.S.C. 1970, c. C-30. Please read the authorization forms which accompany this thesis.

AVIS

La qualité de cette microfiche dépend grandement de la qualité de la thèse soumise au microfilmage. Nous avons tout fait pour assurer une qualité supérieure de reproduction.

S'il manque des pages, veuillez communiquer avec l'université qui a conféré le grade.

La qualité d'impression de certaines pages peut laisser à désirer, surtout si les pages originales ont été dactylographiées à l'aide d'un ruban usé ou si l'université nous a fait parvenir une photocopie de mauvaise qualité.

Les documents qui font déjà l'objet d'un droit d'auteur (articles de revue, examens publiés, etc.) ne sont pas microfilmés.

La reproduction, même partielle, de ce microfilm est soumise à la Loi canadienne sur le droit d'auteur, SRC 1970, c. C-30. Veuillez prendre connaissance des formules d'autorisation qui accompagnent cette thèse.

THIS DISSERTATION HAS BEEN MICROFILMED EXACTLY AS RECEIVED

LA THÈSE A ÉTÉ MICROFILMÉE TELLE QUE NOUS L'AVONS REÇUE

NL-339 (r. 82/08)

Canada

THE BASE BALANCE MEASUREMENT TECHNIQUE AND APPLICATIONS TO DYNAMIC WIND LOADING OF STRUCTURES

by

Tony Tschanz
Department of Engineering Science

Submitted in partial fulfillment
of the requirements for the degree of
Doctor of Philosophy

Faculty of Graduate Studies
The University of Western Ontario
London, Canada
July, 1982

ABSTRACT

Wind tunnel testing is the only confident method of predicting the response of buildings to natural wind currently available. Modelling techniques are well developed, but rely in most instances on representation of the turbulent boundary layer in a wind tunnel, and complete modelling of all the structural parameters such as shape, mass, damping and stiffness. The resulting dynamic responses of the aeroelastic models can directly be scaled to full scale values. Aeroelastic models, however, are expensive, require much time before availability of results, and are specific to the structural parameters modelled.

The subject of this study is to directly measure the total dynamic modal forces, using a high frequency, balance-model system with a "flat" frequency response. The foam models are mounted on a sensitive, but rigid five-component balance which is described in detail. This balance is believed to represent the state of the art for the intended load ranges.

Practical applications of direct force measurements to estimate the response of structures are presented. Theoretical considerations, and comparisons of results with conventional wind tunnel experiments, show that the method is an economical alternative for many conventional structures. Advantages, in addition to a less costly and time consuming experiment, include the straightforward revisions of predicted responses for modifications to the structure. The modal forces are dependent only on the structure shape and not on its dynamic properties.

Knowing the dynamic force permits structures to be studied for non-linear behaviour. Forces can either be used directly as measured by the balance-model combination, or simulated with a digital computer. Low order auto-regressive processes are shown to give an efficient simulation of most forces. A collection of modal forces with computed parameters are presented, which are suitable for application in the frequency domain (linear problems) or time domain (non-linear problems).

Applications of simulated modal forces is illustrated with studies of simple

yielding structures. Simulation studies provide useful information on building behaviour. Only a digital computer is necessary after initial measurements are conducted in a wind tunnel.

ACKNOWLEDGEMENTS

I would like to express my sincere appreciation to my supervisor, Dr. A.G. Davenport, for his continuous interest, assistance and support during my studies. His pioneering efforts in the gust factor approach and development of other theories to predict the response of structures to wind inspired this study. I would also like to thank the staff of the Boundary Layer Wind Tunnel Laboratory for their support and especially thank Dr. N. Isyumov for many valuable suggestions and Mr. K.N. Allen for his technical assistance.

The balance was expertly machined and assembled by Mr. P. Teunissen of the Co-ordinated Shop at The University of Western Ontario. Mr. R. Kaeger of the Co-ordinated Shop also provided valuable assistance. I am also indebted to Mr. G. Aartsen of the Electronics Shop of the Faculty of Engineering Science for his expertise in helping me design the electronic components.

A special note of appreciation is due to Ms. G. Hayman who typed the manuscript and to Messrs B. Allison and S. Lusk who drafted the diagrams.

Many thanks go to my wife, Linda, who proofread the manuscript, plotted the Appendices and gave me much support during the long time this work required.

I would also like to acknowledge the National Sciences and Engineering Research Council of Canada and the Boundary Layer Wind Tunnel Laboratory for their financial support.

TABLE OF CONTENTS

TABLE OF CONTENTS (CONT'D)

TABLE OF CONTENTS (CONT'D)

TABLE OF CONTENTS (CONT'D)

TABLE OF CONTENTS (CONT'D)

TABLE OF CONTENTS (CONT'D)

LIST OF TABLES

LIST OF FIGURES

LIST OF FIGURES (CONT'D)

LIST OF FIGURES (CONT'D)

LIST OF FIGURES (CONT'D)

INTRODUCTION AND SCOPE OF THE STUDY

The trend towards the construction of tall, slender, and lightweight structures, built with high strength materials and connections which exhibit little structural damping demands an increasing degree of attention to their behaviour in the wind. Analytical procedures are not sufficiently developed to predict the response of structures, and building codes treat only the along wind response with well established procedures.

In the absence of analytical methods it is often necessary to determine the response of buildings to wind experimentally in a boundary layer wind tunnel. Modelling techniques are well established, relying in most cases on complete modelling of all structural parameters, such as building shape, mass, damping and stiffness parameters. The resulting responses, such as displacements, bending moments and accelerations can be directly converted to full scale values using the scaling laws. Aeroelastic models, however, are expensive, entail much time delay until results are available and allow only limited prediction extrapolations for structural properties which differ from the measured ones.

The main components of the response of tall buildings are primarily due to the excitation in the fundamental modes by the modal forces. If these forces can be measured, the mechanical transfer function relating the load function to the response is straightforward. A high frequency model, mounted on a balance measuring the base bending moments measures sway modal forces corresponding to a straight line mode shape. The difficulties in the experimental determination of the dynamic forces lie primarily in the demanding frequency response of the measuring system. This requires the design and construction of a sensitive, but rigid, five-component balance.

Knowledge of the dynamic forces enables the study of non-linear building responses. Forces can be either used as measured by the balance-model combination, or generated numerically on a digital computer by simulations. The study, hence, consists of four parts which are presented in four self-contained chapters:

i) design of five-component balance;

ii) linear structural response predictions;

iii) wind force simulations; and

iv) non-linear building response.

Force measurements on systematic building shapes are shown in Appendicies A and B.

The main efforts, in time and expenditure, were to develop the five-component balance. To measure the force components for a wide range of building sizes, with sufficiently high frequency response as not to distort the measured forces, requires a good design with compromises between contradictory requirements. The design is described in detail, aiding other investigators to build balances for different requirements. The new five-component balance is believed to represent the state of the art in balances for the intended load range.

Linear structural response predictions using the proposed force methods are relatively straightforward. Models are simply cut to the desired shape from rigid lightweight foam and mounted on the balance and placed in the wind tunnel with the desired proximity roughness models. Tests consist of measuring the force coefficients and force spectra for desired wind directions at one velocity. Response predictions are done analytically. Theoretical considerations and practical applications are described in Chapter II. This method assumes that aerodynamic damping effects can conservatively be neglected or an estimated amount can be included. Comparisons with the National Building Code of Canada and with aeroelastic tests show the proposed method to be an economical alternative.

Simulations of wind induced forces enable investigators to study the behaviour of buildings, with the only required tool being a digital computer. This economizes on the amount of time the wind tunnel and other valuable resources, such as instrumentation and manpower are required. Further advantages are that the response evaluations are not tied to a physical time scale and can be considerably accelerated using high speed computers, enabling parameter studies to be done which would be prohibitively long in real time. The methods used most successfully are low order autoregressive processes. These are described in detail in Chapter III. The forces are described by the autoregressive parameters both in the frequency domain (for linear response predic-

tions) or in the time domain (for non-linear response predictions).

Non-linear response predictions are not usually performed for wind induced loads. There are indications, however, that the wind speed only needs to be increased by typically 20% from those velocities which just produce yielding, to cause serious damage. The simulations described in Chapter III enable a straightforward step-by-step evaluation of a building with any assumed non-linear properties. In Chapter IV methods are described to solve the response in the time domain with applications to yielding structures. The most important parameter is shown to be the damping. Little information, however, is known on the damping values of real structures at large displacements.

The measurement of the total dynamic force can be seen from the above applications to be useful in various areas in wind engineering.

CHAPTER I

DEVELOPMENT OF SENSITIVE FIVE–COMPONENT BALANCE

1.1 INTRODUCTION

In natural wind buildings respond to a number of mixed forces. These forces have to be determined in many instances by experimental methods in a Boundary Layer Wind Tunnel (referred to as BLWT below). Modelling techniques are well developed and are discussed in more detail in Chapter II. This chapter describes the development and construction of a new sensitive, high frequency, five-component balance. The force balance is a critical part of the experiments to determine wind induced loads. The balance output is usually in the form of electric signals which vary the voltages proportionately to the applied forces. These analogue signals can be further processed manually or digitized for use by computers.

The rapidly varying forces, combined with the steady forces present special problems for the measuring instrumentation. The design chosen for the balance is believed to represent the best compromise of desirable attributes for the intended load ranges. The latest electronics, transducers, materials and machining technologies are used to optimize the performance for the physical contradictions of a "soft" system with good resolution, long term stability, and high output, and a "stiff" system with good dynamic response (or small "overshoot" for rapidly varying loads), necessary to make a few hundred measurements per second.

Three critical components are described in detail, of both the design and the manufacture : 1) the miniature force transducers, 2) the overload protection devices to al-

leviate harmful forces on the load cells from any direction, and 3) the housing and mounting platform.

Further described are a calibration rig with jewelled watch bearings, and the instrumentation and electronics which form an integral part of the experimental measuring system. Several exploratory prototypes were machined to find the best possible design and performance for most of the components of the balance.

The technique to determine building responses described in Chapter II relies on a high frequency response of the balance-model combination. Suitable foam models are described in this chapter as part of the experimental test set-up.

A number of designs and transducer systems used by other authors are described, in addition to suggestions for further research to improve the current state of the art of force balances.

1.2 REQUIREMENTS FOR A FORCE BALANCE

The ideal balance capable of measuring the complete time history would require the following attributes:

a) infinite sensitivity;
b) infinite rigidity;
c) stability and freedom of temperature and environmental drift; and
d) uncoupled response to the orthogonal force components.

The sensitivity has to be high, since the processing of the output from the balance introduces errors which are in general smaller for larger outputs from the balance. The quasi-static force which has to be resolved is approximately one hundred times smaller than the resonant response of a conventional aeroelastic model. The wide range of forces from large buildings with high wind speeds, to small buildings with low wind speeds, also require high output to resolve small forces accurately.

The rigidity has to be high in order to reduce kinematic effects. This is contradictory to the sensitivity requirement, since, in general, high sensitivity is achieved using flexible transducers. The dynamic response of the balance model combination with high natural frequencies can be shown from Figure 1.1.

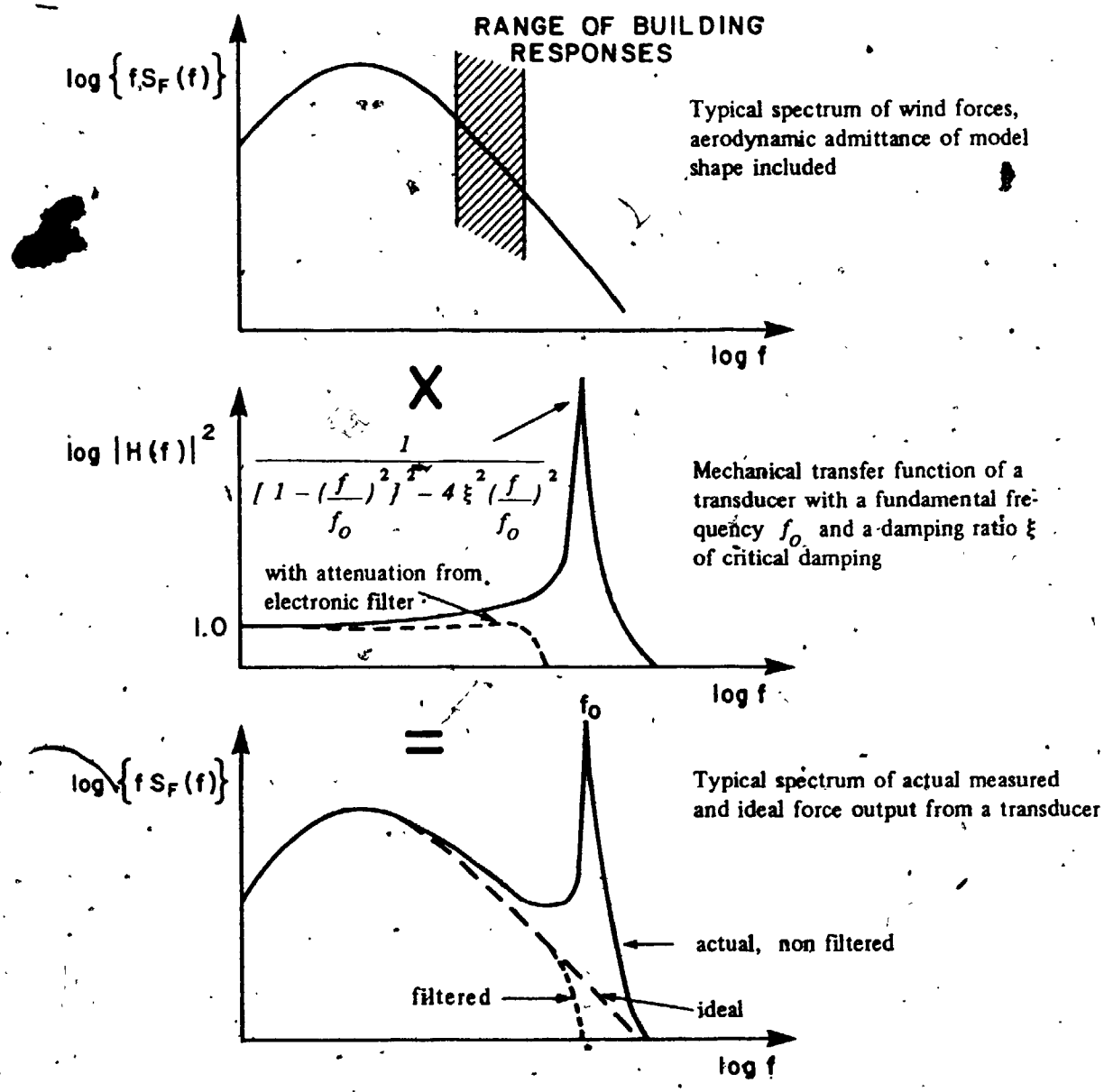

FIG. 1.1 DYNAMIC RESPONSE OF BALANCE–MODEL COMBINATION

The response is greatly distorted for input frequencies near the fundamental frequency of the measuring system. It is, hence, desirable to have high rigidity which gives a high fundamental frequency. The quality of a balance, or for that matter any strain gauged force transducer for rapid measurements, could primarily be assessed by a high product of stiffness times strain output per unit load, with units of strain/length for forces and strain/radian for moments. What the distribution between sensitivity and stiffness should be, depends on the measurement problem, i.e. for dynamic measurements the stiffness is of primary importance so that concessions on sensitivity may be made.

Good stability is required to accurately measure the loads in the lower force ranges, since drift is independent of the load level. Great attention to mechanical and electronic design can provide better stability, but drift errors can best be masked by high output levels from the balance. For durations of typical wind tunnel tests, the stability can be maintained within roughly one micro strain. For short times, i.e. purely dynamic measurements, the stability requirements are less severe. If the same balance has to measure the mean as well as the dynamic loads, the stability and related sensitivity is a critical requirement.

An ever recurring problem in multi-component balances is that of interaction, which may be defined as the electrical output of a transducer element to forces or moments along axes perpendicular to the measuring axis. Coupling of orthogonal force components can be minimized by careful mechanical design and especially by good workmanship. First order effects can be corrected by multiplication with a matrix containing all coupling terms, however computer time is increased and flexibility from the independent monitoring of components is reduced. Linear interaction effects can also be corrected by electronic circuits, or by connecting one corner of a Wheatstone bridge with a specific resistor to a corner of the Wheatstone bridge of the transducer which measures the interacting force component.

The ideal balance is not realizable, therefore compromises have to be made, especially between sensitivity and rigidity. The following secondary requirements should also be taken into account; output from six components available simultaneously,

preferably referred to a common origin at the centre of the model at the base elevation, ease of mounting different models on balance and economy of building models, low hysteresis and creep, ruggedness, repairability in case of breakdown, low mass, high damping, basic design applicable to different load ranges, good signal to noise ratio, and cost of the balance.

1.3 EXISTING AND PRELIMINARY BALANCE CONFIGURATIONS

The forces encountered by wind tunnel models are of the order of 1 lb (4.45 N) for shear forces or 1 lb-ft (1.3 N-m) for moments. These relatively low values preclude many designs which would be possible for larger capacity transducers, such as multi-component transducers machined from one homogeneous part. Section 1.3 is a description of the intermediate steps of the balance design, and configurations used by other investigators. The final design is described in Section 1.4.

1.3.1 Balances in Use at the University of Western Ontario

Two strain gauge balances have been used successfully in the BLWT Laboratory for the last ten years. One measures the two translational moments and the torque, and the other measures the lateral shear forces and torque.

1.3.1.1 BLWT moment balance

The moment balance is used primarily to measure base bending moments for aeroelastic models. It is a version of the sting type balances commonly used in aeronautical wind tunnels. A schematic configuration to measure one moment component, with strain gauges arranged to form a Wheatstone Bridge circuit, is shown in Fig. 1.2. The gauges detect the surface stresses in the sting caused by any of the six force components. With perfect symmetry of the machined material and gauge positioning, the Wheatstone Bridge circuit cancels all components except the desired drag moment component, of which the voltage output is nearly a linear function. Thermal and other environmental interaction can also be kept small with careful machining, and selecting and positioning of the gauges.

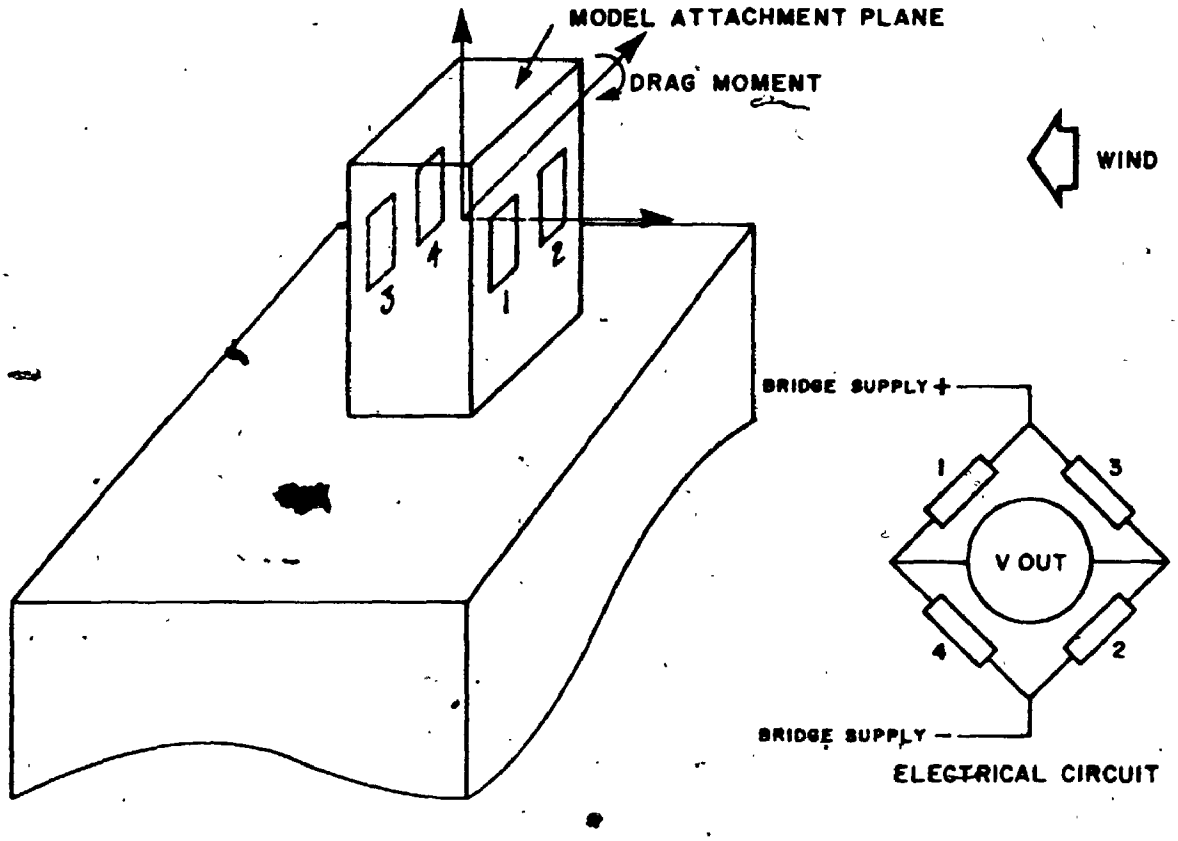

FIG. 1.2 SCHEMATIC DIAGRAM OF BLWT MOMENT BALANCE

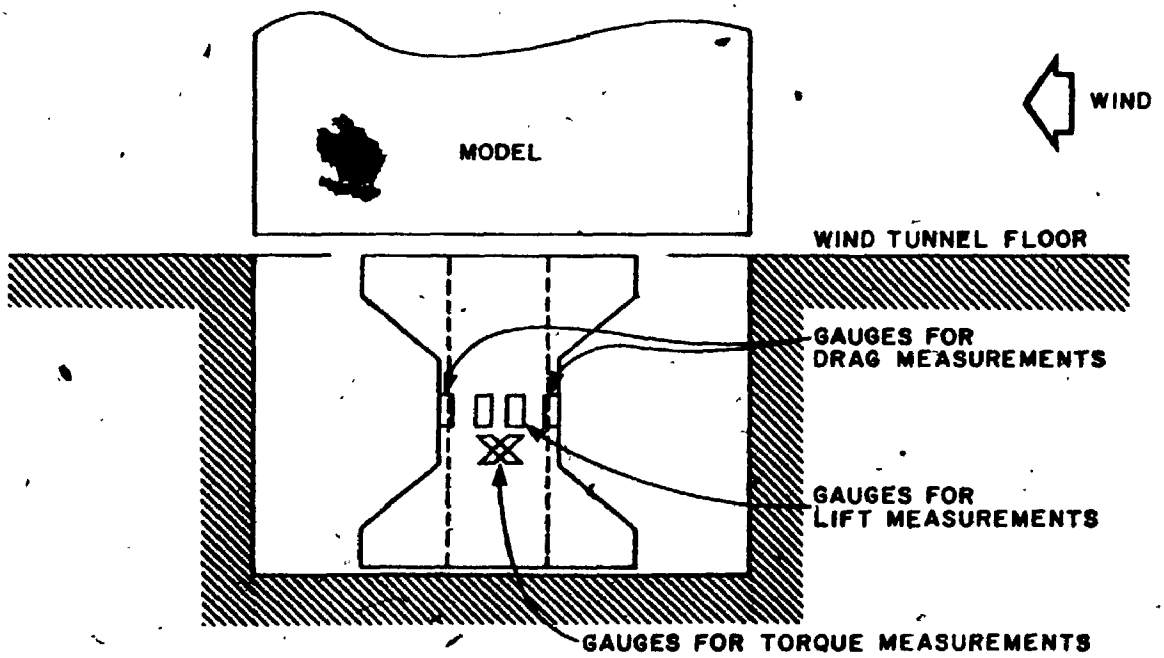

FIG. 1.3 REALIZATION OF BLWT MOMENT BALANCE

The strain gauged part of the BLWT moment balance was machined from a solid piece of aluminum and looks like a thin walled bobbin, as shown in Fig. 1.3. The balance is rugged, relatively inexpensive to build, and different models are easily mounted on top of the bobbin. The stiffness times strain outputs are approximately 0.5 strain/radian for the lateral moments, and approximately 0.08 strain/radian for the torsional moment. These values are typical for well designed sting type balances and are much inferior to the values of 6.7 strain/radian for both lateral moments and torsion of the new five-component balance described in Section 1.4. In spite of the low torsional stiffness performance for practical reasons it is not possible to get a high strain output for the torsional forces encountered with the small building models.

Other shortcomings from the ideal balance requirements described in Section 1.2 include: (1) only three force components are measured, (2) the origin to which the forces are measured is approximately one inch below the base of the building, and (3) the design is not applicable if the loads are small, such as for low building models. Variations of this type of balance, used by other investigators, include letting the sting protrude into the wind tunnel and covering it with a shell of the building model. In this way it is possible to improve on shortcomings (2) above, of the models, but the mounting is more complicated.

1.3.1.2 BLWT shear force balance

The shear force and torque balance used by the BLWT works as a structural frame with a rigid girder and four columns, deforming primarily in shear. A schematic of the design is shown in Fig. 1.4. The shear forces induce large strains near the top and the bottom of the columns, which can be further amplified mechanically by cuts as shown in the detail *A* of Fig. 1.4. This balance is simple to machine, and both lift and drag shear forces, as well as the torsional moment, can be measured. The balance is also rugged and different models are easily mounted on top of the model attachment plane. The design is applicable to almost any load range.

The stiffness times strain product is approximately 0.03 strain/inch (1.18 ϵ/m) for the shear forces and 0.3 strain/radian for the torque, much lower than the corresponding

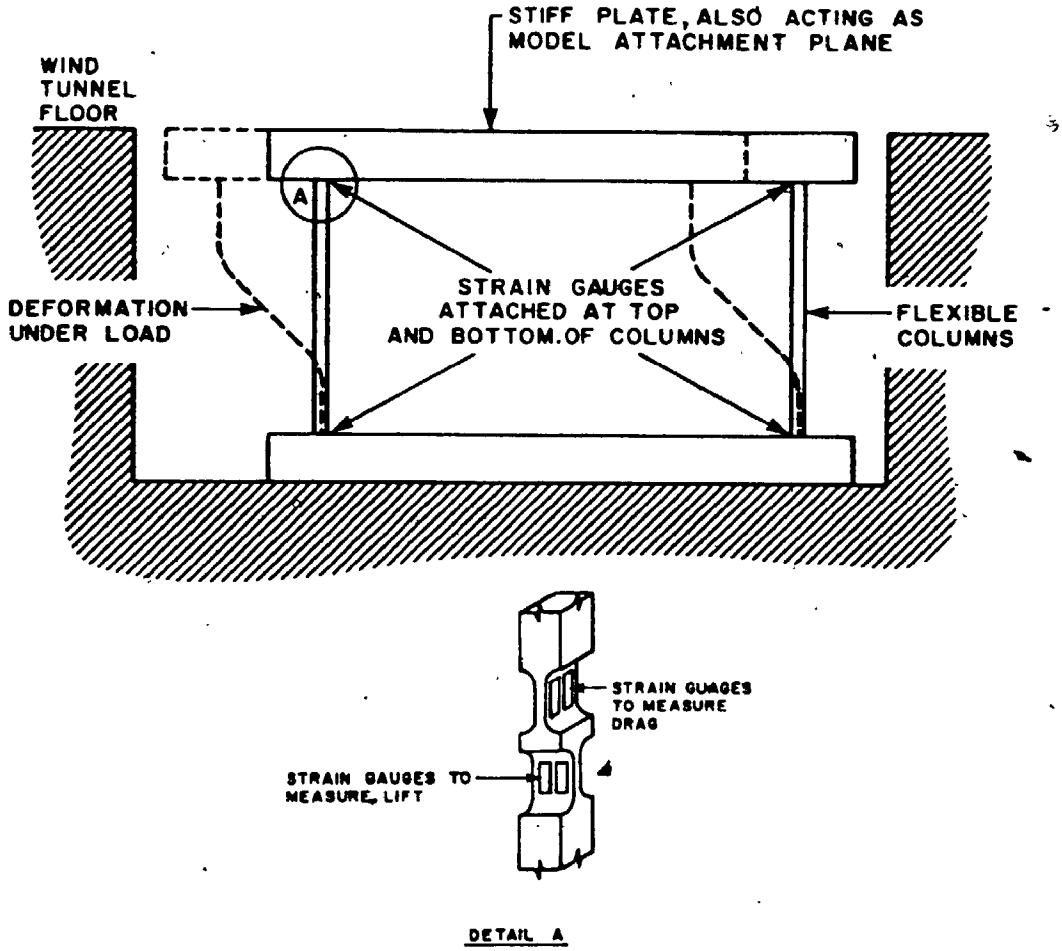

FIG. 1.4 SCHEMATIC DIAGRAM OF BLWT SHEAR FORCE BALANCE

values of 1.7 strain/inch (67 ϵ/m) and 6.7 strain/radian, respectively for the new five-component balance. Due to these low products, combined with the relatively high mass, this balance is not applicable to measure dynamic loads and is used primarily to measure mean responses of buildings and wing sections.

Although it was considered to be an acceptable compromise as a shear force balance for mean loads, it is not even ideally suited for this purpose. The system is statically indeterminate and sensitive to temperature gradients, as not all columns are strain gauged and gauges are exposed and widely separated. Coupling of the orthogonal force components can only be kept at an acceptable level with extreme care. As mentioned above, the balance measures only three components.

1.3.2 Prototype for BLWT Five-Component Balance

Initially the attempt to make a five-component balance led to a combination of the moment and force balances with some improvements of their shortcomings. The moment sensing part was to be mounted on top of a shear force and torsion measuring part, as shown schematically in Fig. 1.5. The shear and torsion were to be measured with three load cells. The flexible columns would have made the system almost statically determinate. Calculations showed the temperature effects in the columns to have a negligible effect on the force measurements in the load cells. The torsional sensitivity would have been better than for the balances in Figs. 1.3 and 1.4. Critical components would have been the load cells which are described in detail in Section 1.4. From continued modifications to further improve the stiffness times strain product evolved the five-component balance described in Section 1.4.

1.3.3 Balances Surveyed From Published Papers

Balances are essential to wind tunnel experiments and great efforts have been made by many investigators, resulting in many designs and publications. The possibilities of load measurements with strain gauges has led to new conceptions in wind tunnel balance design. Formerly wind tunnels often used complicated linkages to measure the forces. Most balances are designed for specific applications and are not suitable for general purpose applications.

A two-component balance with good sensitivity and stiffness was developed by Whitbread [1975], who made a 12 inch tall carbon fibre shell of the CAARC standard building model [Wardlaw and Moss, 1970]. The moment and shear were measured at the base using integrated silicon sensors, as indicated in Fig. 1.6. The output from the upper shear links is proportional to the base bending moment and the summed output from both levels is proportional to the shear force. Not enough information is given to calculate the stiffness times strain product, but with a big compromise in sensitivity a lowest frequency of the balance model combination apparently above 250 Hz was achieved. The strain output of 0.332μ in/in/lb-in (2.94 μm/m/Nm) for the moment and 0.712 μin/in/lb (0.16 μm/m/N) for the shear force compares to values of

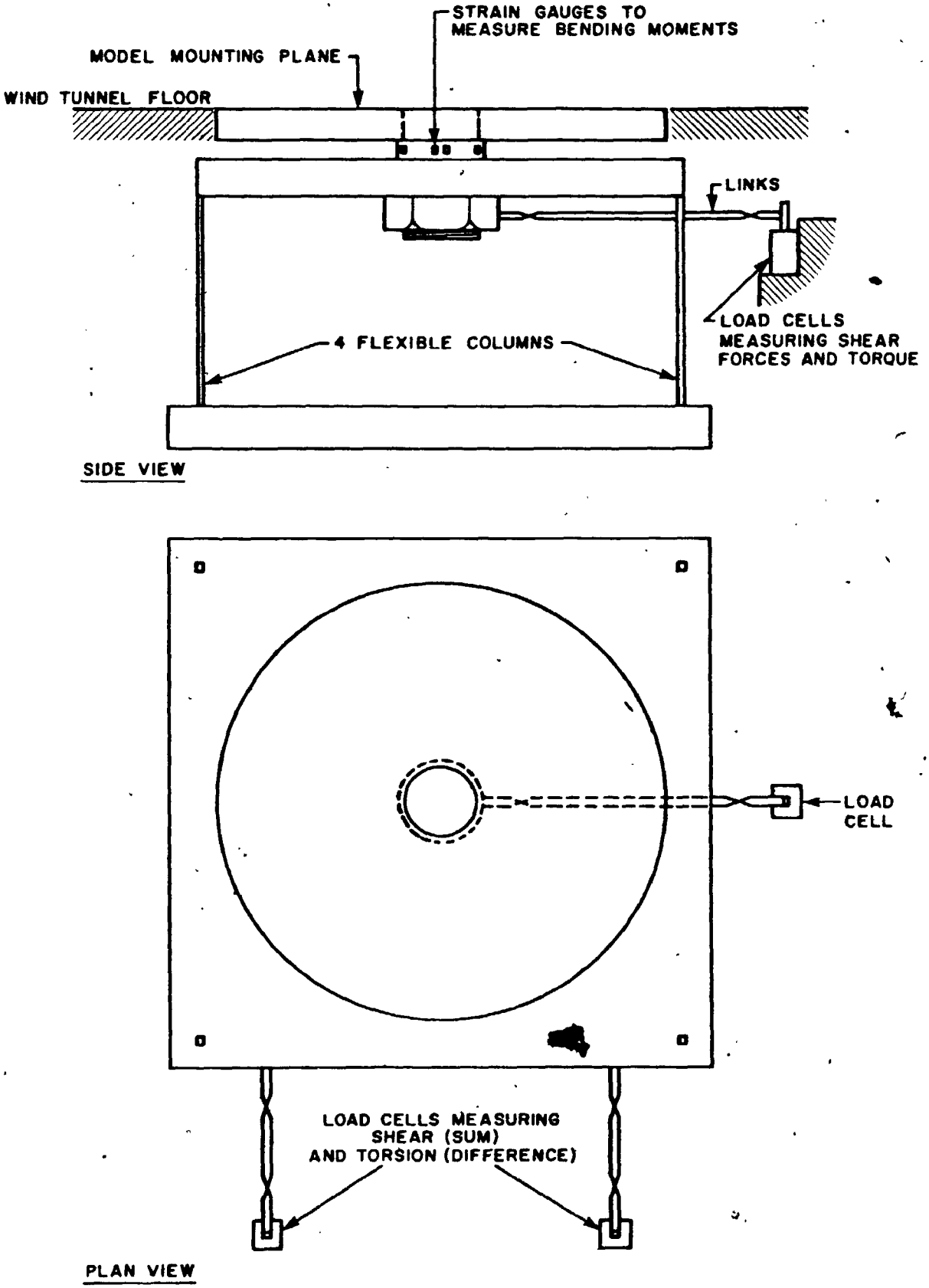

FIG. 1.5 PROTOTYPE OF FIVE-COMPONENT BALANCE

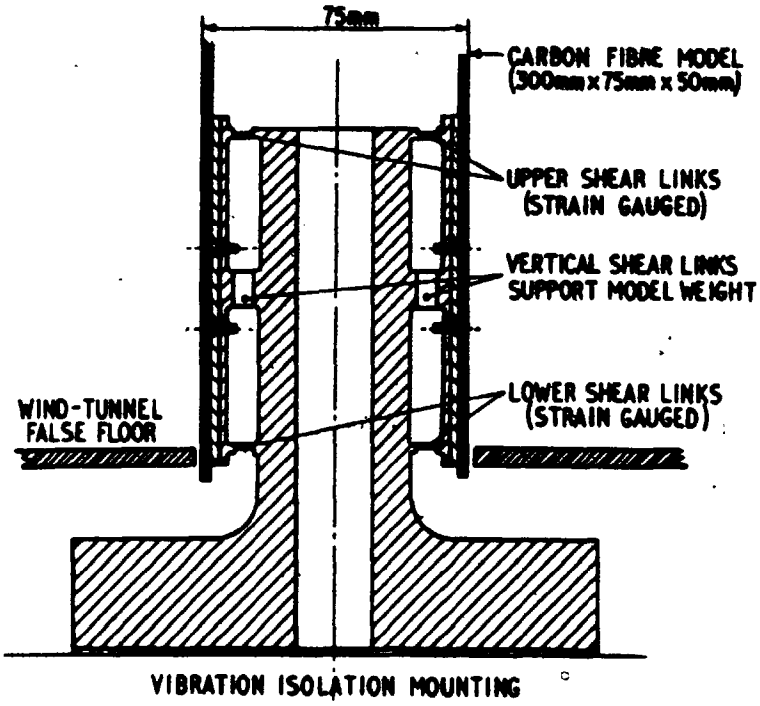

FIG. 1.6 WHITBREAD'S [1975] TWO-COMPONENT BALANCE

150 μin/in/lb-in (1327 μm/m/Nm) and 600 μin/in/lb (135 μm/m/N) respectively, for the new five-component balance of the BLWT. Whitbread's [1975] balance is designed for one time use only and, as mentioned above, measures only two components. The system, being statically indeterminate, is sensitive to temperature effects. Some problems were experienced with the shear force calibrations. Noticeable is the good frequency response and this subject is discussed at greater length below and in Chapter II.

A flexible approach is offered by the quartz multicomponent platform built by the Kistler Instrumente AG in Wintherthur, Switzerland, designed primarily for biomedical applications. The Building Research Station in Watford, England uses this system for conventional wind tunnel studies. The platform measures all six components simultaneously with piezoelectric transducers. Many requirements for an ideal force balance, such as stiffness, sensitivity and ruggedness, are excelled. Imperfections include

(1) the slow zero drift associated with piezoelectric transducers, which can be corrected in some cases at the end of the test, and (2) some temperature drift. Coupling of orthogonal components is not a problem according to the specifications, but this may not be fully verified. The system is expensive compared to strain gauge transducers, partly because of the advanced electronics of the charge amplifiers. For dynamic measurements this method is probably the most advanced state of the art, and further improvements in electronics and design could make it the best choice in every application.

The piezoelectric force transducers and electronics are also available separately and can be used for custom-made balances. Bridel [1978] designed and built a six-component balance, which is in principle similar to the final design of the new five-component balance of the BLWT. The piezoelectric transducers are superior in stiffness and output criteria, but have some disadvantages as mentioned above for the Kistler piezoelectric measuring platform. This balance and the BLWT balance were designed independently and during the same time period.

Aeronautical wind tunnels have different requirements for force measurements than boundary layer wind tunnels. Because of the different types of models tested, sting type balances are frequently used. An extensive survey of this type and other designs used in French wind tunnels was presented by Rebuffet [1956], and for wind tunnels in the United Kingdom by Anderson [1956]. All the described balances are strain gauged designs.

Extensive endeavors have not only been done by research laboratories, but also by industry, i.e. the Anglo-Swedish strain gauge balance collaboration by TEM and ROLLAB. Users of multicomponent balances might find a standard model "off the shelf" which meets their requirements and is likely to be cheaper than developing a new balance system.

1.4 NEW BLWT FIVE–COMPONENT BALANCE

1.4.1 Introduction

From the different balance configurations described in Section 1.3 evolved a new balance design, believed to represent the best compromise for the applicable load ranges. The intended application, to measure the total dynamic load, requires a high frequency response. In order to achieve maximum rigidity, the measurement of vertical forces was forgone. The remaining five components are measured with respect to the turntable centre and at the base of the building model, as indicated in Fig. 1.7. The photograph shows the finished balance with a typical building model.

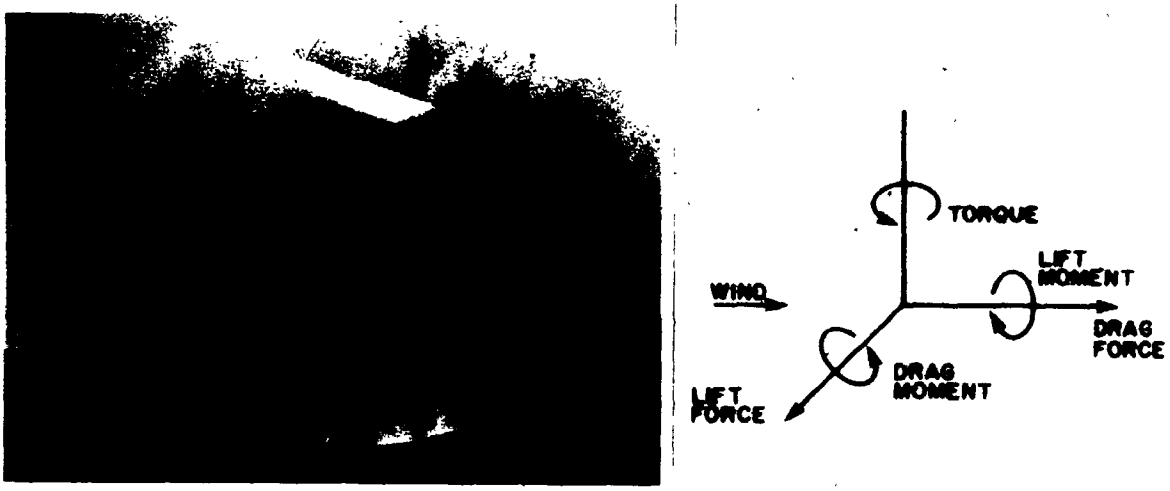

FIG. 1.7 PHOTO OF BLWT FORCE BALANCE WITH INDICATION OF THE FIVE MEASURED FORCE COMPONENTS

The principle of operation and the design and construction of the critical components is now described in detail.

1.4.2 Principles of Operation

The balance system is basically a statically determinate frame with a rigid girder,

force links, and miniature load cells. The instantaneous force is split into orthogonal force components. Fig. 1.8 is a schematic diagram of the cross-section in one direction.

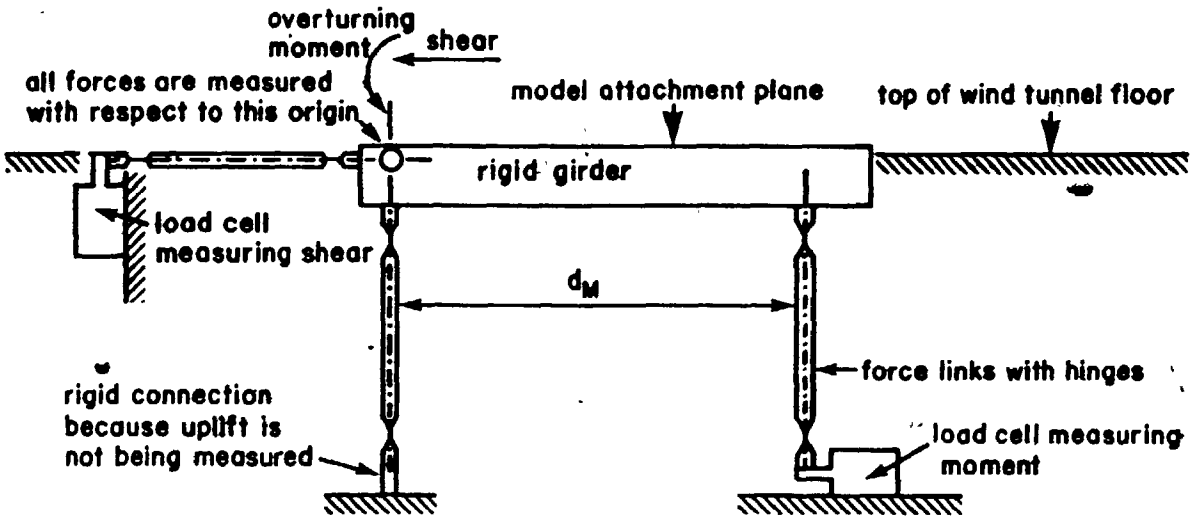

FIG. 1.8 SCHEMATIC CROSS-SECTION FOR MEASURING FORCES IN ONE PLANE

The rigid girder preserves the structural integrity, and the force links split up the instantaneous forces. Acting forces in this plane are the base shear, base overturning moment, and the uplift force. The force links are rigid in the axial direction, but have hinges near each end. Because no moments are transferred through the hinges, only axial forces can be transmitted by the force links, acting exactly through the centre line of the hinges, i.e. through the centre line of the force links. Solving the three equilibrium conditions in this plane ($\Sigma H = 0$, $\Sigma V = 0$, $\Sigma M = 0$; the sum of horizontal forces vertical forces and moments), leads directly to the decomposition of the forces indicated in Fig. 1.8. The origin, to which the output of the load cells is related, is at the elevation of the horizontal force link, and above the centre line of the column on the rigid support. The location where the model is mounted has no influence on the transducer output, but the vertical centre line of the model is usually made to coincide with the origin to which the forces are referenced, i.e. above the fixed column. Deformations are kept to less than 0.0005 inch (13 μm) for maximum loads, making second order effects, such as coupling between orthogonal force components, virtually nonexistent.

The uplift force flows directly into the mounting platform and is not measured. If desired, however, this force could be measured as well by supporting the column by a third load cell, in which case no change would occur in any other detail described above. The only additional difficulties may be expected in the assembly of the balance, and in a decrease in its ruggedness.

The cross-section in the perpendicular direction is similar, except that two shear load cells are required. At least one of the load cells has to be out of the plane defined by the vertical columns to provide rigidity to the torsional moments. This is shown schematically in the plan view of Fig. 1.9.

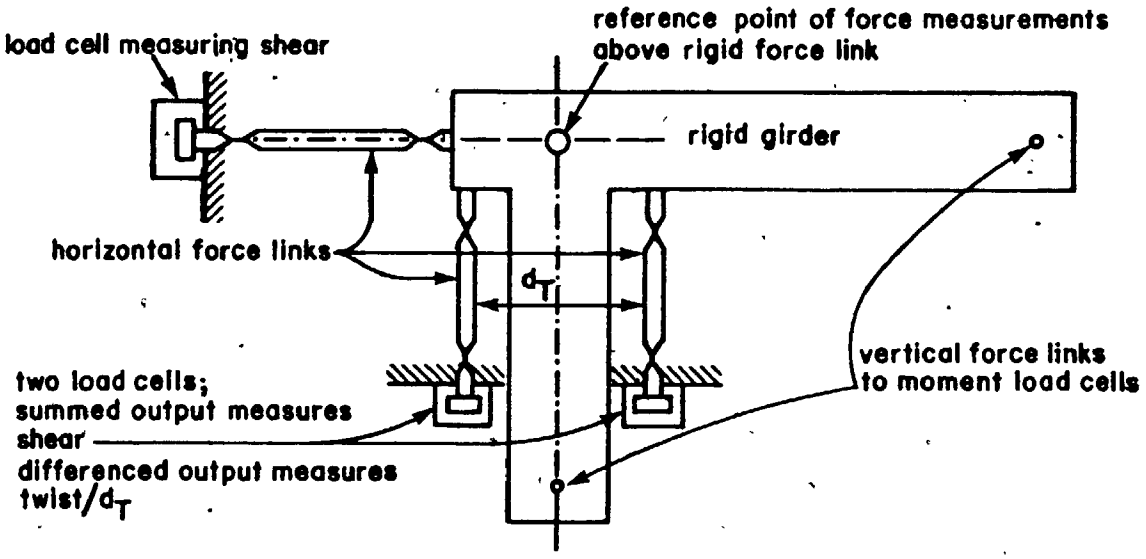

FIG. 1.9 SCHEMATIC PLAN VIEW OF THE FIVE-COMPONENT BALANCE

Both of the two load cells are shown offset from the plane formed by the vertical columns, by a distance $d_T/2$, as adopted for the final design of the BLWT five-component balance. In this way it was possible to use the same capacity load cells and details for all five required places. The force and torsional moment are measured by electronic summing and differencing of the output signal from the two load cells. The electronics are simple, but the method relies on exactly the same gain of the two shear load cells and no drift, creep, hysteresis or nonlinearities should be present. The twist, usually a small value, is formed as the difference of two larger values for the shear

force. Experience from applications of the balance suggests that the above mentioned critical assumptions are not always ideally met, leading to small apparent coupling terms between the torque and the shear in one direction. As an improvement it is suggested to place only one load cell out of the plane to give torsional rigidity and directly measuring the torsional moment, without differencing. For the shear, however, the two signals still have to be summed.

The dimensions of the column spacings d_M and d_T have to be chosen to achieve high rigidity, but at the same time to provide enough output from the load cells to measure the loads accurately. Optimization studies show that the distances between the columns should be of the same order as the model height, and 4 inches is a good compromise for the intermediate size building models intended to be studied. Interchanging load cells of higher or lower capacity makes this balance applicable to practically all scale models to be tested in the Boundary Layer Wind Tunnel Laboratory.

A photo of the balance with the top plate removed is shown in Fig. 1.10. The girder, the three horizontal force links and three load cells are visible. The load cells are mounted on elaborate overload protection devices, described in detail in Section 1.4.3.3.

The underside of the balance with the bottom plate removed is shown in Fig. 1.11. The two load cells measuring the overturning moments and the support for the column without a load cell are visible.

The balance system, being statically determinate, is totally insensitive to temperature gradients and support displacements. Slight fabrication tolerances have virtually no effect on the forces to be measured. The main efforts have to be concentrated on rigid construction, and on designing and fabricating supreme load cells. The cost of fabrication is high due to the many parts which have to be manufactured. Details of the design and the fabrication of the balance are now described.

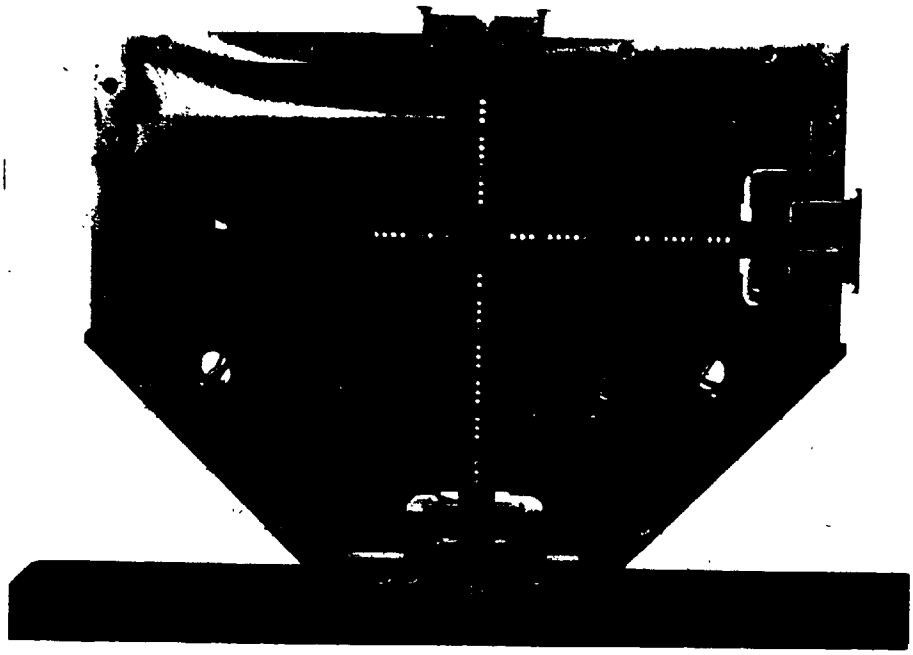

FIG. 1.10 PHOTO OF THE TOP OF THE BALANCE WITH THE TOP PLATE REMOVED

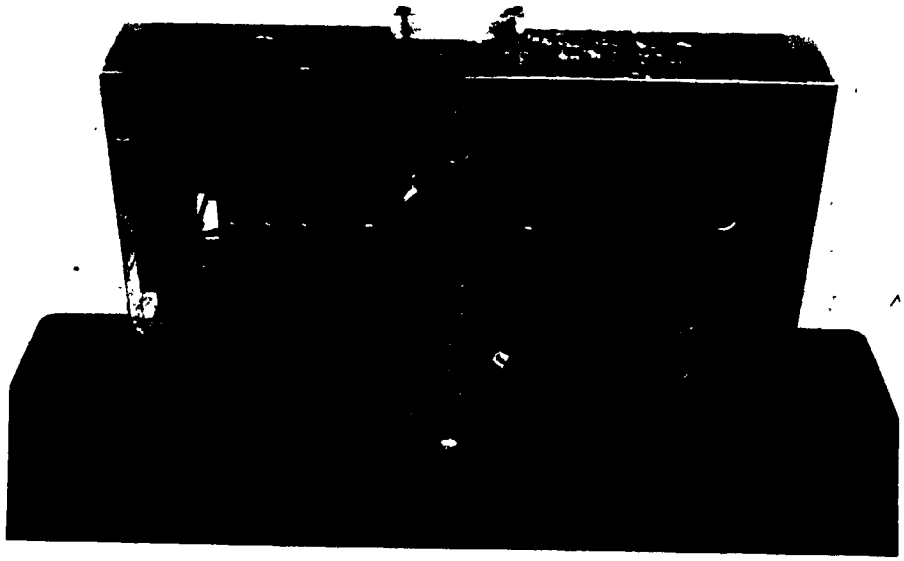

FIG. 1.11 PHOTO OF THE UNDERSIDE OF THE BALANCE WITH THE BOTTOM PLATE REMOVED

1.4.3 Design and Fabrication Details of the Balance

1.4.3.1 The girder

The girder of the balance has to serve two functions: (1) as a base which permits easy fastening of the building models, and (2) as the preservation of structural integrity, so that all force components remain in the linear range. These requirements can be satisfied with a heavy member, but an optimum light mass has to be found which does not reduce the natural frequencies of the balance-model combinations while preserving the rigidity requirements. A photo of the underside of the final girder, machined from AZ31B Magnesium alloy, is shown in Fig. 1.12. Models are fastened to the girder by screws through the holes visible in the girder, into the base plate of the models. Some prototype force links were attached only to indicate the location of the operational ones.

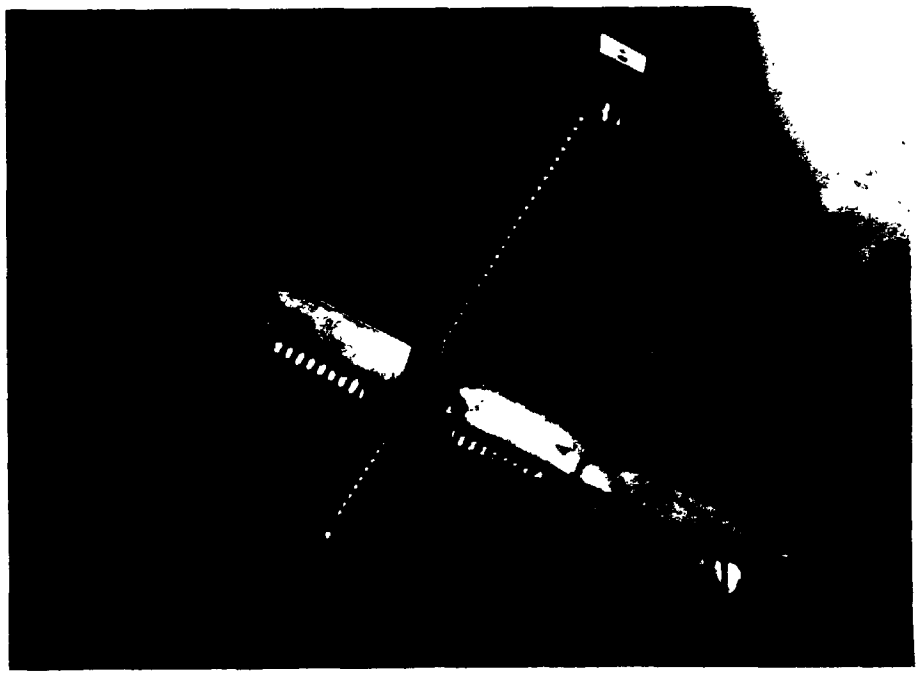

FIG. 1.12 PHOTO OF THE GIRDER OF THE BALANCE

A plan view of the girder with the critical dimensions is shown in Fig. 1.13.

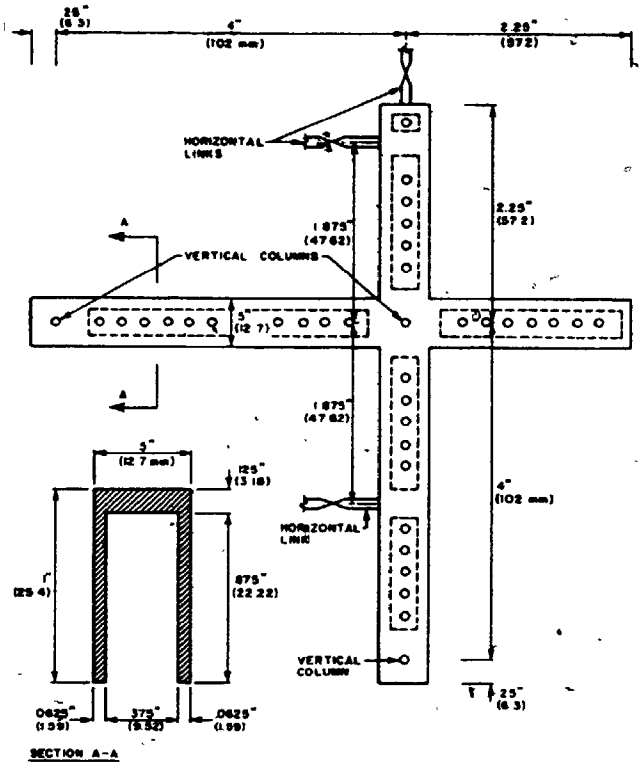

FIG. 1.13 PLAN VIEW OF THE GIRDER WITH DIMENSIONS

1.4.3.2 The force links

The only requirement for the force links are high axial rigidity, two hinges or good hinge approximations near the end, and sufficient safety against buckling. A suitable compromise was found using 1/16 inch (1.59 mm) brass rods and turned down to 0.01 inch near the end as shown in Fig. 1.14. Force links are also visible in Fig. 1.12. The rate of breakage during fabrication is high but of no consequence, as many can be machined in a short time. None broke in use of the balance to this date.

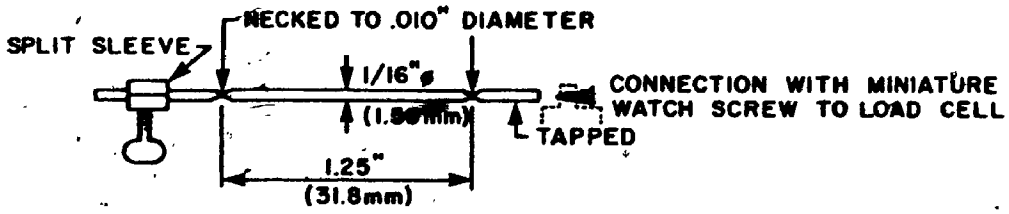

FIG. 1.14 FORCE LINKS WITH CONNECTIONS

The connections to the load cells and girder required investigations with prototypes. It is advisable in general to machine the whole transducer system from one homogeneous piece of material, to avoid degrading effects on the stiffness and hysteresis from connections. A miniature connection to the load cells was found using watch screws. The brass force links permitted easy tapping for the threads. The connection to the girder was studied by pull-out tests. The best connection would have been LOCTITE cement: 0.25 inch (6.4 mm) long embedding gave a stiffness in the order of 50,000 lbs/inch (8.8×10^6 N/m). A glued connection, however, would not enable replacing a damaged link. The next best solution was found using a split sleeve compressed by a lateral screw from the girder. This gives a stiffness in the order of 30,000 lbs/inch (5.3×10^6 N/m), approximately the same value as for the force links and sufficiently larger than the value of the load cells, and does not degrade the overall stiffness significantly.

1.4.3.3 The overload protection devices

Typical wind forces transmitted to the load cells for medium rise buildings amount to only ± 1 lb (4.5 N). Although this range would rarely be exceeded, higher risk of damage occurs from handling the balance and mounting the models. Usually protection can be accomplished by mechanical stops, but the rigid nature of this balance would need clearances of less than 0.001 inches (.025 mm). The displacements of the moving parts of the balance under maximum loads are less than .0005 inches (0.0125 mm), of the same order as deformations due to temperature.

The solution was to mount the load cells on precompressed spring mechanisms, where the displacement remains zero until the precompression load is exceeded. At the critical load the devices give way, without increasing the forces on the load cells any further. Mechanical stops limit the displacements of the girder in any direction to 0.010 inches (0.25 mm), absorbing any load after the overload protection devices are displaced by this amount. The stops, having small pins, can be seen in Fig. 1.10 at the end of each arm of the girder.

Requirements for the devices to work bi-directionally add considerable complexity. A prototype using knife edge type supports on a plane parallel to the force, prestressed

by springs, failed to remain rigid for the full range of the safe load and had to be rejected. An improved device which is working well is shown in Fig. 1.15. The devices are applicable to any load range, the springs can be exchanged for load cells with different loading capacities. Brass was used for easy machining of all parts, since there were no special requirements for a particular material.

These devices were essential during the assembly of the balance and may also be required for higher capacity balances. The mechanical stops were temporarily replaced to provide no clearance and the connections were tightened at each end of the force links. It was impossible to assemble the balance to less than 0.0005 inches (0.01 mm) tolerance and the overload protection devices protected the load cells already during the assembly. The mechanical stops were replaced with the ones providing clearance and those devices have protected the balance from failures to this date.

1.4.4 The Load Cells

1.4.4.1 Requirements

The range of forces to be measured for the building models and balance dimensions is of the order of ± 1 lb. (4.5 N). The stiffness should be at least 1500 lbs/inch (0.25×10^6 N/m) to insure a high natural frequency for the balance – model combination. Strains can be measured with confidence to approximately 1 $\mu\epsilon$ and a desirable output for the largest wind induced loads should be approximately 600 $\mu\epsilon$ (micro-strains). This gives a safety factor of at least 2.5 for all elements of the balance.

The dynamic range of the forces, however, is large. It is roughly linearly dependent on the building width, quadratically dependent on the building height and velocity, and otherwise dependent on surrounding terrain and dynamic effects. Therefore, conditions with smaller loads produce strains only of the order of 6 $\mu\epsilon$, which have to be measured with sufficient accuracy.

The load cells are the key to the performance of the balance. Since commercially bought load cells performed much worse than indicated by the specifications, it was

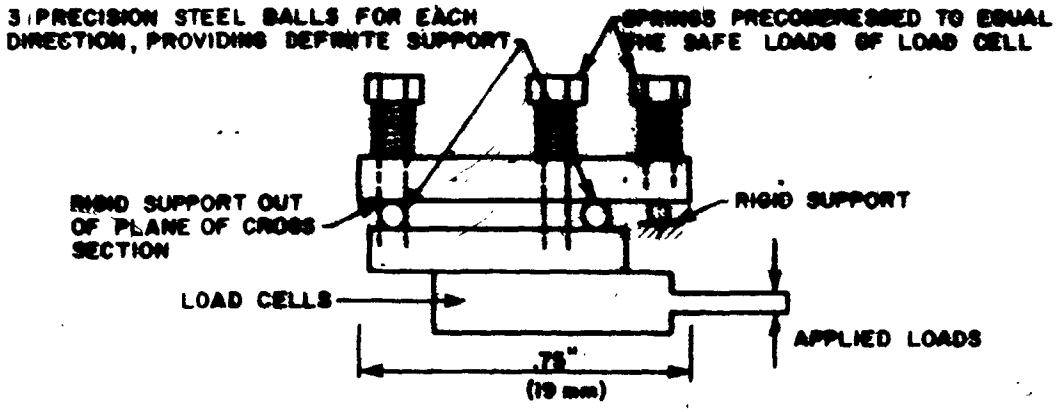

a) SCHEMATIC CROSS SECTION OF DEVICE WITHIN NORMAL ±LOAD RANGE

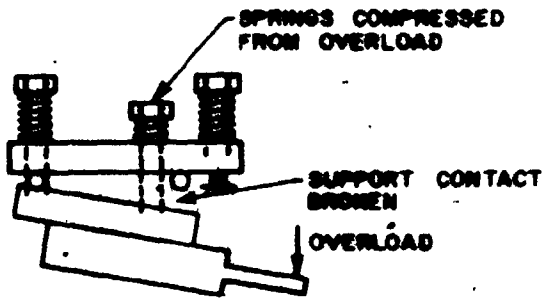

b) SCHEMATIC DIAGRAM OF OVERLOAD DOWNWARDS

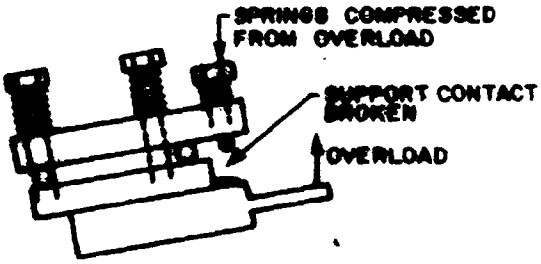

c) SCHEMATIC DIAGRAM OF OVERLOAD UPWARDS

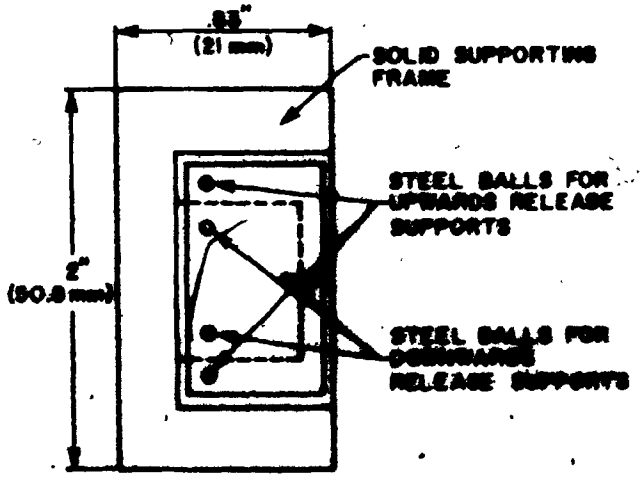

d) PLAN VIEW

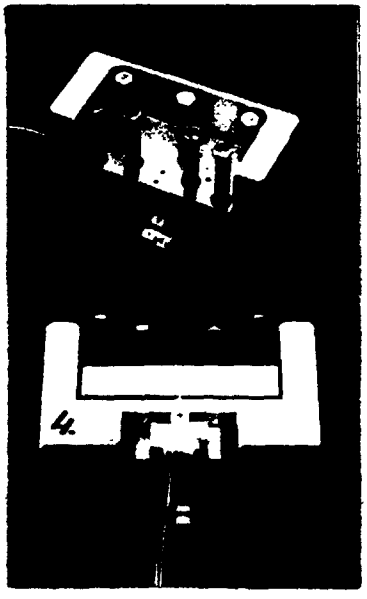

e) PHOTOS OF TWO VIEWS OF THE DEVICES WITH MOUNTED LOAD CELLS

FIG. 1.15 OVERLOAD PROTECTION DEVICES

necessary to develop new load cells. Manufacturers of commercial load cells are more concerned about sensitivity and other parameters than about stiffness.

An overview of force transducers used in wind tunnels is given in Section 1.4.4.2 and the design of the load cell used in the five-component BLWT balance is presented in Section 1.4.4.3.

1.4.4.2 Force transducers

The force transducers are the key elements for the good performance of a balance. An overview of various types, usable in wind tunnel applications, is given below. Only the bending beam type gives a suitable compromise to all the requirements present for the new five-component BLWT balance, all other types are rejected because of the small required load capacity, insufficient technical development at this time, or other shortcomings. For different load ranges or applications another type might be more suitable and the comprehensive treatment of various types is given as an aid to designers of future balances.

1.4.4.2.1 Axial strain transducer

A simple force transducer can be formed by cementing a pair of strain gauges on the sides of a prismatic member, which is stressed by axial loads. The output from the gauges is proportional to the applied load. The strain, ϵ, the stiffness, k, and the stiffness times strain product, $k\epsilon$ per unit load (the performance rating described in Section 1.2), are:

$$\epsilon = \frac{1}{AE} \times P \qquad (1.1a)$$

$$k = \frac{AE}{L} \qquad (1.1b)$$

$$\frac{k\epsilon}{P} = \frac{1}{L} \qquad (1.1c)$$

where P is the load, A the cross-sectional area, E the modulus of elasticity, and L the length of the member. The effective $k\epsilon$ product should only be taken as ½ the value of equation (1.1c) for comparative purposes with other 4-arm bridge transducers with tension and compression strains, which add in a Wheatstone bridge circuit.

Assuming a square section of aluminium 0.02 inch by 0.02 inch (.5 mm x .5 mm) cross section, 0.5 inch (12.7 mm) long and 1 lb (4.45 N) load results in:

$$\epsilon = \frac{1\ lb}{.03\ in \times .03\ in \times 10 \times 10^6\ lb/in^2} = 111 \times 10^{-6}\ in/in/lb\ (24.5 \times 10^{-6}\ \epsilon/N)$$

$$k = \frac{.03\ in \times .03\ in \times 10 \times 10^6\ lb/in^2}{.5\ in} = 18{,}000\ lb/in\ (3.15 \times 10^6\ N/m)$$

$$\frac{k\epsilon}{P} = \frac{1}{.5\ in} \times \frac{1}{2}\ (penalty) = 1.0\ \frac{in/in}{in}\ (39.4\ \epsilon/m)$$

The above beam with minimum usable dimensions does not produce enough strain and is, hence, not applicable to the BLWT balance design. The minimal dimensions also would not permit the mounting of transverse gauges for temperature compensation. This type of force transducer is suitable for very heavy loads, i.e. truck loading stations, silo gross weight, etc.

1.4.4.2.2 Shear strain transducers

Flexures can be strain gauged to measure the direct strain resulting from shear. The maximum strain in a diagonally oriented gauge at the centre line of a web, the stiffness, and the strain times stiffness product, based on simple theory for a cantilever, are:

$$e = \frac{.75}{A \times G} \times P \qquad (1.2a)$$

$$k = \frac{G \times 5/6A}{L} \qquad (1.2b)$$

$$\frac{k\epsilon}{P} = \frac{5}{8L} \qquad (1.2c)$$

where A is the cross-sectional area and G the shear modulus. Note the good attribute: the strain is not dependent on the distance of the load application point.

Inspecting equation (1.2c) shows that for a high $k\epsilon$ product the length should be short. For practical purposes it would also be best to use a thin web and material with a low shear modulus, which would result in a larger area to mount the gauges. Unless gauge rosettes are to be used, the effective $k\epsilon$ product should also be penalized by about one half for comparative purposes.

Assuming a prismatic cantilever of aluminium, .3 inches (7.6 mm) long, .3 inches (7.6 mm) deep and .015 inches (.381 mm) wide gives for a load of 1 lb (4.45 N):

$$\epsilon = \frac{.75}{.3\ in \times .015\ in \times 3.3 \times 10^6\ lb/in^2} \times 1\ lb = 50.5 \times 10^{-6}\ in/in/lb\ (11.34 \times 10^{-6}\ \epsilon/N)$$

$$k = \frac{3.3 \times 10^6\ lb/in^2 \times 5/6 \times .3\ in \times .05\ in}{.3\ in} = 41250\ lb/in \qquad (7.23 \times 10^6\ N/m)$$

$$\frac{k\epsilon}{P} = \frac{5}{8 \times .3\ in} = 2.08\ in/in/in \qquad (81.9\ \epsilon/m)$$

The above beam with minimum usable dimensions does not produce enough strain and is, hence, now applicable for the BLWT balance. This type, however, might be useful for higher load ranges.

In practical applications it is necessary to improve the stability by machining an I-profile in the region of the strain gauges, and to keep the width of the section large at other places. An apparently efficient design described by Gommers [1978/1981] is shown in Fig. 1.16. The device has a high stress strain product for short length transducers. The strain is:

$$\epsilon = 1.5 \times \frac{P\,L^2}{8\,EI}\left(\frac{h}{s} + 1\right) \qquad (1.2d)$$

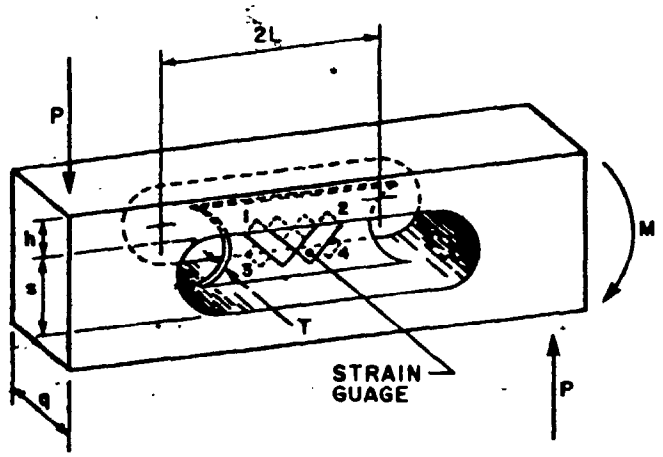

FIG. 1.16 PRACTICAL SHEAR STRAIN SENSING TRANSDUCERS
(After Gommers, 1978/1981)

1.4.4.2.3 Bending beam transducers

Forces can be measured by relating bending strains to applied forces. A suitable arrangement of the strain gauges and electric circuit to form a Wheatstone bridge is shown in Fig. 1.2. Although the bending beam could have any support conditions, it is most advantageous to use a cantilever, which is not sensitive to the rigidity of the fixed end or to strains due to temperature effects. For a prismatic member, the strain, stiffness and stiffness times strain product, based on simple theory for cantilevers, are:

$$\epsilon = \frac{d/2\, L'}{EI} \times P \qquad (1.3a)$$

$$k = \frac{3\, EI}{L^3} \qquad (1.3b)$$

$$\frac{k\epsilon}{P} = \frac{3 \times \frac{d}{2}\, L'}{L^3} \qquad (1.3c)$$

where L' is the distance from the load to the centre line of the strain gauge, L is the distance from the load to the support, d is the depth of the section, and I is the moment of inertia of the cross section.

Inspecting equation (1.3c) shows that for a high $k\epsilon$ product the beam should be deep (i.e. use a low modulus of elasticity), have a long distance to the gauges (i.e. use small gauges) and a short length L. The length has the most significant effect and miniaturization is the key to a high $k\epsilon$ product.

Assuming a beam of aluminium of 0.06 inch (1.5 mm) width, 0.05 inch (1.3 mm) depth, 0.175 inch (4.45 mm) length (for both L and L') and a load of 1 lb (4.45 N) gives:

$$\epsilon = \frac{.025\ in \times .175\ in}{10 \times 10^6\ lb/in^2 \times \frac{.06\ in \times .05^3\ in^2}{12}} \times 1\ lb = 700 \times 10^{-6}\ \frac{in/in}{lb}\ (157.3 \times 10^{-6}\ \epsilon/N)$$

$$k = \frac{3 \times 10 \times 10^6\ lb/in^2\ \frac{.06\ in \times 0.05^3\ in^3}{12}}{.175^2} = 3\,498\ lb/in \qquad (0.613 \times 10^6\ N/m)$$

$$\frac{k\epsilon}{P} = \frac{3 \times .025\ in \times .175\ in}{.175^3\ in^3} = 2.45\ \frac{in/in}{in} \qquad (96.4\ \epsilon/m)$$

These values satisfy the minimum requirements described in Section 1.4.4.1, and show that this type is applicable to the small load range required. The effective mechanical amplification of this transducer type makes it suitable to a wide range of loads.

This type is employed in the new five-component BLWT balance, and is described in detail in Section 1.4.4.3. Note that the load has to be at an accurate and reproducible distance, a criterion which is satisfied by the construction with force links of the BLWT balance.

Both balances shown in Fig. 1.3 and Fig. 1.4 measure bending strains to determine forces. As a variation, strain gauges can be located at several places along the length of the cantilever. By appropriate summing and differencing of the output it is possible to measure multiple force components. The $k\epsilon$ product, however, is greatly reduced. If the resultant loads act inside the gauged part of this system, it is referred to as a sting balance in aeronautical wind tunnels. If the resultant load acts outside the gauged part, it is referred to as a wall balance.

1.4.4.2.4 Other types of strain gauged transducers

By machining homogeneous material to different shapes, an almost infinite number of variations of transducers can be derived. One example is the ring force transducer, which has strain gauges at two diagonally opposite places. Loading the ring in the plane of the ring, perpendicular to this diagonal results in an output from the gauges, which is proportional to the force. This type of load cell is used in numerous wind tunnel balances [Rebuffet, 1956], but was found not feasible for the five-component BLWT balance.

None of the many other types of strain gauged transducers investigated was found to be applicable.

1.4.4.2.5 Unbonded strain gauge transducers

Tensile or compressive forces can be measured with transducers using non-adhesive type resistance wires. Such devices are commercially available, i.e. by Kyowa, Japan or by Pioden Controls, Ltd., Canterbury, England. Many load transducers of this type are used in wind tunnel balances. For load cells of 1 lb (4.45 N) capacity, the stiffness is apparently around 900 lb/inch (0.158 x 10^6 N/m), much less than required in Section 1.4.4.1. The accuracy is specified as 1%, worse than the 0.2% expected from bending beam type transducers. The physical size of typically 2 x 1.3 x 7 inches (50 x 33 x 180 mm) is large and might obstruct the wind flow in some applications.

1.4.4.2.6 Linear variable differential transformers (LVDT's)

These are not force measuring devices in the strict sense, but are capable of measuring small displacements. If used to measure linear deformations of a load carrying member their output is proportional to the load, i.e. they could be used to measure the displacements of a frame such as shown in Fig. 1.4. LVDT's are not strained, and are, hence, not damaged. There is, however, no possibility to eliminate drift due to temperature deformations of the load carrying member, and even in dynamic applications the accuracy is not better than for the bending beam type transducers.

1.4.4.2.7 Integrated semi-conductor sensors

Semiconductor gauges (described in Section 1.4.4.5.1) can be manufactured and arranged as a four arm Wheatstone bridge on a silicon substratum of any desirable thickness. The monocrystalline system is theoretically a perfect elastic material, without creep and hysteresis. The sensor is atomically bonded with the substrate, and since there is no differential expansion from temperature; the drift is negligible. The voltage output is fifty times higher than from foil gauges and small physical sizes are possible. Custom manufactured elements are economically feasible and prototypes of the size .02 x .02 x .1 inch (0.5 x 0.5 x 2.5 mm) were tried out. These devices are very brittle (like glass), and unfortunately, no solution was found for clamping and loading fixtures.

1.4.4.2.8 Passive piezoelectric transducers

The piezoelectric effect is the interaction of mechanical and electrical stress-strain variables in a medium. Crystal classes which do not possess a centre of symmetry develop polarization parallel to the strain. Piezoelectric polarization is proportional to the strain, and is linear and reversed when the strain changes from compression to tension. Quartz is used most often, because of its great mechanical strength, and cutting the transducer at different directions with respect to the crystal grid makes the transducer sensitive to shears or normal forces. The electric charge at the opposing surfaces can be tapped by electrodes and amplified and converted to a voltage using an electronic charge amplifer.

Since the transducer does not rely on mechanical magnification of the strain, such as the bending beam transducer, the stiffness can be made much higher than for strain gauged transducers. The devices are rugged and allow ratios of maximum to minimum loads of 10^4 to be resolved. Bridel [1978] employed transducers of 112 lbs (500 N) capacity in his balance. The transducers and amplifiers are commercially available from Kistler Instrumente AG in Winterthur, Switzerland. A description of piezoelectric transducers and piezoelectric theory can be found in Spescha and Volle (n.d.).

Piezoelectric transducers and the elaborate electronic charge amplifiers are expensive. These instruments also drift with time due to discharge. This is not critical for short time force measurements, such as impact loads, but for force measurements of several minutes duration the zero has to be measured before and after each test and corrections have to be made on the measured values. This was judged to be not acceptable for the five-component BLWT balance, since a drift free time history was desired for nonlinear response determinations of building. Further improvements in electronics and transducer design could, however, make this transducer system competitive with other systems.

1.4.4.2.9 Resonating Piezoelectric Transducers

The piezoelectric effect can also be employed inversely to cause a crystal to expand or contract by application of an electric field. If the field is varied rapidly at a natural frequency of the quartz members it will respond to vigorous resonant vibrations. This effect is used, for instance, in quartz watches as the frequency reference for timekeeping.

From the theory of dynamics it is known that the natural frequency of a stressed column depends on the supporting load. A practical application of this phenomenon is used by miners by hitting supporting columns with a hammer and listening to the sound, a lower sound indicating problems of overload. If a quartz crystal column is driven at resonance, the frequency is a predictable function of the load. Referenced to a stable frequency source, much higher than the resonating frequency, the amount of deviation from the zero loading position can be accurately predicted. A schematic description of the piezoelectric crystal and the resonator is shown in Fig. 1.17.

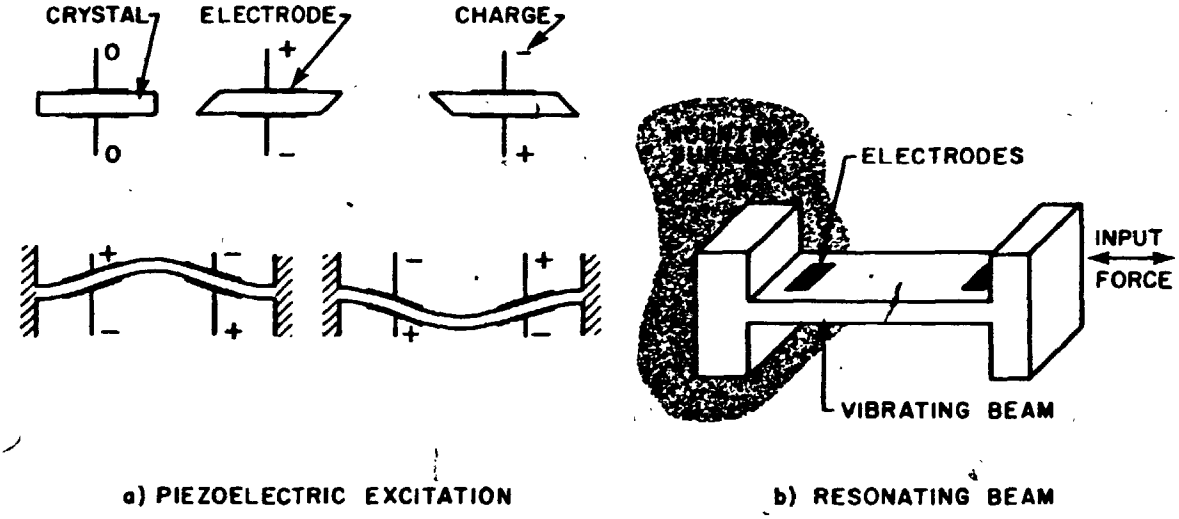

FIG. 1.17 QUARTZ CRYSTAL RESONATOR

The inherent stability of quartz crystals and frequency measurements would make it an excellent measuring system. The output would not be in the form of an analog voltage, but a digital value, i.e. the number of vibrations in the sampled period. This could be used directly as input to the computer data acquisition system, without need of the usual filtering and analog to digital conversion. The computer would then

translate the number of vibrations to an average load during the sampling period. The trend to digital information processing is well advanced in other fields.

No commercial application to dynamic load measurements is known to the author at this time, but the system is used in a high precision digital static pressure transducer by Paroscientific, Inc. Redmond, Washington [Paros, 1976]. The nominal frequency of the oscillating beam is 40,000 Hz, and as an illustration of its accuracy, the null stability for six months is given as 0.008%. It is virtually insensitive to temperature and has a high rigidity.

Theoretically an active piezoelectric transducer system shows many advantages over any other force transducer. The development of a working system, however, was beyond the scope of this study. Practical problems include the placing of the crystal in a high vacuum, and the development of electronic circuits. The performance, however, may be close to an ideal force transducer.

1.4.4.2.10 Discussion

Of the simple transducers it is shown that the bending beam type offers good performance. Passive piezoelectric transducers are expensive and have problems with drift, but otherwise have good attributes. Resonating piezoelectric transducers have not been developed at this time for dynamic force measurements, but show great promise. For the five-component BLWT balance it was decided to design a bending beam type transducer for the best possible performance. This force transducer is now described.

1.4.4.3 The machined bending beams

A basic description of bending beam transducers is given in Section 1.4.4.2.3. The details of the machined bending beams and refined equations are presented in this section. Miniaturization is essential for good performance; as described in Section 1.4.4.2.3 the beam should be short and deep, and the strain gauges should be small. Further improvements result if the beam is weakened only for the length of the gauges. An empirical rule which is valid for any strain gauged transducer is: to take as much

material away for the length of the gauges and keep heavier sections elsewhere.

The dimensions for the optimized stiffness times strain output transducer are shown in Figure 1.18. The width and length of the weakened part of the cantilever depend on the size of the smallest suitable strain gauges. The depth has been selected to give approximately 600 μ strain for the full scale load of 1 lb. For gauges with large terminals it is advantageous to locate the terminals as indicated in Figure 1.18 in order to keep the weakened length small.

The average strain at the strain gauge for the bending beam for 1 lb (4.45 N) load as given by equation (1.3a) is:

$$\epsilon = \frac{d/2 \times L'}{EI} \times P = \frac{1\ lb \times .145\ in \times .024\ in}{10.4 \times 10^6 \frac{lb}{in^2} \times \frac{.060\ in\ (0.048\ in)^3}{12}} = 605\ \mu\epsilon/lb\ (136\ \mu\epsilon/N)$$

The displacement, δ_B, due to a unit load at the centre line of the load by elastic bending theory is:

$$\delta_B = \int_0^L \frac{M(x)\ x}{EI(x)}\ dx \qquad (1.4)$$

$$= \frac{1}{3 \times 10.4 \times 10^6 \frac{lb}{in^2}} \left[\frac{(.175^3 in - .115^3 in^3)}{\frac{.060\ in \times (.048\ in)^3}{12}} + \frac{.115^3 in^3}{\frac{.125\ in \times .118^3\ in^3}{12}} \right] = 0.00023\ in\ (0.0058\ mm)$$

where x is the distance from the load towards the support.

The short and deep beam produces elastic distortions in the support which allow the cantilever to rotate at the built-in end. This rotation produces a deflection in addition to that caused by the bending and shear stresses in the beam itself, and can be a significant addition

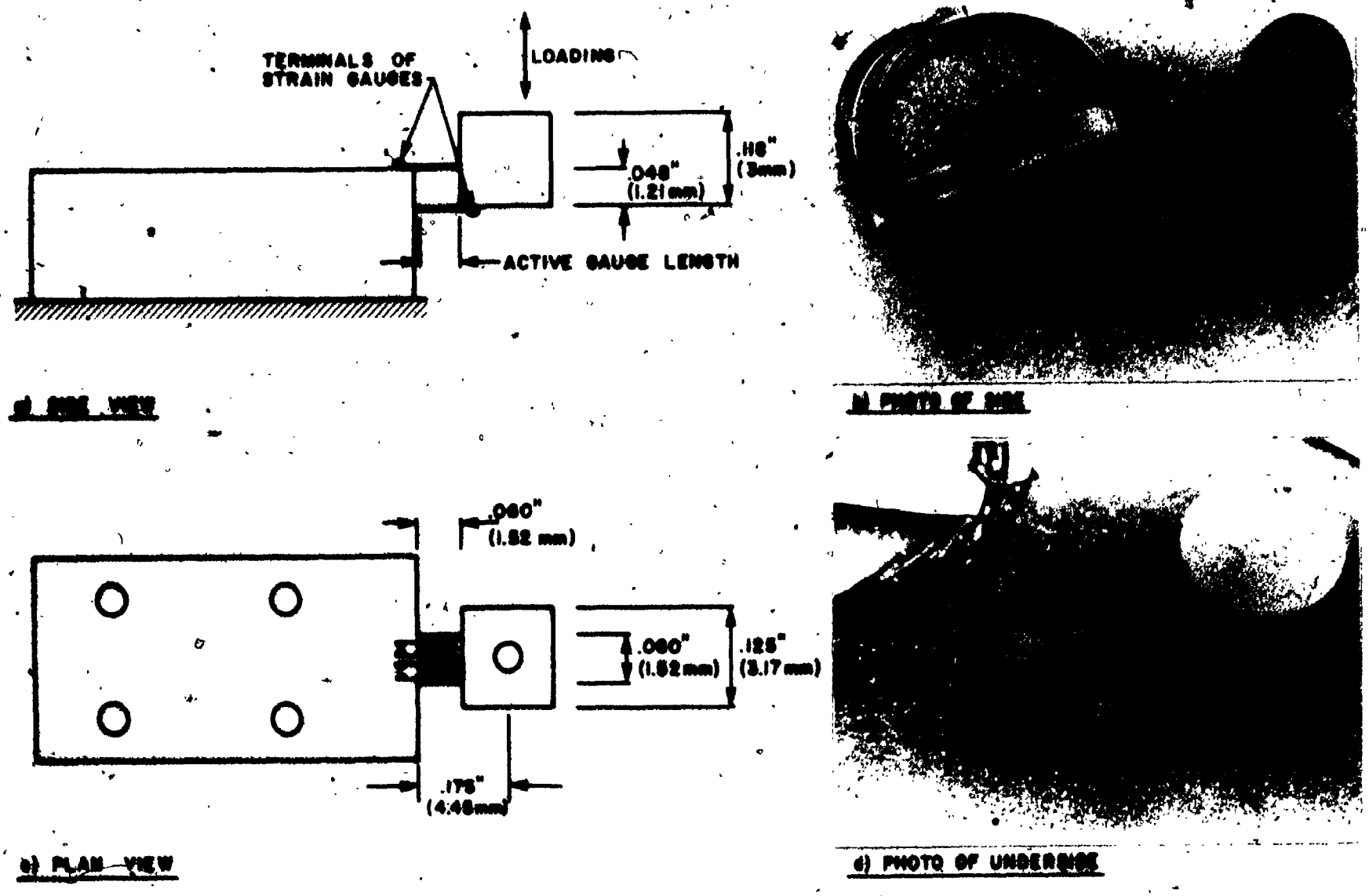

FIG. 1.18 BENDING BEAM FORCE TRANSDUCERS USED IN BLWT BALANCE

to the value given by equation (1.4). O'Donnel [1960] confirmed with experimental studies the equations derived by Timoshenko [1955] for the additional deflection of a cantilever due to the elasticity of the support. Ignoring the negligible shear term, the displacement due to support conditions δ_s is:

$$\delta_s = \frac{16.67 \times M_u \times x}{\pi E (h')^2} \qquad (1.5)$$

where M_u = Moment at support per unit width

h' = Effective depth of cantilever

For the beam in Fig. 1.18 this term is:

$$\delta_s = \frac{16.67 \times \frac{.175 \text{ lb in}}{.06 \text{ in}} \times .175 \text{ in}}{\pi \times 10.4 \times 10^6 \frac{\text{lb}}{\text{in}^2} \times (.048 \text{ in})^2} = 0.00011 \text{ in} \quad (0.0028 \text{ mm})$$

Adding the two contributions results in a total deflection of 0.00034 in (0.0086 mm) for a unit load of 1 lb (4.45 N), equivalent to a stiffness of 2.9 x 10^3 lbs/inch (0.51 x 10^6 N/m). The resulting stiffness times strain product is approximately 1.7 in/in/in (67 ϵ/m).

Experimental confirmation of the stiffness was difficult because of the small size of the transducer. The best method, which also allowed visual observation that the support did not move, was to use a microscope with an etched scale. This way the displacements were confirmed as 0.0003 ± 0.00005 inches (0.0076 ± 0.001 mm).

The effective stiffness for the balance assembly is reduced further by the deformations and connections of the force links, the subsidence of the load cells on the overload protection devices, and, significant for bending moments, the deformation of the girder. The effective stiffness times strain product of the balance is approximately

1.6 in/in/in (63 ϵ/m) for shears, and with 4 inch distance between the columns approximately 6.0 in/in/radian (6.0 ϵ/radian) for moments.

Extensive surveys of the literature were conducted throughout the development of the five-component balance. A slightly more efficient design, first described by Chevallier and Cabot [1954], was discovered after the load cells of Fig. 1.18 were finished. The gamma-shaped bent blade shown in Fig. 1.19 uses the same principle of having the gauge terminals on the unweakened part of the material as the bending beams shown in Fig. 1.18. The output of the gamma-shaped transducer is higher because the average strain for the whole length of the gauge is higher.

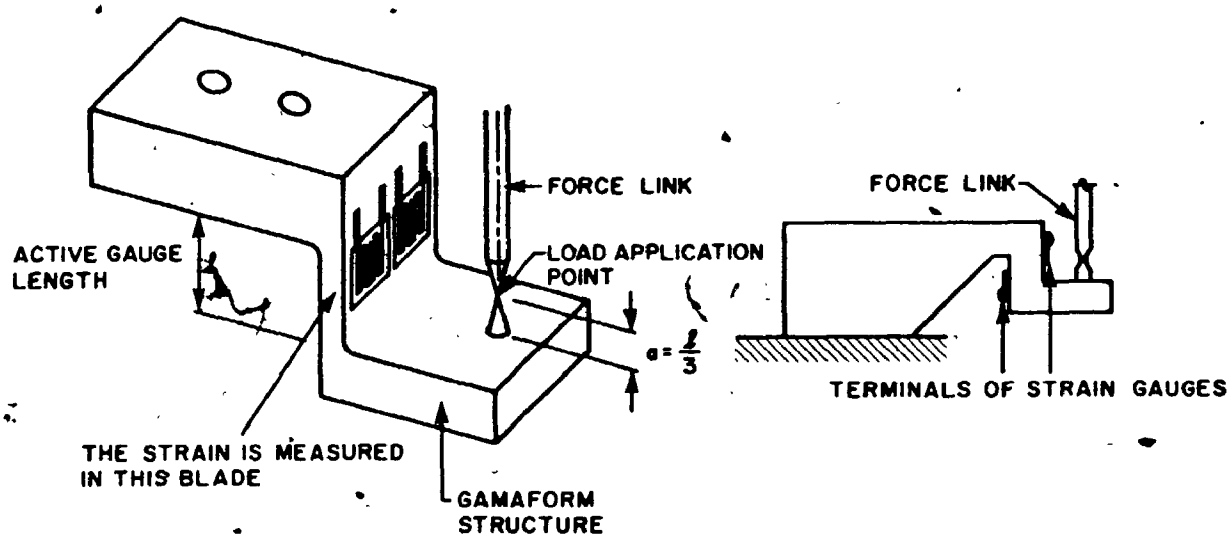

a) Schematic Design

b) Schematic Diagram of Prototype for BLWT Balance

FIG. 1.19 GAMMA–SHAPED BENDING LOAD CELL

Care has to be taken that the force is applied at exactly the right point, as indicated in Fig. 1.19 a). At any other point would the output be non-linear, as the blade bends in circular arc form under load. The hinges of the force links for the BLWT balance could easily be located at this point.

A prototype, as shown in Fig. 1.19 b), was machined and tested, with dimensions to be interchangeable with the load cells of Fig. 1.18. The same stiffness time strain

product was achieved using foil gauges as for the bending beams in Fig. 1.18. Using smaller semiconductor gauges and weakening the blade by reducing the width of the blade near the gauges, is expected to bring an additional small improvement, making this the ultimate design known to the author in terms of stiffness times strain output. Although the prototype was more elaborate than shown in the schematic diagram of Fig. 1.19 b), the actual machining was slightly less difficult than for the bending beams used in the BLWT five-component balance.

1.4.4.4 Suitable metals for transducers

The following attributes are beneficial to the good performance of transducers:

a) low modulus of elasticity to give larger physical dimensions;
b) good linearity to high strain levels;
c) low fatigue;
d) a good heat sink for strain gauge heating effects;
e) low coefficient of thermal expansion; and
f) easy machineability

Aluminium was chosen for the balance as the best compromise as described below, but other materials might be more suitable for different load ranges or applications.

Aluminium has a low modulus of elasticity of around 10×10^6 lb/in^2 (69×10^9 N/m^2), and a thermal coefficient of expansions of 13×10^{-6}/°F (7×10^{-6}/°C). It satisfies points (b) and (c) reasonably well and points (d) and (f) very well. Care has to be taken in curing the strain gauge cement, because elevated temperatures have a detrimental effect on the properties of alloys. Tests were performed to find optimum curing conditions. For the aircraft aluminium alloy 7075–T6 it was found that a cure of 90 min at 350°F and a postcure of 90 min at 350°F reduces the proportional limit (0.002 percent permanent set for a line drawn parallel to the initial slope of the force-displacement curve) from 6250 $\mu\varepsilon$ for the untreated material, to 4200 $\mu\varepsilon$ after the heat cure. These values were determined with the available facilities at the structures laboratory of the University of Western Ontario and are approximate. Some guidelines

on reheating effects can be found in the ASME Material Handbook [Lyman, 1961] and aluminium properties in ALCAN research reports, i.e. Lidstone [1970]. One characteristic of the 7075-T6 alloy is the 8 per cent difference of the modulus of elasticity for tension of 10.0 x 10^6 lb/in^2 (69 x 10^9 N/m^2) to 10.8 x 10^6 lb/in^2 (74.5 x 10^9 N/m^2) in compression. Very accurate positioning of the gauges is essential to achieve the same calibration slopes in compression and tension of the bending beam transducers. Accurate positioning and matching of the gauges is also important to keep the drift small due to the relatively large thermal coefficient of expansion. Other aluminium alloys have much lower proportional limits, i.e. untreated alloy 2024-T4 has a proportionality limit of 3600 $\mu\epsilon$. Alloy 7075-T6 is not generally available. Alloy 2024-T4 is in good supply.

Beryllium copper is often used for transducers. The modulus of elasticity is 19 x 10^6 lb/in^2 (131 x 10^9 N/m^2), the coefficient of thermal expansion is 9.3 x 10^{-6}/°F (5.2x10^{-6}/°C) and the proportional limit is greater than 5000 $\mu\epsilon$. It is the best heat sink. The material can be machined in the annealed state, the strain gauges placed and the heat treatment could possibly be done at the same time as the curing of the strain gauge cement. Reheating, however, has no negative effects.

Stainless steel, especially 17-4PH, is also used in precision transducers. The modulus of elasticity is 30 x 10^6 lb/in^2 (207 x 10^9 N/m^2), the thermal coefficient of expansion is 9.6 x 10^{-6}/°F (5.3 x 10^{-6}/°C), but the thermal conductivity is only 10 per cent of the value for aluminium.

Titanium alloys have not been used for transducers to the authors knowledge, but they have, with the exception of low thermal conductivity (similar as steel) good attributes: Modulus of elasticity 16 x 10^6 lb/in^2 (110 x 10^9 N/m^2), coefficient of thermal expansion of 4.6 x 10^{-6}/°F (2.5 x 10^{-6}/°C), and a high proportionality limit.

Magnesium has a low modulus of elasticity (6.5 x 10^6 lb/in^2), (45 x 10^9 N/m^2) but a high coefficient of thermal expansion (15 x 10^{-6}/°F), (8.3 x 10^{-6}/°C) and a low proportionality limit.

Non-metallic materials have the lowest modulus of elasticity, but have poor thermal conductivity. The coefficient of thermal expansion is of the order of 50 x 10^{-6}/°F (28 x 10^{-6}/°C). The bridge excitation voltage would have to be reduced considerably, probably outweighting the advantage of a low modulus of elasticity.

Because of the low load range and the minimum dimensions only aluminium satisfied the requirements of the BLWT balance. For higher loads where physical size requirements are not near the practical limit, alternate materials may be better. The final load cells were fabricated from 7075-T6 aluminium alloy.

1.4.4.5 Strain gauging of transducers

1.4.4.5.1 Strain gauges

The resistance strain gauge is an electrical conversion element which translates small changes in dimension into an equivalent change of resistance. The state of the art in strain gauges permits two types of strain gauges, foil and semiconductor gauges, to be used with nearly the same error at the end of the measuring chain. The following discussion applies to the conditions encountered by the BLWT balance, other conditions, i.e. large temperature variations or physical dimensions, may make one type of gauge more advantageous than the other. The detailed treatment of strain gauges and their application may be found in Perry and Lissner [1962], Dean [1962], or from strain gauge manufacturers. State of the art applications, including wind tunnel balances, is published in Journals such as "Strain" (The Journal of the British Society for Strain Measurement) and "Experimental Mechanics" (The Journal of the Society for Experimental Stress Analysis, Westport, CT).

Foil gauges are etched or die cut from thin metallic foils, such as constantan, which can be made to have a similar coefficient of thermal expansion as the transducer material. A single uncompensated gauge can not discriminate between a strain due to a change in temperature or load, but multiple gauges electrically wired to form a Wheatstone Bridge give good temperature compensation. In this case there is little difference by using compensated or matched, but uncompensated gauges. Foil gauges

are economical and can be applied readily. Dual elements on a common carrier were used for the prototypes, (BLH–FAQ2–06–35S13), facilitating precision installation even further. A disadvantage is the relatively low output of the gauges, resulting in a smaller signal to noise ratio, and requiring good strain gauge amplifiers. Die-cut gauges from platinium-tungsten are available from Dentronics Inc., which have twice the gauge factor of other foil gauges.

Semiconductor gauges use the piezoelectric effect of crystals which are grown with a controlled impurity content. Different doping levels control the gauge factor, resistance, linearity, and other properties. Their main advantage lies in the 20 to 100 times higher output than foil gauges, and, hence, lower noise level at the end of the measuring chain. The smaller size of the semiconductor gauges makes it also possible to design transducers of approximately 80 per cent higher stiffness, than by using foil gauges, for the same strain output.. A disadvantage is the low coefficient of termal expansion [1.9 $\mu\epsilon$/°F versus 13 $\mu\epsilon$/°F (1 $\mu\epsilon$/°C versus 7.2 $\mu\epsilon$/°C) for transducer material such as aluminium], and even with most careful matching and installation of semiconductor gauges, the errors due to temperature variation are larger than for foil gauges. Nonlinearity increases with increasing strain levels, but was found to be negligible in the BLWT balance application.

Studies were performed with prototype bending beams, installed with both types of strain gauges. The best performance which can be expected, for comparative purposes are:

nonlinearity:	0.1%	for foil gauges
	0.35%	for semiconductor gauges
temperature drift:	0.001%/°F	for foil gauges
	0.005%/°F	for semiconductor gauges, fully compensated

The above values are referred to full scale output, i.e. one percent equals 6 $\mu\epsilon$ or 0.01/lb, (0.0045N) for the load cells described above. Material properties, such as nonlinearity, are in addition to the above values. Dorsey [1977] and McFarland and

Dimeff [1966] give similar error estimates for transducers. The output from the Wheatstone Bridge is amplified to a desired level, approximately 50 times for semiconductor gauges and 2000 times for foil gauges. This, of course, also amplifies the noise, resulting in a similar combined error from all sources of approximately ½ $\mu\epsilon$, or 0.001 lb (0.005 N) for either type of gauge. To reduce drift from heating effects of the gauges, the gauge resistance should be chosen as high as possible for both types of gauges, i.e. 350Ω for foil gauges.

No clear advantage was found for either foil or semiconductor gauges, the final choice was partially based on finding a supplier. Entran Devices, Inc., Little Falls, NJ, supplied and expertly installed the ESU-030-500 (U-shaped, .030 in (0.76 mm) gauge length, 500 Ω) semiconductor gauges as a full bridge on each bending beam shown in Fig. 1.18.

1.4.4.5.2 Backing of strain gauges

Strain gauges are available with various carrier materials to provide support to the gauge. The highest quality backing for foil gauges in transducer applications is an Epoxy type, available from most manufacturers. They have high rigidity and freedom from creep, but have to be handled with more care because of their brittle nature.

Semiconductor gauges are also available with epoxy or other type backings. Unbacked gauges were used to take full advantage of their small size and to get best performance. Unbacked units require extreme care during the mounting.

1.4.4.5.3 Adhesives and temperature cure

The adhesive should have the thinnest glue line possible for high performance transducers, to get good strain transmission from the transducer to the gauge and good heat transmission from the resistance gauges to the transducer. Heat cured epoxy resins are recommended for highest accuracy and stability. A post cure is also recommended but as described in 1.4.4.4, care has to be taken as not to degrade the transducer material.

1.4.4.5.4 Coating of strain gauges

Protective coatings have to be used to protect the gauges from mechanical or chemical damage, including humidity. Microcrystalline wax is suitable for the application of the load cells in a BLWT balance.

1.5 ANALOGUE SIGNAL CONDITIONING

1.5.1 Bridge Supply

A strain gauge is a non-self-generating transducer, and therefore has to be fed by a supply voltage. Four gauges are best wired as a full Wheatstone Bridge as shown in Fig. 1.2, resulting in an output voltage of:

$$\textit{Differential Output Voltage} = \textit{(Differential Bridge excitation voltage)} \times \textit{(Gauge factor)} \times \textit{(Strain in gauges)} \qquad (1.6)$$

The resulting output voltage for 1 $\mu\epsilon$ and a gauge factor of 2 for foil gauges, from equation (1.6) is only 2 μ volts per one volt bridge excitation.

To obtain a higher output voltage per strain, the excitation should be as high as possible. This insures that small strains can be measured without a large error from noise and other unwanted signals. On the other hand, the supply voltage should be kept as low as possible to avoid heating of the strain gauge and the transducer. For transducers the power density should not exceed a range of 1 to 5 watts/in^2, (1.5 to 7.8 milliwatts/mm^2) the lower values for gauges mounted on thin members or poor heat sinks. A 3 volt bridge supply gives values of 3.6 watts/in^2 (5.9 milliwatts/mm^2) for the semiconductor gauges and 1.9 watts/in^2 for the foil gauges used on the prototypes described in Section 1.4.4.5.1. This is clearly an upper limit, and the excitation used for the semiconductor gauges was set at 1.0 volts for the BLWT balance.

It is evident that the bridge supply must be highly stable and free of noise. Such units are readily available or can be built inexpensively as described by Unvala and Green [1974].

1.5.2 Signal Amplification

The small output described above has to be amplified approximately 50 times for semiconductor gauges and approximately 2000 times for foil gauges to interface with the data acquisition and other lab equipment. Foil gauges clearly require more stable instrumentation. Commercially available units exhibit a drift equivalent to several $\mu\epsilon$ during the time of a typical wind tunnel test, or per °F temperature change. This electronic drift would, in addition to the drift of the gauges, produce a relatively large error for small building models.

Solid state chopper stabilization techniques can eliminate both short-term and long-term drift, and suitable instruments are commercially available. For high frequency measurements, however, the noise is larger than for the best instrumentation amplifiers. Some of the advantages of stability are, hence, traded off for a larger noise component in the signal.

The state of the art in strain gauge signal conditioners is available in form of integrated circuits. These units are suitable to special applications, such as the BLWT balance, where the gain and bridge excitation are not changed, and form an integral part of the balance-model measuring system. The SGA 103 AT strain gauge signal conditioners shown in Fig. 1.20 were supplied by CIL Electronics Ltd., Worthing, West Sussex, UK. A strain gauge amplifier is to the right, the filters are to the left. A load cell is in the foreground and in the background are some building models. The high performance, low cost and compact signal conditioners are available on 2½ inch by 3½ inch (65 mm by 90 mm) boards, incorporating adjustable bridge excitation, adjustable amplifier gain and zero offset. The bridge supply is constant to within 20 μV/°C. The amplifier is stable to 0.1 μV/°C temperature change, 1 μV/month has less than 1 μV peak to peak noise, all values referred to the input of the amplifier (output change equals input change times amplifier gain). This reduces all errors from the signal conditioning instrumentation

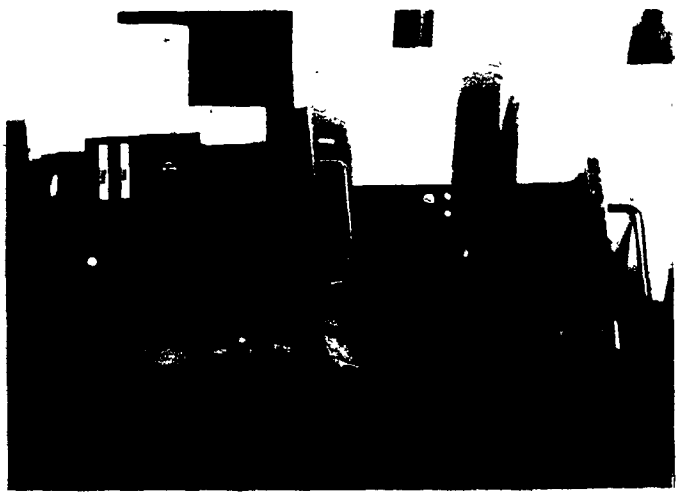

FIG. 1.20 INSTRUMENTATION REQUIRED FOR EACH FORCE COMPONENT

to second order effects, compared to errors from the load cells, even at high amplifier gains. Before the units can be used it is necessary to place them in a suitable housing and add an extended bridge balancing range.

The CIL strain gauge signal conditioners, however, are not ideally suited for semiconductor gauges which produce a large change in resistance due to strain (high gauge factor). They work by keeping the positive bridge supply exactly regulated (i.e. at 0.5 volts for a 1.0 volt bridge excitation), and by keeping one neighbouring arm of the Wheatstone Bridge at common ground (0.0 volts) by varying the negative supply (nominally at -0.5 volts for a 1.0 volt bridge excitation). Amplifying the fourth corner of the bridge with respect to common ground results in the same output from the Wheatstone Bridge as the usual way of keeping the bridge supply constant and amplifying the differential output from the other two arms of the bridge. The unique way of signal conditioning apparently results in supreme stability and has the added advantage that two arm bridges do not need any dummy resistors, all desirable attributes for foil gauges where stability is critical because of the large amplification. For semiconductor gauges, however, this results in a non-linearity for large load reversals. Extensive electronic modifications were performed by the author to produce a linear calibration value. The modified strain gauge signal conditioners perform several times better than the best transducers from either foil gauges or semiconductor gauges, and do

not need any attention in service.

Integrated strain gauge amplifiers, working the conventional way, but having less outstanding specifications, are available from Analog Devices, Norwood, Mass. (model 2B31J on AC1211 mounting cards).

1.5.3 Bridge Balancing

The initial zero adjustment compensates for normal variations of the nominal strain gauge resistance, which can be large after the cement is heat cured or if the gauges have a high gauge factor, such as semiconductor gauges. Zeroing the output for zero load also simplifies the interpretation of the data. A commonly used zeroing method, shown in Fig. 1.21, shunts two arms of the Wheatstone Bridge.

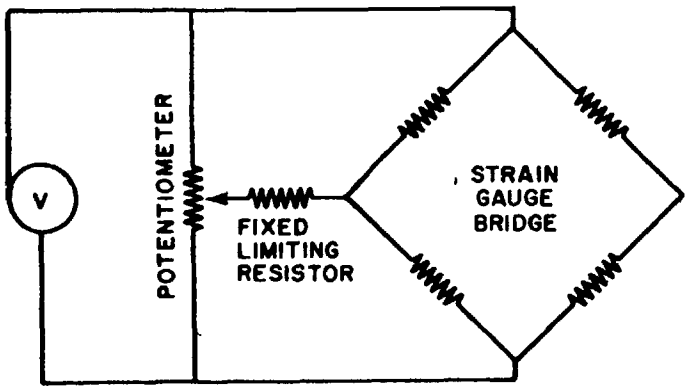

FIG. 1.21 TRANSDUCER BALANCE CONTROL

A network analysis shows that the bridge gets non-linear and that the calibration changes for a large zero offset correction. It is also harmful to the temperature compensation for internally temperature compensated transducers and can put the transducer well outside the stated specifications. The value for the fixed resistor in Fig. 1.21 has to be as large as possible, and the value of the potentiometer should be at most approximately four times larger than the fixed resistor to keep the balancing system as linear as possible.

No shunting of the bridge was used for the 5-component BLWT balance. The linear amplifiers described in Section 1.5.2 permit the summing of a compensating voltage to the output signal from the amplifier, hence, not affecting the transducer specifications. This simple method performs well and proved to be extremely stable.

1.5.4 Filtering of Signal

The fan used in the BLWT Laboratory has a variable pitch to regulate the wind speed, but rotates at a constant rate of 585 revolutions per minute. The 6 fan blades generate acoustic waves at harmonics of 58.5 Hz, which, with a balance of the sensitivity described in this chapter, contribute significantly to the measured signal. An example of an unfiltered spectrum is shown in Fig. 1.22. The stepped horizontal line represents the contribution to the variance up to that frequency, with the scale on the right showing the percentage. It is evident that filtering is necessary for the high frequency testing method proposed in Chapter II.

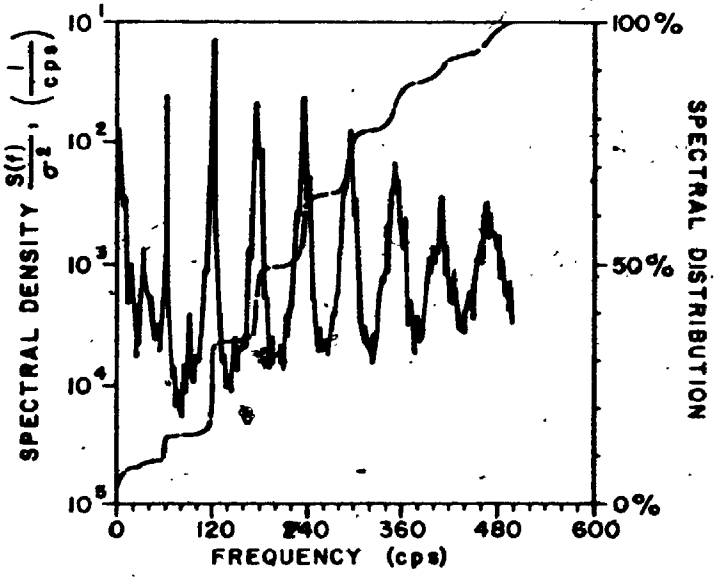

FIG. 1.22 SPECTRUM OF PRESSURES IN THE BLWT

The spike at the lowest frequency is removed with a notch filter and the second and higher spikes are removed with a low pass filter. Fixed frequency modules are suitable and the best filters were found from Frequency Devices Inc., Haverhill, Ma. The notch filter has a Q of 100 at a centre frequency of 58.5 Hz. The low pass filter is a 6-pole Cauer-Ellyptic type, flat to a frequency of 103 Hz, has an infinite rejection ratio at 117 Hz, and more than 60 db above this frequency. Contributions above 100 are negligible at the applicable model scales in the BLWT. A photo of the board with the filters was shown in Fig. 1.20.

The limited achievable frequency response shown in Fig. 1.1 results in a slow gain increase with higher frequencies. A first order correction is easily performed by inserting a one-pole Butterworth filter after the amplifier. The CIL strain gauge amplifier has already provisions for a low pass filter on the board, but such a filter could be easily added to any amplifier. The effect of the correction is demonstrated in Fig. 1.23.

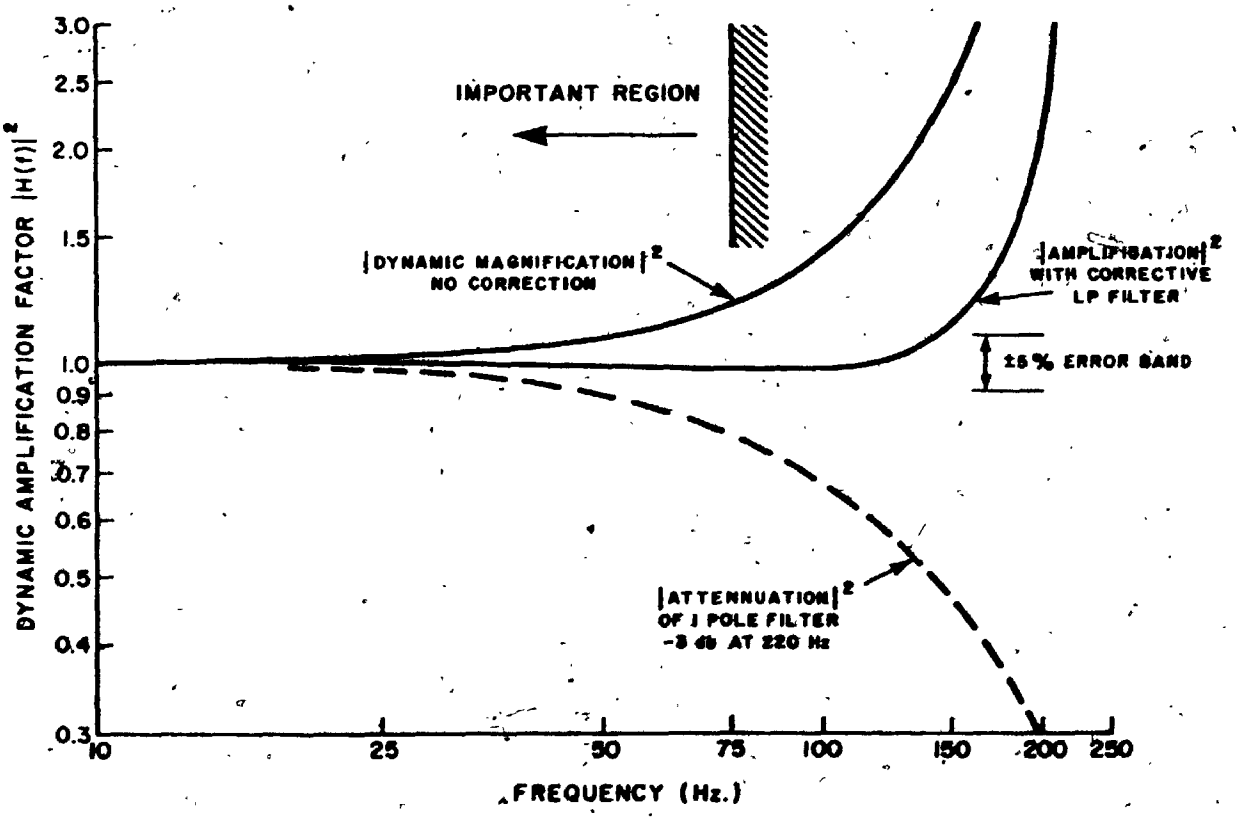

FIG. 1.23 CORRECTION FOR LIMITED FREQUENCY RESPONSE

The summing and differencing amplifiers which form the shear force and moment output, as indicated in Fig. 1.9, are easily added to the strain gauge amplifier boards. With the modification suggested in Section 1.4.2, however, the differencing amplifier to form the torque is not required.

The signal conditioning described above is suitable to the majority of models tested at the BLWT. Additional filtering may be necessary, i.e. to prevent aliasing in spectrum measurements as is standard practice for digital data acqusition. A schematic diagram of the total signal conditioning is given in Fig. 1.24.

The output from the balance system is processed by the standard methods used in the BLWT, such as displaying on oscilloscopes, real time analogue to digital conversion and processing by the PDP-11/60 computer system of the BLWT Laboratory, or direct processing with the Hewlett Packard HP5423A Structural Dynamics Analyzer (FFT analyzer) of the BLWT Laboratory.

1.6 CALIBRATION OF THE FIVE-COMPONENT BALANCE

A balance of the type described in this chapter requires a comprehensive calibration which includes the determination for each component of: calibration slope, interaction effects to other components, non-linearity, hysteresis, creep and drift due to temperature effects.

A calibration frame was designed and constructed to facilitate the application of forces and moments of known magnitude and direction, individually or in combination, by means of pulleys. The completed calibration rig is shown in Fig. 1.25. The alignment is critical for the determination of the cross talk. Interaction has two causes:

i) cross talk due to inexact assembly, or due to changes in measurement elements during the application of the load; or

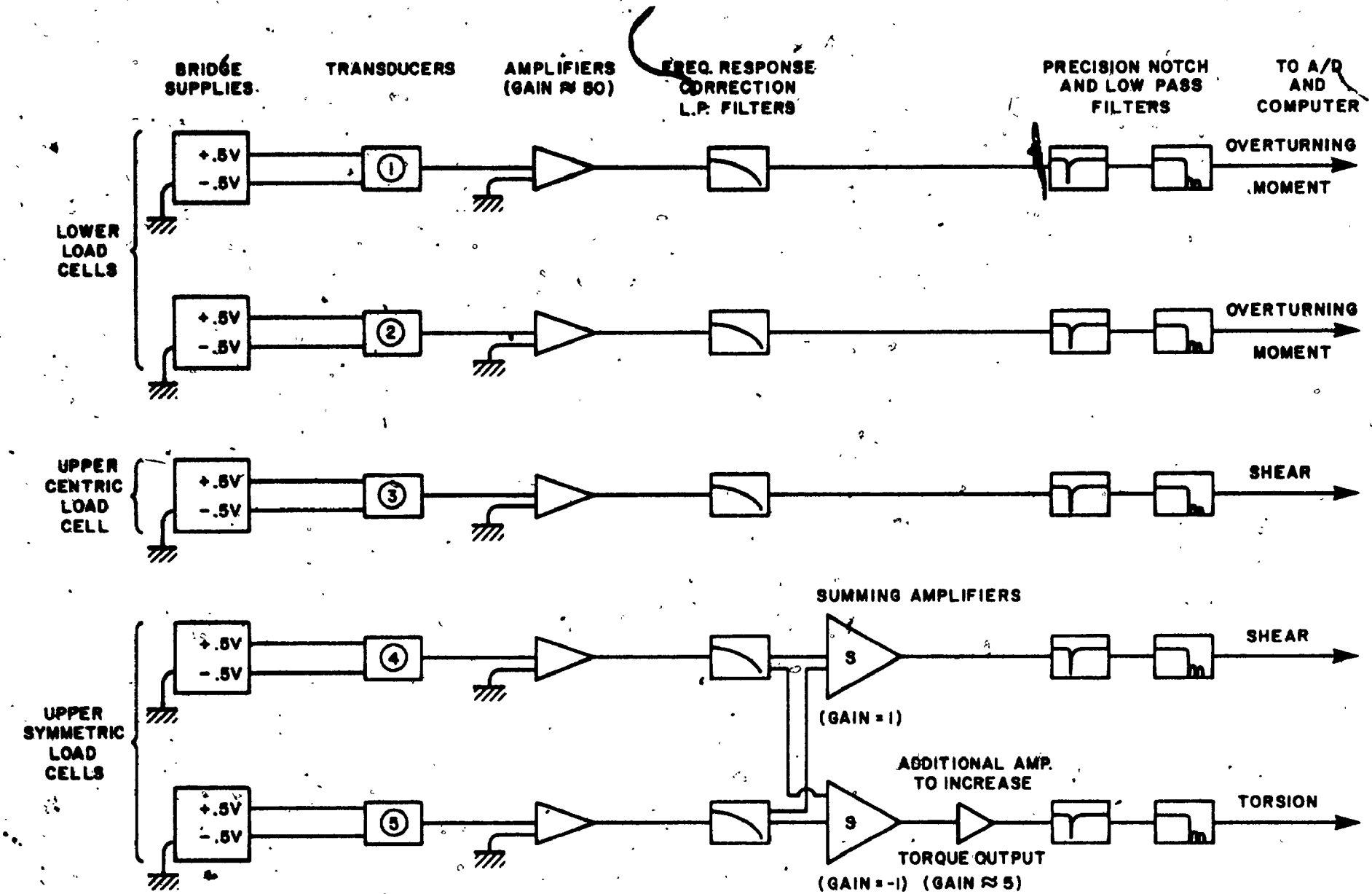

FIG. 1.24 ANALOGUE SIGNAL CONDITIONING DIAGRAM

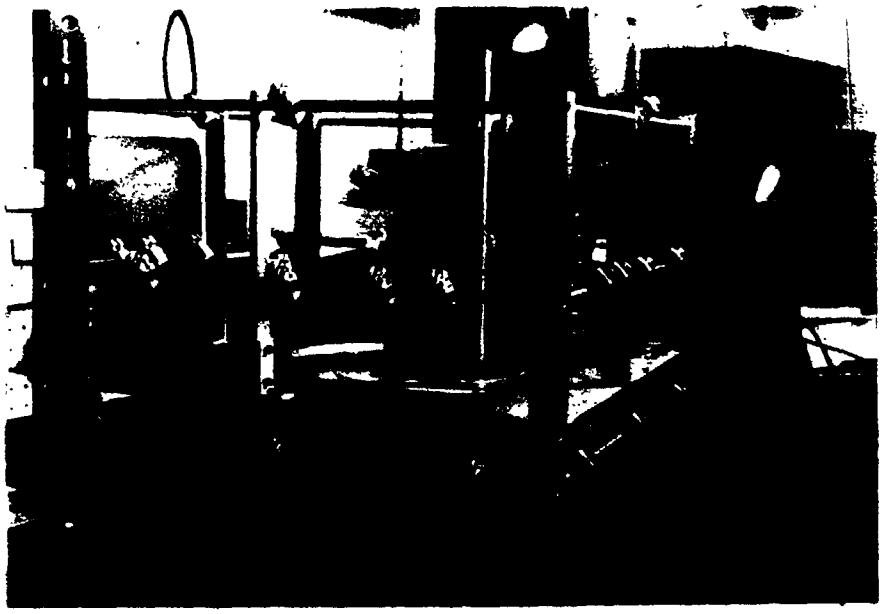

FIG. 1.25 PHOTO OF THE CALIBRATION RIG

ii) cross talk resulting from a deviation of the proper direction of loading during the determination of the cross talk. This pseudo cross talk cannot be distinguished from the real cross talk.

The alignment does not have a marked effect on the direct calibration slopes. More important, however, is the correct value of the force, and complicated loading schemes, as the applications of pure shear loads, or pure torsion, rely on multiple pulleys. Existing pulleys proved to have too much static friction and hysteresis, which can be easily checked by a test shown in Fig. 1.26. The unbalance required to overcome friction is determined by slowly adding weight on one side.

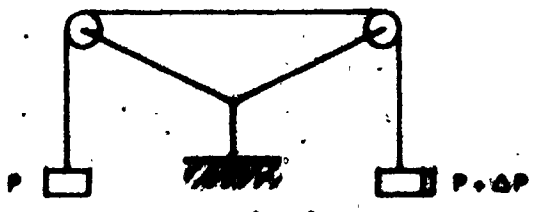

FIG. 1.26 HYSTERESIS AND FRICTION TEST FOR PULLEYS

A simple solution was found using jewelled watch bearings (supplied by Swiss Jewel Company, Philadelphia, Pa.). These are available as assemblies mounted in a threaded axle, and can be easily assembled to form bearings for the pulleys visible in Fig. 1.25. The friction and hysteresis over two pulleys was measured to be approximately one percent, much better than the 5 percent of typical pulleys made from Delran and steel bearings.

To determine the calibration slopes, it is common practice to plot the full value of voltage output versus the load. A perfect transducer is often concluded, since a good transducer fits with a straight line, and errors of several percent full scale do not show up. It is much better to subtract from the voltage output values corresponding to a constant slope, and to plot the residuals, as shown in Fig. 1.27 for a bending moment. This plot can be used to determine the calibration slope, hysteresis, non-linearity, creep, and estimation of the error bands. Note that this exaggerated scale shows up the errors clearly.

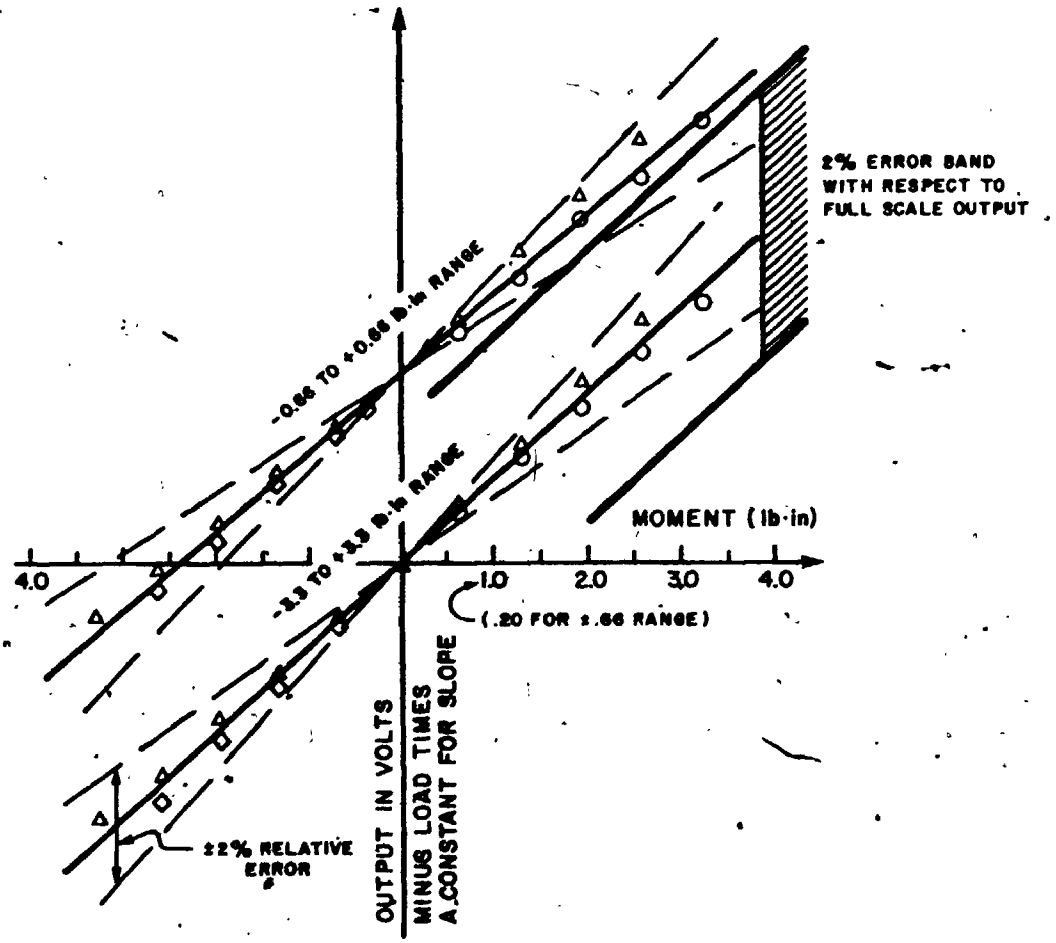

FIG. 1.27 RECOMMENDED CALIBRATION PLOT

Quick calibrations for the moments can be performed by placing a selected weight on the girder above the particular load cell. Placing a 50 gram weight flush with the outside of the girder near the vertical columns for instance gives an instant check on the calibration to within ± 3 percent.

Although identical load cells and details were used for all five components, some differences were observed in the calibrations. The moments performed well, as shown in Fig. 1.27. One shear load cell, however, showed 2 percent creep of the highest load applied, making the gain adjustment for summing and differencing difficult from the shear load cells. The cause is not known, but it could be due to problems with strain gauges, or an accidental overload. The resulting cross coupling is approximately 2 percent between torque and shear. Cross talk between all other components is less than 0.1%.

The errors from all sources (non-linearity, cross coupling, creep, hysteresis, temperature drift, etc.) based on the calibration tests can be summarized as follows:

Overturning moments:	2 percent relative error
Shears and Torque:	2 percent referred to the maximum load induced between zero readings

Note that errors are usually referred to the full scale output (i.e. maximum designed capacity) resulting in smaller percentage values, but the BLWT balance performs well for all load ranges. A summary of all the specifications for the five-component balance is given in Table 1.1.

1.7 HIGH FREQUENCY BUILDING MODELS

The new balance is intended to measure the dynamic force on buildings, as described in Chapter II. This method relies on a high frequency response of the balance-model combination. Both the building model and the balance interact with each other and form an integral part in the measuring system. The design of high natural frequency building models is now described.

Design Capacities:

Each Load Cell	1 lb	(4.45N)
Shear, direction with one load cell	1 lb	(4.45N)
Shear, direction with two load cells	2 lbs	(8.9N)
Moments (resulting from 4" spaced force links)	4 lb-in	(.45Nm)
Torsion (resulting from 3.75" spaced force links)	3.75 lb-in	(.42Nm)

Overload Capacities

For all components roughly 250% of design capacities. Overload protection devices, however, are set at design capacity.

Strain Outputs from Load Cells

Each load cell	605$\mu\epsilon$/lb	(136$\mu\epsilon$/N)
Shear, direction with one load cell	605$\mu\epsilon$/lb	(136$\mu\epsilon$/N)
Shear, direction with two load cells	303$\mu\epsilon$/lb	(68$\mu\epsilon$/N)
Moments	151$\mu\epsilon$/lb-in	(1300$\mu\epsilon$/Nm)
Torsion	161$\mu\epsilon$/lb-in	(1400$\mu\epsilon$/Nm)

Stiffnesses

Each load cell (measured	2900 lb/in	(0.51 x 10^6 N/m)
Shear, direction with one load cell	2600 lb/in	(0.45 x 10^6 N/m)
Shear, direction with two load cells	5200 lb/in	(0.90 x 10^6 N/m)
Moments	40,000 lb-in/rad.	(4500 Nm/rad)
Torsion	36,000 lb-in/rad	(4100 Nm/rad)

Performance Values (Stiffness Times Strain Per Unit Load)

Each load cell	1.75 ϵ/in	(69 ϵ/m)
Shears	1.6 ϵ/in	(61 ϵ/m)
Moments	6.3 ϵ/rad	
Torsion	5.8 ϵ/rad	

TABLE 1.1 SUMMARIZED SPECIFICATIONS FOR THE FIVE-COMPONENT BALANCE

Errors from Non-Linearity, Hysteresis, Drift, Coupling etc. as Measured at Time of Detailed Calibration

Shears and Torsion	2% as referred to the maximum load induced between readings
Base bending moments	2% relative to the instantaneous reading

Inertial Masses (Only Girder Considered)

Lateral mass (for shears)	0.0053 slugs	(78g)
Mass moment of inertia (for moments)	0.0142 slugs-in^2	(.133 gm^2)
Mass moment of inertia (for torsion)	0.0259 slugs-in^2	(.243 gm^2)

Natural Frequencies (Theoretical, without any mounted model)

Lateral	386 Hz
Rotational (for moments)	928 Hz
Rotational (for torques)	650 Hz

Electrical Specifications

Excitation for each load cell	1 volt
Gauge factor, nominal	135
Electronic amplification, nominal	50
Electronic amplification for torsion, nominal	250
Full scale output, after amplification roughly	5 volts

TABLE 1.1 SUMMARIZED SPECIFICATIONS FOR THE FIVE-COMPONENT BALANCE (CONT'D)

The building model has to have a small density, otherwise the overall frequency would be significantly reduced by the high inertial mass acting on the stiffness of the balance. Only lightweight building models are, hence, considered below.

The natural frequency of a homogeneous cantilever on a rigid support can be described as follows:

$$f_i = k^2 \sqrt{\frac{EI}{\rho A L^4}} \qquad (1.7)$$

where k = a constant, 1.875 for the fundamental frequency of a rigidly clamped cantilever

E = modulus of elasticity of the material

ρ = density of the material

A = area of the cross section

L = length of the cantilever

Equation (1.7) shows that the frequency for a particular building model, where the dimensions A and L are defined by the model scale, is only dependent on the value of $\sqrt{E/\rho}$. This is the wave propogation velocity in a material, i.e. the speed of sound, a fairly constant value for many materials, including metals and wood, of roughly 16,000 ft/sec. (4900 m/sec). The objective is, hence, to find a light weight material with a high velocity of sound.

Models made from light weight styrofoam were used for all tests, with the light-weight white foam performing better than the blue one. The wave propagation velocity is approximately $[(110 \times 10^3 \text{ lb/ft}^2)/(.025 \text{ slugs/ft.}^3)]^{-1/2}$ = 2100 ft/s (640 m/s). New materials were being sought, including exotic materials such as NASA space shuttle tiles, but no better material was found. Material on order at the time of writing was Rohacell 31 with a wave propogation velocity of $[(751 \times 10^3 \text{ lb/ft}^2)/(.059 \text{ slugs/ft}^3)]^{-1/2}$ = 3560 ft/s (1080 m/s), but no material was available for experimentation. For the

rigid balance, the frequency of the balance-model combination depends primarily on the material and construction of the building models. Hence, it is of prime importance to find suitable materials for the building models.

The effect of finite rigidity of the balance can be estimated from Fig. 1.28 (after Goldenblat and Sizov, 1955). The curve gives a modified value of k for equation (1.7). The rotational stiffness of the balance is approximately 40,000 lb-in/rad (4500 N-m/rad). Typical models give values from the flat part of the curve, i.e. close to the value of 1.875 in equation (1.7) for a rigidly clamped beam. Inversely the maximum density for the models could be determined from Fig. 1.28, as not to reduce the frequency significantly due to the inertia mass of the model. This curve implies no mass for the girder. Including the girder would lead to a family of curves for buildings with different masses, giving smaller values of k for very lightweight models. Fig. 1.28 is intended to introduce the idea for developing aids to estimate the frequency of proposed models.

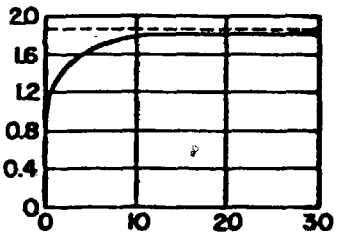

ORDINATE: VALUE OF k IN EQ. 1.7

ABSCISSA: $40{,}000 \frac{\text{lb-in}}{\text{rad}} \cdot \frac{\text{HEIGHT OF MODEL}}{(E \cdot I)_{\text{MODEL}}}$

$(4500 \frac{\text{N-m}}{\text{rad}})$

(40,000 lb-in/rad = STIFFNESS OF BALANCE, ALL OTHER VARIABLES SAME UNITS, ie. lb AND inch)

FIG. 1.28 FREQUENCY OF A CANTILEVER ON FLEXIBLE SUPPORT

Experiments showed large differences between predicted and measured frequencies, with predicted values being higher than measured ones. In addition to neglecting the balance mass, the model itself cannot be rigidly fastened to the girder, and that the epoxy glue joint which bonds the foam model to the base plate is not fully rigid. Experiments with different base plate configurations showed no change in frequency, hence the base plates recommended are of exactly the same dimensions as the building cross section and 1/8 inch (3 mm) thick, machined from magnesium. The base plates contain threaded holes for mounting screws from the girder and constitute the major part of the labour to build the models.

Experimental variations on the building models in an attempt to increase the frequency included making longitudinal voids in the interior of the foam. Although this should increase the frequency, a decrease was actually observed in the experiments, indicating the difficulty of bonding the model to the base plate. The only significant increase in frequency resulted from attaching a stretched fibre glass tape to the broad sides of the model over a height of approximately 60 percent, as shown in Fig. 1.7. The lowest natural frequency of the 6 in by 6 in by 1½ in (152 x 152 x 38 mm) model in this figure was measured to be 280 Hz. Without the tape, the frequency was 180 Hz. Both values are for the flexible model, mounted on the flexible balance.

More elaborate fabrication methods than the simple foam models described above could theoretically bring a significant improvement in the frequency response. Shells from carbon fibre reinforced plastic were used by Whitbread [1975], and Evans and Lee [1981]. Carbon fibres, impregnated by an epoxy resin, are available in rolls of 50 feet (15 m) length. To make panels suitable for building models they have to be cured under high pressure and temperature. To inhibit panel vibrations, the shell should also be filled with foam. The increased frequency is, hence, achieved at much greater cost and time required to fabricate the models.

The simple foam models used in this study are inexpensive. Quick fabrication allows many models to be built for parameter studies. Some typical foam models before the application of the fibreglass tape are shown in Fig. 1.29.

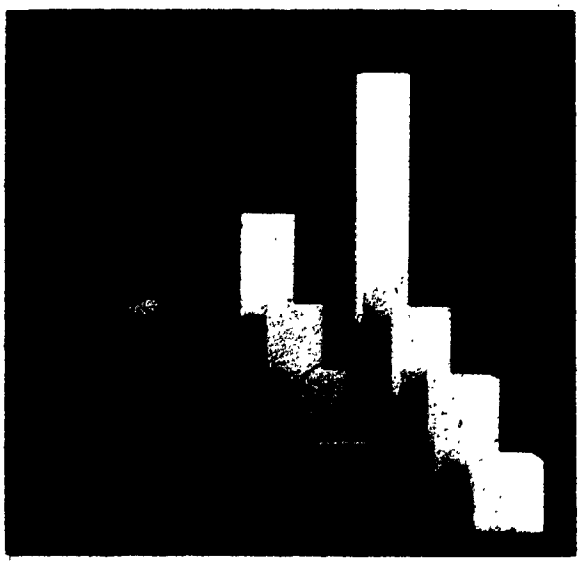

FIG. 1.29 PHOTO OF SOME TYPICAL BUILDING MODELS

1.8 SUMMARY

A systematic description of the design and construction of a new five-component balance for high frequency dynamic force measurements in a Boundary Layer Wind Tunnel is presented. All components are described, including a detailed treatment of high efficiency load cells, which are the key to good performance in the adopted frame type balance. The relatively small loads induced in building models are difficult to measure if high rigidity is also required. The balance satisfies the primary requirements of high sensitivity and stiffness, and meets many additional good attributes.

The balance is believed to represent the state of the art in design, construction and electronic signal conditioning, all of which are an integral part of the balance.

Related topics, such as strain gauging of transducers and calibration are also discussed. Existing balances are reviewed and compared to the new design.

High frequency building models are described which are suitable for the new testing method proposed in Chapter II.

CHAPTER II

EXPERIMENTAL STUDIES ON TYPICAL BUILDING SHAPES AND LINEAR STRUCTURAL RESPONSE PREDICTIONS

2.1 INTRODUCTION

This chapter describes a new and simplified experimental approach to evaluate the response of medium and high rise structures subjected to loads from turbulent wind. The Boundary Layer Wind Tunnel experiments involve high frequency rigid foam models mounted on the five-component balance, designed for this application and described in Chapter I. The output from the balance is the time history of the modal forces, which can be used to analytically predict the response of buildings in a simple manner. This method is similar to the gust factor approach for drag response described in the National Building Code of Canada.

The force spectra used in response calculations are valid for the particular building shapes and exposures tested, and are normalized to be independent of velocity and structural parameters such as stiffness, mass and damping. The responses can be calculated for any direction for which force spectra are measured. Approximations assume straight line mode shapes, with deviations having a negligible effect. Aerodynamic damping is assumed to be positive and hence conservatively neglected for most standard building shapes at realistic velocities. Aerodynamic damping is described at greater length.

Conventional wind tunnel tests are reviewed, and results are compared from aeroelastic and force model experiments. The force spectra are also shown to compare well

with the National Building Code of Canada.

Consideration in practical applications has to be given to the torsional response, which is believed to be non-conservatively predicted, but correction factors are suggested. Coupled mode shapes are easily accommodated.

Comparisons with direct force measurements by other investigators show the proposed balance-model combination to be versatile and economical.

2.2 METHODS TO PREDICT STRUCTURAL RESPONSE FROM WIND TUNNEL TESTS

2.2.1 Introduction

The trend towards construction of tall, slender and lightweight structures, built with high strength materials and connections which exhibit little structural damping, demands an increasing degree of attention to their behaviour in the wind. The above progressions have had the effect of increasing the response to wind. The traditional design for static loads was more suitable for the structures built in the first half of this century.

Definition of the elastic response, both static and dynamic, to wind, has been considerably clarified in recent years, [Davenport, Mackey and Melbourne, 1966]. The wind induced forces on structures depend upon the oncoming flow and the geometry and mechanical properties of the building. The geometry of buildings has long been recognized to affect the drag coefficients for static loads. The dependence on the structural parameters for mechanical vibrations was also known for many decades, and the general availability of high speed computers during the last two decades eased dynamic analysis problems considerably. The most recent advances, however, came from improved understanding of the oncoming flow, starting with the meteorological wind climate, to the recognition of the dependence of mean velocity with height, different energy content of the turbulence at different frequencies and decreasing cross correlation with increasing spatial separation, and awareness of other phenomena such as vortex shedding and aerodynamic damping. The National Building Code of Canada [1980] outlines a gust factor

approach to predict the along wind response. Analytical methods to solve the flow and induced pressures around bluff bodies are being developed by some investigators. At present only simple shapes and flow conditions have been solved with some success. Hunt [1973] developed a theory for the rapid distortion of weak turbulence impinging onto bluff bodies in which the equations are linearized by neglecting the local effects of viscosity. Durbin and Hunt [1979] extended the theory to predict surface pressure fluctuations around the obstacle in terms of the fluid density and the upwind mean and r.m.s. velocities. Surface pressure spectra were estimated which could be multiplied with the mode shape and correlation length and integrated to yield modal force spectra. Sufficiently accurate estimation of the instantaneous wind load and spectral density still pose serious obstacles. The wake is not being treated and the fluctuating pressures are assumed to be produced only by turbulent eddies on the stagnation line. The theory, however, gives valuable theoretical insight, such as why the lattice approach gives aerodynamic admittance values too small for bluff bodies, and relative changes due to different upwind integral scales.

In the absence of analytical methods capable of describing the wind load phenomenon, or of previous experience with similar structures or environments, the response of buildings has to be measured experimentally. Two basically different approaches are possible:

i) measurement of response using complete aeroelastic modelling, simulating the stiffness, mass and damping characteristics; and

ii) measurement of total dynamic forces with rigid models.

The latter method is the subject of this chapter and is discussed at greater length below.

2.2.2 Aeroelastic Models

From dimensional analysis it can be shown that if all or most similarity requirements are fulfilled, then the results of tests on models can be scaled to full scale structures. The important requirements include the modelling of oncoming flow, including velocity

(2.2) shows that this is automatically achieved if the lowest natural frequency of the transducer has a high value. It is also desirable to have high damping to keep the function flat to a higher frequency and to reduce the resonant peak. As shown in Section 1.2, this is the principle of operation for most tranducers. The balance-model combination described in Chapter I is designed for a high natural frequency.

The structural response for linear systems can best be evaluated using generalized coordinates. The response for tall buildings subjected to wind loads essentially consists of a mean response plus resonant responses in each of its fundamental modes. Computation of the mean response is fairly straightforward, but computation of the modal responses is complicated because of the need to include factors such as the mode shape, correlation and size of the gusts and aerodynamic effects.

The generalized force – its instantaneous value $F(t)$, its mean value $\bar{F}$, its variance σ_F^2, and its spectral density $S_F(f)$ are defined from the pressures by:

$$F(t) = \int_A p(z,t)\,\phi(z)\,dA \qquad (2.3a)$$

$$\bar{F} = \int_A \overline{p(z,t)}\,\phi(z)\,dA \qquad (2.3b)$$

$$\sigma_F^2 = \int_A \int_A \overline{p(z,t)\,p(z',t)}\,\phi(z)\,\phi(z')\,dA\,dA' - \bar{F}^2 \qquad (2.3c)$$

$$S_F(f) = \int_A \int_A S_p(z,z',f)\,\phi(z)\,\phi(z')\,dA\,dA' \qquad (2.3d)$$

In these $p(z,t)$ and $\phi(z)$ are the instantaneous pressures and mode shapes at point z, respectively. $S_p(z,z',f)$ is the cross spectrum of pressures at points z and z' at frequency f, and dA and dA' are elementary areas at positions z and z' of the projected area A.

Multi-degree of freedom aeroelastic models require much labour to design, build and calibrate the model, and to apply the correct amount of damping by a trial and error procedure. This makes them the most expensive part of a typical wind tunnel study comprising: 1) pressure studies for the cladding design; 2) aeroelastic study to design the structural framework and to assess the comfort for the occupants in the upper floors; and 3) ground level wind environment studies to ensure acceptable conditions for pedestrians within a built-up environment.

The time span from the start of the design of a multi-degree of freedom model until its completion is roughly two months. Any changes which might be made on the full scale structure are difficult or impossible to accommodate. Extrapolations to different structural properties from the modelled values can only be done reliably over a small range.

A significant simplification is achieved by using a rigid model, pivoting near the base and restrained by appropriate springs. This method can be used if the main contributions come from the fundamental sway modes and the torsional response can be neglected. A pivoting model represents straight line fundamental mode shapes. An example of this type of model at the BLWT is shown in Fig. 2.2. The mass distribution is not critical as long as the mass moment of inertia about the base is the same as that for the correct density distribution. The damping is controlled with an electric eddy current damper.

This approach allows for much flexibility, such as readily varying the building mass (by adding or removing mass anywhere at the pivoting assembly), the ratio of fundamental frequencies (by changing springs), and the structural damping (by varying the current to the electromagnet). Test results, however, are only valid for the structural parameters used in the experiment, and later changes may require a new test to be performed.

Multi-degree of freedom models are the preferred method for structures with finalized structural properties. If the torsional response is suspected to be critical (such as for uncommon building shapes, the torsional period lower than sway periods, or the mass and elastic centre at different locations), a multi-degree of freedom model is necessary.

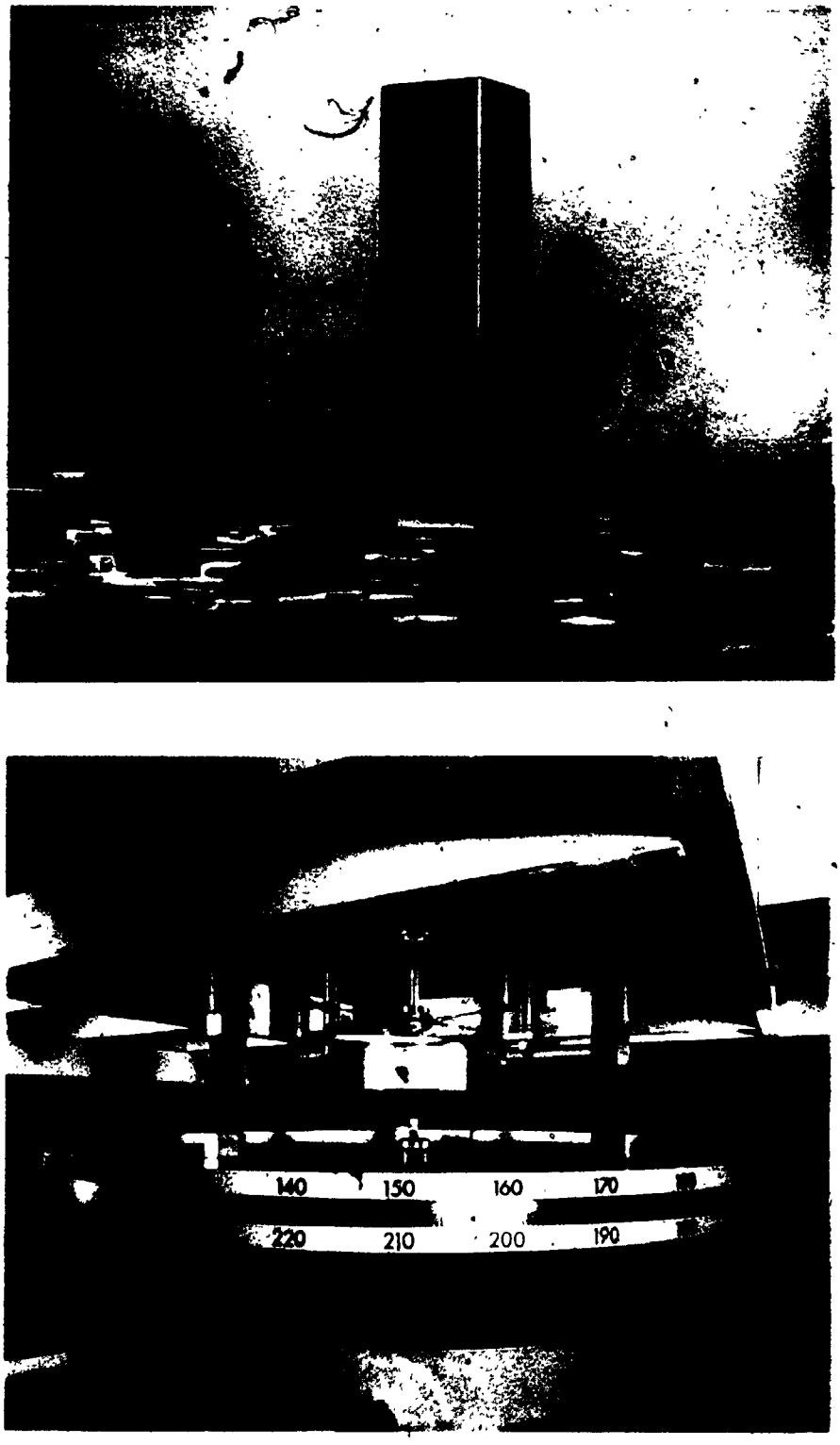

FIG. 2.2 TYPICAL CONVENTIONAL RIGID-PIVOTING AEROELASTIC MODEL

Composite photograph of rigid element model mounted on flexure pivots to allow along-wind and cross-wind displacements pivoting about base of building at University of Western Ontario Boundary Layer Wind Tunnel Laboratory *(Photo by Ron Nelson Photography)*

for the experimental response determination. The response in higher modes, which can also not be determined from rigid pivoting models, can be important for accelerations where the contribution from higher modes is more significant than for displacements.

The dynamic component in the X-sway direction of displacement is given by the relationship [Dayenport, 1967]:

$$\overline{x'^2} = 4 \frac{\overline{F^2}}{\overline{V^2}} \frac{1}{k^2} \int_0^\infty J^2 \left(\frac{fD}{\overline{V}}\right) |H(f)|^2 S_v(f)\, df \qquad (2.1)$$

where $\overline{x'^2}$ = mean square displacement
$\overline{F^2}$ = mean square wind force
V = velocity
k = stiffness of structure
J^2 = joint acceptance function
f = frequency
D = typical building dimension
S_v = power spectrum of the velocity

The functions appearing in the integral of Equation (2.1) are illustrated in Fig. 2.3 [Davenport, 1967]. Transforming the stochastic velocity function into the frequency domain gives the gust spectrum for uniform boundary layer flow shown at the top left. The slope at high frequencies is assumed to approach the value of $-2/3$ in the "Gust Factor Approach" when plotted on a log-log scale as used in Fig. 2.3. The reduced correlation of the gusts at higher frequency reduces the effective force at higher frequencies, i.e. the joint acceptance function in Fig. 2.3 falls off at higher frequencies. This takes into account, in addition to the relation of the size of the disturbance to the size of the structure, also such effects as the aerodynamics of the body and the variation of the mean wind speed profile. Line-like structures also have to include the interaction between the turbulence and the structural modes of vibration, hence the term "joint acceptance function", which can be thought of as a "modal

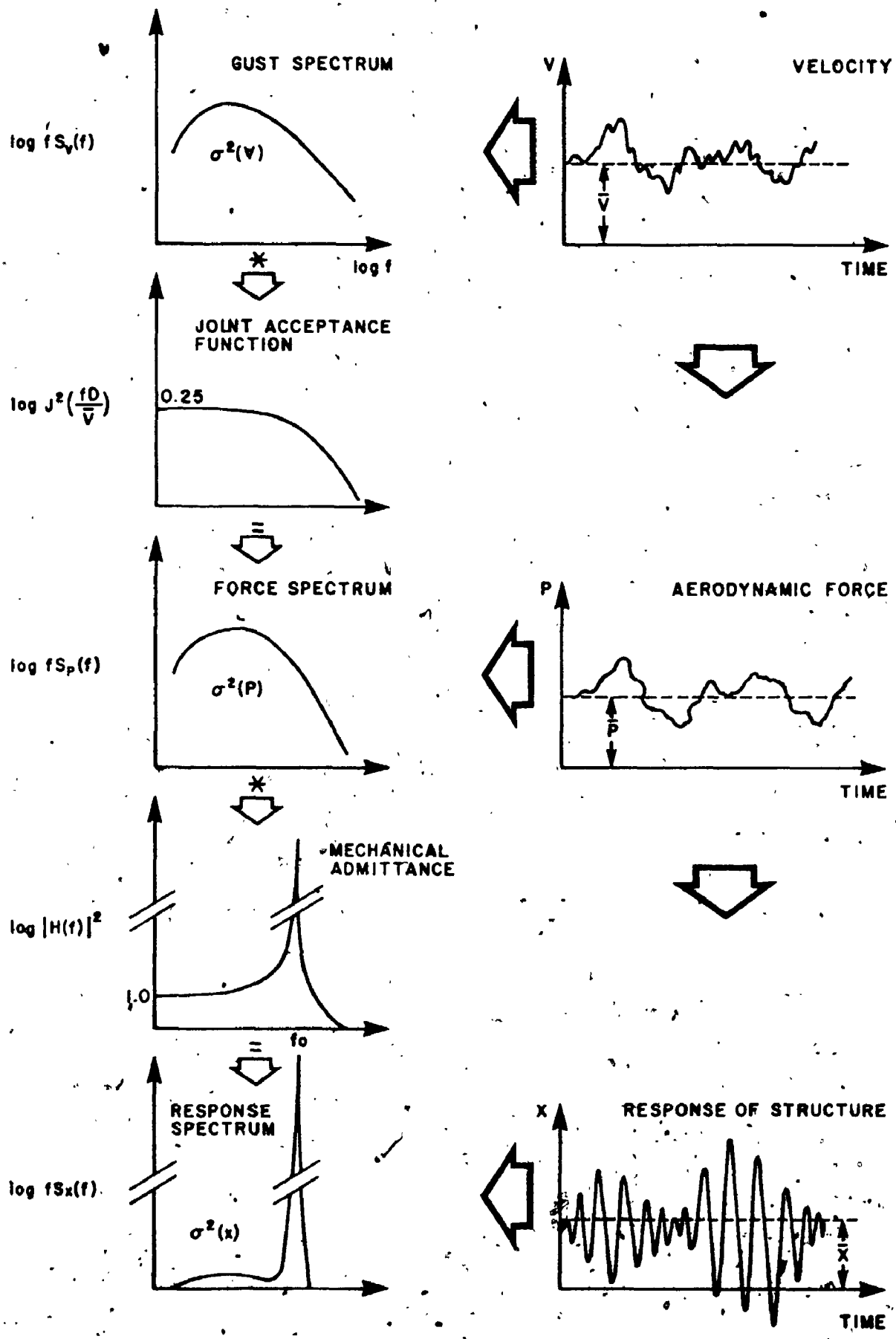

FIG. 2.3 ELEMENTS OF THE DYNAMIC BUILDING RESPONSE COMPONENTS

aerodynamic admittance function". Vickery and Davenport [1967] measured the aerodynamic admittance function experimentally and found it to be dropping off at approximately $-4/3$ at high frequencies. For very tall structures the drop-off would be steeper, and for most non-along-wind vibrations, the function would show magnifications around the vortex shedding frequencies.

The product of the velocity spectrum and the joint acceptance function gives the power spectrum of the force, dropping off with a slope of roughly -2 for simple, not very tall structures in along-wind loading.

If the structure is regarded as a single degree of freedom system with an undamped fundamental natural frequency f_o, a damping ξ (as a fraction of critical), then the mechanical admittance function $|H(f)|^2$ can be expressed as:

$$|H(f)|^2 = \frac{1}{[(1 - (\frac{f}{f_o})^2]^2 + 4\xi^2 (\frac{f}{f_o})^2} \qquad (2.2)$$

which accounts for the dynamic resonant response arising from inertial effects. The product of the force spectrum with the mechanical admittance function gives the power spectrum of the response at the bottom of Fig. 2.3. The spectrum shows a broad peak which is related to the background (or low-frequency) contribution and a resonance peak at the natural frequency. This periodic content can be clearly seen in the response time history. The above formulations are valid for linear systems, but in Chapter IV other methods are discussed to investigate the response of nonlinear structures.

Comparing the analogue parts in the wind tunnel experiment in Fig. 2.4 with the functions described above, it can be seen that the roughness elements upstream generate the velocity profile and velocity spectrum. The geometry of the building, combined with the flow, models the aerodynamic admittance function, and the mechanical properties of an aeroelastic model represent the mechanical admittance function. The model is mounted on a balance which measures the sway response overturning moments and for

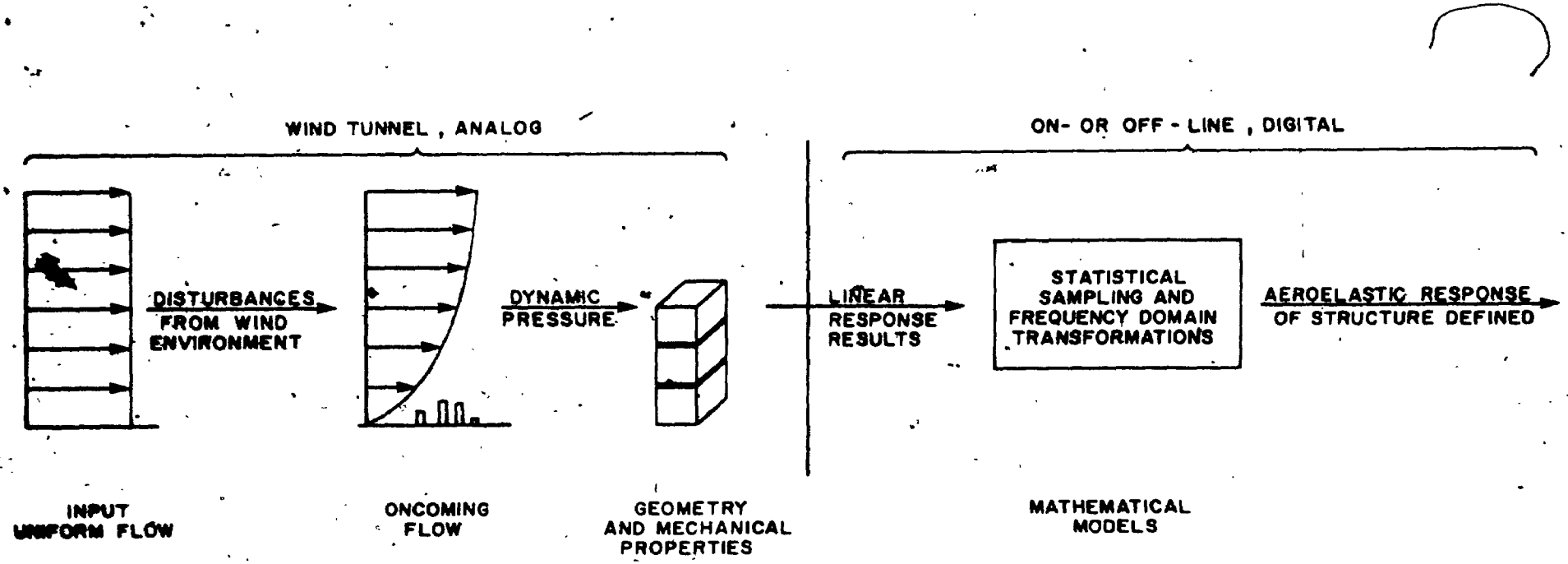

FIG. 2.4 SCHEMATIC DIAGRAM OF ELEMENTS IN AEROELASTIC WIND TUNNEL TESTS

multi-degree of freedom models it also measures the torsional moments.

The aerodynamic force is, hence, not directly observable or measurable with conventional aeroelastic models.

The wind tunnel studies in Fig. 2.4 can be seen to consist of two main parts:

i) the analogue modelling; and

ii) the digital processing done by computer

The use of the balance significantly reduces the analogue component. Most of the cost of wind tunnel studies is related to the analogue modelling. The wind tunnel and its models can be compared with an analogue computer the input being air with a uniform velocity, the output being a voltage signal from the balance proportional to the building model response. It would be desirable to eliminate the analogue part altogether, but for the present time this is not feasible, as analytical methods are not yet fully developed for describing the wind load phenomenon. Moving the digital processing further ahead, however, would be cost effective and time saving.

The main objective of this study is to directly measure the aerodynamic force. There are many ways of doing this, some alternative methods are described in 2.4. The method chosen for the analysis in this chapter was to use high frequency rigid models, mounted on the especially designed rigid high frequency balance described in Chapter I.

2.3 DIRECT AERODYNAMIC FORCE MEASUREMENTS WITH MODELS HAVING A HIGH NATURAL FREQUENCY

The magnification function in Fig. 2.3 asymptotically approaches a unit value at low frequencies. If a measuring system can be built with a magnification function value close to 1.0 for all frequencies where the gust spectrum contains significant energy, then

(2.2) shows that this is automatically achieved if the lowest natural frequency of the transducer has a high value. It is also desirable to have high damping to keep the function flat to a higher frequency and to reduce the resonant peak. As shown in Section 1.2, this is the principle of operation for most tranducers. The balance-model combination described in Chapter I is designed for a high natural frequency.

The structural response for linear systems can best be evaluated using generalized coordinates. The response for tall buildings subjected to wind loads essentially consists of a mean response plus resonant responses in each of its fundamental modes. Computation of the mean response is fairly straightforward, but computation of the modal responses is complicated because of the need to include factors such as the mode shape, correlation and size of the gusts and aerodynamic effects.

The generalized force – its instantaneous value $F(t)$, its mean value $\bar{F}$, its variance σ_F^2, and its spectral density $S_F(f)$ are defined from the pressures by:

$$F(t) = \int_A p(z,t)\,\phi(z)\,dA \qquad (2.3a)$$

$$\bar{F} = \int_A \overline{p(z,t)}\,\phi(z)\,dA \qquad (2.3b)$$

$$\sigma_F^2 = \int_A \int_A \overline{p(z,t)\,p(z',t)}\,\phi(z)\,\phi(z')\,dA\,dA' - \bar{F}^2 \qquad (2.3c)$$

$$S_F(f) = \int_A \int_A S_p(z,z',f)\,\phi(z)\,\phi(z')\,dA\,dA' \qquad (2.3d)$$

In these $p(z,t)$ and $\phi(z)$ are the instantaneous pressures and mode shapes at point z, respectively. $S_p(z,z',f)$ is the cross spectrum of pressures at points z and z' at frequency f, and dA and dA' are elementary areas at positions z and z' of the projected area A.

Tall buildings have a fundamental mode shape which is more or less a straight line. Vickery [1970] derived expressions for estimating the errors in calculating the response by assuming a straight line. Even for large deviations of the actual mode shape the errors are roughly 1% to 3%, making the effect of moderate deviations from a straight line mode shape insignificant.

The elements of the dynamic force measurements are shown in Fig. 2.5. For linearly increasing mode shapes the generalized forces correspond to the moment measurements at the base of the building models. As shown in Section 2.14, the moment measurements are also applicable to coupled mode shapes. Torsional forces and aerodynamic effects need special consideration and are described at greater length in Sections 2.13 and 2.7, respectively.

The major difficulties in the experimental determination of modal forces have been the demanding requirements on the frequency response of the system and on the sensitive balances necessary to avoid distortion of the quantity being measured. This has been addressed in more detail in Sections 1.2 and 1.7. The frequency of the balance-model combination should be at least 4 to 5 times higher than the lowest natural frequency of conventional aeroelastic models. As an illustration, assuming a time scale of 1:100 and a period of 1 second per 10 storeys, demands a frequency response for a 20 storey building of:

$$\frac{10}{20} \times 100 \times 5 = 250\ Hz$$

a formidable task for a mechanical system larger than of miniature size. At the same time the force is not mechanically magnified as for conventional aeroelastic models, making it necessary to have a much more sensitive balance.

The Boundary Layer Wind Tunnel test for direct force measurements is similar to the schematic diagram shown in Fig. 2.4. The main difference is that only the

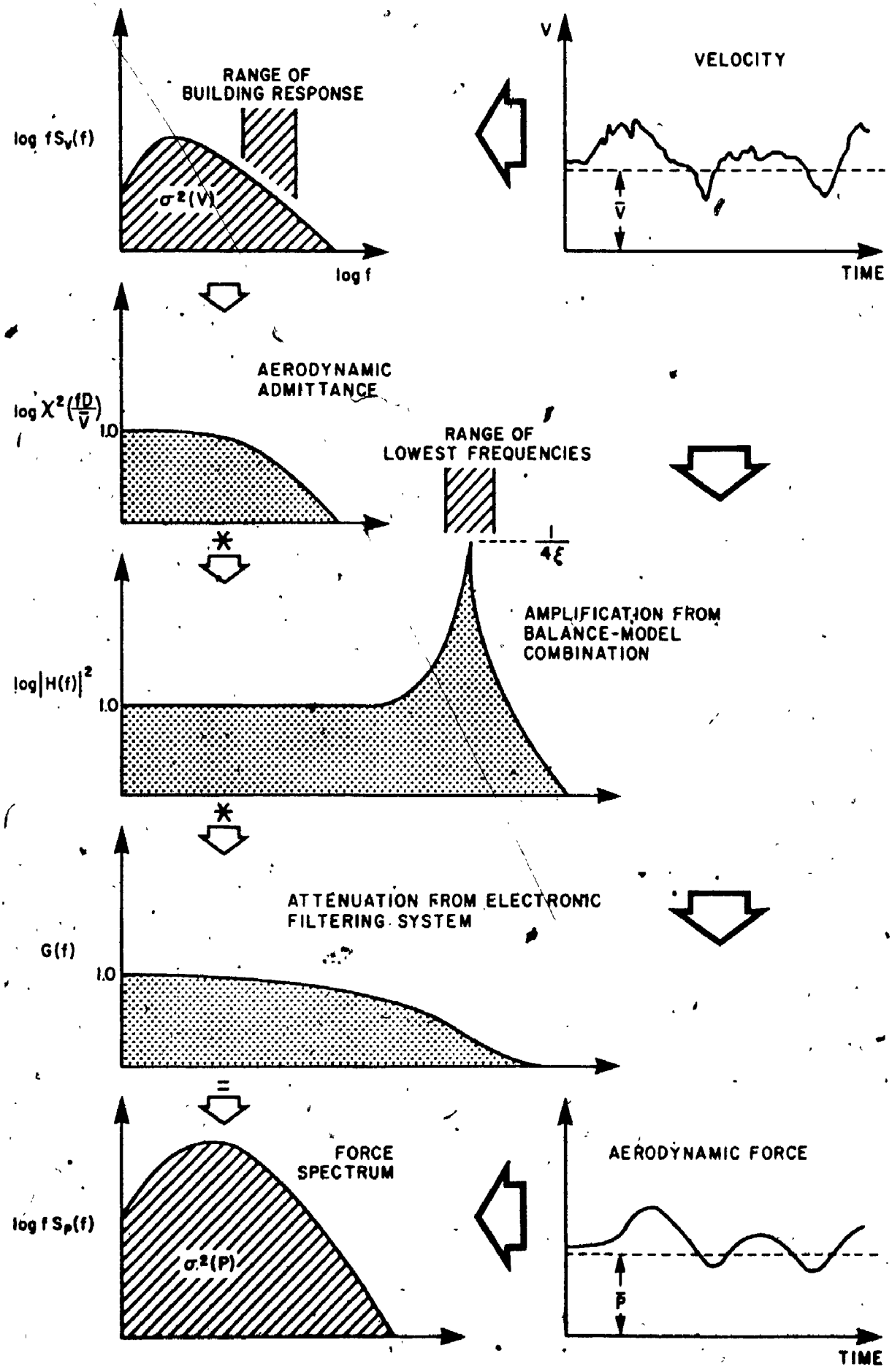
RANGE OF
BUILDING RESPONSE
log f S_v(f)
σ²(V)
log f
V
VELOCITY
V̄
TIME
AERODYNAMIC
ADMITTANCE
log χ²(fD/V̄)
1.0
RANGE OF
LOWEST FREQUENCIES
1/4ξ
AMPLIFICATION FROM
BALANCE-MODEL
COMBINATION
log|H(f)|²
1.0
ATTENUATION FROM ELECTRONIC
FILTERING SYSTEM
G(f)
1.0
FORCE
SPECTRUM
log f S_p(f)
σ²(P)
AERODYNAMIC FORCE
P̄
TIME

the expense of increased digital processing.

The force measurement approach has the following main advantages:

i) It is a simplification over conventional aeroelastic models in situations where body motional (aeroelastic) effects are not significant. Tall chimney stacks, excited in the cross-wind direction, would be an example requiring full aeroelastic tests;

ii) If changes occur in the design stages of the full scale structures, the force measurements are totally independent as long as the geometry remains the same. This is usually the case in real buildings;

iii) The forces have to be evaluated at only one wind speed. In contrast, measurements at several wind speeds are needed in aeroelastic tests.

iv) Because of the much reduced delay between the start and completion of the study, severe responses due to the wind are recognized early and the structural design can be modified if necessary;

v) Many structures which might not be tested in a wind tunnel because of the expense and long time delay of results from conventional aeroelastic tests, can be investigated with the simple force measurement technique;

vi) The total dynamic force can be directly measured in the time domain, and for response calculations the structural properties can be modified at each time step depending on the current value of displacement, as well as the past history of deformation to account for hysteretic material. In this approach the response is evaluated for a series of

short time increments with step-by-step integration procedures described in Chapter IV.

The labour to design and fabricate the simple models described in Section 1.7 is approximately one hour, most of the time being required to machine the base plate with threaded holes for mounting. This lends itself to parameter studies and codification. A photograph with some of the models tested for the analysis in this chapter is shown in Fig. 2.6.

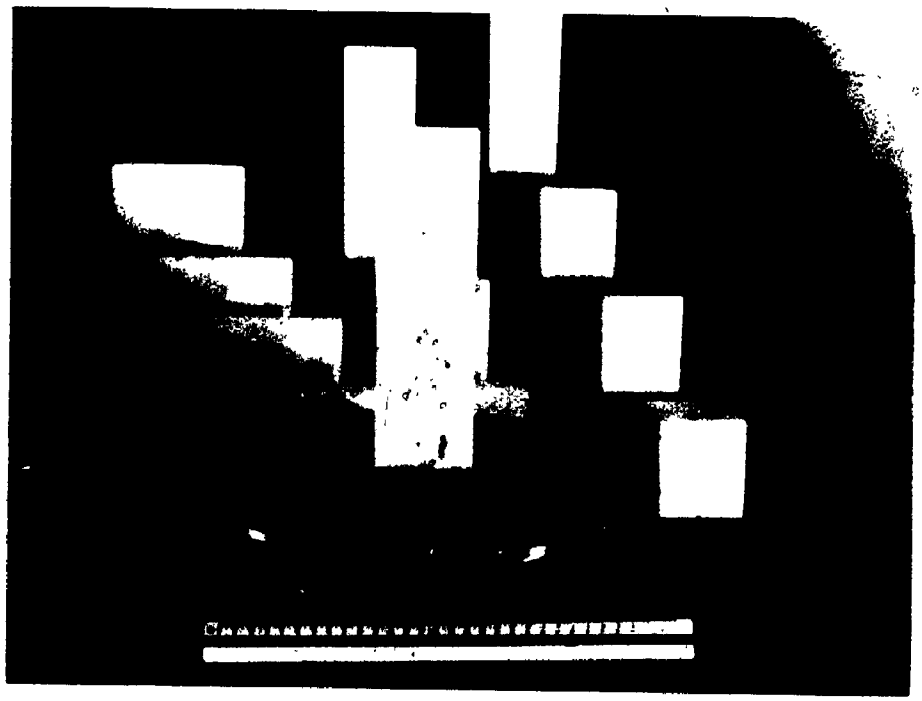

FIG. 2.6 PHOTOGRAPH OF FINISHED BALANCE WITH SOME TYPICAL BUILDING MODELS

2.4 DYNAMIC FORCE MEASUREMENTS BY OTHER INVESTIGATORS

2.4.1 Applications Relying on a Force Balance

The technique of obtaining the modal wind-load spectra and computing the corres-

appropriate to a particular building or structure has been known for a long time and is gaining popularity.

One of the first attempts at direct force measurements of quasi-static wind load spectra has been described by Cermak et al [1970]. Their approach used a simple strain gauged blade at the base of a building model. The 5 inch long beam protruded into the wind tunnel, and was covered by a shell of the building model of the correct dimensions (20.75 x 7 x 3.9 in. for height, width and depth respectively). The natural frequency of 200 Hz is impressive, but the stiffness-strain product is only 0.2 strain/radian, assuming a reasonable guess of the missing details in their paper. Compared to the value of 6.7 strain/radian for the five-component BLWT balance described in Chapter I, it is obvious that the sting type balance does not provide the best possible stiffness-sensitivity combination. Other shortcomings are that it measures only one component, and the relative difficulty of mounting different building models. An advantage is the cheap fabrication of the balance.

Whitbread [1975] measured the base overturning moment and base shear in one direction using a carbon fibre model and semi-conductor gauges diffused on a chip. The system is described in more detail in Section 1.3.3. A high frequency of the balance-model combination was achieved with a big compromise in sensitivity. The system is also statically indeterminate, making it sensitive to temperature effects.

English and Durgin [1981] constructed a sting type balance measuring five components with a model from a balsa wood shell. The lowest natural frequency for the 8 x 12 x 3 inch model was only 65 Hz, but considerable emphasis was given to increase the damping. From the transfer function shown in Fig. 1.1, it can be seen that for sufficiently high damping the high frequency requirements are somewhat less severe, but it is questionable if sufficiently high damping values can be practically achieved. Their paper does not show any spectra, the time history figure appears to show some periodicity and the rms force coefficients show some inconsistencies. Details are not available to

2

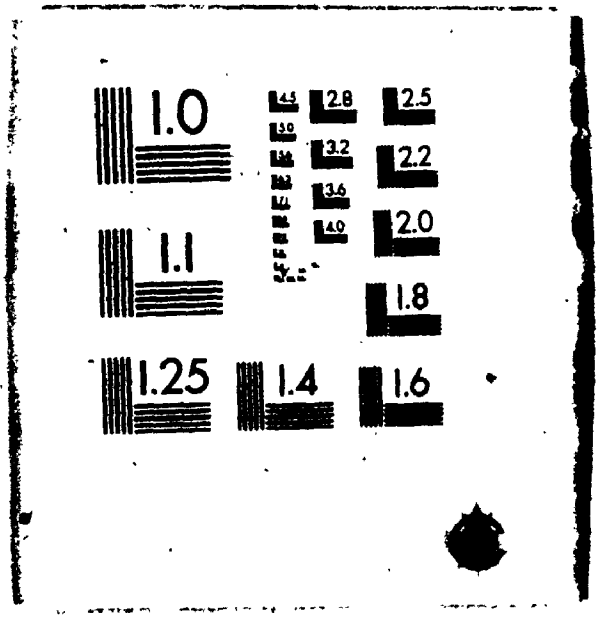

Torsional moments may be difficult to measure because of insufficient sensitivity and coupling effects.

A different approach, using low frequency models and inferring the force from response measurements, was used by Saunders and Melbourne [1975]. Knowing the frequency and the damping of the transfer function shown in Figure 1.1, a correction can be made at each measured frequency to compute the spectrum of the force. The main difficulty is that the damping has to be known exactly, including the aerodynamic damping contribution, because of the sensitivity to the damping value near the natural frequency of the balance-model combination.

Evans and Lee [1981] use a one component balance, measuring the base bending moment on models. The frequency and damping of the model is scaled to the values required by the scaling laws. Their frequencies and damping can apparently be varied independently, but this makes their method more comparable to the conventional pivoting aeroelastic models. The mass has to be scaled as well, or taken into account when converting to full scale values. Noteworthy are their carbon-fibre reinforced plastic models, but with the low frequencies required for pivoting models it might be economical to use a more efficient balance and simple balsa wood models.

2.4.2 Application Without a Force Balance

Modal forces can be directly determined using rigid models, instrumented with pressure transducers, without employing a balance. This approach was followed by Reinhold and Sparks [1979] to compute the modal forces for the fundamental translational modes and the fundamental torsional mode of a building, by summing the products of pressure times area times mode shape throughout the height of the building according to Equations (2.3). The stringent frequency response requirements are eliminated, as the response for pressure measurements is flat to beyond 100 Hz for routine test set-ups at the BLWT. This is the only method besides conventional aeroelastic tests, theoretically permitting arbitrary mode shapes, including realistic ones for the torsional modes.

In practical applications, however, a number of compromises are required. The ideal case would be to use the same pressure model which is routinely being used in wind engineering studies to determine the cladding pressures, with one pressure transducer, signal conditioning, sampling and digitizing port in the computer for each pressure tap, and to perform simultaneously all operations according to Equations (2.3). While the signal conditioning, the digitizing and the computers are getting cheaper and more powerful, the total cost, including the transducers and labour involved, makes this approach not feasible. Practical approximations include proportional spacing of pressure taps according to mode shape and pneumatic averaging or, like Reinhold and Sparks [1979], selecting as many taps as pressure transducers are available, and summing and multiplying the contributions to the modal forces with analogue circuits as required.

2.4.3 Discussion

All methods discussed, including the five-component balance of the BLWT used for the analysis in this chapter, make some approximations. No rigid model technique can take body motion dependent forces into account. The method using pressure transducers enables realistic torsional mode shapes to be used, but it is estimated that the limited number of transducers which can be used in practical applications do not improve the accuracy.

Judging by the simplicity of mounting the economical foam models on the balance, and by the direct availability of all five components, the BLWT balance-model combination is most attractive.

2.5 LINEAR ELASTIC RESPONSE PREDICTIONS WITH THE BLWT BALANCE

The linear response of an elastic system can be expressed in the general form:

$$R = \bar{R} + g\,\sigma_R \qquad (2.4a)$$

where $\bar{R} = \frac{\bar{F}}{k}$ (2.4b)

$$\sigma_R = \frac{1}{k}\sqrt{\int_0^\infty S_F(f)\,|H_{(f)}|^2\,df} \qquad (2.4c)$$

$$|H_{(f)}|^2 = \frac{1}{\left\{1 - (\frac{f}{f_o})^2\right\}^2 - 4\,(\xi_s + \xi_a)^2\,(\frac{f}{f_o})^2} \qquad (2.4d)$$

where $\bar{R}$ is the mean response, k the generalized stiffness (e.g. $(2\pi f_o)^2 \rho A H^3/3$), ξ_s the structural damping, ξ_a the aerodynamic damping, σ_R the rms response and, g a dimensionless time varying factor. A particular response of interest is the peak response $\hat{R}$, in which case the corresponding value of g is roughly 3 to 4 [Davenport, 1964]. The mean generalized force, $\bar{F}$, the rms generalized force, σ_F, and the power spectrum of the generalized force $S_F(f)$ are defined in Equations (2.3).

Integrals are often required to be evaluated in wind engineering problems, i.e. in the Equation (2.4c), or even fourfold integrals such as for computation of joint acceptance functions described in Section 2.2. Recent advances in numerical methods simplify the problem and a short, but generally applicable summary is presented in the following paragraph.

The exact evaluation of the integral in Equation (2.4c) presents some difficulties because of the rapidly varying mechanical magnification function, $|H(f)|^2$, in the resonance range for low damping values. Novak [1967] presented a solution based on the "residua theory". If a high speed computer is available, the integral can be solved efficiently to any accuracy, up to the word length of the computer, by adaptive quadrature methods. These are automatic routines, requiring no decision by the investigator such as spacing of points in the function to be integrated, and are usually most efficient in computer time. The fastest algorithm tested by the author for problems of the type in Equation (2.4c) is "SQUANK" (Simpson Quadrature used adaptively), written by Lyness [1970].

Slightly slower, but more reliable in some "theoretically created, difficult to integrate functions" is the routine "AGM" (Adaptive Gaussian Quadrature) by Robinson [1976]. Both algorithms are published in FORTRAN and easily implemented. The author evaluated the quadruple integrals common in some theoretical wind response calculations in a maximum of 5 seconds using "SQUANK" on the PDP 11/60 computer of the BLWT Laboratory. (An application note: the accuracy parameter was set to 0.01 for each integration level.)

A good approximation of the response is obtained by evaluating Equation (2.4c) as two components: a quasi-static component σ_B and a resonant component σ_{Re}. σ_B is evaluated for a value of 1.0 for the mechanical magnification function, and σ_{Re} is evaluated assuming the spectrum to be constant, with a value of $S_F(f_o)$ for all frequencies. This results in the well known equations:

$$\sigma_B = \frac{\sigma_F}{k} \qquad (2.5a)$$

$$\sigma_{Re} = \sqrt{\frac{\pi}{4} \frac{1}{\xi_s + \xi_a} \frac{f_o S_F(f_o)}{k^2}} \qquad (2.5b)$$

Using mean square addition of the components results in:

$$\sigma_R = \frac{\sigma_F}{k} \sqrt{1 + \frac{\pi}{4} \frac{1}{\xi_s + \xi_a} \frac{f_o S_F(f_o)}{\sigma_F^2}} \qquad (2.6)$$

This representation has been given in various references [Davenport, 1966, for example] and is the basis of the gust factor approaches. The difficult problem in evaluating Equation (2.6) has always been the determination of the rms generalized force, σ_F, its spectrum $f_o S_F(f_o)/\sigma_F^2$ and the aerodynamic damping ξ_a.

Force spectra $f_O\ S_F(f_O)/\sigma_F^2$ are shown in this chapter, and a comprehensive collection is presented in Appendix A. With typical values for $(\pi/4)\ x\ (\xi_S + \xi_a)^{-1}$ of roughly 100, the background and the resonant contribution are equal for spectral values $(f_O S_F(f_O)/\sigma_F^2)$ of 0.01. The reduced velocity corresponding to this value (0.01) is easily determined, and at higher velocities the dynamic response is primarily due to resonance. At values corresponding to 0.001 the resonant response is only about 10 percent. The dynamic effects of buildings become more important as the resonant component becomes more important.

The generalized forces and its spectra are easily measured using the five component BLWT balance. The aerodynamic damping, however, is motion dependent and can only be measured with conventional aeroelastic models. This subject is discussed in Section 2.7.

2.6 PRESENTATION OF FORCE SPECTRA

As shown in Section 2.5, the spectra of the generalized force are of fundamental importance to the determination of the dynamic response. The energy of the fluctuating force is distributed over a large range of frequencies. This distribution of energy with frequency f can be described with the power spectral density, $S_F(f)$. $S_F(f)$ is measured by averaging Fast Fourier Transforms (FFT's) of 50 to 100 time histories of the balance output. The FFT's are computed in real time with the PDP–11/60 computer of the BLWT Laboratory, or with the HP 5423A FFT Analyser.

The relationship between the power spectrum and variance is:

$$\int_0^\infty S_F(f)\ df = \sigma_F^2 \qquad (2.7)$$

Fig. 2.7a shows a typical force spectrum as a function of the independent variable during the test; the normalized frequency $\frac{nD}{V_T}$, where D is a typical building dimension and V_T the mean velocity at the top of the building. Most of the energy is concentrated

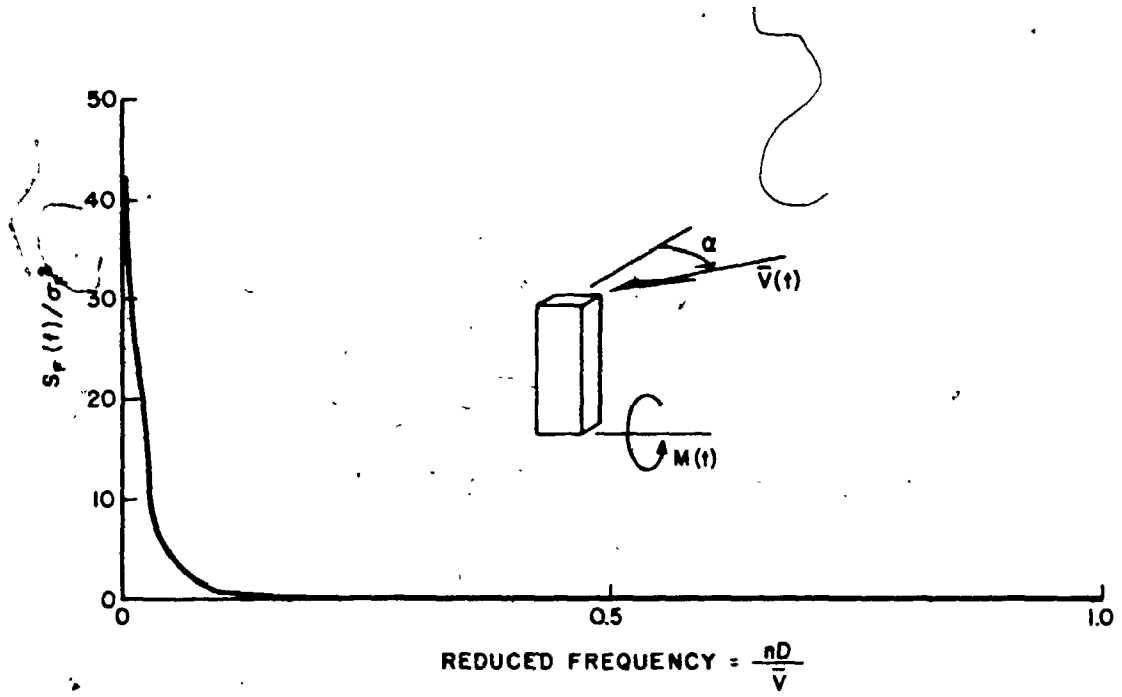

a) SPECTRUM WITH LINEAR SCALES

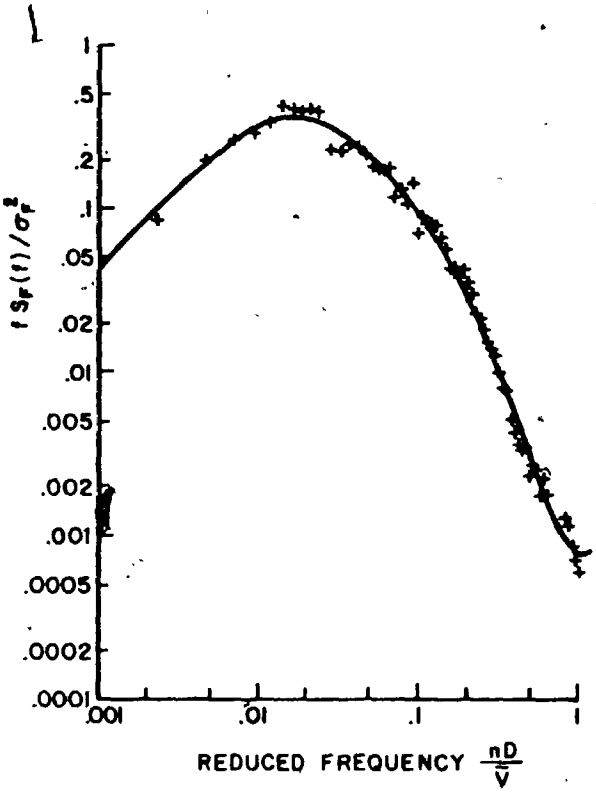

b) LOGARITHMIC SPECTRUM AS A FUNCTION OF REDUCED FREQUENCY

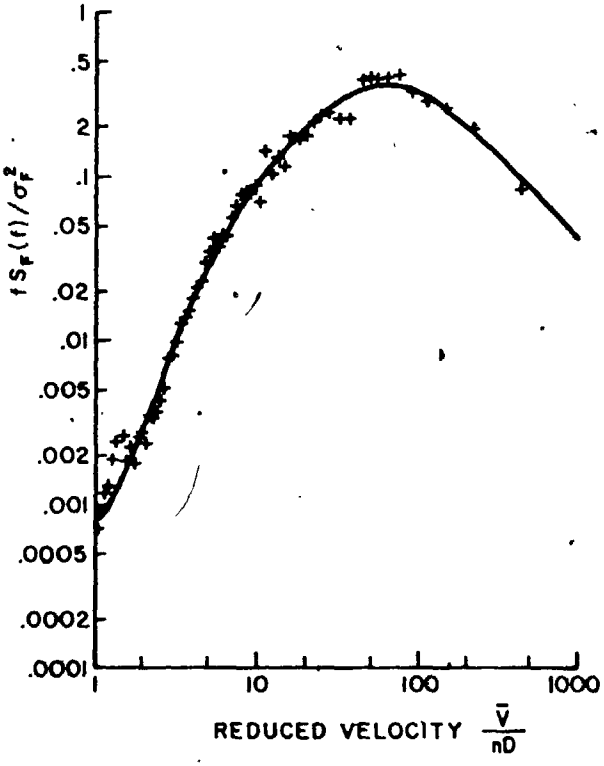

c) LOGARITHMIC SPECTRUM AS A FUNCTION OF REDUCED VELOCITY

FIG. 2.7 THREE DIFFERENT WAYS OF PRESENTING DYNAMIC FORCE SPECTRA

at low frequencies, and it is appropriate to draw the "logarithmic spectrum", with an ordinate of $f\,S_F(f)/\sigma_F^2$. This form of the spectrum is dimensionless and preserves the relative contributions to the variance at different frequencies represented on a logarithmic scale. The integral of the spectrum is:

$$\int_0^\infty \frac{f\,S_F(f)}{\sigma_F^2}\, d\ln f = 1 \qquad (2.8)$$

If the normalized power spectral density is drawn with a logarithmic scale, the curve falls off in the range of the important normalized frequencies $(fD/\bar{V}_T)$ with a nearly constant slope, as shown in Fig. 2.7b.

In applying results, it is generally more convenient to consider this spectrum as a function of the reduced velocity $(\bar{V}_T/fD)$ rather than its inverse, the reduced frequency. The frequency, f, and the characteristic dimension, D, have a fixed value for a projected building; variable are the design wind speeds at the top of the building, $\bar{V}_T$. This then permits the interpretation as a resonant response factor which varies with wind speed. The analogy with the gust factor approach gives the mean square dynamic force as:

$$\sigma_{R_f}^2 = \sigma_F^2 \left(1 + \frac{\pi}{4}\,\frac{1}{\xi}\,\frac{f_o\,S_F(f_o)}{\sigma_F^2}\right) \qquad (2.9)$$

as shown in Equation (2.6). This can be also expressed as :

$$\sigma_{R_f}^2 = \sigma_F^2 \left(1 + \frac{\pi}{4}\,\frac{1}{\xi}\,\frac{\left(\frac{\bar{V}_T}{f_o D}\right)\,S_F\,\left(\frac{\bar{V}_T}{f_o D}\right)}{\sigma_F^2}\right) \qquad (2.10)$$

This form of representation, the normalized spectral density as a function of the reduced velocity for the top of the building in logarithmic scales, is used throughout this

study. The Appendix A contains force spectra for a collection of building models and exposures tested.

2.7 AERODYNAMIC DAMPING

In addition to the time dependent loads measured on rigid models, are time dependent loads induced only by movement of the structure as it moves through the fluid in response to the external forces.

Aeroelastic forces fall into three classes [Davenport, 1977]; those proportional to accelerations, those proportional to velocity (or more correctly dependent upon rather than proportional to), and those proportional to displacement. Only forces dependent upon the velocity are of significance for buildings. They act in parallel with the structural damping and are referred to as aerodynamic damping forces.

The aerodynamic damping ξ_a can be expressed as [Davenport, 1979; Davenport and Tschanz, 1981):

$$\xi_a = -\frac{\rho D^2}{M} C_a \left(\frac{\bar{V}}{f_o D}\right) \qquad (2.11)$$

where C_a is an aerodynamic damping coefficient; it is a function of the reduced velocity $\bar{V}/f_o D$, where $\bar{V}$ is the mean wind speed, D a typical diameter and f_o the frequency of the oscillation. The factor $\rho D^2/M$ represents the ratio of the air density ρ to the nominal building density M/D^2 where M is the mass per unit length.

2.7.1 Damping in the Drag Direction

For damping in the drag direction the aerodynamic damping coefficient C_a can be expressed as:

$$C_a\left(\frac{\bar{V}}{f_o D}\right) = -\frac{1}{4\pi}\,\frac{\bar{V}}{f_o D}\,C_D\left(\frac{\bar{V}}{f_o D}\right) \qquad (2.12)$$

where $C_D(\bar{V}/f_o D)$ is an unsteady drag coefficient. At large values of the reduced velocity the unsteady drag coefficient approaches the steady drag coefficient. This is illustrated in Fig. 2.8, which shows the unsteady drag coefficient [Davenport, 1961b; Davenport, 1979] for a flat plate. It is positive throughout the range shown.

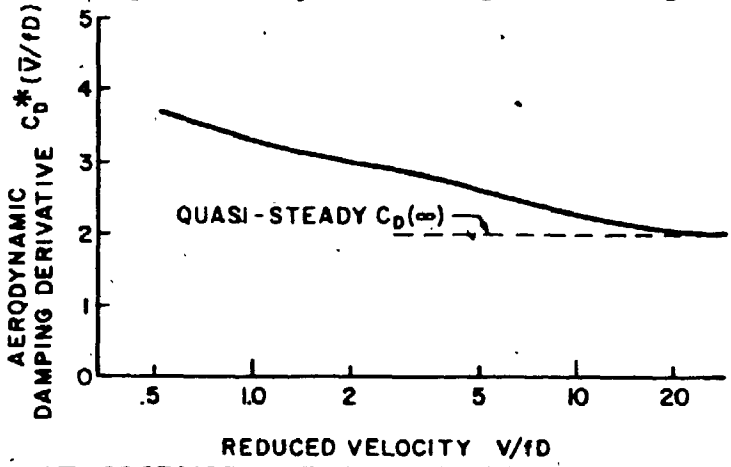

FIG. 2.8 AERODYNAMIC DERIVATIVE FOR DRAG DAMPING FOR A FLAT PLATE

Combining Equations (2.11 and 2.12) results in:

$$\xi_a = \frac{1}{4\pi}\,\frac{\rho D^2}{M}\,\frac{\bar{V}}{f_o D}\,C_D\left(\frac{\bar{V}}{f_o D}\right) \qquad (2.13)$$

Assuming typical values (i.e. the World Trade Center) of $M/\rho D^2 \approx 182$, $\bar{V}/f_o D \approx 10$, $C_D \approx 2$ gives $\xi_a \approx 0.87\%$, a value clearly significant for higher wind speeds.

The values for a flat plate in the drag direction may be indicative for prismatic bodies. Few observations are published for buildings, both full scale or wind tunnel studies. Davenport [1977] also gave the following equation for buildings vibrating in a straight line first mode:

$$\xi_a = \frac{1}{2\pi} \frac{\rho D^2}{M} \frac{\bar{V}(H)}{f_o D} \frac{3}{2(3+\alpha)} C_D \qquad (2.14)$$

where α is the exponent of the velocity profile. Assuming the same values as above and an exponent, α, of 0.2 and a drag coefficient C_D of 1.2 gives a value for $\xi_a \approx .5\%$. Rosati [1968] found good agreement of Equation (2.14) with his aeroelastic tests of a tall square section. The difference with Equation (2.13) may be explained by the effect of the velocity gradient, which averages the effective reduced velocity over the structure and "blurs" the dominant peak of the damping curve.

2.7.2 Damping in the Lift Direction

The discussion in the section is only concerned with buildings, where displacements occur with small amplitudes (i.e. less than 1% of the diameter). At large displacements, i.e. for chimneys, other mechanisms may become important.

In the lift direction, aerodynamic damping can have either a positive or a negative value. Fig. 2.9 shows the lift damping derivative for a square prism calculated from measurements by Otsuki et al [1978]. The diagram shows that at the critical reduced velocity for vortex shedding (roughly 8 for the square prism) the sign of the derivative changes and the damping suddenly becomes negative. This worsens the potential for excitation already made severe by the vortex shedding peak! Below the critical velocity the lift damping is positive (C_a negative). At very high reduced velocities the damping approaches the quasi-steady "denHartog" value. Assuming a value of $M/\rho D^2 \approx 182$ gives values for ξ_a of roughly +0.25%, 5.5% and −4% for critical velocities much below the onset of vortex shedding, just below vortex shedding and at vortex shedding, respectively.

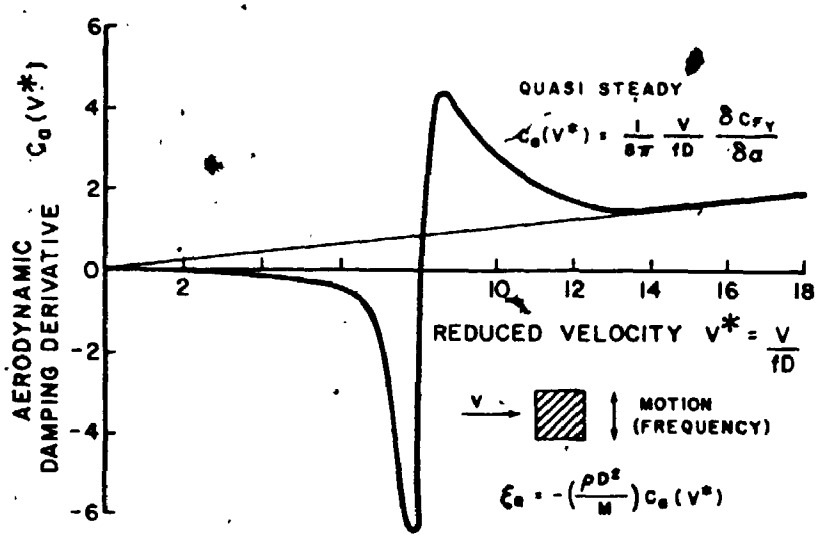

FIG. 2.9 MEASUREMENTS OF AEROELASTIC DAMPING DERIVATIVES FOR ACROSS-WIND MOTION BY OTSUKI ET AL [1978] (after Davenport and Tschanz, 1981)

2.7.3 Discussion

More measurements or theoretical derivations of the aerodynamic damping are desirable, which would enable accurate response predictions from rigid model force measurements. Some observations, however, can be made from the estimates described above. Practical ranges of $M/\rho D^2$ are between 80 and 250, and the examples show typical values for aeroelastic damping. It is therefore quite apparent that motion dependent forces in drag and lift are most significant for structures with a low structural damping value, i.e. ξ_s of 1% or less. The structural damping is usually not known to better than ± 0.5% of the actual value.

An important conclusion from the available data is the indication that aerodynamic damping for velocities below the critical velocity for vortex shedding, both the lift and drag damping are positive. The reduced velocity where vortex shedding occurs is readily observed in the force spectra by a dominant narrow band response. Thus, if the critical velocity lies above the range of probable wind speeds, then the response can be safely and conservatively estimated by neglecting the aerodynamic damping.

2.8 U.W.O. BOUNDARY LAYER WIND TUNNEL

The Boundary Layer Wind Tunnel at The University of Western Ontario has been described elsewhere (i.e. Davenport and Isyumov, 1967), and therefore only a brief summary to describe the turbulence structure used for the tests in this study is given.

The working section of the BLWT is approximately 80 ft. (24 m) long, 8.0 ft. (2.44 m) wide and has an adjustable height, variable from 5½ ft. (1.7 m) at the entrance to 7½ ft. (2.3 m) at the end. The adjustment of the roof height allows control over the pressure gradients along the tunnel length.

The tunnel velocity is continuously adjustable to a maximum of 50 ft./s (15 m/s). The test velocity and the geometric model scale determine the time scale to convert the test results to full scale values for the structure. (The reduced velocity, $\bar{V}/fD$, has the same value for full scale and model, where $\bar{V}$ is the mean velocity, f the frequency of the turbulence, and D a typical diameter of the structure.) Matching the longitudinal turbulence intensity in the BLWT with natural wind flow, results in a geometric scale of roughly 1:500 [Davenport and Isyumov, 1967]. The velocity can be selected freely, as long as the mean velocity profile, the turbulence intensity and spectral distribution of the gusts is preserved. To get the least distortion from the limited frequency response of the balance-model combination, however, it is beneficial to use a low wind speed. For low buildings the lowest wind speed is determined by the sensitivity of the balance, and for tall buildings by the requirements to have a correct model of the turbulence structure. The gradient wind velocities used were, hence, between 15 ft/s and 35 ft/s (4.5 m/s and 11 m/s), most often values between 20 ft/s and 30 ft/s (6 m/s and 9 m/s).

The turbulence is formed upstream in the long working section with an artificially roughened tunnel floor. An open country type exposure is simulated with an especially rough carpet and a suburban type exposure with small foam blocks. Examples of the two exposures are shown in Fig. 2.10.

Mean velocity profiles for the two roughness surfaces are shown in Fig. 2.11. The measurements seem to be in good agreement with the power law velocity variations

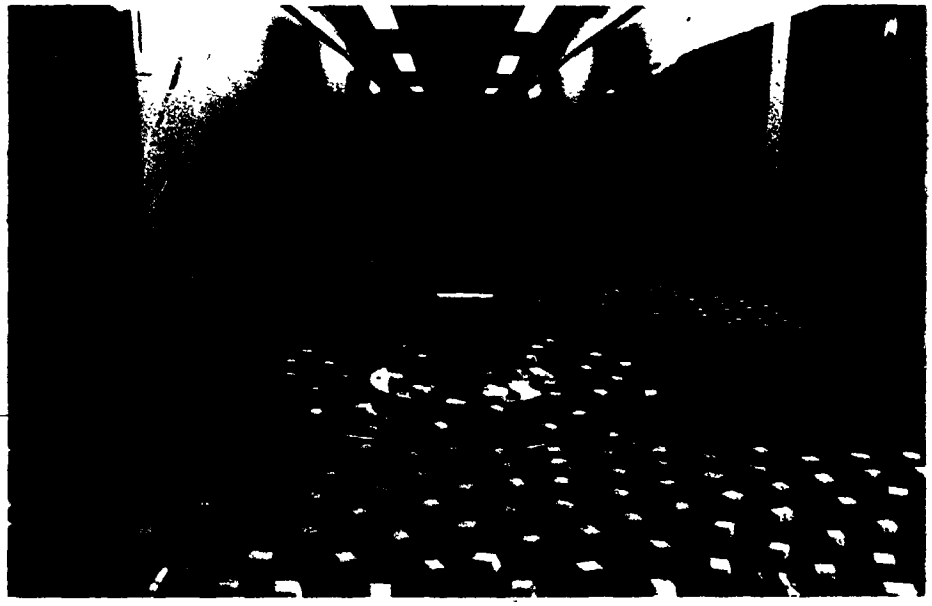

a) open country exposure

b) suburban exposure

FIG. 2.10 PHOTOGRAPHS OF TYPICAL EXPOSURES USED IN STUDY

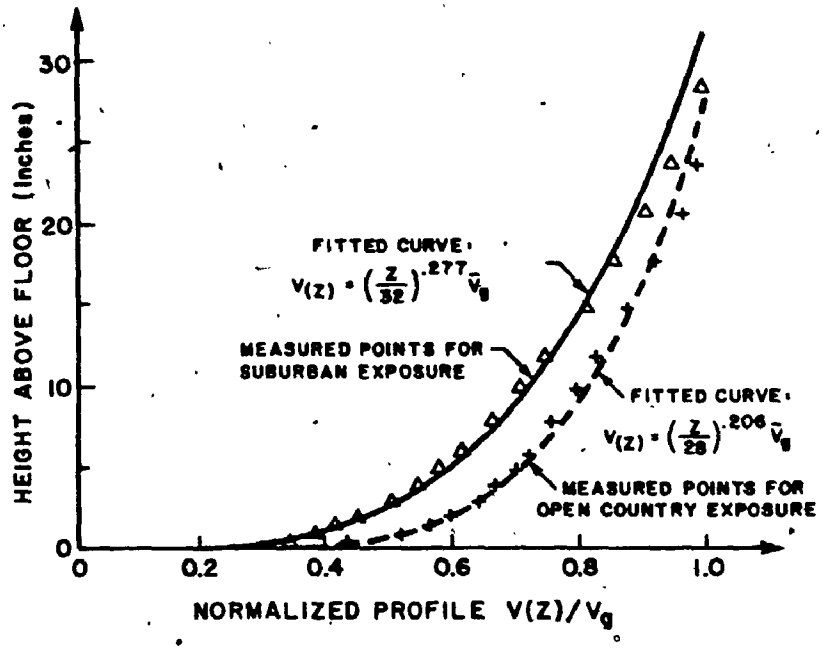

a) MEAN VELOCITY PROFILES

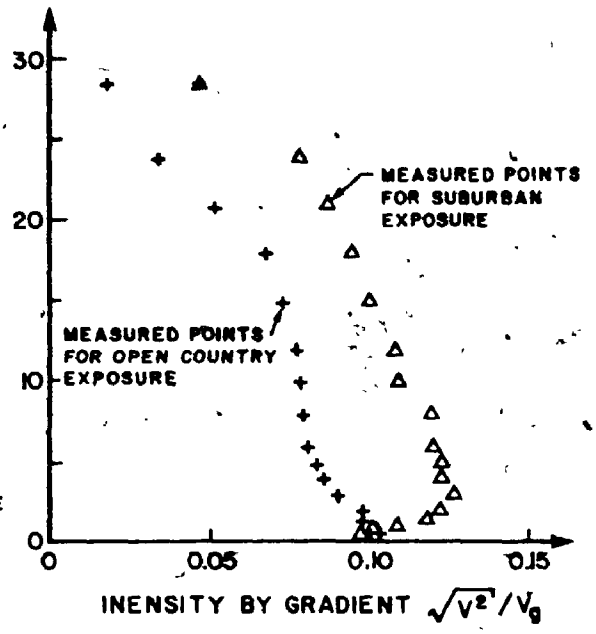

b) TURBULENCE INTENSITY

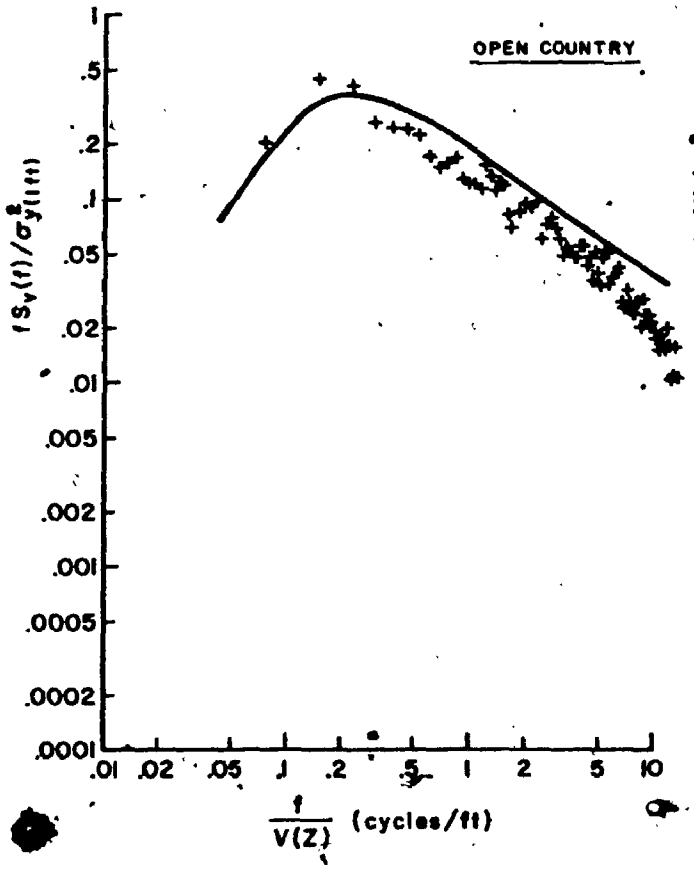

c) POWER SPECTRAL DENSITY; OPEN COUNTRY

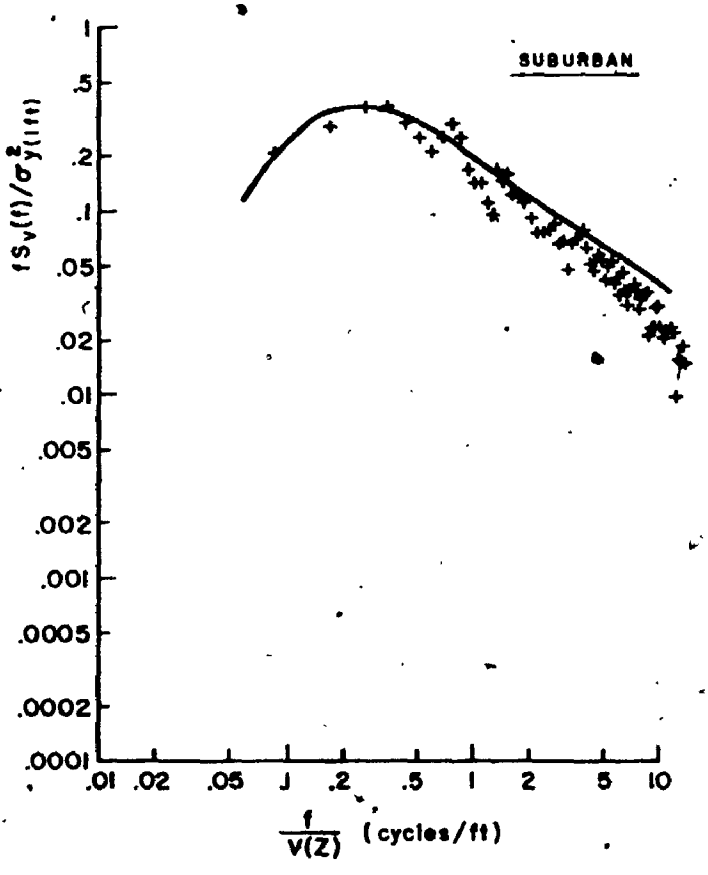

d) POWER SPECTRAL DENSITY; SUBURBAN

FIG. 2.11 LONGITUDINAL TURBULENCE IN U.W.O. BOUNDARY LAYER WIND TUNNEL

given in Equation (2.15) [Davenport, 1961b]:

$$\bar{V}(z) = \bar{V}_g \left(\frac{z}{z_g}\right)^{\alpha} \qquad (2.15)$$

where $\bar{V}(z)$ = mean velocity at height z
$\bar{V}_g$ = mean velocity at gradient height
z = height above ground
z_g = gradient height
α = exponent

Longitudinal turbulence intensities for the same surfaces are shown in Fig 2.11b These were measured with constant temperature hot-wire anemometers.

Spectra of the longitudinal velocity for the two tunnel flows are presented in Figs. 2.11c and d. These spectra are obtained by Fast-Fourier-Transforms of hot-wire anemometer velocity measurements. Spectra were measured at various heights at the building location, with the model removed. The spectra shown are for a height above ground of 1.0 ft. (.30 m). The spectra show good agreement, especially if the parameters would have been fitted, with Davenport's [1961] strong wind spectrum given in Equation (2.16):

$$\frac{f\, S_{V(z)}(f)}{\sigma^2_{V(z)}} = \frac{2}{3} \frac{\left(\frac{L f}{\bar{V}_{30}}\right)^2}{\left[1 + \left(\frac{L f}{\bar{V}_{30}}\right)^2\right]^{4/3}} \qquad (2.16)$$

where $S_{V(z)}(f)$ = power spectral density at height z
f = frequency
$\bar{V}_{30}$ = mean velocity at height 30 ft. (10 m)
$\sigma^2_{V(z)}$ = variance at height $z = 6\, \kappa\, \bar{V}^2_{30}$
κ = surface drag coefficient, e.g. 0.0005 for open country
0.015 for suburban exposure
L = 4000 ft. (1200 m)

The instrumentation specific to this study is described in Chapter I. Descriptions of other Laboratory instrumentation and procedures can be found in Davenport and Isyumov [1967], and Surry and Isyumov [1975].

2.9 COMPARISONS OF AEROELASTIC AND FORCE MODEL RESPONSE PREDICTIONS

The validity of a new test procedure should be confirmed by comparing results to full scale measurements. There are, however, problems in that full scale results are rarely available, and important parameters, such as reference wind speeds, turbulence conditions, structural damping, etc., are not accurately enough defined to reject different results as being in error.

An alternative is to compare results to currently used wind tunnel testing methods in order to assess if the new procedure gives similar results. Tests carried out during the same time period in the wind tunnel give better control over the above mentioned parameters than tests carried out at separate times and again better control than over full scale tests. Ideally a multi-degree-of-freedom aeroelastic test should be performed as a comparison to give information, in addition to the fundamental lateral responses, of the torsional response and of higher modes, but due to time and cost constraints only results for pivoting aeroelastic models are compared. One comparison test was performed by the author during the same time period, and another building test was carried out by Rosati [1968] more than a decade earlier under similar conditions.

2.9.1 Comparison of Identical Test of a Rectangular Building

A pivoting aeroelastic model of a tall building was retested by the author for a uniform roughness exposure corresponding to a suburban wind flow. Fig. 2.12 shows the tests for the aeroelastic model on the left and of the high-frequency force method on the right. The models in the wind tunnel are built from balsa wood in the case of the aeroelastic model, and simply cut from styrofoam for the direct force measurements.

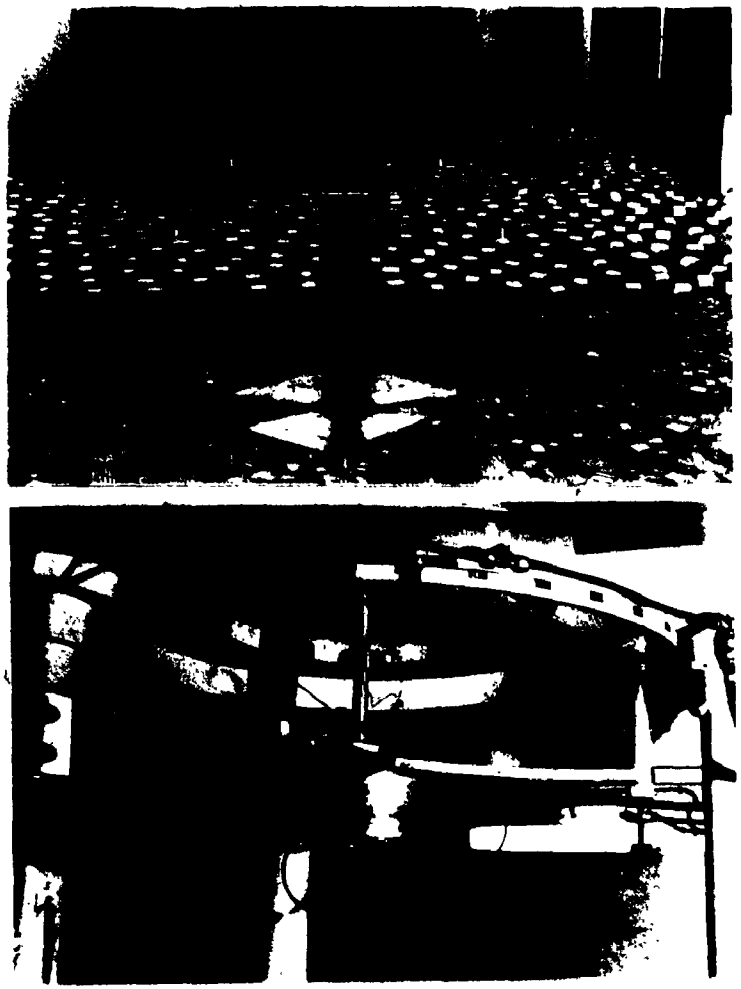

a) Conventional Pivoting Model

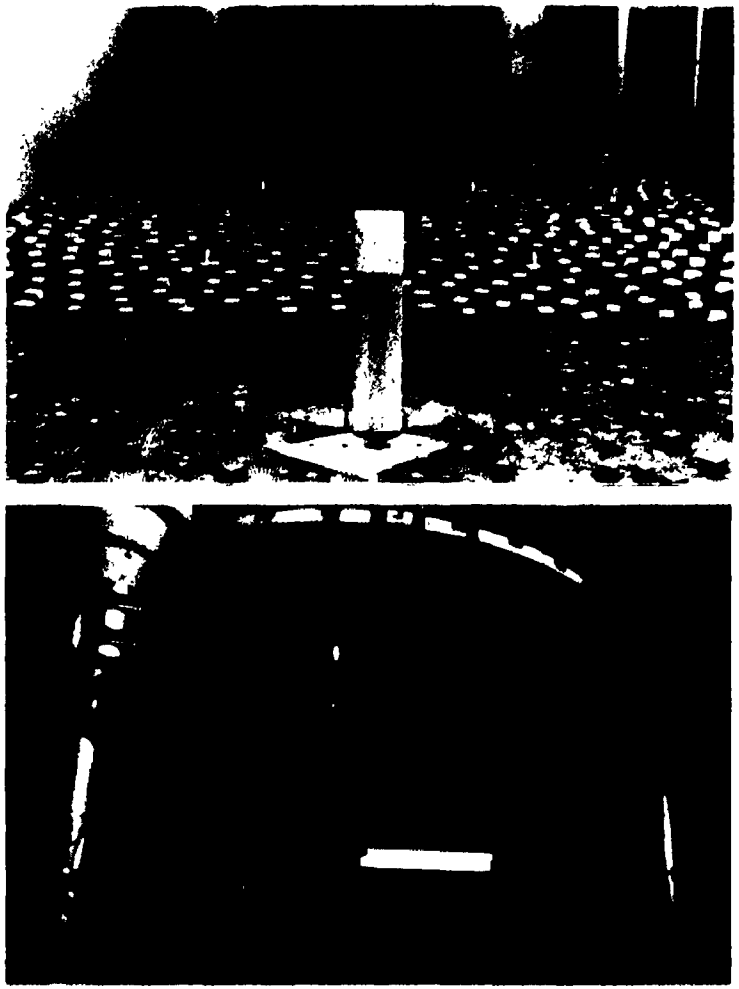

b) Proposed Force Measurements Using High Frequency Balance

FIG. 2.12 PHOTOGRAPHS OF WIND TUNNEL MODELS FOR COMPARISON OF AEROELASTIC AND FORCE METHODS

The aeroelastic model is mounted on gimbal bearings, and the lower part of Fig. 2.12a shows the underside of the tunnel and the model post with the mass compensation, the restraining springs and the external eddy current damper. The forces are measured with strain gauged links near the post where the springs are connected. The underside of the wind tunnel for the force method is independent of the structure as no mass, stiffness or damping needs to be modelled. The foam models are simply fastened to the balance with screws through the balance-girder.

The top graphs in Fig. 2.13 show measured force spectra for the drag and lift overturning moments on the broad face. The measured points of the power spectrum are fitted with equations for autoregressive processes as described in Chapter III. The forces are, hence, defined both in the frequency domain, and with the correct probability distribution in the time domain. The parameters in the denominator represent autoregressive constants, and the parameters in the nominator represent scaling factors and time scales. Other fits are possible, as presented in Section 2.11.

The force spectra are shown in non-dimensionalized form. The abscissas show the reduced velocity at the top of the building. Reduced velocities greater than 5 to 10, depending on building size, are not probable and small reduced velocities produce insignificant structural response. Although spectra are measured and presented over a broad range of reduced velocities only a narrow range is of significance, for both fitting purposes and response predictions. The abscissa can easily be converted to express the velocity by inserting the applicable frequency and dimensions for a particular building.

The ordinates show the dimensionless normalized power spectral densities $f \times S_F(f)/\sigma^2_F$ where f is the inverse of the reduced velocity. As described in Section 2.5, above a reduced velocity corresponding to an ordinate value of approximately 0.01 is the response primarily resonant at the fundamental frequency. It is important to restate that the force spectra as presented are only dependent on the turbulent flow and aerodynamic shape of the structure; and independent of the wind velocity or structural parameters such as mass, stiffness, or damping. The n in the absicssa (in Figs. 2.13 and 2.14) are the frequency of the gusts from experiments, and f in the ordinates are non-dimensional frequencies. At other places of this investigation n and f are used interchangeably.

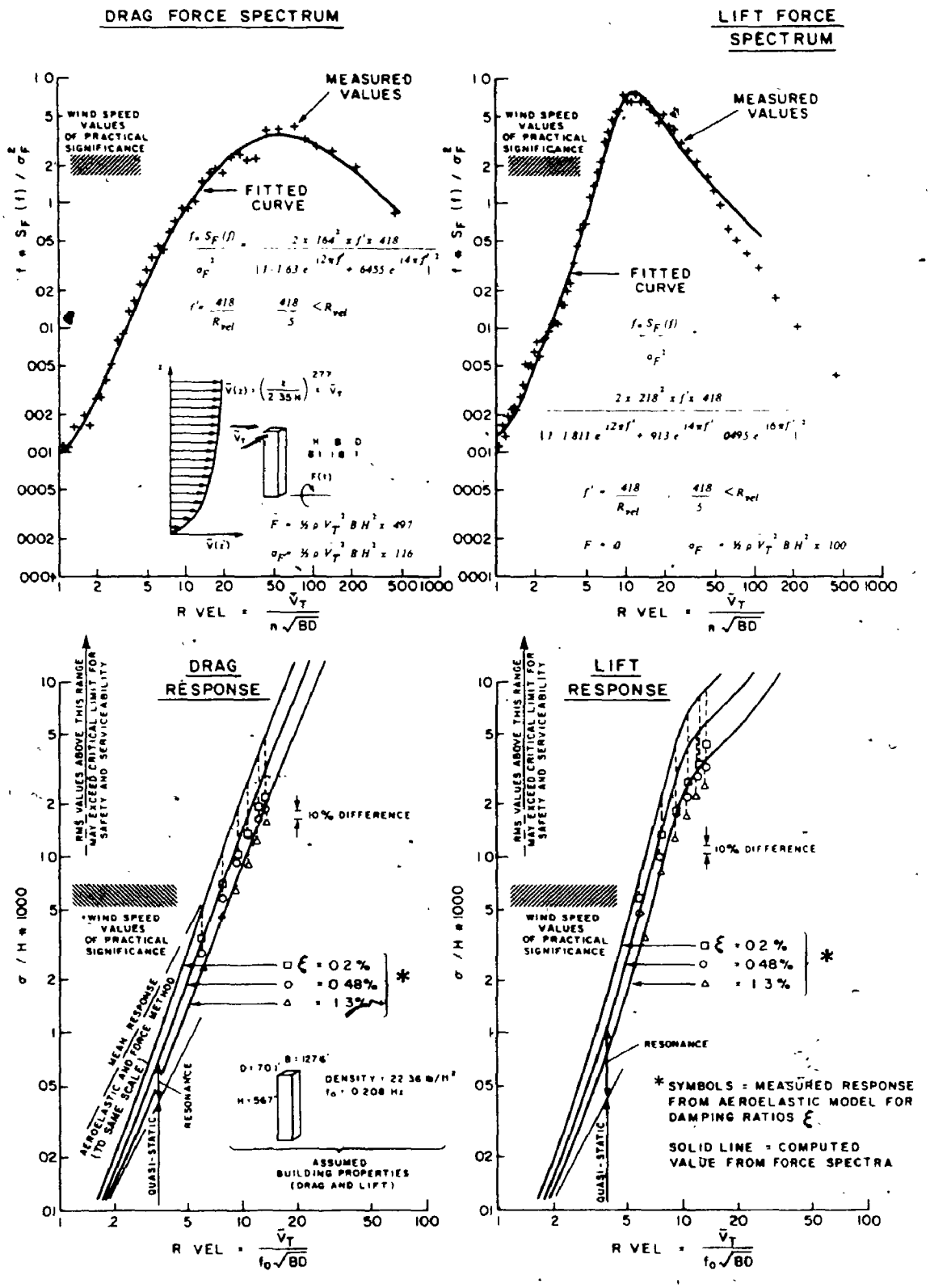

FIG. 2.13 FORCE SPECTRA AND COMPUTED RESPONSE COMPARED TO AEROELASTIC TESTS ON A RECTANGULAR BUILDING FOR SUBURBAN EXPOSURE

The graphs in the bottom half of Fig. 2.13 are specific to the building for which the aeroelastic study was performed. The dimensions are $H = 567$ ft. (172.8 m), $W = 127.6$ ft. (38.89 m), $D = 70.1$ ft. (21.37 m), and the period is 4.8s. The density of 22.36 lb/ft^3 (358.2 kg/m^3) is roughly twice the value of typical high rise structures, resulting in smaller response values than for lighter buildings. Shown are results for three damping values: 0.2%, 0.48% and 1.3%, the latter representing the estimated value for the full scale structure. The wide range of reduced velocities shown is not of practical significance for actual structures, i.e. the reduced velocity for the particular building in New York City corresponding to a 100 year return period is roughly 6. Most of the results of the aeroelastic test are for higher wind speeds. At lower wind speeds the signals get progressively more contaminated by electrical noise and would not be accurate for comparative purposes. Some problems also arise at very low damping values, they are difficult to keep at a controlled level and the sensitivity of the response to the damping is immense.

To assess the validity of the force model tests versus the aeroelastic model, more emphasis should be given to points for realistic velocity and damping values. The solid lines are evaluated using Equation (2.6) and aerodynamic damping is neglected. This leads to an overestimate from the force method for positive aerodynamic damping, which is expected to be positive for drag forces, and for lift forces below the critical velocity for vortex shedding. As described in Section 2.7, the effects are roughly proportional to the wind speeds, and therefore most important for high reduced velocities. Differences at high velocities between the two methods may therefore be attributed to body motional effects.

The response graphs in Fig. 2.13 show that the force method overestimates the response in all cases for this building, even at all tested velocities in the lift direction. The results agree well for realistic values of damping and velocity. The response at high wind speeds, especially in the lift direction, are of theoretical interest only, as the structure would have: (a) exceeded the safe displacement limits, and (b) behave non-linearly.

2.9.2 Comparisons of a Tall Square Building with Rosati's Aeroelastic Measurements

Rosati [1968] performed aeroelastic tests of a tall building similar to the World Trade Centre in New York City for various uniform turbulence levels and damping ratios. A high frequency force model was tested by the author for an open country type exposure, similar to the "moderately rough boundary" exposure in Rosati's test.

Fig. 2.14 shows comparisons between the two testing methods. The descriptions of Fig. 2.13 in Section 2.9.1 also apply to this figure. The reduced velocity for a 100 year return period for this building in New York City is less than 10, but the exposure would not be appropriate. The structural details in Rosati's test are $H = 980$ *ft. (298.7 m)*, $B = D = 140$ *ft. (42.67 m)*, the period is 10 seconds and the average density is *14 lbs/ft*^{3} *(224 kg/m*^{3}*)*. This is also heavier than typical contemporary high rise structures.

The drag response shows good agreement for high damping values, and for low damping values at realistic velocities. At high wind speeds the force method overestimates the response, indicating positive aerodynamic damping. The aeroelastic values at the lowest velocity are suspected to be too large, possibly due to noise in the signal.

The force model deduced lift response shows results which overestimate and others which underestimate the aeroelastic model response. The aerodynamic damping effects are obviously important at velocities above the critical velocity for vortex shedding, responses for low structural damping values are severely underestimated. Values for very low damping are outside the borders of the graph, but are not physically meaningful as the structure would have exceeded safe limits for both testing methods. Values for realistic conditions show good agreement.

2.9.3 Discussion

The direct force measurement approach proposed in this study provides good results for practical wind velocities and damping ratios. The limits of the applicability can be

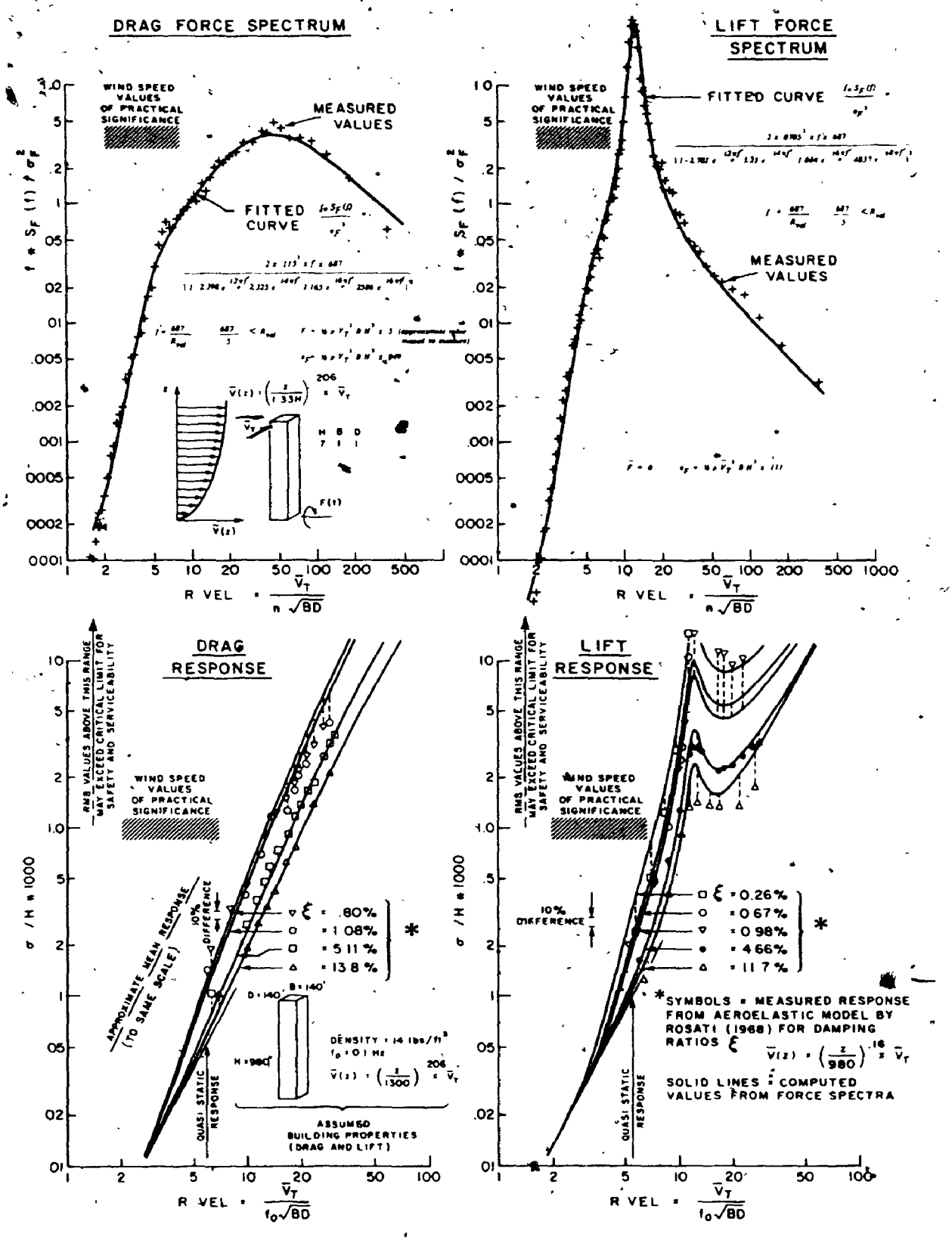

FIG. 2.14 FORCE SPECTRA AND COMPUTED RESPONSE COMPARED TO AEROELASTIC TESTS OF A TALL SQUARE BUILDING FOR OPEN COUNTRY EXPOSURE

recognized by vortex shedding energy bands in the force spectra. Differences at low velocities and damping values in the above comparisons may be partially due to unavoidable measurement errors in aeroelastic tests. Considering the significant effect damping has on the results, by the solid lines for different values, and the uncertainty of roughly ± 0.5% of the actual damping value for the full scale structure, the results are all acceptable, from either method. Improvements in the theory for aerodynamic damping values would improve response estimations from high frequency force models. The economy and short time in which a direct force model test can be performed, makes this method attractive for structural response predictions.

2.10 COMPARISONS WITH THE NATIONAL BUILDING CODE OF CANADA

A number of researchers, including Davenport [1961b and 1967], Vickery [1966], Velozzi and Cohen [1968], and Simiu [1973], have proposed methods of estimating gust response factors (the ratio of the peak value of the response of a building to the mean value of the response). Davenport developed such an approach for the Danish Standards and similar procedures are now the basis of various codes, i.e. The National Building Code of Canada [1980].

The gust factor approach in the National Building Code of Canada has the following equation:

$$C_g = 1 + g \cdot \sqrt{\frac{k}{C_e}\left(B + \frac{s\,F}{\beta}\right)} \qquad (2.17)$$

where C_g = the gust factor

g = the peak factor in Equation (2.4a)

k = a factor related to surface roughness: .08 for open country
.10 for suburban
.14 for downtown

C_e = an exposure factor based on the mean wind speed profile

B = a background excitation factor

s = a size reduction factor

β = the damping ratio

One method would be to compare the values of the square root in Equation (2.17) with the values σ_R of Equation (2.6), but any differences could not be attributed to a particular parameter. The relative contributions from the background and resonant excitation, however can be written as:

$$\frac{k}{C_e} B = 1.0 \qquad (2.18)$$

$$\frac{k}{C_e} \frac{s F}{\beta} = \frac{\pi}{4} \frac{1}{\beta} \frac{f_o S_F(f_o)}{\sigma_F^2} \qquad (2.19)$$

Thus the assumed spectral distribution of the National Building Code of Canada can be calculated as:

$$\frac{f_o S_F(f_o)}{\sigma_F^2} = \frac{4}{\pi} \frac{k}{C_e} \frac{s F}{\beta} \qquad (2.20)$$

Fig. 2.15 shows comparisons of measured values from high frequency models for a selection of building shapes and exposures. As an exception, the spectra are not given as a function of the reduced velocity. The good agreement gives confidence in the National Building Code approach and in the proposed method in this study. This agreement, also shown in Davenport and Tschanz [1981], has not previously been so explicitly demonstrated from model experiments.

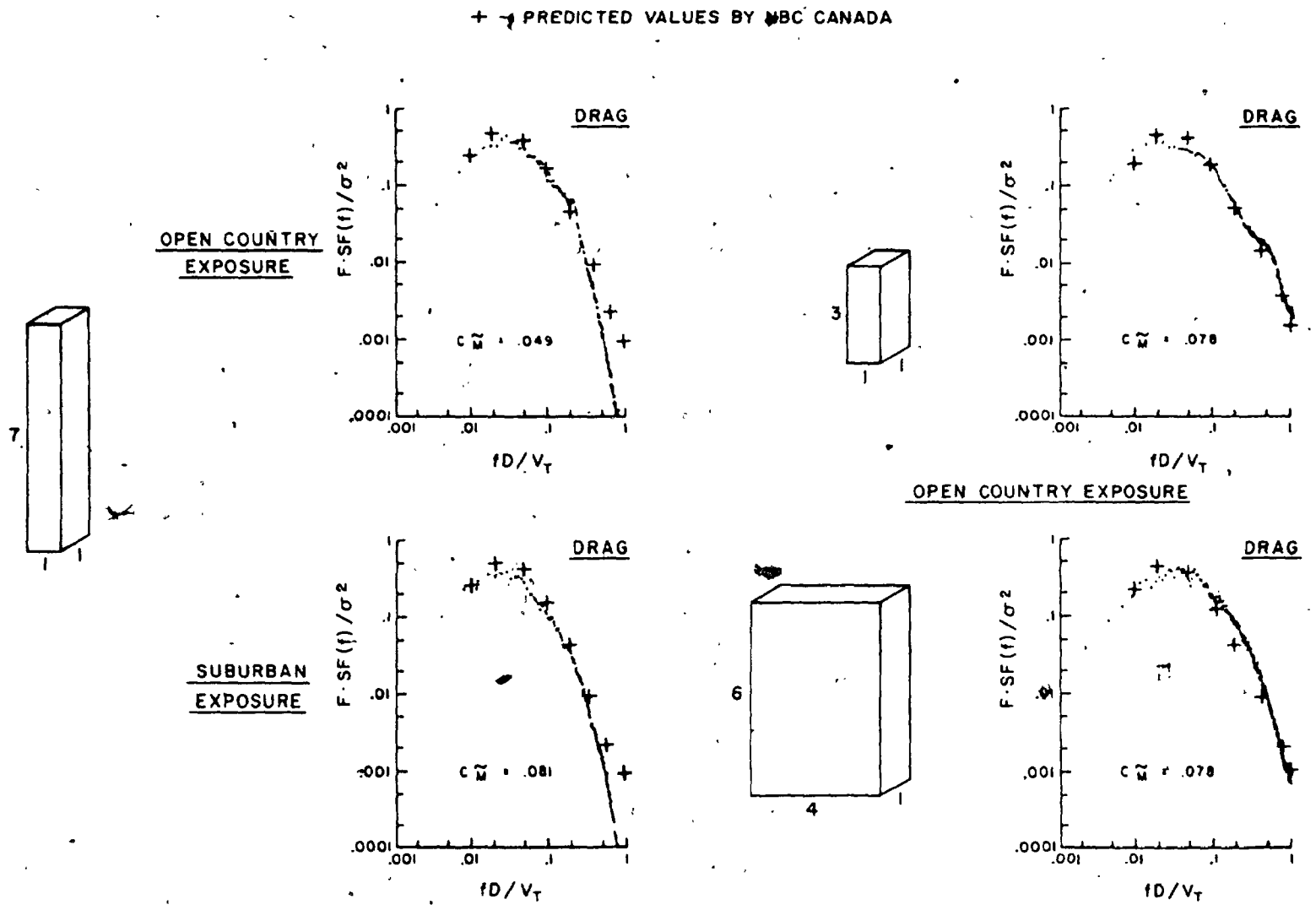

FIG. 2.15 FORCE SPECTRA COMPARED WITH THE NATIONAL BUILDING CODE OF CANADA

2.11 FITTING OF MEASURED SPECTRA

Spectra for several hundred variables were measured in the course of this study, each spectrum containing typically 512 points which were averaged from 50 to 100 Fast-Fourier-Transforms. This represents a large amount of data, which is not directly applicable for response prodictions or parameter studies. The first procedure, applied to specific studies at the BLWT, is to smooth the spectrum by averaging with neighbouring points, and to interpolate for the required velocity. Noise contaminations, however, can locally influence the response predictions significantly.

The spectra shown in Figs. 2.13 and 2.14 are fitted with regard to time series simulations, as described in Chapter III. Good fits were achieved with few parameters and the parameters fulfill the dual purpose of stochastic time series simulation and spectrum fits. The spectra presented in this thesis are, hence, fitted with equations for time series simulations.

For applications exclusively in the frequency domain, such as parameter studies for different shapes and exposures, it may be preferable to use other equations. This is straightforward using the optimization technique presented in Section 3.7, only the basic equation and no derivative need to be evaluated or coded in a FORTRAN subroutine. As an illustration, the drag spectra shown in Figs. 2.13 and 2.14 are refitted with an equation showing similarities with the wind velocity spectrum times an aerodynamic admittance function in Equation (2.1):

$$\frac{f\, S_{F_D}(f)}{\sigma_{F_D}^2} = c_1 \frac{(c_2\, f)^{c_3}}{1 + (c_4 f)^{c_4}} \left(\frac{1}{1 + (c_5\, f)^{c_6}} \right)^2 \qquad (2.21)$$

where S_{F_D} = drag force power spectrum

c_i = constants found by fitting measured values, as seen in Fig. 2.16

f = $\frac{f_W\, D}{V}$ = (reduced velocity)$^{-1}$

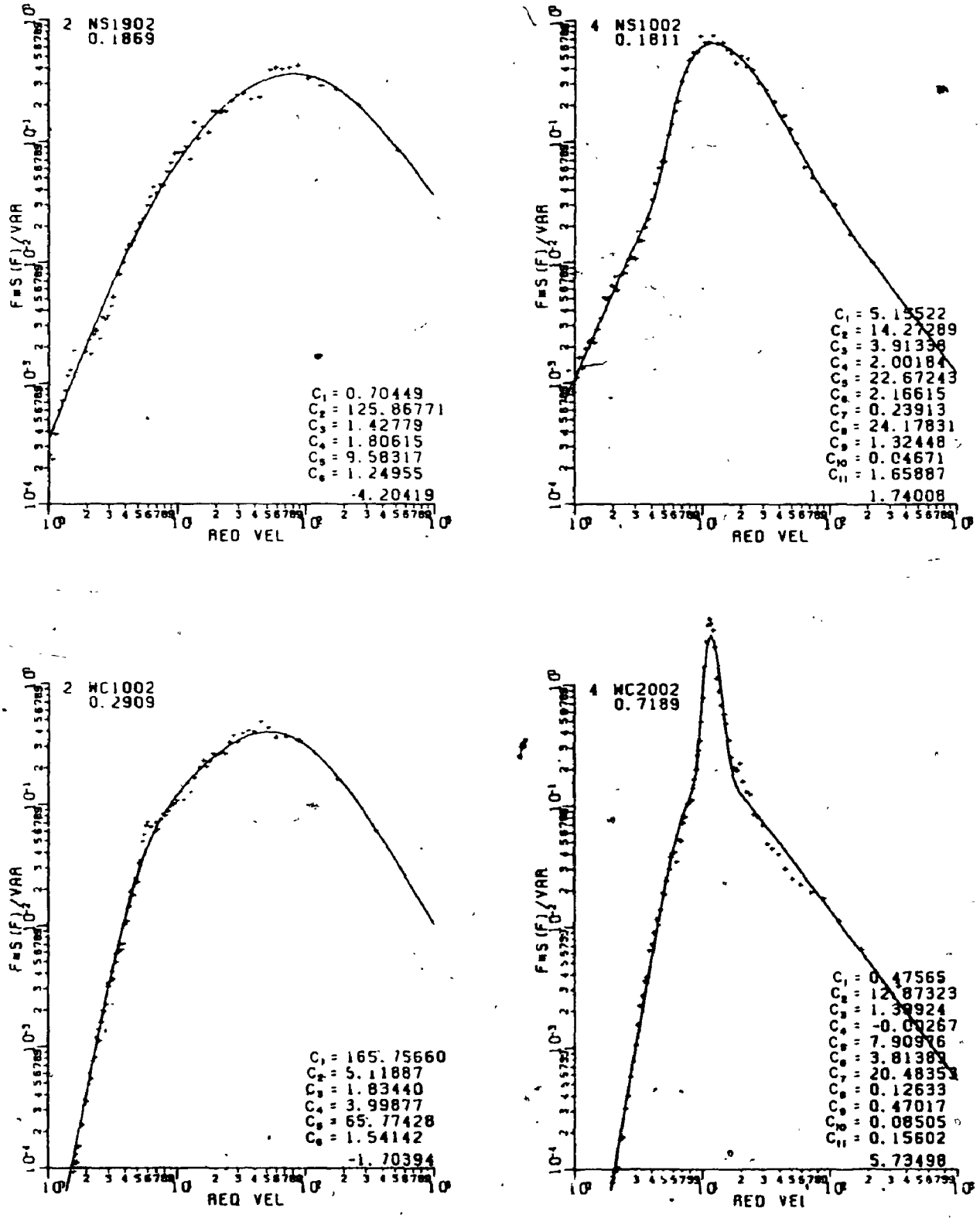

FIG. 2.16 FORCE SPECTRA FITTED WITH VARIOUS EQUATIONS

For the lift direction it is necessary to add another term to take into account the vortex shedding contributions, i.e.:

$$\frac{f\,S_{F_L}(f)}{\sigma^2_{F_L}} = \frac{f\,S_{F_D}(f)}{\sigma^2_{F_D}} + c_7 \times (c_8\ f)^{c_9}\ e^{-\left(\frac{1\ -\ f/c_{10}}{c_{11}}\right)^2} \qquad (2.22)$$

where $S_{F_L}(f)$ is the lift force spectrum.

The results are shown in Fig. 2.16. By comparing Fig. 2.16 with Figs. 2.13 and 2.14, it appears that many different equations give good fits. Equations (2.21) and (2.22) generally use more parameters than autoregressive models, but for example are more directly applicable to determine the slope at particular frequencies. The autoregressive model approaches asymptotically a wrong slope at the lower limiting reduced velocities, but this is of little significance as the force is small. A certain amount of judgement is required to select equations, number of parameters, range of data to be fitted, weighting functions, etc. The fitting is best done interactively on the computer.

2.12 FORCE COEFFICIENTS

Wind induced forces, mean, RMS and peak, are proportional to the velocity squared. Of the structural response only the mean component is proportional to the velocity squared, and the dynamic components are roughly proportional to the velocity to the power of 2.5 to 3.5.

Forces can, therefore, easily be described with nondimensional force coefficients and the following normalizing dimensions are used:

$$c_M = \frac{M}{\frac{1}{2}\rho \bar{V}_T^2 B\ H^2} \qquad (2.23a)$$

$$c_S = \frac{S}{\frac{1}{2}\rho \bar{V}_T^2 B H} \qquad (2.23b)$$

$$c_T = \frac{T}{\frac{1}{2}\rho \bar{V}_T^2 B D H} \qquad (2.23c)$$

where c_M, c_S, c_T = the force coefficients for base bending moments, base shears and base torques

M, S, T = base bending moments, base shears and base torques. From mean values result mean force coefficients, from rms values rms coefficients etc.

ρ = density of air, e.g. $0.0025 \frac{slugs}{ft^3}$ $(1.29\ kg/m^3)$

$\bar{V}_T$ = mean velocity at the top of the building

B = building dimension corresponding to the face producing the overturning moment or shear force

H = building height

D = other building dimensions, e.g. BD = *floor area*

Maximum, minimum, average, and RMS values are simultaneously determined for all five components for a selection of angles at a particular wind velocity. Only one velocity is necessary to form the force coefficients, but a least square fit with the power prescribed as 2.0 can be used if measurements were performed at several velocities.

Fig. 2.17 shows the force coefficients for a typical building, and further force coefficients are given in Appendix B. Dividing the moment coefficients by the shear coefficients gives an effective height for the resultant horizontal loads, which is also shown in Fig. 2.17.

2.13 TORSIONAL RESPONSE

The motions due to the twisting moment can be particularly disturbing to occupants. Of the buildings causing problems, full scale or wind tunnel measurements often show that

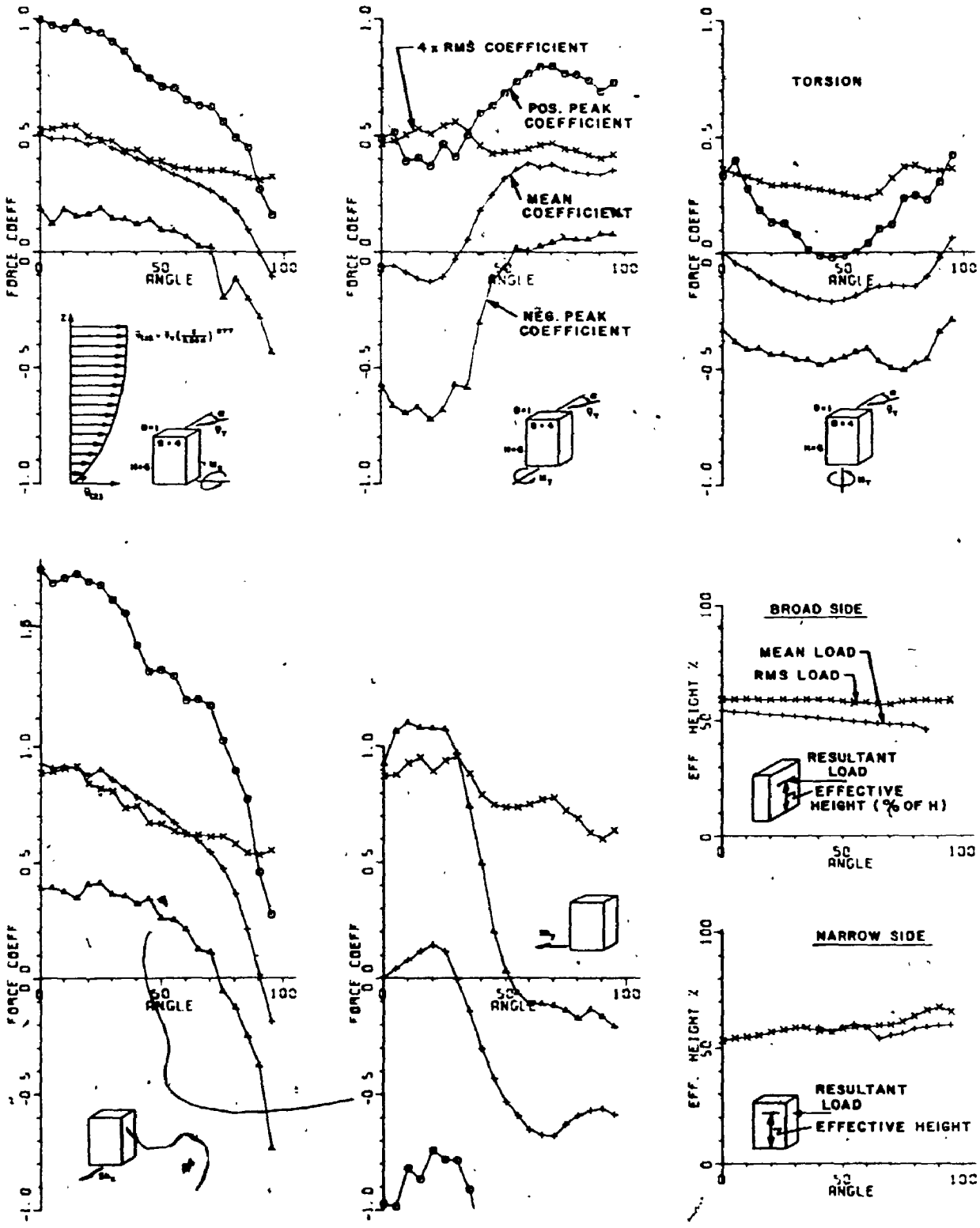

FIG. 2.17 FORCE COEFFICIENTS FOR A 6:4:1 BUILDING, SUBURBAN EXPOSURE

the torsion is the culprit. It is, hence, important to assess the torsional response, especially if there are eccentricities in mass or stiffness. Torsional motions, if not considered in the design, could also result in overstressing of the columns at the periphery of the structure or damage to cladding attachments.

All tall buildings possess torsional degrees of freedom that are excited by wind action. The contribution comes from two major parts: (i) resultants of steady and unsteady aerodynamic forces which act away from the shear centres of each floor, and (ii) coupling between sway and torsional modes of vibration. The coupling, caused by an offset between the elastic axis and the centre of mass of the building, results in a rotation about an axis that is not coincident with the elastic axis. This coupling effect can be accounted for, as described in Section 2.14. The problem concerning (i) above is more difficult.

Few investigators have considered the rotational vibrations of structures. Simple pivoting models only give information on the translational response and expensive multi-degree-of-freedom models are required for truthful assessment of the torsional response. The BLWT force balance-model combination gives an approximation of the torsional response, having in effect a constant magnitude mode shape in Equations (2.3) instead of a mode shape varying with height, and with a maximum value at the top of the structure. The response depends on the degree of coordination of the eddies in the wind, multiplied by the mode shapes. The correlation, decreasing with increasing separation distance, is likely to be overestimated by a uniform mode shape, resulting in a nonconservative modal force spectrum at higher frequencies.

Specific knowledge of the load distribution and correlation is required to improve the accuracy of torsional response predictions using the BLWT balance. Theoretical torsional response predictions have been attempted by Foutch and Safak [1981], assuming the torsional forces result only from pressures on the front and leeward faces. The resulting equations involve spectra of the wind velocity and aerodynamic admittance functions as proposed by Davenport [1961b] for line like structures, such as cantilever bridges. The aerodynamic admittance function involves the coherence length of the velocity and mode shapes, and requires four-fold integrations. The integrations can be

done numerically (i.e. using "SQUANK" as shown in Section 2.5), or using approximations suggested by Davenport [1977].

There are, however, indications that for typical three-dimensional buildings the assumptions by Fputch and Safak [1981] are too simplistic: (i) Torsional force coefficients shown in Appendix B are not necessarily largest for buildings which face with the broad side normal to the wind, (ii) The eccentricity of the resultant load from the force coefficients is often observed to be larger than expected from a simple unsymmetric pressure distribution on the windward and leeward faces, and (iii) the torsion moment spectra in Appendix A show more energy concentrated at specific frequencies than the along-wind moment spectra.

Interpreting (i), (ii) and (iii) above indicate that (a) a large contribution to the torsional response may be caused by shedding eddies near the front of the across-wind faces, (b) unsymmetrical pressure distributions on the windward face produce most of the remaining contribution. Current work is indicating significant differences from the above explanations.

The forces on a flat plate are defined by the pressures as:

$$\textit{Measured Shear} = \iint p(x,z)\, dxdz \qquad (2.24a)$$

$$\textit{Measured Moment} = \iint z\, p\,(x,z)\, dxdz \qquad (2.24b)$$

$$\textit{Measured Torque} = \iint x\, p(x,z)\, dxdz \qquad (2.24c)$$

$$\textit{Modal Torque} = \iint z\, x\, p(x,z)\, dxdz \qquad (2.24d)$$

where x = running coordinate across the width

z = running coordinate along the height

$p(x,z)$ = wind induced pressure

A hypothesis stated from above is that the measured torque, and the more realistic modal torque, have the same ratio as the shear and moment, i.e.:

$$\frac{\iint x\ p(x,z)\ dxdz}{\iint x\ zp(x,z)\ dxdz} \doteq \frac{\iint p\ (x,z)\ dxdz}{\iint zp(x,z)\ dxdz} \tag{2.25}$$

or

$$\iiiint x_1 p(x_1,z_1)\ z_2\ p(x_2,z_2)\ dx_1 dx_2 dz_1 dz_2 \tag{2.26}$$
$$\doteq \iiiint x_1 z_1 p(x_1 z_1)\ p(x_2,z_2)\ dx_1 dx_2 dz_1 dz_2$$

this is true if the z_1 on the right hand side of Equation (2.26) can be replaced by a z_2, i.e. if:

$$\overline{p(x_1,z_1)\ p(x_2,z_2)} = \overline{p(x_1,z_1)^2}\ \ \overline{R(|x_1-x_2|,\ |z_1-z_2|)} \tag{2.27}$$

where R is a narrow band type cross correlation function.

This can only be confirmed by measuring the coherence of the velocity on pressure models equipped with a large number of pressure transducers, and the author suggests that fundamental research should be carried out to study the torsional aerodynamic forces. If experiments result in predictable aerodynamic admittance functions, then torsions could be solved analytically, similar to the along wind response.

Some suggestions for correction factors to the torsional spectra measured by the BLWT balance to get modal generalized torsions are now presented without confirmation to the validity, as no comparison results were available from multi-degree-of-freedom aeroelastic models.

Equivalent load diagrams are known for a number of buildings tested at The University of Western Ontario. Some buildings could be reanalyzed using a constant magnitude mode shape and investigated if a predictable conversion factor existed.

A practical method involving the BLWT balance-model combination might be to cover the lower part of the foam model with a shell, leaving a small airspace between the model and the shell. Then it would be possible to measure the dynamic force for the upper part of the building, where the contribution to the modal force is most significant and the mode shape value is near unity.

Alternatively it might be argued that the difference between a constant mode shape, and the more realistic linearly varying mode shape with a maximum at the top of the building, is of the same order as the ratio from moment and shear force measurements. The shears and moments are measured simultaneously in both lateral directions. The shear force corresponds to a modal force with constant amplitude. The moment corresponds to a modal force with linearly proportionally to the height, increasing mode shape. The ratio, given by Equation (2.25), appears to be a reasonable assumption.

Similar arguments may be stated for all faces of a building, suggesting that the true modal response can be estimated from the measured torsional response spectrum adjusted by a correction factor equivalent to the ratio of the moment spectrum by the shear spectrum. For an angle of 0° and a typical building the spectra and correction factors are shown in Fig. 2.18. The effect is seen to be largest at high frequencies (or low reduced velocities), and becomes less important for wind speeds where significant responses of the buildings occur. The correction factor is similar from either the drag or lift spectra. The apparently necessary spectrum correction factor is roughly 30% for a reduced velocity of 5. Not applying this correction factor results in an underestimation of roughly 15% in the response of the building at that reduced velocity, using Equation (2.6).

More research is suggested and experiments should be made comparing identical force models and multi-degree of freedom aeroelastic models. The evaluation of torsional response with the five-degree-of-freedom balance-model combination of the BLWT is believed to give a good approximation at important wind speeds to the torsional response.

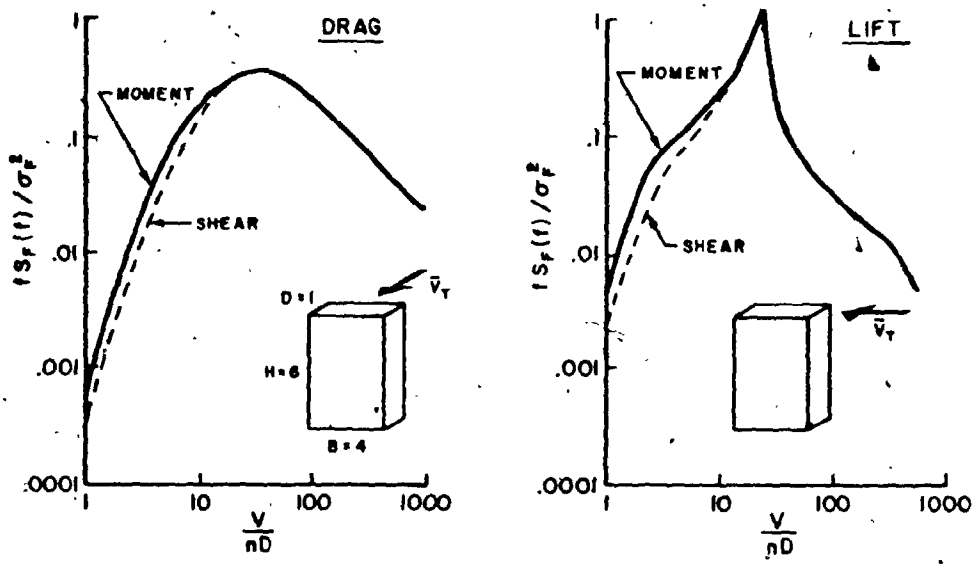

a) MODAL FORCE SPECTRA

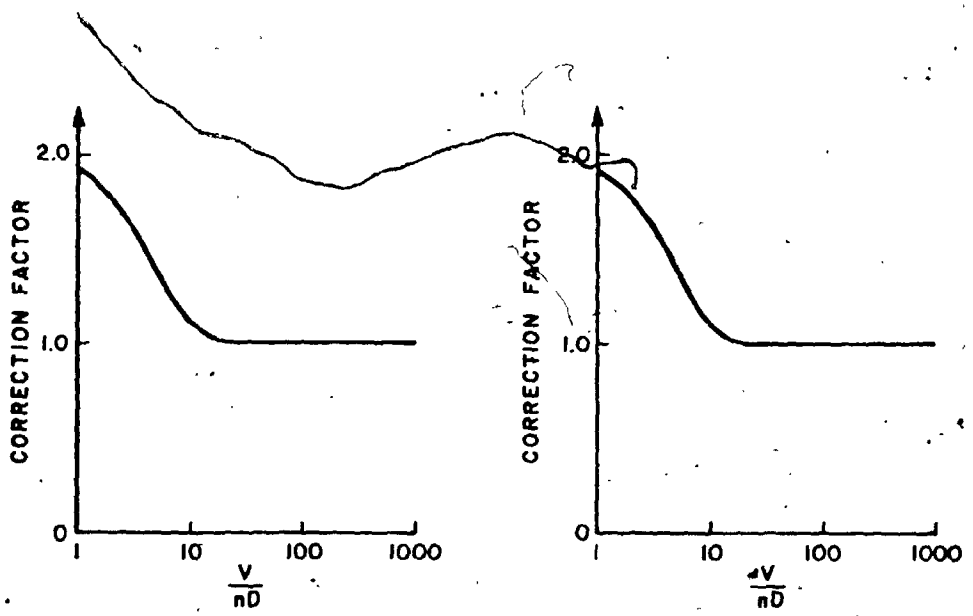

b) CORRECTION FACTORS

FIG. 2.18 CORRECTION FACTORS FOR TORSIONAL MODAL FORCES

2.14 MULTI-DIMENSIONAL VIBRATIONS (COUPLED MODES)

2.14.1 Normal Mode Analysis for Coupled Modes

Mechanical systems having the centre of mass not coinciding with the elastic centre show multi-dimensional mode shapes. Several modes contribute to the total response. The differential equations of motion can be decoupled when the displacements are expressed in terms of the normal modes. If z is a running coordinate (such as height, for example) of a structure, and the mode shapes of free vibration are expressed as $\phi_i(z)$, where $i = 1, 2, 3 \ldots$ number of modes, then any deflection $x(z,t)$ may be expressed as the sum:

$$x(z,t) = \sum_{i=1}^{n} \phi_i(z)\, A_i'(t) \qquad (2.28a)$$

$$= \{\phi(z)\}^T \{A_i'(t)\} \qquad (2.28b)$$

where n = the number of modes which contribute significantly to the response

$A_i'(t)$ = the generalized coordinate for mode i as a function of time, with the same units as $x(z,t)$

For multi-dimensional modes, the equation for the displacement has to include constants a_{di} to make the amplitudes consistent. A building with a multi-dimensional fundamental mode shape (mode 1) is shown in Fig. 2.19.

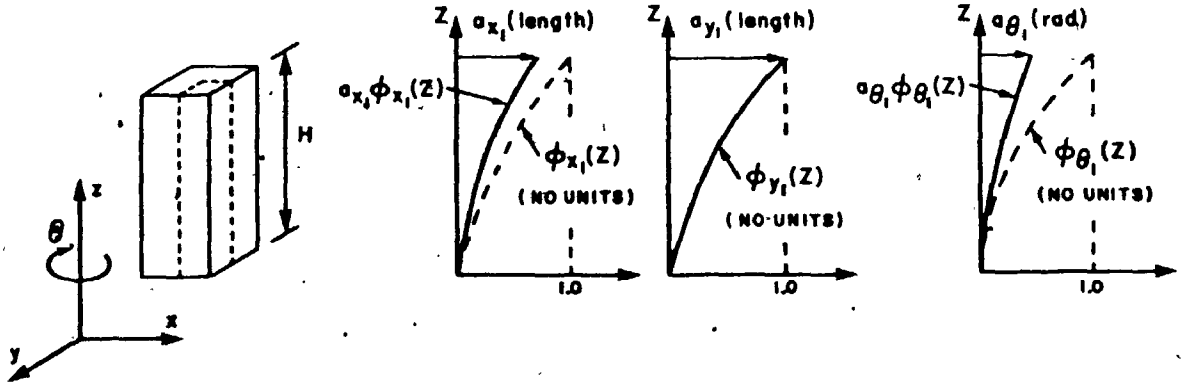

FIG. 2.19 MODE OF VIBRATION OF A TYPICAL STRUCTURE SHOWING THE THE CONSISTENT DISPLACEMENT AMPLITUDE CONSTANTS

The displacements D can now be expressed in matrix form

$$\begin{Bmatrix} x(z,t) \\ y(z,t) \\ \theta(z,t) \end{Bmatrix} = \begin{bmatrix} a_{x1}\phi_{x1}(z) & a_{x2}\phi_{x2}(z) & \cdots & a_{xn}\phi_{xn}(z) \\ a_{y1}\ \phi_{y1}(z) & \cdots & & \\ a_{\theta 1}\phi_{\theta 1}(z) & a_{\theta 2}\phi_{\theta 2}(z) & & a_{\theta n}\phi_{\theta n}(z) \end{bmatrix} \begin{Bmatrix} A_1(t) \\ A_2(t) \\ \vdots \\ A_n(t) \end{Bmatrix} \qquad (2.29a)$$

$$= \{D_d(z,t)\} = [a_{di}\phi_{di}(z)] \{A_i(t)\} \qquad (2.29b)$$

where d stands for direction. The units for the constants a_{di} are length or radians, as shown in Fig. 2.19, the mode shapes $\phi_{di}(z)$ and generalized coordinates $A_i(t)$ have no units.

The magnitude of the amplitudes a_{di} could normally be 1.0 for at least one direction for each mode, and if there is no coupling to the other directions, the value is zero. For no coupling of any two directions in any mode, Equation (2.29b) gives equations in each direction in the form of Equation (2.28b).

The generalized coordinates $A_i(t)$ can be found from: (bold letters below indicate quantities for coupled systems)

$$\mathbf{M}_i\ddot{A}_i(t) + \mathbf{C}_i\dot{A}_i(t) + \mathbf{K}_i A_i(t) = \mathbf{Q}_i(t) \qquad (2.30a)$$

where $\mathbf{M}_i$ = generalized mass for mode i

$$= \int_0^H m_x(z)\, a_{xi}^2\, \phi_{xi}^2(z)\, dz + \int_0^H m_y(z)\, a_{yi}^2\, \phi_{yi}^2(z)dz + \int_0^H m_\theta(z)\, a_{\theta i}^2\, \phi_{\theta i}^2(z)dz$$

$$= \sum_d \int_0^H m_d(z)\, a_{di}^2\, \phi_{di}^2(z)dz$$

$$= \sum_d a_{di}^2\, M_{di} \qquad (2.30b)$$

$m_x(z)$ = mass per unit height

$m_\theta(z)$ = mass moment of inertia per unit height

M_{di} = generalized mass as used for uncoupled modes = $\int_o^H m_d(z)\phi_{di}^2(z)dz$

C_i = generalized damping for mode i = $2\xi_i(2\pi f_i)\,M_i$ (2.30c)

ξ_i = damping ratio for mode i

K_i = generalized stiffness for mode i = $(2\pi f_i)^2 . M_i$ (2.30d)

$Q_i(t)$ = generalized force for mode i

$$= \int_o^H p_x(z,t)\, a_{xi}\phi_{xi}(z)dz + \int_o^H p_y(z,t)\, a_{yi}\phi_{yi}(z)dz + \int_o^H p_\theta a_{\theta i}\phi_{\theta i}(z)dz$$

$$= \sum_d \int_o^H p_d(z,t)\, a_{di}\phi_{di}(z)dz$$

$$= \sum_d a_{di}\, Q_{di}(t) \qquad (2.30e)$$

$p_x(z,t)$ = force from air pressures per unit height

$p_\theta(z,t)$ = torsion from air pressures per unit height

$Q_{di}(t)$ = generalized force as used for uncoupled modes = $\int_o^H p_d(z,t)\phi_{di}(z)dz$

The response in terms of generalized coordinates can be solved for periodic loads directly, and for stationary random loads using spectral analysis.

The dynamic response for direction x for an uncoupled structure can be described as

$$\overline{x(z,t)^2} = \sum_{i=1}^{n}\sum_{j=1}^{n} \phi_i(z)\phi_j(z)\, \overline{A_i'(t)A_j'(t)} \qquad (2.31)$$

However, in slightly damped systems with well-separated frequencies, the cross-products are insignificant and can be neglected. Then, only term subscripts $i=j$ are maintained and the double series reduces to the single series:

$$\overline{x(z,t)^2} = \sum_{i=1}^{n} \phi_i^2(z)\, \bar{A}_i'^2(t) \qquad (2.32a)$$

$$= \left\{ \phi_i^2(z) \right\}^T \left\{ \bar{A}_i'^2(t) \right\} \qquad (2.32b)$$

This can be expanded to multi-dimensional modes similar as Equation (2.29b).

Using the spectral analysis approach, the modal amplitudes are given as:

$$\bar{A}_i^2 = \int_0^\infty S_{A_i}(f)\, df \qquad (2.33a)$$

$$S_{A_i}(f) = \frac{1}{K_i^2} |H_i(f)|^2\, S_{Q_i}(f) \qquad (2.33b)$$

$$|H_i(f)|^2 = \frac{1}{[1-(\frac{f}{f_i})^2]^2 + 4\xi_i^2 (\frac{f}{f_i})^2} = \text{mechanical magnification function} \qquad (2.33c)$$

$$S_{Q_i}(f) = \sum_d \sum_{d'} a_{di}\, a_{d'i}\, 2\int_{-\infty}^{\infty} \overline{Q_{di} Q_{d'i}}\; e^{-i2\pi f\tau}\, d\tau$$

$$= \sum_d \sum_{d'} a_{di}\, a_{d'i}\, S_{Q_{di}\, Q_{d'i}}(di,\, d'i,\, f) \qquad (2.33d)$$

$$S_{Q_{di}Q_{d'i}}(di,\ d'i,\ f) = \int_0^H\int_0^H S_{p_{di}p_{d'i}}(z,z';f)\ \phi_{di}(z)\ \phi_{d'i}(z')\ dzdz' \qquad (2.33e)$$

$$S_{p_{di}p_{d'i}}(z,z';f) = 2\int_{-\infty}^{\infty} \overline{p_{di}(z)\ p_{d'i}(z')}\ e^{-i2\pi f\tau}\ d\tau \qquad (2.33f)$$

For structures, buffeted by the wind, it has often been found that the cross-correlations between the different directions are small enough that they can be neglected. In this case Equation (2.33d) is considerably simplified:

$$S'_{Q_i}(f) = \sum_d a_{di}^2\ S'_{Q_{di}}(di,\ f) \qquad (2.34a)$$

where $$S'_{Q_{di}}(f) = \int_0^H\int_0^H S'_{p_{di}}(z,z';f)\ \phi_{di}(z)\ \phi_{di}(z')\ dzdz' \qquad (2.34b)$$

$$S'_{p_{di}}(f) = 2\int_{-\infty}^{\infty} \overline{p_{di}(z)\ p_{di}(z')}\ e^{-i2\pi f\tau}\ d\tau \qquad (2.34c)$$

Equation (2.34) is equivalent to Equation (2.3b).

The total response of a structure can be represented from contributions from three parts: i) mean response $\bar{A}_i$, ii) background turbulence or quasi static response $(\sigma^2_{A_i})_B$ and iii) resonant response $(\sigma^2_{A_i})_R$.

$$\bar{A}_i = \frac{\bar{Q}_i}{K_i} = \frac{1}{K_i}\left[a_{xi}\bar{Q}_{xi} + a_{yi}\bar{Q}_{yi} + a_{\theta i}\bar{Q}_{\theta i}\right]$$

$$= \frac{1}{K_i}\sum_d a_{di}\,\bar{Q}_{di} \qquad (2.35a)$$

$$(\sigma^2_{A_i})_B = \frac{1}{K_i^2} \sum_d a^2_{di} \int_0^{fi-\Delta f} S_{Q_{di}}(di,f)|H_i(f)|^2 \, df$$

$$\approx \frac{1}{K_i^2} \sum_d a^2_{di} \, \sigma^2_{Q_{di}} \qquad (2.35b)$$

$$(\sigma^2_{A_i})_R = \frac{1}{K_i^2} \sum_d a^2_{di} \int_{fi-\Delta f}^{\infty} S_{Q_{di}}(di,f)$$

$$\approx \frac{1}{K_i^2} \sum_d a^2_{di} \, \frac{\pi}{4\xi_i} \, fi \, S_{Q_{di}}(di,fi)$$

$$\approx \frac{1}{K_i^2} \, \frac{\pi}{4} \, \frac{1}{\xi_i} \sum_d a^2_{di} \, \sigma^2_{Fd} \left(\frac{fi \, S_{Q_{di}}(di,fi)}{\sigma^2_{Fd}} \right) \qquad (2.35c)$$

the last equation is usually employed because the spectra are usually determined in normalized form $\frac{f\,S(f)}{\sigma^2}$, as described in Section 2.6.

2.14.2 Coupled Mode Response Predictions Using the Force Balance

The balance output is proportional to the instantaneous forces at the base of a building model for five degrees of freedom (see Fig. 1.7). The online data acquisition system of the BLWT Laboratory simultaneously determines the generalized forces according to Equations (2.3). The instantaneous generalized forces for the overturning moments and torsion are restated as:

$$F_{M_x}(t) = \int_0^H p_x(z,t)\phi_x(z) \, dz \qquad (2.36a)$$

$$F_{M_y}(t) = \int_0^H p_y(z,t)\phi_y(z) \, dz \qquad (2.36b)$$

$$F_{M_\theta}(t) = \int^{H} p_\theta(z,t)\, \phi_\theta(z)\, dz \qquad (2.36c)$$

The effective weighting functions of the balance are:

$$\phi_x(z) = \phi_y(z) = z \qquad (2.37a)$$

$$\phi_\theta(z) = 1.0 \qquad (2.37b)$$

Since the generalized forces Q_i of Equation (2.30) have to be computed with consistent displacement amplitude constants (see Fig. 2.19), the measured forces have to be converted accordingly, e.g. if $a_{x1}\, \phi_{x1}(H) = 1.0$, then the Q_{x1} to be used with Equation (2.30e) has to be divided by the height of the building. The torsional forces are measured with a mode shape weighting function which deviates from mode shapes of buildings. The torsional response is described in more detail in Section 2.13.

Neglecting higher modes than the first mode for each direction, the response for the x-direction can be summarized as:

$$\bar{x}(H) = a_{x1}\bar{A}_1 + a_{x2}\bar{A}_2 + a_{x3}\bar{A}_3 = \textit{mean displacement at the top of the building} \qquad (2.38a)$$

$$\sigma_x^2(H) = a_{x1}^2\left\{(\sigma_{A1}^2)_B + (\sigma_{A1}^2)_R\right\} + a_{x2}^2\left\{(\sigma_{A2}^2)_B + (\sigma_{A2}^2)_R\right\}$$

$$+ a_{x3}^2\left\{(\sigma_{A3}^2)_B + (\sigma_{A3}^2)_R\right\} \qquad (2.38b)$$

and similar expressions for the other directions

$$\hat{x}(H) = \bar{x}(H) + g\sigma_x(H) = \text{peak displacements at top of the building in units of length} \qquad (2.38c)$$

$$\hat{\theta}(H) = \bar{\theta}_{(H)} + g\sigma_\theta(H) = \text{peak twist at top of building} \qquad (2.38d)$$

where g is a peak factor described in Section 2.5.

Accelerations can be described as:

$$\sigma^2_{\ddot{x}}(H) = [(2\pi f_1)^2]^2 \, a^2_{x1}(\sigma^2_{A1})_R + [(2\pi f_2)^2]^2 \, a^2_{x2}(\sigma^2_{A2})_R + [(2\pi f_3)^2]^2 \, a^2_{x3}(\sigma^2_{A3})_R \qquad (2.38e)$$

$$\sigma^2_{\ddot{\theta}}(H) = [(2\pi f_1)^2]^2 \, a^2_{\theta 1}(\sigma^2_{A1})_R + [(2\pi f_2)^2]^2 \, a_{\theta 2}(\sigma^2_{A2})_R + [(2\pi f_3)^2]^2 \, a_{\theta 3}(\sigma^2_{A3})_R \qquad (2.38f)$$

$$\hat{\ddot{x}}(H) = g\,\sigma_{\ddot{x}} = \text{peak x-sway acceleration (length/time}^2) \qquad (2.38g)$$

$$\hat{\ddot{\theta}}(r,H) = g\,r\,\sigma_{\ddot{\theta}} = \text{peak linear acceleration at radius } r \text{ due to torsion (length/time}^2) \qquad (2.38h)$$

For structures having no coupled modes and having a linearly varying basic mode shape, the Equations (2.38) can be simplified. The displacement and acceleration therefore simplifies, identically as shown in Section 2.5, to:

$$\bar{x} = \frac{\bar{F}_{M_x}}{K_x} \quad (radians) \tag{2.39a}$$

$$K_x = (2\pi f_x)^2 \, M_x \tag{2.39b}$$

$$M_x = \int_0^H m(z) \, \phi_x^2(z) \, dz \tag{2.39c}$$

$$= \frac{1}{3} \, m \, b \, d \, H^3$$ for uniform mass distribution of a building with a mass of $m/(length)^3$ and width b, depth d, height H and $\phi_x(z) = z$

$$\sigma_x = \frac{\sigma_{F_{M_x}}}{K_x} \sqrt{1 + \frac{4}{\pi} \, \frac{1}{\xi_s + \xi_a} \, \frac{f_x S_{F_{M_x}}(f_x)}{\sigma^2_{F_{M_x}}}} \tag{2.39d}$$

$$\sigma_{\ddot{x}} = \frac{(2\pi f_x)^2 \sigma_{F_{M_x}}}{K_x} \sqrt{\frac{4}{\pi} \, \frac{1}{\xi_s + \xi_a} \, \frac{f_x S_{F_{M_x}}(f_x)}{\sigma^2_{F_{M_x}}}} \tag{2.39e}$$

$$\hat{x}(H) = H \, (\bar{x} + g \, \sigma_x) \tag{2.39f}$$

$$\hat{\ddot{x}}(H) = H \, (g \, \sigma_x) \tag{2.39g}$$

A photo of an early building model where the above procedure for multi-dimensional modes was applied is shown in Fig. 2.20. The force model is an architectural model,

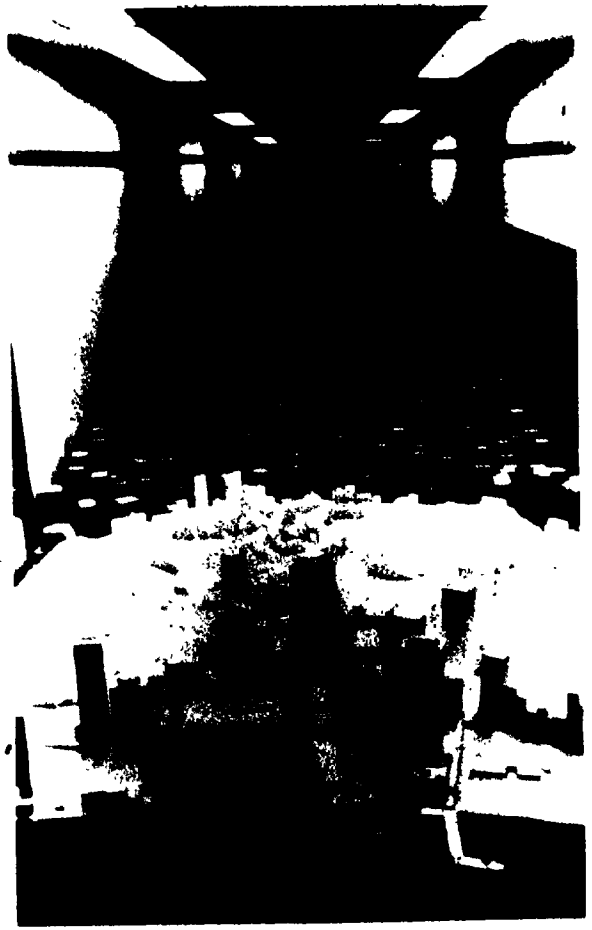

(a) with surrounding buildings

(b) close-up of balance-model

FIG. 2.20 PHOTOGRAPHS OF AN EARLY FORCE MODEL WIND TUNNEL STUDY

built of foam, and was not originally intended to be used for response predictions.

2.15 SUMMARY AND SUGGESTIONS FOR FURTHER STUDY

The direct measurement of the total dynamic force using high frequency models has been shown to be an economical alternative to full aeroelastic tests in many instances. The method assumes that aerodynamic damping effects can be neglected or an estimated amount be included.

To realize the full potential of the method, further research should be carried on in several areas: i) building models from new materials result in even higher frequencies, simplifying the testing further by allowing for higher wind speeds and measured forces, and eliminating corrections due to limited frequency response and filtering, ii) the torsional response should be confirmed by some comparisons with multi-degree of freedom aeroelastic tests, iii) higher mode shapes may be accounted for by using information from both the unit mode shape (shear) force and the straight line mode shape (moment) force, similar to the use for torsion loads, and iv) aerodynamic damping effects, being the major source of uncertainty in response predictions from force models, should be better known. Other effects, such as deviations from straight line mode shapes are secondary in terms of errors, but could be accounted for.

Simplified studies allow new areas of investigation, which were not feasible until now, such as studies on medium rise buildings, or effects on neighbouring buildings from a projected tall structure. Other areas of potential research are systematic studies on building shapes, which may lead to codification for different wind directions in addition to drag loading which is currently the only force treated by building codes. The dynamic response in the lift direction is for many building shapes more critical than the along wind response, both for accelerations and for peak displacements. Better information on the directional response could lead to integration with the meteorological factors, resulting in more economical designs. Torsion, on the other hand, is sometimes critically underestimated and would benefit from systematic investigations and codification.

Comparisons of response predictions from conventional aeroelastic models and the new method described in this chapter show good agreement for realistic wind speeds and damping ratios. The force model tests, being independent of structural parameters, are more versatile and allow for easily revised predictions due to changes in stiffness, mass or damping. The good agreement with the National Building Code of Canada gives confidence both in the Building Code and the proposed method.

Alternative approaches by other investigators for direct dynamic force measurements were described and shown to be less versatile than the proposed method in this chapter.

Further applications of the direct dynamic force measurements for non-linear building response predictions are shown in Chapter III and IV.

CHAPTER III

WIND FORCE SIMULATIONS

3.1 INTRODUCTION

Chapter II demonstrated the usefulness of the force balance to determine the response for linear elastic structures. Another incentive for providing tools to directly measure the wind force is to permit the evaluation of the response for nonlinear structures. One approach to the determination of the response is through step-by-step integration of the motion, which requires the force to be known at each time step. The subject of this chapter is to describe methods of supplying suitable time series.

When desired the wind force can be used directly as measured with the force balance. Alternatively the force measurements can be stored on mass storage devices or regenerated with numerical simulation techniques. The autoregressive processes give suitable time series simulations and are presented in detail. All important elements particular to the wind load time series are discussed, including the order of the autoregressive process, the estimation of the parameters and the time scales.

Applications of the simulated time series to evaluate non-linear building response are given in the following chapter.

3.2 METHODS TO PREPARE THE WIND FORCE TIME SERIES

To determine the response for non-linear structures requires more advanced techniques than the spectral approach used for linear structures in Chapter II. Evaluations in the

time domain require the force to be known at small time increments. Time domain analysis may be desirable even for linear structures for the purpose of obtaining information such as first excursion probability. This chapter treats the methods available to supply a time series of the force, and in Chapter IV are applications given for use of the force time series to evaluate the response of structures.

The force balance described in Chapter I supplies the necessary information on the nature of the modal forces. The time series of these forces can be supplied as input in a computer program in various ways, including:

i) real time from balance output,
ii) from an analogue taped record,
iii) from a digitized record,
iv) recreated with a simulation.

3.2.1 Real Time

The voltage output from the force balance is an analogue of the actual instantaneous modal force of a real structure. This signal is converted to a digital number with an analogue-to-digital converter at the front end of the computer with a chosen sampling rate. The digitized numbers are scaled to full scale values using the usual model scaling laws for wind tunnel models. The sampling rate has to be rapid enough to follow the variation of the force at frequencies as high as there is significant energy in the signal. The time steps of the time series also depend on the natural frequencies of the full scale structures, scaled to the model with the required model scale. To minimize errors in the integration of the response, more than 15 time steps are required per period as described in Chapter IV. These requirements demand a sampling rate of several hundred points per second, during each step the computer has to sample, digitize, convert to full scale, and evaluate the response. This is a formidable task even for today's high-speed computers. The time scale is approximately one hundred times faster than in nature.

A sophisticated wind tunnel is necessary with the complementary manpower and

equipment such as a force balance, electronic signal conditioning units, electronic filtering, analogue-to-digital converters, sampling electronics and a high-speed computer.

3.2.2 Analogue Records

Alternatively the output from the force balance in the wind tunnel can be stored on an analogue FM recorder. The signal can be recorded filtered or unfiltered, depending on later needs. Filtering sacrifices some of the flexibilities of choosing the time scales at the time of the evaluation of the response, but reduces requirements of electronic equipment at the time of evaluation. The requirements for a high speed computer are still the same, unless the tape is played back at a lower speed than recorded. Any high-speed computer used still has to be equipped with an analogue-to-digital converter and sampling electronics. The computer can be located at the laboratory where the measurements were done, or the data can be processed at a remote location.

3.2.3 Digitized Records

The signal can be digitized in real time and stored on disc or computer tape. The filtering and time scale is fixed at this time, but as shown in Section 3.8, it is possible to interpolate for other points in between the digitized samples at the expense of additional computer time.

Any computer can be used to evaluate the response of a building, the only equipment necessary is a tape drive to read the time series from the tape. The high speed requirements are not applicable, since the computer can read and process the data at the speed set by the computer itself. The only time sophisticated equipment and wind tunnel facilities are required, is when the records are collected.

3.2.4 Simulations

After the information on modal loads has been measured, it is possible to recreate statistically similar time series entirely in numerical form with a computer. The main

effort lies in finding suitable techniques and estimates for the necessary parameters. The simulation techniques are suitable if they are simple enough to be applied to a wide range of buildings and modal forces for different degrees of freedom. This chapter describes in detail the autoregressive processes used for later evaluations of the response of structures, using only random numbers generated by computer. No equipment is necessary in addition to a computer and core and speed requirements are not critical.

3.2.5 Discussion and Advantages of the Methods

The most flexible method is real time analysis, because it allows instant evaluation of the response for any building shape, exposure, degree of freedom, wind direction, sampling rate and combination of different degrees of freedom. However, the cost is high because of the need for sophisticated wind tunnel facilities and manpower, which are not generally available, and even in well equipped laboratories time may be limited or the computer might not have the required speed.

Intermediate storage of time series, analogue or digital, gives more flexibility over the limited time available in real time evaluations. Data can be made more widely available, because it can be copied easily and distributed to different locations. Due to time deferred analysis more data may be measured than required later, as a safeguard to avoid necessary retesting in the wind tunnel in case the records are too short or otherwise inadequate. This lengthens the time the wind tunnel is required and the records, especially if recorded digitally are very bulky. The need for physical movement of magnetic tape is inconvenient and demands careful cataloguing.

The preferred method is to simulate the time history entirely numerically by computer when needed. No equipment is needed besides a computer, which does not need to be large or fast. Total flexibility is gained over the time scale. In real time, depending on the size of the wind tunnel and wind speed, the time scale is fixed at approximately one hundred times faster than full scale, however, with simulations this can be faster or slower, since each new time step is done at the speed of the computer, i.e. a fast computer can speed up lengthy parameter studies. The simulations discussed below are simple and require little memory space, and can even be implemented on programmable

calculators, but execution times would become prohibitively long. Therefore, simulations can be done anywhere, with minimal facilities after the basic parameters are estimated from a wind tunnel test. Only about six parameters are necessary for most simulations, eliminating the need of physical movement of bulky records.

Parameter studies such as for finding the influence of different yielding models, different damping values etc., can be done for exactly the same sets of time series or for different ones, the starting seed of the random number generator determining the exact time history of the process, but not its statistical values.

Simulation studies require slightly more computer time, because the force generation is done numerically. Computer time is also used to estimate the parameters before the simulation can be done. Since computer time is getting cheaper, overall cost savings can be achieved because of the minimal hardware and manpower requirements, after a short series of wind tunnel tests.

3.3 REQUIREMENTS FOR TIME SERIES SIMULATIONS

The advantages of time series simulations for wind forces to evaluate the response of buildings in the time domain are outlined above. It is presumed that the simulations satisfy the following requirements:

i) correct statistical values;
ii) correct spectral distribution;
iii) stationarity and ergodicity;
iv) "parsimony";
v) arbitrarily long records.

3.3.1 Statistics

The statistical distributions for simulations have to be the same as for the actual time series. From measurements using the force balance, it is found that the wind forces are normally distributed. Therefore, the mean, variance and higher moments of the simulated

distribution must be equivalent to the measured values determined from model tests.

3.3.2 Spectral Distribution

The statistical distribution does not sufficiently ensure similarity of the time series. The building response has a contribution from the slowly varying quasi-static forcing function and another contribution from the turbulence near the natural frequency of the structure. It is important that the energy is correctly distributed at all frequencies which contribute to the response. Matching the shape of the spectral density function also ensures that the time scale is simulated correctly.

3.3.3 Stationarity

The measured wind forces are stochastic but stationary. The simulated time series has to remain in equilibrium about a constant mean level as well. The autoregressive processes described below are not stationary for arbitrary parameter values and most of the spectral distributions for wind forces could theoretically be matched more closely with parameter values which cause the time series to be non-stationary. It is essential that the parameter values, which are determined for different time series than the examples shown below and in Appendix A, are confirmed to simulate stationary time series, before they can be accepted for time series simulations.

3.3.4 Parsimony

The aim of keeping the number of computed operations per time step at a minimum is referred to as parsimony. For practical use of simulations it is important to employ economical models which use the smallest number of parameters and calculations, while ensuring adequate representation of the time series. Parsimoneous models may also use less computer memory, but the reduction of computer time is more important.

3.3.5 Length

Wind load studies differ from earthquakes primarily in duration. Low level damage

accumulations require simulations in the order of hours duration in real time scale. It is desirable to supply an uninterrupted time series to the simulation process until a chosen damage criteria is reached.

It is difficult to achieve all requirements with any particular simulation technique. An obvious approach to generate a time series with a given spectral distribution would be to use an inverse FFT transformation, but this falls short in satisfying parsimony and gives only a record of limited length. A method which provides an acceptable compromise of the stated requirements is described below.

3.4 BASIC METHODS TO SIMULATE RANDOM PROCESSES

Simulations of a discrete random time sequence having spectral representation can be generated by various methods which follow different philosophies, including

i) direct inverse FFT transform;
ii) using spectrum and random phase angle;
iii) filtering of a white noise process.

3.4.1 Inverse FFT Transform

This method generates the time series by initializing complex Fourier coefficients in the frequency domain of a Fast Fourier Transform algorithm, and then inverting the Fourier Transform back to the time domain. This provides a simulation for a limited time length and could be useful for simulating the periodic-random type of excitation required for many dynamic testing applications. Hudspeth and Borgman [1979] developed a stacked FFT algorithm and gave additional references for inverse FFT transform techniques.

3.4.2 Using Spectrum and Random Phase Angle

Digital simulations of a time series can be done as a series of cosine functions with weighted amplitudes, almost evenly spaced frequencies, and random phase angles. A

detailed treatment can be found in Shinozuka and Jan [1972] and the following description is an attempt to give a brief summary:

$$P(t) = \sqrt{2} \sum_{i=1}^{N} \sqrt{2\, S_p(\omega_i)\, \Delta_\omega} \cos(\omega_i' + \phi_i) \qquad (3.1)$$

where $P(t)$ = the stationary random process with mean zero and spectral density function $S_p(\omega)$

Δ_ω = $\dfrac{\text{upper circular frequency of spectrum}}{N}$

ω_i = $(i - 0.5)\,\Delta_\omega$

ω_i' = ω_i + small random frequency

ϕ_i = independent random phase angles, uniformly distributed between 0 and 2π

The simulated process is Gaussian and ergodic, regardless of the size of N, but N should be at least 50. The small random frequency is apparently introduced to avoid the periodicity of the simulated process and is uniformly distributed over an absolute value of the order of $\Delta_\omega/20$. Whether this is necessary has not been attempted for this thesis as it appears that the randomness of ϕ_i may be enough to avoid periodicity.

Equation (3.1) is a special case for a one-dimensional one variable random process which appeared before in Rice [1954] but Shinosuki and Jan give the general formula for multivariate or multidimensional processes.

3.4.3 Filtering of White Noise Process

The stochastic models employed for this study are based on passing a white noise process through a numerical filter. A sequence of random numbers, which can be regarded as random drawings from a fixed distribution, is called white noise if the spectral density has the same value for all frequencies. The values of the random number vector $R_{(t)}$ are normally distributed with zero mean and variance σ_R^2. The linear filtering process

is shown schematically in Fig. 3.1.

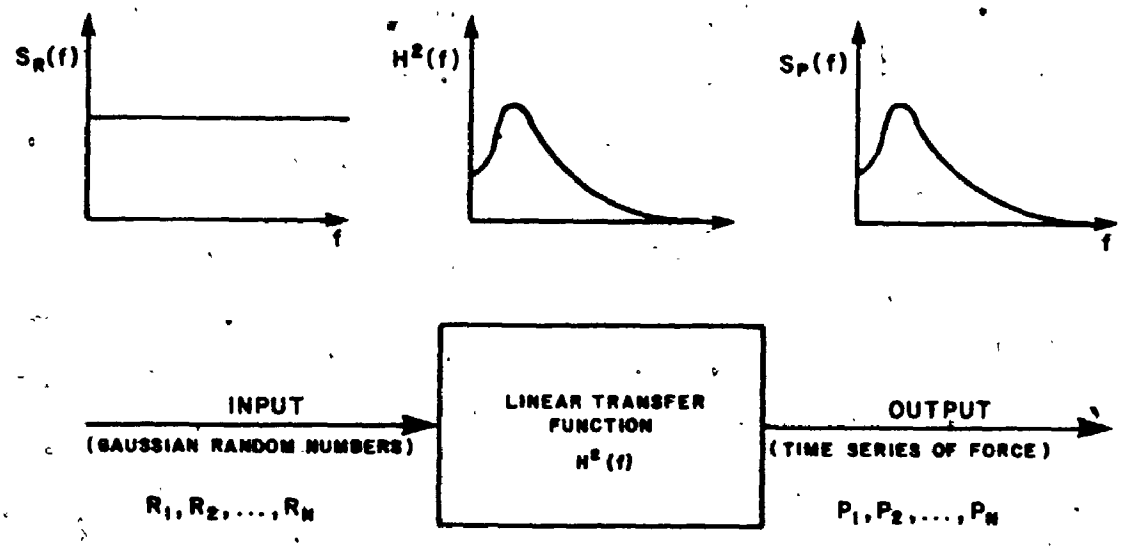

FIG. 3.1 SCHEMATICAL REPRESENTATION OF WHITE NOISE FILTERING

Given that a good white noise source and a suitably versatile stable digital filter algorithm is available, it is possible to generate a stochastic process with any given spectrum. The main criteria for accepting a linear filter are parsimony and how well the spectrum is approximated.

3.4.4. Discussion

The method to be favoured for application of the simulation studies has to closely satisfy the requirements of Section 3.3. Easy implementation is also desirable, but as a rule, the easiest implementation of a procedure often requires more computer time for processing later.

The inverse FFT transform is easy to implement, but it does not satisfy the requirement for generating arbitrary long records and uses much computer time.

The method using the spectrum and random phase angle is also easy to implement, since an arbitrary long time series can be simulated immediately after the spectrum is measured. Some difficulties arise from the fact that spectral values required for Equation (3.1) are not necessary at the frequencies measured in the test. This can be solved by interpolation between the measured spectral values, but it would also be desirable to introduce some smoothing and reduction of noise in the measured spectrum Smoothing cannot be done completely automatically and requires some judgement for each record, therefore this method is somewhat more suitable for simulating time series for which a closed formula is known, i.e. Davenport's spectrum of horizontal gustiness of the wind [1961a]. The execution time per time step is considerable, even without smoothing or interpolation, because it involves a large number of cosine and square root evaluations.

Numerical filtering of white noise has the potential for fast time series generation, provided the white noise is generated efficiently, and a simple filter model approximates the required transfer function closely. All requirements of Section 3.3 are closely satisfied, including arbitrary long time series and, only with this method, parsimony. The difficulty with this method lies in the permutation of possible filter models, requiring the most judgment per record of the described methods. Once the model is chosen and the constants determined, time series can be generated efficiently. Fitting the model to the transfer function introduces smoothing of the spectrum, which can be used advantageously to reduce noise in the measured spectra. As shown below, the autoregressive processes are suitable for generating time series for most wind forces, with an estimated required computer time a hundred times less than the other two methods described above.

3.5 WHITE NOISE GENERATION

The generation of white noise is the first major step in the time series simulation. The pseudo-random Gaussian deviates are not usually available as system subroutines, but can be formed by a variety of methods from uniformly distributed random numbers which are generated from standard functions on any computer system. More computer time may be needed to generate the white noise process than for the transformation to the force time

series per time step. Therefore, it is important to use efficient methods, some easy programmable ones are discussed in more detail below. All generate random numbers R which form a distribution having a mean of 0.0 and a variance of 1.0:

3.5.1 Summing of Groups

By using the central limit theorem of probability, sums of an arbitrary number of uniformly distributed random numbers will be asymptotically normally distributed. This is one of the earliest known methods, but can be found, e.g. in Hamming [1962]:

$$R = \frac{\sum_{i=1}^{k} r_i - \frac{k}{2}}{\sqrt{k/12}} \qquad (3.2a)$$

where r_i = uniformly distributed random numbers, $0 < r_i < 1$

k = the number of values r_i to be used.

R approaches a true normal distribution as k approaches infinity. To reduce execution time, k can be chosen as 12, which gives a reasonable normal distribution from the simpler formula:

$$R = \sum_{i=1}^{12} r_i - 6.0 \qquad (3.2b)$$

An assessment of its accuracy, given by Muller [1959] who compared all methods known until 1958, does not rate this method well for generating normal deviates outside the ± 3.0 limit.

3.5.2 Inverse Transformation

Another well known method of generating a normal deviate R from a uniform

deviate r is to apply an inverse transform using the cumulative probability distribution which, like r, has a value from 0 to 1. The actual determination of the cumulative probability distribution offers certain difficulties, especially for large values of R. Approximations can be made by fitting polynomials or storing large look-up tables as used by the International Mathematical and Statistical Library [1977] which is available at most computing centres.

3.5.3 Direct Polar Method

A theoretically exact method was developed by Box and Muller [1958] using logarithmic and trigonometric function evaluations and returning a pair of normal deviates per pair of supplied uniform random numbers which are statistically independent.

$$R_i = \sqrt{-2 \ln r_i} \quad \cos(2\pi r_{i+1}) \qquad (3.3a)$$

$$R_{i+1} = \sqrt{-2 \ln r_i} \quad \sin(2\pi r_{i+1}) \qquad (3.3b)$$

Justification can be found by finding the joint density of R_i and R_{i+1} from the inverse relationships:

$$r_i = e^{-\frac{1}{2}(R_i^2 + R_{i+1}^2)} \quad \text{and} \quad r_{i+1} = -\frac{1}{2\pi} \arctan \frac{R_{i+1}}{R_i}$$

which gives the desired Gaussian probability density, including independence of R_i and R_{i+1}. Integrating the probability density function gives, for each Equation (3.3a and b), a mean of 0 and a variance of 1. Either formula can, hence, be used also on its own. This, however, uses more computer time, because two uniformly random numbers have to be generated per normally distributed random number and more square root evaluations are required. Equation (3.3a) is used throughout the study for compatibility reasons, because

this was the fastest method known at the beginning of the study.

3.5.4 Polar Method Without Trigonometric Function Evaluations

An improvement in execution speed was found by Marsaglia and Bray [1964] by avoiding sine and cosine calculations. Normal random deviates are generated according to :

$$R_i = V_i \sqrt{-2 \frac{\ln (V_i^2 + V_{i+1}^2)}{(V_i^2 + V_{i+1}^2)}} \qquad (3.4a)$$

$$R_{i+1} = V_{i+1} \sqrt{-2 \frac{\ln (V_i^2 + V_{i+1}^2)}{(V_i^2 + V_{i+1}^2)}} \qquad (3.4b)$$

where V_i are uniform random deviates, in this case from -1 to $+1$ with an additional condition that:

$$(V_i^2 + V_{i+1}^2) < 1$$

Therefore this method is stochastic in execution time but the expected number of uniform deviates to be generated per accepted Gaussian deviate is only 1.3.

Since the implementation can make a good algorithm look worse if badly implemented, a Fortran code is given in Table 3.1 as adapted from Best [1979] where the array R contains the number NUMR of desired Gaussian Random deviates. RANF (SEED) is usually an intrinsic function of the machine to generate uniform deviates r_i.

```
      SUBROUTINE GR(NUMR,R)
      DIMENSION R(1)
      DATA SEED /123498./
      DO 1000 I = 1, NUMR, 2
10    U = RANF (SEED)
      V = RANF (SEED)
      U = U + U - 1
      V = V + V - 1
      SUM = U x U + V x V
      IF (SUM.GE.1.) GO TO 10
      SLN = SQRT (- 2 x ALOG (SUM)/SUM)
      R(I) = U x SLN
1000  R(I + 1) = V x SLN
      RETURN
      END
```

TABLE 3.1 ALGORITHM FOR MARSAGLIA AND BRAY'S POLAR METHOD

3.5.5 Ratio of Uniform Variates

Kinderman and Monahan [1977] published a method using the ratio of uniform deviates. The values are rejected if the coordinate pair (r_i, r_{i+1}) falls outside a prescribed boundary, and a new pair is generated. Random variables can be generated for any distribution, but the efficiency also depends on the coding. Per accepted Gaussian deviate, it is expected to require 2.8 uniform deviates, but only 0.5 ALOG evaluations.

The following Fortran function is adapted from Best [1979]:

```
      FUNCTION R(D)
1     R1= RANF (D)
      R = 1.715527769 x (RANF (D) - .5)/R1
      RR = .25 x R x R
      IF(RR.LE.(1.-R1)) RETURN
```

```
      IF(RR.LE.-ALOG(RJ)) RETURN
      GO TO 1
      END
```

TABLE 3.2 ALGORITHM FOR KINDERMAN AND MONAHAN'S METHOD

3.5.6 Discussion and Recommendations

It is not possible to declare any of the above pseudo-normal algorithms as the "best". The execution speed may be most important, but the speed depends on the machine, the uniform random number generator, and the speed at which elementary functions such as the square root are evaluated. It is also desirable to have few lines of programming code. For keystroke programmable computers (calculators) the speed is closely associated with program length and the direct polar method may be the fastest one. At the beginning of the simulation studies only the first three methods were known and tested for execution speed on the PDP 11–60 computer of the Boundary Layer Wind Tunnel Laboratory. The direct polar method, with only Equation (3.3a) known, was the fastest and is used throughout the study for compatibility purposes.

Best [1979] gives comparisons of the methods above and others, excluding the sum of groups method, for a CDC 7600 computer. His execution timings favour the Ratio of Uniform Variates method, and polar method without trigonometric function evaluations. Algorithms using a longer code or many table constants may execute even faster, as Best found for the convenient method of Marsaglia and Bray [1964]. This method is a compromise between algorithms with few table constants and those requiring many, and the code is only about three times longer than the above recommended methods. Marsaglia, MacLaren and Bray [1964] published a procedure which is approximately four times longer than the convenient method but can be almost twice as fast as the convenient method by their own timings on IBM computers.

These considerations suggest for white noise generation, the user tries the two Fortran coded algorithms above, and perhaps the Marsaglia convenient method (algorithm available from McGill University) and checks the timing for, perhaps, 10000 generated

Gaussian Random deviates. Further speed is gained by in-line programming which eliminates subroutine linkages, or programming the important steps in machine language.

3.6 AUTOREGRESSIVE PROCESSES

An autoregressive process is a special form of modifying white noise by digital filtering to produce a load function that has the required distribution and power spectral properties.

In 1921 the statistician Yule described a discrete second order autoregressive process (taken from Jenkins and Watts [1968]):

$$P(t) - \mu = C_1 \times [P(t-\Delta t) - \mu] + C_2[P(t-2\Delta t) - \mu] + R'_{(t)} \qquad (3.5)$$

where $P(t)$ = time series with mean value μ

C_1, C_2 = constants

$R'_{(t)}$ = purely random process

Yule argued that with $R'_{(t)} = 0$ in (3.5) this model would describe the behaviour of a simple pendulum damped by air resistance proportional to its velocity. If $R'_{(t)}$ is a purely random process, then the pendulum is subjected to random shocks in displacement at equidistant times. Instead of damping out, the pendulum now oscillates with a disturbed periodic motion.

Since the 1960's Box and Jenkins [1976] further developed approaches to time series analysis, forecasting and control, based on a particular class of linear stochastic models. These are applied in various areas such as chemical processes, stock prices, sunspot numbers, and patterns of airline ticket sales.

Autoregressive processes, in particular, are finding application in wind simulations. Fortier and Scanlan [1979] used autoregressive processes to simulate local pressures on cooling towers. Their paper emphasizes the suitability of second order autoregressive models to the simulation of fluctuating time histories at all points around the throat of a cooling tower. No attempt has been made, however, to simulate modal loads, i.e. to incorporate mode shapes and correlations between the different pressure transducer locations.

Wyatt and May [1972] simulated wind loads by taking the load function as the sum of a component containing low frequencies, leading to the quasistatic response, and a component containing mainly frequencies near the natural frequency, leading to the narrow band response. The broad band component was generated by applying 17 term "linear autoregressive filters", very similar to what are more generally known as 16th order moving average processes (Box and Jenkins [1976]). The narrow band excitation was generated using a 6-term "autoregressive filter". The paper contains many valuable details on simulating wind loading but their procedure uses, as estimated, perhaps fifty times more excecution time than the method proposed in this thesis.

The spectra measured with the force balance show usually one peak, or when periodic effects, such as vortex shedding, become important a secondary narrower peak at a higher frequency. For single peaked spectra, such as all drag spectra, autoregressive processes often as low as order two, give acceptable spectral distribution. Detailed description on autoregressive, moving average and mixed processes can be found in Box and Jenkins [1976], and only the main features for autoregressive processes are summarized below. For simplicity the mean is assumed to be zero and can be simply added to the time series after all values are generated.

The time series to be generated for an AR(p) process (autoregressive process of order p) is expressed as a finite, linear aggregate of previous values of the process and a shock:

$$P(t) = C_1 P(t-\Delta t) + C_2 P(t-2\Delta t) + \ldots + C_p P(t-p\Delta t) + C_r R_{(t)} \qquad (3.6)$$

which simplified for a second-order autoregressive process as:

$$P(t) = C_1 P(t-\Delta t) + C_2 P(t-2\Delta t) + C_r R(t) \qquad (3.7)$$

where $P(t)$ = simulated wind force at time t, which can be used, i.e. to evaluate the building response at the next time step

C_1, C_2 = constants, particular to building shape, degree of freedom of building, mean wind direction and terrain roughness; independent of wind speed or mechanical properties of the structure. These two constants determine the shape of the spectrum.

C_r = constant used to scale the spectrum to the correct variance, proportional to the velocity squared. Changing C_r shifts the spectrum with respect to the spectral amplitude, but the shape remains the same.

$R_{(t)}$ = white noise with mean 0, and variance 1.0 as described in Section 3.5.

Δt = time step, proportional to the reduced frequency.

Parsimony of the process is evident, requiring only two parameters plus a mean and RMS constant to be known. Execution is fast, only two additions and three multiplications are necessary per time step in addition to generating the white noise sample.

Figure 3.2 shows examples of simulations for part of two time series from the same white noise process. For comparative purposes, the three graphs have the same time scale, and the ordinates are scaled to have the same variance of 1.0 and a mean of 0.0. For actual force simulations the process would be scaled to have the correct variance and all points would be offset by the mean component of the force.

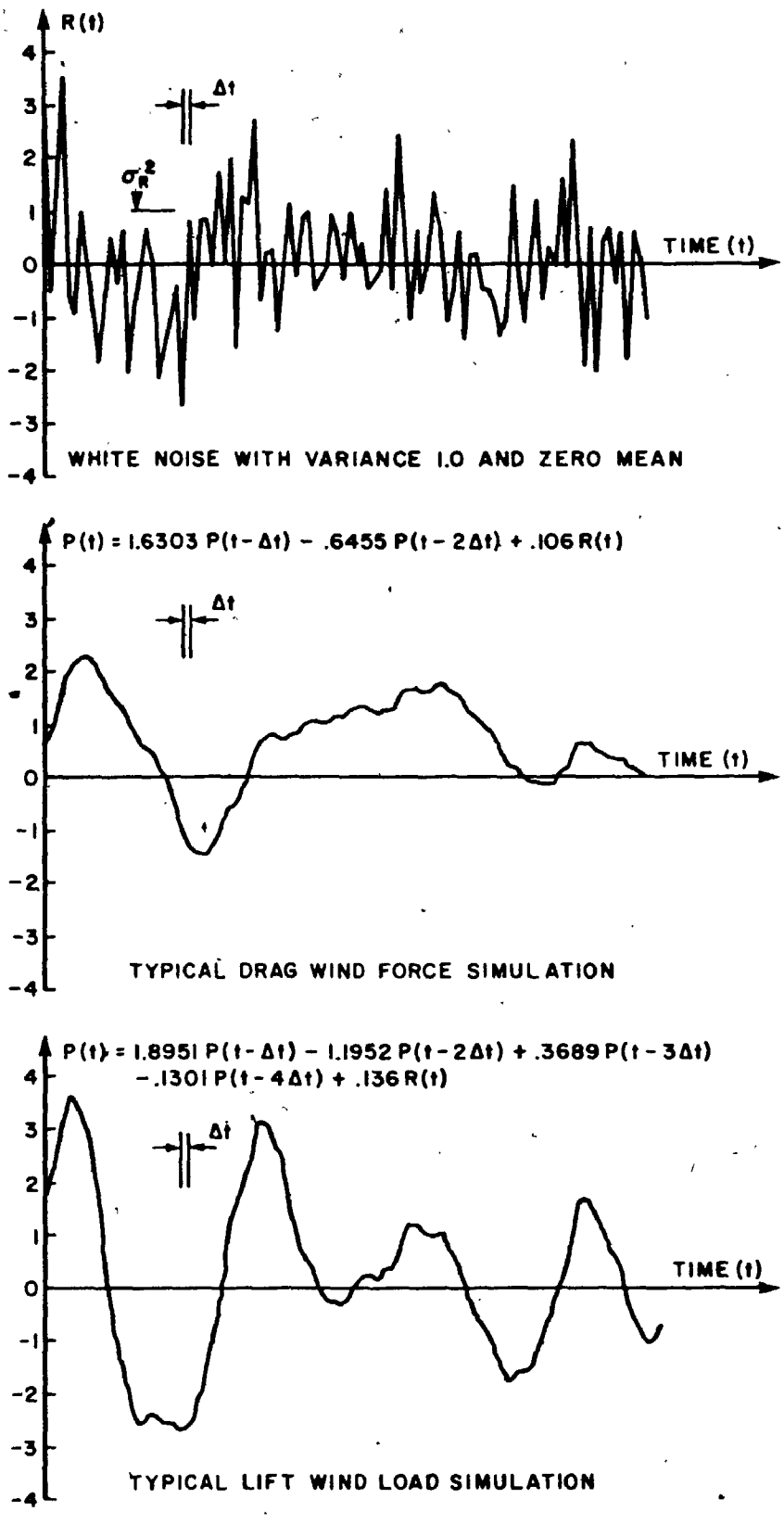

FIG. 3.2 EXAMPLES OF WHITE NOISE AND TIME SERIES SIMULATION

The top figure shows an example of white noise, these values were used for both time series below. The simulated time series in the middle is typical for forces in the drag direction, simulated by an $AR(2)$ process. Along wind forces have a broad band low frequency content.

The bottom figure is an example of a lift force simulation with a narrow band component in the range of the vortex shedding frequencies. An $AR(4)$ process gives a better approximation in this case to the measured process as described below in Section 3.9.

Measured spectra from the wind tunnel tests and estimated simulated spectra are shown below in Figure 3.6.

The spectral distribution $S_p(f)$ for an $AR(p)$ process is of the form (Box and Jenkins [1976]):

$$S_p(f) = \frac{2 \times C_r^2}{|1 - C_1 e^{-i2\pi f} - C_2 e^{-i4\pi f} - \ldots - C_p e^{-ip2\pi f}|^2} \qquad (3.8a)$$

with $0 < f < ½$

which can be simplified for an $AR(2)$ process as:

$$S_p(f) = \frac{2 \times C_r^2}{[1 + C_1^2 + C_2^2 - 2C_1(1-C_2)\cos 2\pi f - 2C_2 \cos 4\pi f]} \qquad (3.8b)$$

with $0 < f < ½$

The value of the denominator in Equation (3.8a) can be shown in the complex plane as a vector sum. Fig. 3.3 shows an $AR(2)$ process with values scaled for typical wind load simulations. Note that the vector C_2 rotates twice as fast as the vector C_1 for increasing values of f. This leads to the minimum value, and hence largest spectral value, at a low frequency (or highest reduced velocity); with the constants in Fig. 3.3 at $f = 0$, and the maximum value at $f = 0.5$. Both values are reached asymptotically, diverging with a slope of + 1.0 from the $f \times S_p(f)$ versus f plots of the spectra.

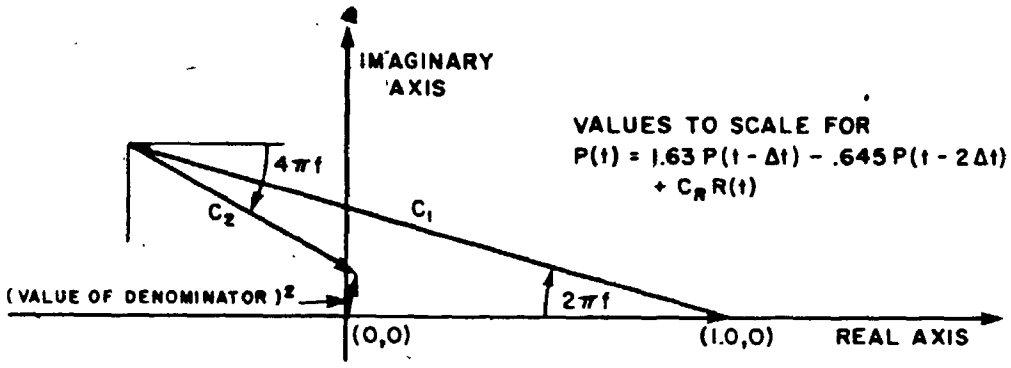

FIG. 3.3 VALUE OF DENOMINATOR IN SPECTRUM EQUATION

At high frequencies it should approach a desired slope of – 2.0 or less. This is not a serious point, however, as the energy at this high frequency is negligible. The slope at the low frequencies is nearly correct with a value of 1.0.

In addition to the low frequency spectra it is also possible to get high frequency spectra or spectra with a peak at an intermediate frequency for an *AR(2)* process, but these are not usually applicable for wind load simulations.

For higher order *AR* processes, spectra may have multiple peaks, which might be useful for simulating wind loads containing near periodic forcing functions such as from vortex shedding.

Section 3.7 describes methods to estimate values for the autoregressive constants C_i, and the order of the *AR* process is discussed in Section 3.9.

The variance σ_p^2 for high order *AR* processes can be found by numerical integration of the spectrum, Equation (3.8), for frequencies from 0 to ½. For an *AR(2)* process it can be shown to be:

$$\sigma_p^2 = \left(\frac{1 - C_2}{1 + C_2}\right) \frac{C_r^2}{[(1 - C_2)^2 - C_1^2]} \qquad (3.9)$$

The constant C_r to be used in a simulation can be found from Equation (3.9) or alternatively using the $C_r(1.0)$ given in the figures and rescaling them for a variance different from 1.0, i.e. for a base bending moment

$$C_{RM} = \frac{\frac{1}{2}\ \rho V^2\ \tilde{C_M}\ B\ H^2}{C_r\ (1.0)} \qquad (3.10)$$

where $(\frac{1}{2}\ \rho V^2\ \tilde{C_M}\ B\ H^2)$ is the desired RMS base bending moment value. The values for C_r in the figures do not give a variance of exactly 1.0 but are a best fit to the data, usually giving a variance of less than ±4% different from 1.0, i.e. ±2% for the RMS value.

If the mean is not zero, it has to be added at each time step after the time series is evaluated using Equation (3.7).

The autoregressive process always requires past values of the time series. This poses some problem at the startup of a simulation. In this study the unknown previous values were taken as zero and the first 1000 generated time series points were ignored. For high order AR processes it may be necessary to ignore the first 10,000 or more points to approach a stochastic time series. Alternatively, an equation like (3.1) might be used to commence the process.

To achieve stationarity, the roots $(B_1, B_2, \ldots B_p)$ of the characteristic equation:

$$C(B) = 1 - C_1\ B - C_2 B^2 - \ldots - C_p\ B^p = 0 \qquad (3.11)$$

must lie outside the unit circle of the complex plane. For high order AR processes the roots can be found by polynomial root finder subroutines. For an $AR(2)$ process the stationarity requirements can be simplified to:

$$C_2 + C_1 < 1 \qquad (3.12a)$$

$$C_2 - C_1 < 1 \qquad (3.12b)$$

$$-1 < C_2 < 1 \qquad (3.12c)$$

From the equations it can be seen that the absolute values of the shape constants are always of the order 1.0, for $AR(2)$ wind load simulations typically C_1 approximately 1.7 and C_2 approximately -0.7.

3.7 ESTIMATION OF SHAPE CONSTANTS IN AUTOREGRESSIVE PROCESSES

3.7.1 Using Spectrum Versus Autocorrelation Function

As described above, the autoregressive parameters define the shape of the spectrum. They also define the shape of the autocorrelation function, which is the Fourier transform of the spectrum and hence mathematically equivalent. Either the spectrum or the autocorrelation function can be used to estimate the values for the autoregressive parameters. The best values for a particular model are those which give the closest approximation to the shape, conditional on the generation of a stationary time series. The choice of using the spectrum or the autocorrelation function depends upon the data and the understanding of their representational values. Many standard texts, i.e. Box and Jenkins [1976] and Jenkins and Watts [1968], describe their models in terms of the autocorrelation function.

For wind load, the autocorrelation function is not as easy to interpret as the spectrum. The primary data acquisition performed in the wind tunnel is fast Fourier transforms of the time series, producing spectral estimates of the data. Since the frequency response functions for structures are well known for linear systems, the power spectra can be used directly to predict the response spectra. As shown in Chapter II, the response

has two contributions with the same order of magnitude: a low frequency component giving rise to the quasi-static response, and a component from frequencies near the natural frequency of the structure, giving rise to the resonant response. This insight suggests some criteria on the closeness of the fit required to the spectral shape; given that the basic shape is correct, the spectral values at low frequencies need not to be matched closely. Only the variance of the process, which is contained mostly in the low frequencies, has to be correct. The only frequencies where a close match of the measured and the simulated spectra is necessary is near the natural frequency of the structure.

Therefore, it is preferable to use the spectrum directly for estimating the constants in the autoregressive processes to simulate wind forces, giving most emphasis to fitting the region of the natural frequencies. A reason for easier interpretation is that the estimates at neighbouring frequencies are approximately independent. This makes it also possible to eliminate noise contamination in the signal by smoothing the spectrum.

The individual spectra are averaged estimates from at least one hundred records, and are statistically much more reliable than individual time series records.

Working directly with the spectrum, the constants for the simulations are found by matching the expected spectral values from Equation (3.8) with the measured values.

Conventionally, curve fitting is done using regression techniques which involve derivatives and simultaneous equations. Since the theoretical best solution is not necessarily, stationary and each different function can only be used after laboriously finding and re-programming of the derivatives, the fitting in this study was done using optimization techniques.

3.7.2 Optimization

Optimization is emerging as an important subject for research, stimulated by the availability and increasing speed of digital computers. Before the advent of high speed computers, optimization problems were insolvable for systems with more than three to

four variables. Optimization and function minimization is, however, so important and generally applicable that a brief description is given here. It is often the way to solve a general problem with the least possible effort.

Optimization can be employed when a problem is formulated to find n parameters $x_1, x_2, \ldots, x_n$ so that the value of a function of these parameters $f(x_1, x_2, \ldots, x_n)$ is a minimum. The minimum can be the minimum cost to build a bridge in one problem, the least square error in curve fitting, or even more general the minimum error to a correct solution in a general problem. The parameters might be the number and individual spacings of the columns which in turn determine the depth of the bridge deck, the constants to be found for the best curve fit, or the values with good accuracy to the correct values in a general problem. The optimization technique can be thought as a well organized trial and error solution approach, where the trial values rapidly approach acceptable values. Solutions by trial and error are usually easily formulated and are often employed in practice.

The organization to solve problems using optimization is usually in the form shown in Fig. 3.4.

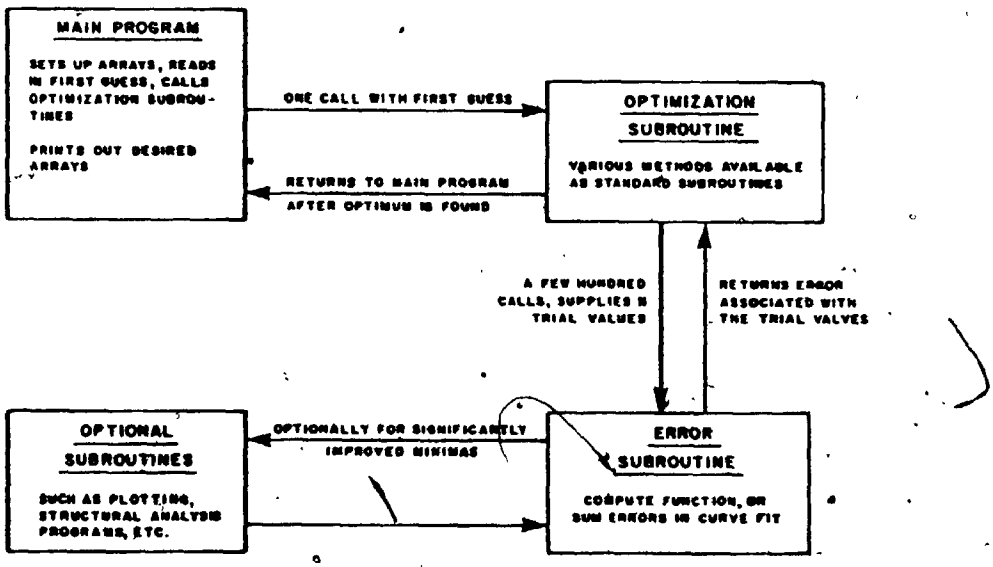

FIG. 3.4 FLOW CHART TO SOLVE PROBLEMS USING OPTIMIZATION TECHNIQUES

The solution of a general problem using trial and error methods is efficient in terms of effort for the engineer at the expense of computer time. With good optimization subroutines the trial values approach the best values in acceptable computer time.

An optimization routine can be thought of as a "black box" providing good trial values. Various methods are employed, but the gradient search can be easily visualized for two parameters: The routine would use the first guess to find the error or "altitude". A few random points near this guess would enable it to form contours. Subsequently it would start moving towards the "valley" following the steepest descent, always keeping the best solution and a few neighbouring good solutions and discarding the worst solution from its table. This is only a basic description and optimization routines have to cope with ridges and any number of parameters, but the problem of minimization is the subject of ongoing research at many institutions. Detailed treatment can be found in the literature on optimization and non-linear programming, i.e. Adby and Dempster [1974], Pierre [1969], Wilde and Beightler [1967] or Zangwill [1969].

The engineer need not be concerned with more than knowing the basic procedure as outlined above to use optimization techniques successfully in various applications. For the curve fitting problems several routines were used, but the most rapid convergence to acceptable values was achieved with a subroutine using the theory found in a paper by Powell [1964]. The routine is available as subroutine VA 04A in the Harwell Subroutine Library. With initial guesses of 0.01, absolute accuracy requirements of 0.0001 and a scale factor of 1000, the program usually converged quickly to the best solution. Methods exist which are faster than Powell's method, but they require derivative evaluations.

3.7.3 Constant Evaluation

The problem of finding the shape parameters C_i to fit the measured spectra using Equation (3.8), is now described. Using all the measured points of the spectrum as shown in Fig. 3.7 would emphasize the upper end of the spectrum, because the points are most dense on a logarithmic plot. The high frequency contribution to the response, however, is small and the relative errors are very high, but referring it to the values at

important frequencies the errors are negligibly small. The best curve fits were found by using points only at a logarithmic spacing. At well chosen spacings the noise spikes are also skipped, eliminating the noise problems. The error criteria used is the logarithm of the residuals squared:

$$Err = \sum_{j=1}^{k} [\log|\text{theoretical value Eq. (3.8)} - \text{measured spectral density}|]^2 \times WF \qquad (3.13)$$

where k = the number of the measured values used for fit (measured – skipped values)

WF = a weight factor, normally 1.0 for all points but a larger value may be assigned to important frequencies if the fit is not acceptable for the whole frequency range.

Equation (3.13) is the core of the error subroutine in Fig. 3.4. The routine keeps the value of the previous smallest error, returns immediately to the optimization routine if the error is larger, but checks for stationarity if the new error is smaller. For non-stationary time series the error is increased by 5% to 10% before returning to the optimization routine, this normally results in stationary time series as the best fit, when the optimization routine returns to the main program. More advanced penalty functions are described in Adby and Dempster [1974]. For drastic reductions of the error Err during the optimization process, the estimated spectrum function (Equation 3.8) may be plotted versus the measured points to monitor the progress in the fitting process.

3.8 TIME SCALES IN AUTOREGRESSIVE PROCESSES

The accuracy of the integration of the equation of motion depends predominantly on the length of the time increment Δt at which the forces are generated. It is shown below in Chapter IV. Integration procedures, that the use of 15 points or more per period of the structure gives reliable response calculations.

Equation (3.8) is valid for a spectrum to be fitted from a frequency of 0 to 0.5. The AR process generates two points per period corresponding to the highest fitted frequency, one point every $1/(2 \times 0.5) = 1.0$ time units. The measured spectra are normalized by velocity and characteristic building dimension at the time of acquisition. For fitting, a maximum reduced frequency $(nD/V)_{max.\ fit}$ is chosen. The frequency constant C_f with which each reduced frequency is multiplied before fitting is:

$$C_f = \frac{0.5}{\left(\frac{nD}{V}\right)_{max\ fit}} \qquad (3.14)$$

Alternately Equation (3.8) can be written as:

$$\frac{f S_p\left(\frac{nD}{V}\right)}{\sigma_F^2} = \frac{2 \times C_r^2 \times C_f^2 \times \frac{nD}{V}}{|1 - C_1 e^{-i2\pi C_f nD/V} - C_2 e^{-i4\pi C_f nD/V} - \ldots - C_p e^{-i2\pi p C_f nD/V}|^2} \qquad (3.15)$$

$$0 < \frac{nD}{V} < \frac{0.5}{C_f}$$

The time increment Δt at which the forces are generated using Equation (3.15) for a building with dimension D for a simulated wind velocity V_{sim} is:

$$\Delta t = \frac{D/V_{sim}}{\left(\frac{nD}{V}\right)_{max\ fit} \times 2} = C_f D \frac{1}{V_{sim}} \qquad (3.16)$$

Each figure showing the fitted spectra also shows the mean and rms force coefficients C_F, $C_{\tilde{F}}$, the shape coefficients, C_1, C_2, . . . C_p, the scale coefficient C_r for a variance of 1.0 and the scale factor for the time steps C_f. A typical presentation of the

simulated spectra with legend is shown in Fig. 3.5.

From Equation (3.16) it can be seen that the time steps decrease with increasing velocity. This is beneficial, because for low wind speeds with small responses a larger relative error is permissible than for large wind speeds where the complexity of non-linear damping and stiffness properties must also be considered.

An acceptable maximum reduced frequency $(n\ D/V)_{max.\ fit}$ chosen to fit the spectrum was found to be approximately $20 \times (n_0 D/V_{100})$ where n_0 is the natural frequency of the structure and V_{100} is a velocity associated with a return period of approximately 100 years.

The above procedure permits the shape factors to be held constant and the time scale to be varied for different velocity simulations. The opposite could be done but the advantage of keeping the shape factors constant would be lost. An example of spectra fitted to two different time scales is shown in Fig. 3.6. It can be seen that the values for the autoregressive parameters change little, but in an indeterminate way, and that the closeness of the fit remains almost unchanged.

If the time scale is too different from an optimum value and the spectrum cannot be refitted to a different time scale, it is still possible to overcome the problem. If too many load points are generated to make the integration process economical, points can be dropped, as long as the time steps are kept constant. It is also possible to interpolate points in between the load function generated by the AR process, but care has to be taken not to introduce high frequency content as would be the case with straight line interpolation. Wyatt and May [1973] have assessed the problem and shown the relationship of a continuous process x(t) in relation to a stochastic discrete process x_j (spaced at time increments Δt) with so-called sinc functions, using the $2(n + j)$ nearest values of x_j:

$$x(k\ \Delta t + \delta t) = \sum_{j=-n}^{n+1} a_j\ x_{j+k}\ \frac{\sin \pi(\delta t/\Delta t - j)}{\pi(\delta_t/\Delta t - j)} \qquad (3.17)$$

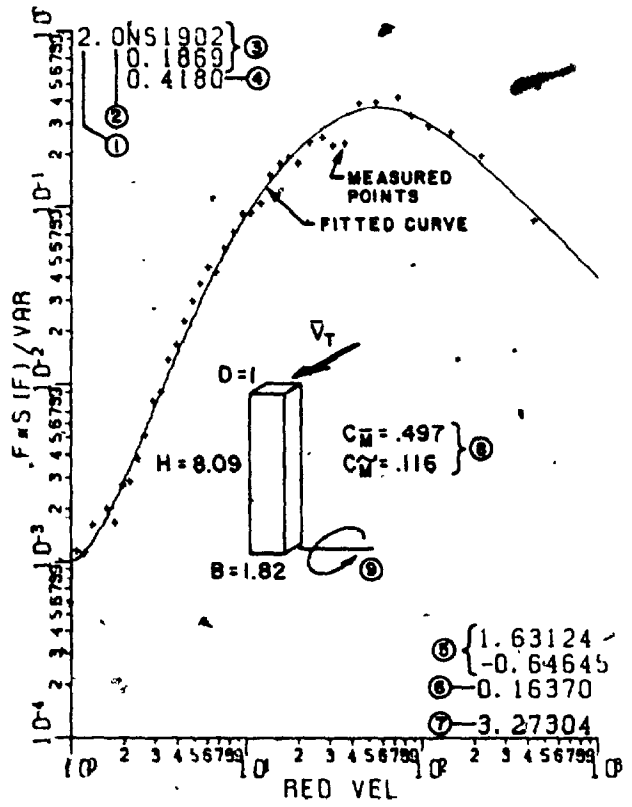

For the AR(2) process, the time series can be generated for a Velocity V_{sym} as:

$$M(t) = 1.63M(t-\Delta t) - .646M(t-2\Delta t) + \tilde{M}^2 \times .164^2 \times R_i$$

$$\Delta t = .418 \times D \times \frac{1}{V_{sym}}$$

An adjustment for the mean is performed after all M(t)'s are generated as:

$$M(t) = \bar{M} + M(t)$$

LEGEND:

1. Number of AR parameters used = n_{AR}
2. Number of MA parameters used = n_{MA}
3. File name
4. Time scale factor C_f for simulations
5. The first n_{AR} numbers are the AR constants, the next n_{MA} numbers are the M_A constants
6. The RMS scale factor C_r
7. A relative constant for the errors in fit (not all plots use the same criteria)
8. Mean and RMS force coefficients
9. Variable measured, i.e. drag base bending moment

The abscissa shows the reduced velocity $R_{vel} = \frac{\bar{V}_T}{nD'}$ where $D' = \sqrt{BD}$

$\bar{V}_T$ = velocity on top of building

The ordinate shows the normalized spectral density $\frac{f\,S_M(f)}{\sigma_M^2}$

The mean moment is: $\bar{M} = \frac{1}{2}\rho\bar{V}_T^2\, C_{\bar{M}}\, BH^2$

The rms moment is: $\tilde{M} = \frac{1}{2}\rho\bar{V}_T^2\, C_{\tilde{M}}\, BH^2$

The fitted curve is the expected spectral density from simulations, i.e. in this case:

$$\frac{f\,S_M(f)}{\sigma_M^2} = \frac{.2 \times f' \times .4180 \times .1637^2}{|1-1.631\, e^{-2\pi f'} + .646\, e^{-4\pi f'}|^2}$$

where $f' = \frac{.418}{R_{vel}}$; $\frac{.418}{.5} < R_{vel}$

FIG. 3.5 TYPICAL PRESENTATION OF MEASURED AND EXPECTED SPECTRAL DISTRIBUTION FOR FORCE SIMULATIONS

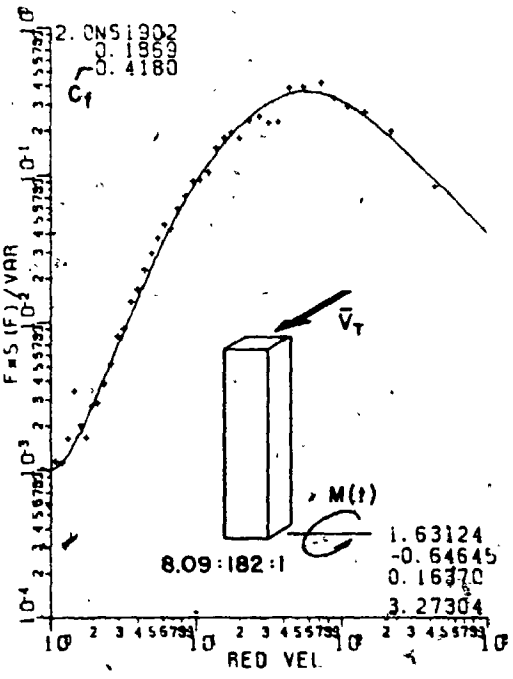

a) DRAG, LOW FREQUENCY

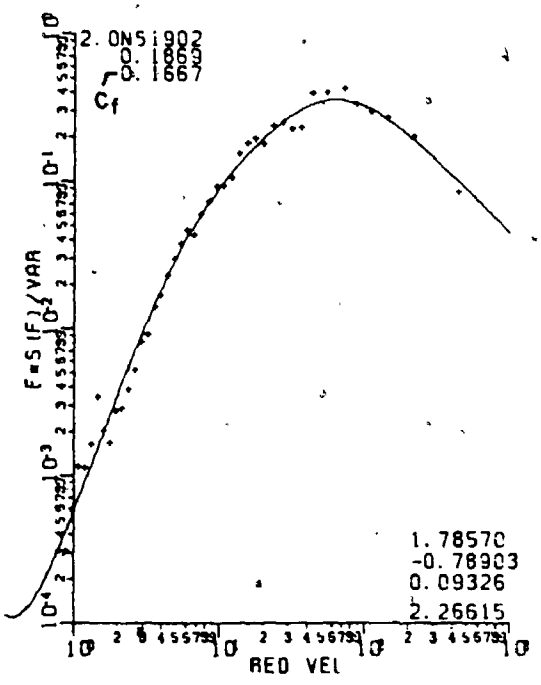

b) DRAG, HIGH FREQUENCY

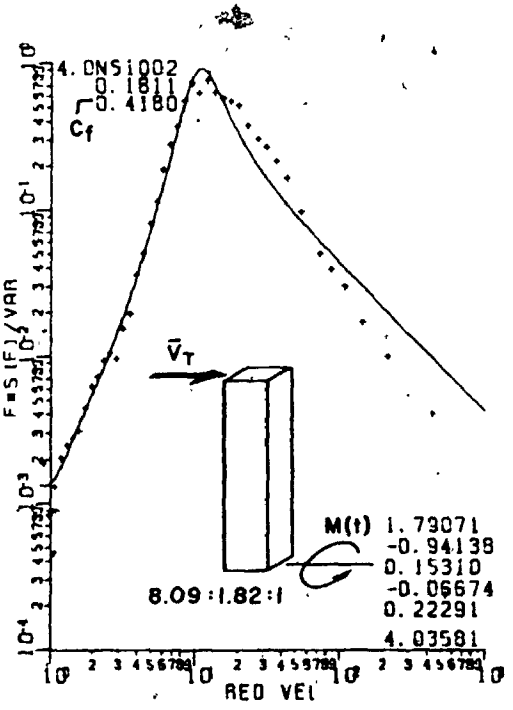

c) LIFT, LOW FREQUENCY

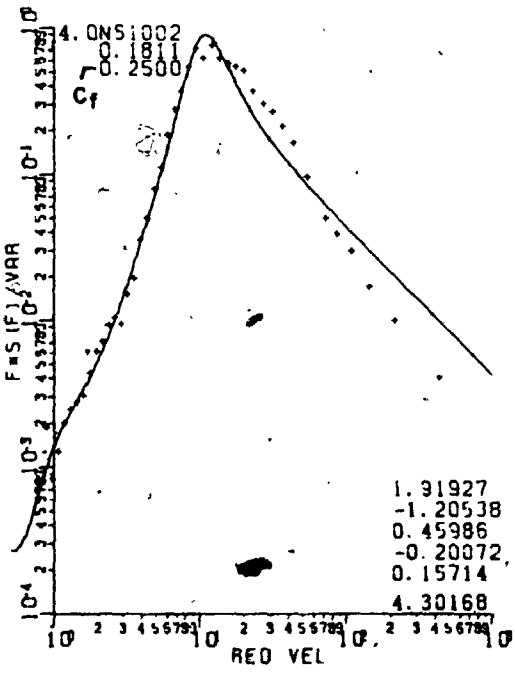

d) LIFT, HIGH FREQUENCY

FIG. 3.6 EFFECT OF FITTING TIME SERIES TO DIFFERENT TIME SCALES

where $a_j = \begin{cases} 1 \text{ for } -n+1 < j < n \\ \frac{1}{2} \text{ for } j = -n \text{ or } (n+1) \end{cases}$

Although theoretically n should be infinite, the amplitude of the sinc function is well damped and for practical applications sufficient accuracy is obtained using eight terms ($n = 3$). The ideal interpolation function for recovering a continuous signal from a sampled signal at equally spaced time increments is sometimes referred to as Whittacker's interpolation formula.

Measured force spectra and associated parameters to simulate the force time history for different buildings, degrees of freedom, wind directions and parameters are shown in Appendix A.

3.9 ORDER OF AUTOREGRESSIVE PROCESSES

The selection of the order of the AR process has to be a compromise between the adequacy of the fit to the data and the requirements of "parsimony". Increasing the number of parameters adds to the long required computer times in simulations, increases the efforts to find the parameter values and choice of order of the process. The parameter values are also more susceptible to experimental errors in the data acquisition as shown below. This could, for example, lead to unnecessary poor estimates of the simulated forcing function.

To be useful the model should reflect the principal physical features of the process and involve as few parameters as possible, i.e. the order of the AR process should be as low as possible to generate the time series. The time steps of the time series should be as large as possible.

Figs. 3.7 and 3.8 show the effect of increasing the order of the AR process for a

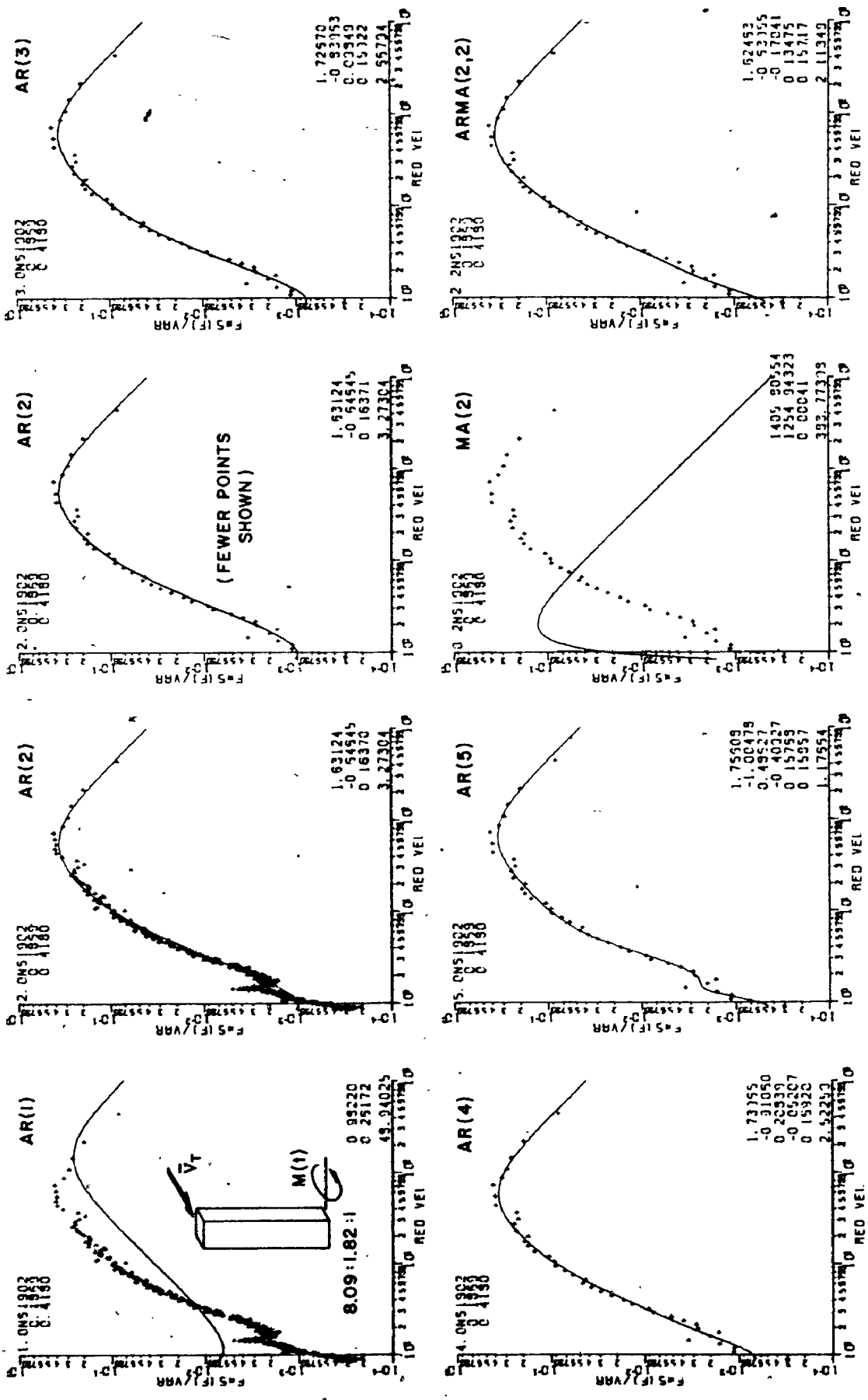

FIG. 3.7 IMPROVEMENT WITH HIGH ORDER AR PROCESSES FOR WELL FITTED SPECTRAL SHAPES

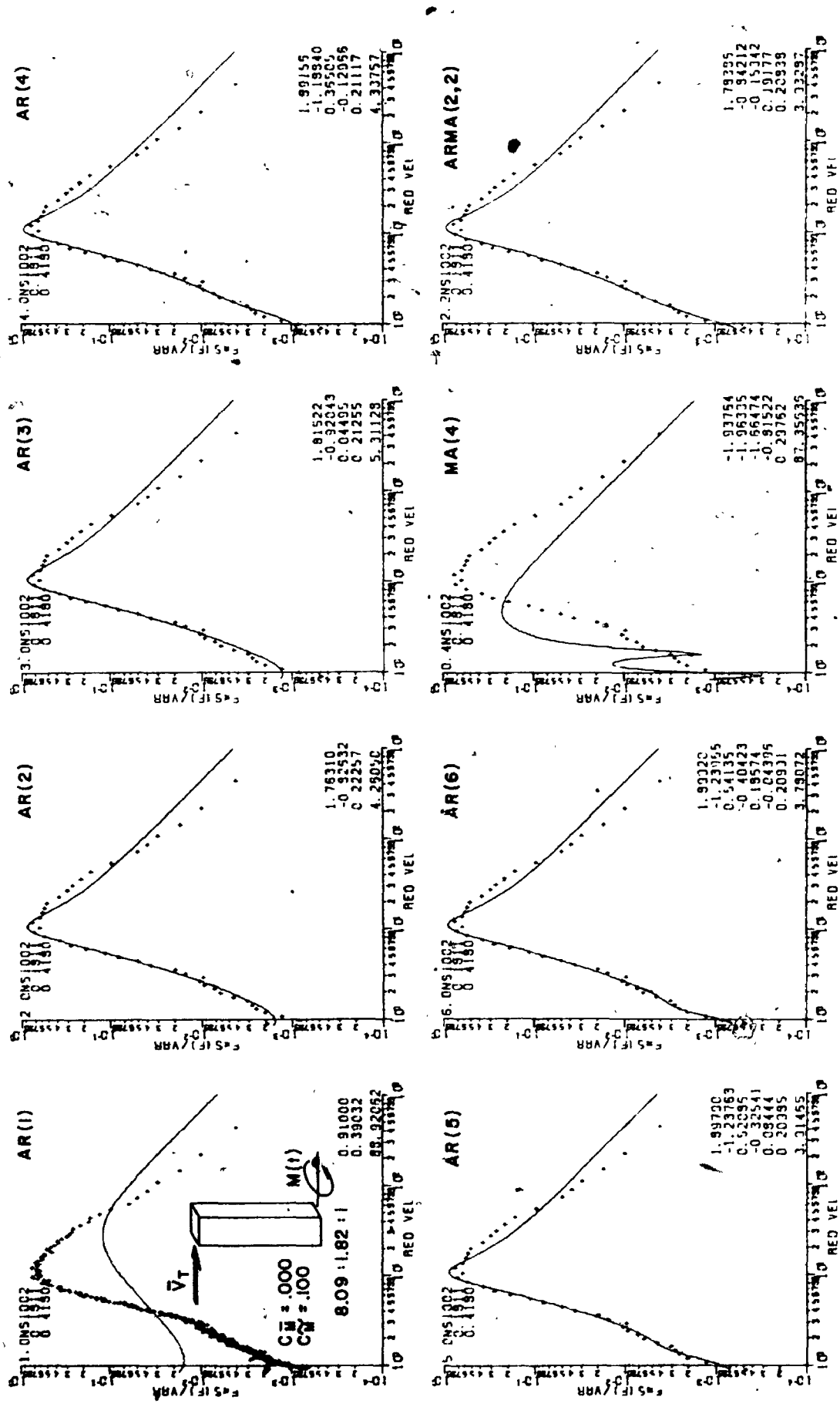

FIG. 3.8 IMPROVEMENT WITH HIGH ORDER AR PROCESSES FOR DIFFICULTLY FITTED SPECTRAL SHAPES

well fitted spectrum, and for a spectrum shape for which a good fit using *AR* processes is difficult to find. As can be seen from both figures, a first order *[AR(1)]* process is not suitable for time series having spectra that are typical for wind forces. An *AR(2)* process gives a notable improvement, and acceptable simulations if judged by the criteria for giving the correct variance from the low frequency part of the spectrum and closely approximating the spectral density at the natural frequency of the building, as described in Section 3.7. The reduced velocity for a typical building for a high wind speed is approximately 2.0 to 6.0, indicating that the important range is to the left of the peak in the spectra if plotted as a function of reduced velocity.

Irregularities at high frequencies in the measured spectra are due to noise contamination of the signal and aliasing effects of higher frequencies and should be ignored. The contribution to the response of structures at high frequencies is negligibly small in all cases. For velocities corresponding to an ordinate value of 0.01, the response was shown in Chapter II to originate about equally from background response and from resonant response. At lower velocities, corresponding to a smaller ordinate value, the relative contribution from high frequency resonant response is less than from the quasi-static background response. With respect to the total response at design velocities, even a large relative error in this small high frequency contribution is not significant. A suggested lower ordinate criteria is 10^{-3} for judging divergencies of either the fit or measured spectra from expected trends. Points with lower ordinate values do not affect the response of structures significantly, even if the points have large relative errors.

Improvements in the fit are small for autoregressive processes having a higher order than two. Low order *AR* processes tend to smooth out irregularities, but above a certain order the apparent improvement in the fit results mostly from fitting these irregularities as shown in Fig. 3.7 for the *AR(5)* process. For spectra having secondary peaks, i.e. due to vortex shedding effects, it is necessary to use higher order *AR* processes. Alternatively a narrow band time series may be added to a broad band time series, as done by Wyatt and May [1972] even for along wind spectra. The narrow band component may be simulated as an *AR* process, independent of the broad band process, or the total time series may be generated using different models, i.e. autoregressive-moving average *(ARMA)* processes, see Box and Jenkins [1976].

Any AR process can be inverted to a moving average process, being represented as a weighted sum of previous shocks of the form:

$$P(t) = C_r[R(t) - \theta_1 R(t-\Delta t) - \ldots - \theta_q R(t-q\Delta t)] \qquad (3.18)$$

but the number of constants θ_i is infinite for a finite order AR process. The spectrum is of the form:

$$S_p(f) = 2 \times C_r^2 \, |1-\theta_1 e^{-i2\pi f} - \theta_2 e^{-i4\pi f} - \ldots - C\, e^{-iq2\pi f}|^2 \qquad (3.19)$$

Note the similarity to Equation (3.8a), the denominator, shown also in Fig. 3.3, is now in the nominator. The MA process is always stationary.

Moving average models do not apply to time series of the type encountered for wind forces. Only high order MA processes give acceptable fits to the spectrum, but AR and MA processes can be combined to form $ARMA$ processes, which give more flexibility. Granger and Morris [1976] have also shown that the sum of two AR processes, such as proposed above for the broad and narrow band frequency range, can be expressed as an $ARMA$ process, with equal or more efficient computation time.

Fig. 3.7 shows an example using a 2nd order moving average, $MA(2)$, process. The fit is poor, confirming that autoregressive processes are more applicable for wind load spectra. An autoregressive – moving average process $ARMA(2,2)$ gives a better fit, but the process is dominated by the autoregressive parameters. Similar observations can be made for Fig. 3.8.

Theories have been developed for automatic choice of autoregressive models, i.e. by Akaike [1970] or Duong [1981]. These methods basically consist of finding a minimum error for increasing orders of processes but adding more penalty to higher order fits. In this study, however, the fits were done interactively and the fits were

observed on plots and accepted or rejected on a visual basis.

Some of the difficult spectra measured in this study were fitted to *ARMA* models, but no satisfactory fits were found using permutations of up to 10 constants. It is possible that using up to 20 parameters would give a closer approximation to the difficult to fit spectra, but this is an extensively elaborate model and systematic investigations should be carried out to study methods to simulate forcing functions for the small number of cases which were not adequately represented by low order autoregressive processes.

3.10 MULTIPLE SIMULATED LOAD FUNCTIONS

The simulations described above are applicable to single degree of freedom structures. To study stresses in corner columns of a building, the forces from both perpendicular directions of the building have to be considered simultaneously. Two independent load functions can be generated for totally uncorrelated forces. Wind forces have only some correlation at low frequencies. Other cases where correlation is more important, include yielding systems where it may be desirable to simulate the shear and bending moment.

Multiple input functions which are correlated have not been explored in detail for this study. It was shown, however, by Wyatt and May [1972] that two correlated load functions can be written in the form:

$$P_1(t) = [p_1(t) + p_{12}(t)] \sigma(P_1)$$

$$P_2(t) = [p_2(t) + p_{12}(t)] \sigma(P_2) \qquad (3.20)$$

where $p_1(t)$, $p_2(t)$, $p_{12}(t)$ are statistically independent processes having power spectra $S_{p_1}(f)$, $S_{p_2}(f)$ and $S_{p_{12}}(f)$ respectively, and $\sigma^2(P_1)$ denotes the variance of P_1, etc. The quadrature component in the cross spectrum $S_{p_{12}}(f)$ is small for wind forces and $S_{p_{12}}(f)$ may be taken as a real quantity.

Hence it may be possible to simulate p_1, p_2, p_{12} using methods described in the sections above and form the correlated input functions using Equation (3.20), which is an efficient way in terms of computer time.

Alternatively the method by Shinozuka and Jan [1972] described in Section 3.4 can be used. This method is valid for multidimensional cases, but at the expense of much computer time.

3.11 SUMMARY

Low order autoregressive processes described in this chapter provide an efficient tool in simulating the majority of wind force time series. Described are the need for simulations, the requirements, comparisons with other methods, determination of parameters, time scales, and order of autoregressive processes required. Special topics having broader application than shown in the context of this chapter are discussed with practical demonstration to force simulations. These include optimization techniques and efficient numerical white noise generation. Methods are suggested for further research into simulation of time series with more irregular spectra, which are not acceptably represented by low order autoregressive processes.

CHAPTER IV

NONLINEAR BUILDING RESPONSE

4.1 INTRODUCTION

In the structural field, the problem of elasto-plastic behaviour has, perhaps, received the most attention under earthquake loadings. The behaviour of similar systems under wind action differs primarily because of the longer duration of the loading, and the presence of a large, mean component on which the dynamic fluctuations are super-imposed in the drag direction.

Most of the predictions of behaviour under wind loadings, including most studies done at the Boundary Layer Wind Tunnel Laboratory, assume linear structures. The analysis in this chapter is an attempt to develop tools to study the nonlinear behaviour of structures under wind loading, and to obtain a preliminary assessment if conventional linear analysis is sufficient, or if a more elaborate analysis is necessary for conventional structures.

A conclusive study would involve more exhaustive simulation runs than were possible under the scope of this work. The analysis which follows represents the initial stages of a study directed towards the determination of the importance of tall buildings under the action of wind. With the presented parameters for load function generation in Chapter III, and with description of methods to evaluate the nonlinear response in this chapter, the groundwork is provided enabling extensive research. Specific applications, or more

4.2 THE DYNAMIC RESPONSE OF NONLINEAR SYSTEMS

The equation of motion for a typical finite element model with n degrees-of-freedom can be written as:

$$[M]\{\ddot{y}(t)\} + [C(y,\dot{y},t,\ldots)]\{\dot{y}(t)\} + [K(y,\dot{y},t,\ldots)]\{y(t)\} = \{P(t)\} + \{A(y,\dot{y},\ldots)\} \tag{4.1}$$

with initial conditions $\{y(o)\}$, $\{\dot{y}(o)\}$ and $\{\ddot{y}(o)\}$, specified, where $[M]$, $[C]$ and $[K]$ are the mass, damping and stiffness matrices, respectively, $\{y\}$, $\{\dot{y}\}$ and $\{\ddot{y}\}$ are the displacement, velocity and acceleration vectors, respectively, and $\{P\}$ and $\{A\}$ are loading vectors. $\{P\}$ in wind loading is the load from integrated pressures over the contributory area, and $\{A\}$ is a body motional dependent force which may include aerodynamic damping. $P-\Delta$ effects can be regarded as a negative stiffness and can best be combined as a negative spring constant with $[K]$.

If it is assumed that $[M]$, $[C]$ and $[K]$ are constant (i.e. not functions of time or motion), then the system described by Equation (4.1) is linear. The solution can be represented by the Duhamel Integral, or by the normal mode method and in the frequency domain as described in Chapter II.

The force $\{P\}$ is determined experimentally as described in Chapter II. If the force balance includes the correct weighting functions, then the experimental values can be directly scaled to full scale modal force values. Alternatively, if a statistically correct time series is required, it can be simulated using methods and parameters given in Chapter III. Neglecting aerodynamic damping terms usually results in conservative response estimates as described in Chapter II, and $P-\Delta$ effects can be accounted for in the stiffness matrix $[K]$ in large displacement-non-linear responses.

The response for high forces is more difficult to estimate, because the structural properties change for different levels of vibrations. These properties are not readily

several hundred percent from computed values, and the ratio of static to dynamic modulus of elasticity varies as much as 40 percent, depending on the age and strength of concrete [Troxel and Davis, 1956]; 2) Dynamic model tests to determine the structural properties do not have enough details such as to model stiffness and energy losses in the individual joints; 3) Steady-state vibration tests of full scale structures are usually performed at relatively low levels of vibrations; 4) Records from structures strained to high levels due to earthquakes or wind loads are scarce.

Indications of non-linear behaviour can already be observed with careful steady-state vibration tests. A five storey concrete building tested by Nielsen [1966], showing the change of frequency (i.e. stiffness) and damping is reprinted in Fig. 4.1a. Both the damping and the frequency show a consistent change with stress level. The damping values are determined from the responses at resonance, using the half power points of the resonant peaks would give a damping value of about 1.8 percent regardless of which excitation level is used. Nielsen [1966] was also able to make tests before the non-structural elements, such as curtain walls, windows and interior partition walls were installed. He found virtually no change in both stiffness and damping values by the addition of these non-structural elements.

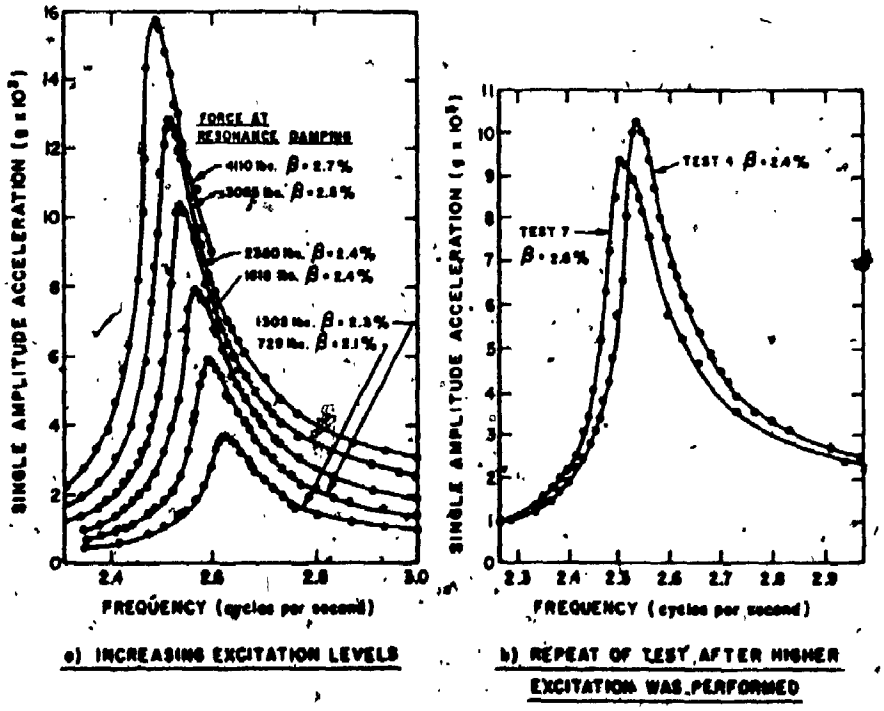

a) INCREASING EXCITATION LEVELS

b) REPEAT OF TEST AFTER HIGHER EXCITATION WAS PERFORMED

The recovery of stiffness and damping are not complete, even at these relatively small excitation levels. Nielsen [1966] repeated a test after the structure had been excited at higher levels of amplitude. The results are shown in Fig. 4.1b. For almost exactly the same excitation level (the excitation being proportional to the square of the frequency for practical reasons), the change in amplitude frequency and damping are clearly visible. This is another indication that structural properties might also change with time.

Tests on a nine-storey steel frame building by Nielsen [1966] showed similar changes in frequencies for different excitation levels, but less changes in damping which was only about 0.5%. Repeats of tests after higher excitation levels showed no change.

Most steady-state vibration tests are performed at lower levels of vibration. It is obviously not feasible to conduct a "performance test" on a full scale structure, since the forces would be too high to be generated artificially. This might explain the low values of damping suggested by many investigators, i.e. 1 percent for concrete buildings by Jeary and Sparks [1977]. An interesting observation in their paper is the case of the 240 ft. Arts Tower in Sheffield, England with a core designed to carry all the wind load, yet contributing only about 2 percent of the stiffness in one direction. The major part of the stiffness is apparently taken by the cladding and brickwork partition walls.

Some full scale measurements for large excitation levels can be found in earthquake related literature. Mulhern and Moley [1973] measured the period before, during and after the 1971 San Fernando earthquake in California on moderately tall buildings. Fig. 4.2 shows that the period increases substantially during the earthquake and shortens again after the earthquake, but the recovery is far from complete. The change in period indicates that the stiffness decreased to less than half its original value. No structural damage, and only minimal partition wall damage was observed.

Another severely damaged structure showed period increases in seconds from 0.65 to 0.83, 0.45 to 0.52 and 0.36 to 0.43 for the two lateral modes and torsion, respectively [Pardoen, Hart and Bunce, 1980].

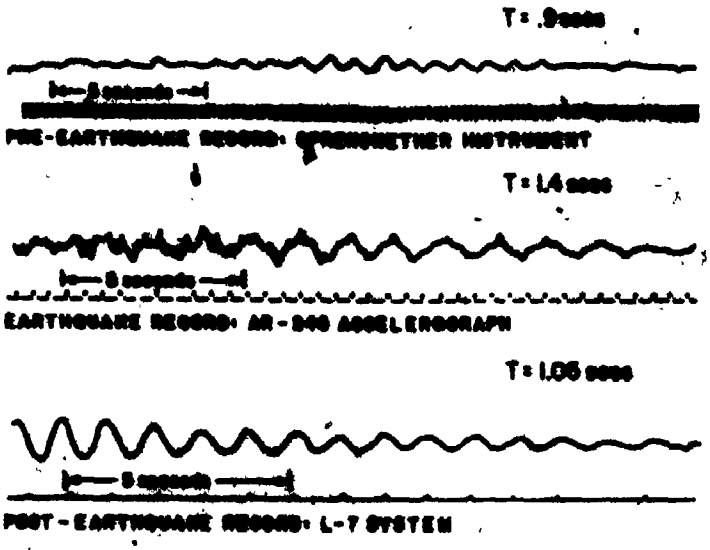

FIG. 4.2 PRE-EARTHQUAKE, EARTHQUAKE AND POST-EARTHQUAKE VIBRATION RECORDS IN A NORTH–SOUTH DIRECTION FROM THE ROOF (12TH FLOOR) AT 7080 HOLLYWOOD BOULEVARD, LOS ANGELES. THERE IS A WIDE RANGE OF SENSITIVITIES AMONG THE THREE INSTRUMENTS.

The damping can also be expected to change significantly after large displacements occur. Measurements in moderately damaged structures from earthquakes gave estimates of 5 percent to 10 percent structural damping ratios [Murphy, 1973]. These two effects, decreasing stiffness and increasing damping, compensate each other to some degree, but to study the behaviour due to large loadings, or to determine limit states or safety factors, the non-linearities should be considered. Assumed structural properties for the simulation studies in this chapter are discussed in Section 4.4.

Such changes in the damping and stiffness coefficients will alter the vibration characteristics of the system. Therefore, the normal coordinate uncoupling of the equation is not possible. The only generally applicable method for arbitrary nonlinear systems is the direct numerical step-by-step integration of the coupled equations of motion.

If the nonlinear deformation mechanisms do not cause major changes in its deflection patterns, the dynamic response still may be expressed efficiently in terms of the original mode shape. The equations of motion will become coupled as soon as any [illegible] in the response. Consequently, the response must be

obtained by integrating these equations simultaneously rather than individually. This is, however, still more efficient than to perform the integration for the original coupled equation system.

Effective methods have been developed and some will now be summarized, including the Runge-Kutta method used for response predictions in this chapter.

4.3 METHODS TO EVALUATE THE NON-LINEAR RESPONSE IN THE TIME DOMAIN

The numerical methods discussed share common assumptions. Direct integration schemes evaluate the response for a series of short time increments Δt. The condition of dynamic equilibrium is established at the beginning and end of each interval. The nonlinear nature of the system is accounted for by calculating new properties, appropriate to the current deformed state, at the beginning and end of each time increment. The complete response is obtained using the velocity and displacement computed at the end of one computational interval, as the initial condition for the next. The process can be continued to any desired time, i.e. to the point where a prescribed level of damage has accumulated.

For single degree of freedom systems only one equation of motion has to be solved. For multi-degree-of-freedom structures, the comparable direct integration involves the simultaneous numerical integration of a set of equations, one equation for each degree of freedom, as described by the equation of motion. The techniques are illustrated for single degree of freedom systems in this chapter.

The amount of numerical work entailed to solve the equation of motion is substantial, and the efficiency of the computational technique employed is of considerable practical importance. Some methods are faster per time step, but require smaller steps for similar accuracy. A good compromise has to be found to minimize the computer time, including generation of the load function, to evaluate the response per period with sufficient accuracy.

well known Runge-Kutta method, are often employed. The Runge-Kutta method is also used for this study, and is discussed at greater length below.

4.3.1 Predictor-corrector Methods

In structural dynamics, methods from the category designated as "predictor-corrector" are most often used. These include the well known Newmark's β method [Chan and Newmark, 1952; Newmark 1959; Tung and Newmark, 1954], which are "single-point" methods as summarized by Humar and Wright [1974]. Single point methods only make use of one previous point in evaluating the dependent variable at a successive location. Newmark's method can be described by the following equations:

$$\dot{y}_{i+1} = \dot{y}_i + \frac{h}{2}(\ddot{y}_i + \ddot{y}_{i+1}) \qquad (4.2a)$$

$$y_{i+1} = y_i + h\,\dot{y}_i + h^2\,\ddot{y}_i\,(\tfrac{1}{2} - \beta) + h^2\,\beta\,\ddot{y}_{i+1} \qquad (4.2b)$$

where y is the response, and the time derivatives are velocity and acceleration

h is the time step increment

β is an arbitrary parameter, chosen i.e. to represent a low order polynomial exactly

Common values used for β are 0, 1/4, 1/6 and 1/8. Using $\beta = 1/6$ gives Newmark's linear acceleration formula:

$$y_{i+1} = y_i + h\,\dot{y}_i + \frac{h^2}{3}\ddot{y}_i + \frac{h^2}{6}\ddot{y}_{i+1} \qquad (4.3)$$

Note that these equations require a value for the acceleration at the next time step for

(4.3) is obtained by setting $\ddot{y}_{i+1} = \ddot{y}_i$

$$y^p_{i+1} = y_i + h\,\dot{y}_i + \frac{h^2}{2}\,\ddot{y}_i \qquad (4.4)$$

The method is stable for $h\omega < \sqrt{12}$, ω being the natural frequency, [Newmark, 1959], and has truncation error terms for displacements of the order of $-\frac{h^4}{24}\,y^{(4)}(\theta)$, where the superscript indicates differentiation with respect to time, t, and θ represents an unknown value of t located in the range $t_i \leq \theta \leq t_{i+1}$ [Humar and Wright, 1974].

Multi-point formulae, which make use of more than one previous point in evaluating the dependent variable have been shown to give an improvement in the accuracy of the solution [Humar and Wright, 1974]. Caution is advised in order to avoid instabilities. The following formulae is stable for $\omega^2 h^2 < 6$.

$$y_{i+1} = -y_{i-1} + 2y_i + \frac{h^2}{12}\,(\ddot{y}_{i-1} + 10\,\ddot{y}_i + \ddot{y}_{i+1}) \qquad (4.5)$$

which has an error term of the order $-\frac{h^6}{240}\,y^{(6)}(\theta)$ where $t_{i-1} \leq \theta \leq t_{i+1}$. This equation has been also previously presented by Hamming [1962].

More general methods, allowing for adjustable step sizes etc. can be most efficient. The efficiency of modern methods have been compared in a comprehensive paper by Hull et al [1972]. An extremely efficient method, based on Adams predictor-corrector formulae, has been presented by Gear [1971a], including the algorithm in Fortran code [Gear, 1971b] This algorithm is self starting and adjusts both for the order (up to seven) and the mesh size to produce the desired local truncation error level. Another method by Bulirsch and Stoer [1966], based on Richardson extrapolation techniques, has been shown to be capable of producing accuracy comparable to other methods, while using step sizes which are much larger than those required by conventional methods.

4.3.2 The Runge-Kutta Method

Direct calculation of the dependent variable at the next time step has been described by Runge [1895] and elaborated by Kutta [1901]. The Runge-Kutta method is well documented, i.e. Hamming [1962] Norris et al [1959] or Wang [1966]. A summary of the equations is given:

Consider the equation:

$$m\frac{d^2y}{dt^2} + c\frac{dy}{dt} + ky = P(t) \qquad (4.6)$$

This can be rewritten into two simultaneous equations:

$$y_1 = \frac{dy}{dt} \qquad (4.7a)$$

$$\frac{dy_1}{dt} = f(t,y,y_1) = \frac{P(t)}{m} - \frac{c}{m}y_1 - \frac{k}{m}y \qquad (4.7b)$$

starting at t_i, y_i, y_{1_i} at each time step the increments in y and y_1 for the next time step, t_i+h can be computed as follows:

t	y	$y_1 = \frac{dy}{dt}$	$f = \frac{dy_1}{dt} = \frac{d^2y}{dt}$
$T_1 = t_i$	$Y_1 = y_i$	$Yl_1 = y_{1_i}$	$F_1 = f(T_1, Yl_1, Y_1)$
$T_2 = t_i + \frac{h}{2}$	$Y_2 = y_i + Yl_1\frac{h}{2}$	$Yl_2 = y_{1_i} + F_1\frac{h}{2}$	$F_2 = f(T_2, Yl_2, Y_2)$
$T_3 = t_i + \frac{h}{2}$	$Y_3 = y_i + Yl_2\frac{h}{2}$	$Yl_3 = y_{1_i} + F_2\frac{h}{2}$	$F_3 = f(T_3, Yl_3, Y_3)$
$T_4 = t_i + h$	$Y_4 = y_i + Yl_3 h$	$Yl_4 = y_{1_i} + F_3 h$	$F_4 = f(T_4, Yl_4, Y_4)$

These quantities are then used in the following recurrence formula:

$$y_{i+1} = y_i + \frac{h}{6}(Y1_1 + 2Y1_2 + 2Y1_3 + Y1_4) \qquad (4.8a)$$

$$y_{1\,i+1} = y_{1\,i} + \frac{h}{6}(F_1 + 2F_2 + 2F_3 + F_4) \qquad (4.8b)$$

Note that the algorithm is self starting.

An efficient code of the above equations which can be directly placed in a Fortran program is shown in Fig. 4.3. In nonlinear problems the constants have to be reset before each pass, in linear problems they can be initialized at the start of the program.

The accuracy of the solution by the Runge-Kutta method depends, like the other methods described above, on the step size h chosen. The local truncation error is of the order h^5, but the exact value of the error cannot be determined. Merluzzi and Brosilow [1978] describe methods with built-in estimates of the accumulated truncation error without increasing the computation per step significantly.

Tests were done to evaluate the local error using the algorithm shown Fig. 4.3 for typical dynamics problems. Referring to the maximum response values, 10 time steps per period of the fundamental mode gave roughly 1% truncation error. Decreasing the time step to 25 steps per period resulted in errors of approximately 0.01%. Naturally the error also depends on the force function. No firm error estimates can be given, but empirical evidence suggests approximately 15 time steps per period, with 10 being a minimum value. Note that each time step requires two force values; one in the middle of the interval and one at the end.

4.3.3 Discussion

The choice of integration algorithm is based on a compromise of advantages and dis-

```
C     THE FOLLOWING STATEMENTS ARE EFFICIENT TO EVALUATE THE 2ND ORDER DIFFERENTIAL
C     EQUATION OF MOTION:  Y''=FORCE/MASS-DAMPING/MASS*Y'-STIFFN/MASS*Y
C     BY THE RUNGE-KUTTA METHOD IN A FORTRAN PROGRAM
C
C     P=FORCE/MASS,  DAMP=DAMPING/MASS,  SI=STIFFNESS/MASS,  Y=DISPLACEMENT(OR ROTATION)
C     P, DAMP, SI  HAVE TO BE SET BEFORE EACH PASS THROUGH THE STATEMENTS BELOW
C     AND CAN BE AS A FUNCTION OF Y ETC.
C
C     THE STATEMENTS BELOW HAVE TO BE INITIALIZED BEFORE THE FIRST PASS ONLY
C     Y=SSY=INITIAL Y, Y1=SY1=P1=INITIAL Y',  ICT=ARRAY INDEX FOR FIRST LOAD,
C     H=TIME STEP (2 FORCES NEEDED PER TIME STEP),  H2=H/2,  H6=H/6
C
      P2=P(ICT)-DAMP*Y1-Y*SI
      Y=Y+H2*Y1
      Y1=Y1+H2*P2
      Y2=P(ICT+1)-DAMP*Y1-Y*SI
      P2=P2+Y2+Y2
      P1=P1+Y1+Y1
      Y=SSY+H2*Y1
      Y1=SY1+H2*Y2
      Y2=P(ICT+1)-DAMP*Y1-Y*SI
      P2=P2+Y2+Y2
      P1=P1+Y1+Y1
      Y=SSY+H*Y1
      Y1=SY1+H*Y2
      ICT=ICT+2
      Y2=P(ICT)-DAMP*Y1-Y*SI
      Y=SSY+(P1+Y1)*H6   <-- Y AT NEXT FULL TIME STEP
      SSY=Y
      Y1=SY1+(P2+Y2)*H6
      SY1=Y1
      P1=Y1
C
C     EACH PASS THROUGH THE ABOVE STATEMENTS EVALUATES THE RESPONSE FOR ONE TIME STEP
```

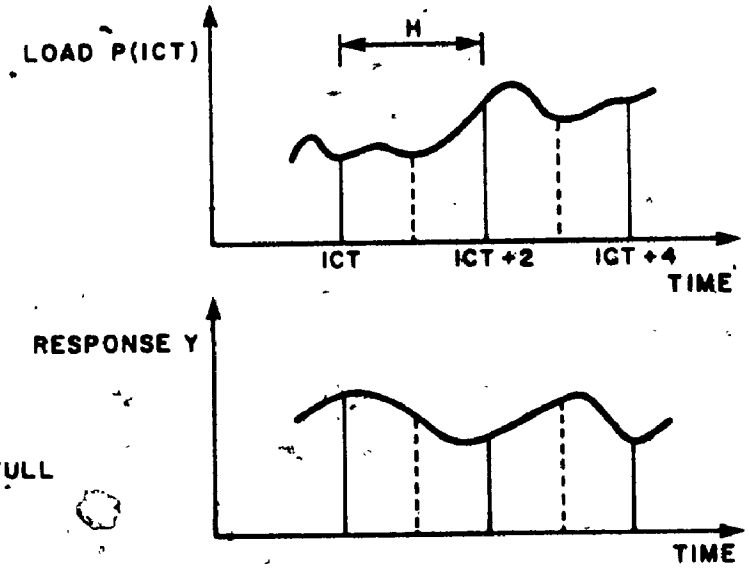

FIG. 4.3 RUNGE–KUTTA FORTRAN STATEMENTS

advantages of the available methods. Desirable attributes are: 1) Computation speed (say per period of vibration, including load generation and modification of structural parameters for nonlinear problems), 2) easy implementation, small computer core requirements, 3) equal time step increments, and 4) self starting. The predictor-corrector algorithms are considered to be the fastest methods, but they require more steps per period than the Runge-Kutta method, and are in general not self starting. Hence, they would require a different algorithm to start the integration, i.e. the Runge-Kutta method. The relative computation speeds of the above mentioned algorithms change with the demanded accuracy. The Runge-Kutta method is best with fairly large tolerances. The algorithm in Fig. 4.3 is efficiently coded, and results in good computation speeds. It is easy to implement if the execution speed is acceptable. The only disadvantage is that local error estimates are difficult to obtain.

The methods of Gear [1971b] and Bulirsch and Stoer [1966] are included in the discussion, because they represent the state of the art. They are, however more applicable for continuous functions and for high accuracy requirements. The computer core requirements are considerably higher than for the other, more simple methods, previously described.

The Runge-Kutta Method represents an acceptable compromise for the simulation studies in this chapter, and is used for all response evaluations. Figure 4.4 shows a typical numerically generated forcing function using an *AR(2)* process on the top, and the corresponding structural response evaluated by the Runge-Kutta method is shown on the bottom. The force is broad band, without any apparent periodicity, but the response is typical narrow band, with most of the energy concentrated near the natural frequency of the structures.

4.4 STRUCTURAL PROPERTIES AND BASIC ASSUMPTIONS FOR NONLINEAR RESPONSE PREDICTIONS

4.4.1 Structural Properties

3

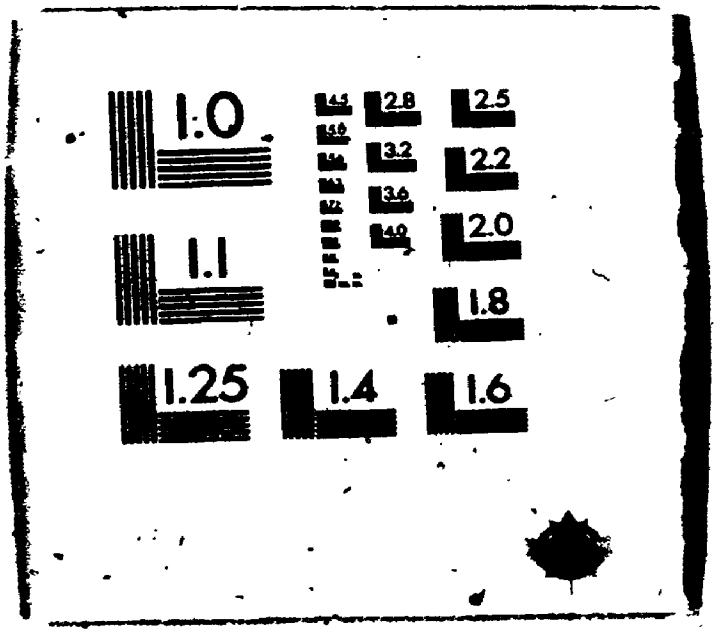

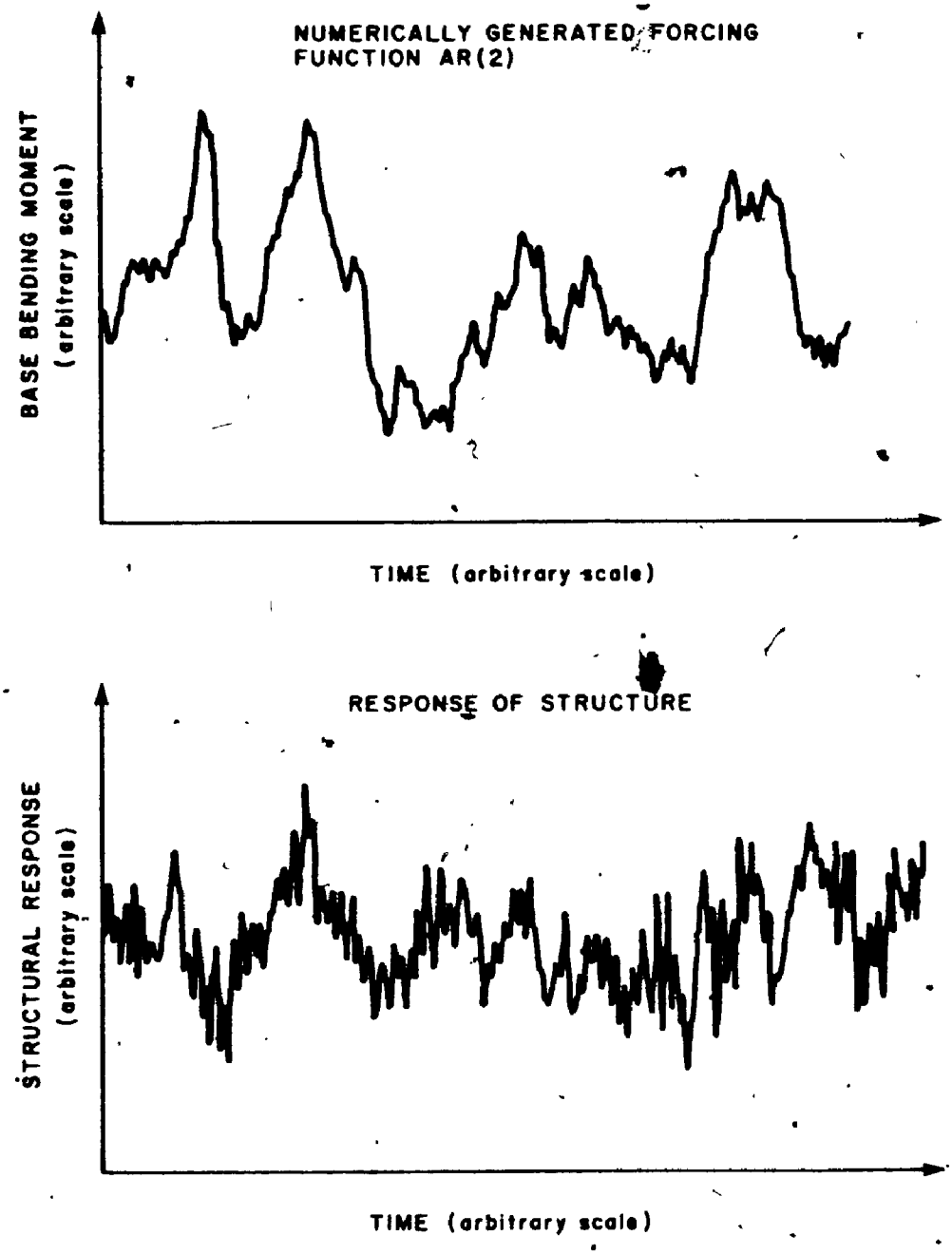

FIG. 4.4 SIMULATED FORCING FUNCTION AND STRUCTURAL RESPONSE

The fact that structural properties change for large displacements is described in Section 4.2. The increase of 55 percent in the fundamental period of Fig. 4.2 suggests that the stiffness decreased to less than half of the original value. Implicit in the development of any nonlinear vibration model are assumptions associated with the behaviour of the material.

Much research has been done on the local nonlinear behaviour of individual joints. The survey paper of Lee [1974] lists some 200 references associated with the investigation and application of dynamic plasticity. The force-deformation relationship can be reliably predicted for steel reinforced concrete, or prestressed concrete for beam column joints [Thompson and Park, 1980]. The Ramberg-Osgoode type function shown in Fig. 4.5 is well known.

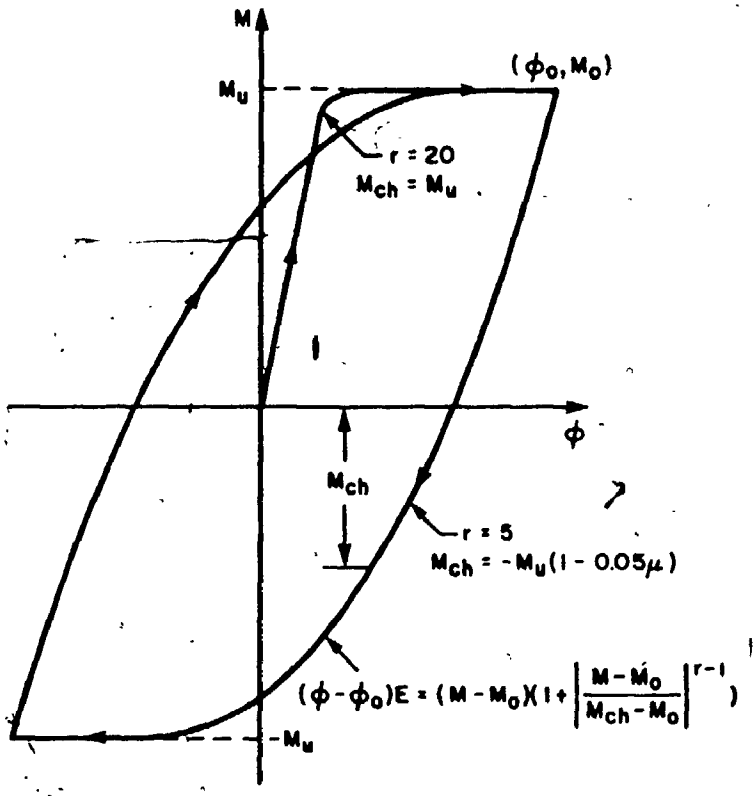

FIG. 4.5 THE RAMBERG–OSGOODE FUNCTION FOR CYCLIC LOADING [after Thompson and Park, 1980]

Little information has been published for complete building frames deforming primarily according to the fundamental mode shapes. It can be assumed that the partition walls would initially contribute to the stiffness, but during large vibrations their effect would be diminished, for instance at a deformation of $\Delta H/500$. At a large deformation, for example

at $\Delta H/100$, the restoring force would not increase any further, or at most at smaller rates than at small displacements. The unloading from a plastic state is usually assumed to change only the elastic state. A typical bilinear force deformation curve is shown in Fig. 4.6.

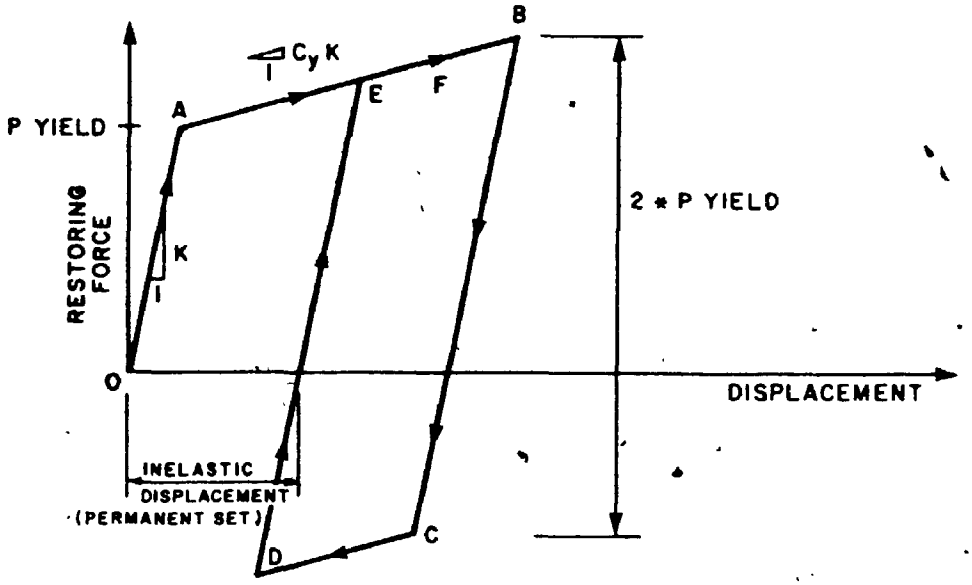

FIG. 4.6 BILINEAR FORCE–DISPLACEMENT CURVE

The initial stiffness, k, is $(2 \times \pi \times f_o)^2 M$ as described in equation (2.30d) in Section 2.14.1, where f_o is the natural frequency and M is the generalized mass. Beyond the elastic limit the restoring force only increases by an amount $Cy \times k$. When strain reversal occurs, the force-displacement curve is assumed to follow the path $BCDEF$ in which BC and DE are parallel to OA, CD parallel to AB. The computer program used in the response predictions is coded to accept up to a trilinear force displacement curve.

The damping increases after large displacements take place, compensating to some degree for the increase in response due to the reduced stiffness. Simulations are done for a wide range of damping values which show the effect of different damping properties. It is sufficiently accurate to assume the damping to be proportional to the velocity. The aim of this study is to keep the assumptions as simple as possible, but at the same time to demonstrate the usefulness of simulations and show the effect of changing parameters, such as damping changes. More complicated assumptions expand the study excessively and may not be justified.

4.4.2 Other Assumptions for Non-Linear Response Predictions

To illustrate the technique, the structures analyzed are assumed to behave as single degree of freedom systems. The degree of freedom corresponds to a straight line mode shape in the drag or shear direction. The forcing function in this case is the measured or simulated modal force.

Response is represented in a nondimensionalized form, as the ratio of the permanent set per hour, divided by an equivalent static displacement above the mean load to cause yield. This is the same convention Vickery [1970] used in his study of wind action on simple yielding structures and is shown in Fig. 4.7.

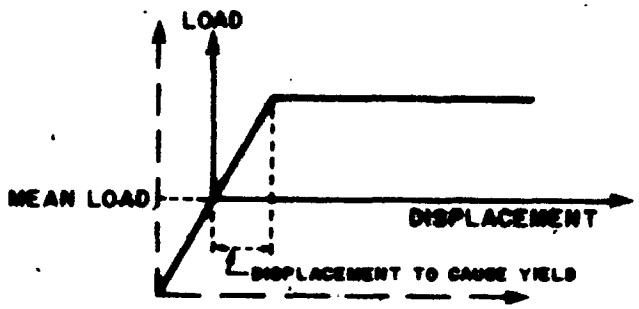

FIG. 4.7 LOAD–DISPLACEMENT CHARACTERISTICS WITH THE ORIGIN SHIFTED TO THE MEAN LOAD POSITION

Using this convention, the mean wind speed necessary to produce a given damage rate is evaluated with the additional assumption that the mean and rms wind loads are proportional to the square of the wind velocity. This is also confirmed experimentally with the BLWT balance in numerous tests. Depending on the yielding pattern of the structure, however, the modal force would not be strictly proportional to the square of the wind velocity. The effect in the predicted response is expected to be small for the investigations in this chapter. Allowing for changes of the modal forces would require assumptions to be made on the force distribution, and make the analysis considerably more complicated.

The rate of damage accumulation in the drag direction is fairly constant, and permanent sets can be computed for any given storm duration (e.g. 1 hour can be estimated). Vickery [1970] indicated that the likely duration of a strong storm to cause serious damage in the entire structure's life would be from one to two hours. The figures in

this chapter are for storms of one hour duration, during which the mean velocity was kept constant. The velocity, however, could easily be varied during the simulation studies.

4.5 SIMULATION STUDIES ON SIMPLE YIELDING STRUCTURES IN THE DRAG DIRECTION

4.5.1 Introduction

The drag direction has a substantial mean component upon which the random fluctuations are superimposed. Virtually all excursions into plastic regions are in the same direction, and the damage can be expected to accumulate at a constant rate. Vickery [1970]studied the behaviour of a simple yielding structure with analytical and numerical methods. His model can be interpreted as a building approximately 600 feet in height subject to wind loads. Approximate analytical methods are derived in Vickery's paper for the rate of development of permanent set in lightly damped systems, based essentially on the elastic behaviour of the system.

As a comparison and check of the simulation method of this chapter, a similar 567 ft. tall building is evaluated for simulated storms of 60 minutes duration. The structure is the same as used for the comparison of aeroelastic model versus force method predictions in Section 2.9.1, Fig. 2.13. The simulation uses an *AR(2)* process with the values for the parameters shown in Fig. 3.6a.

The effects of varying structural parameters are assessed in additional simulation runs. Each response value is taken from the average of 10 storms. This represents a big computational effort. Each graph represents a total central processor unit time of approximately 8 hours on the fast PDP 11/60 computer of the Boundary Layer Wind Tunnel Laboratory.

4.5.2 Basic Simulation Run and Comparisons with Vickery's Results

The structural parameters for the basic simulation run are chosen using the simplest possible models: 1) the stress-strain curve is bilinear, initial stiffness and full yield, and

2) the damping remains constant for both ranges. The results are shown in Fig. 4.8, the new simulation studies to the left and Vickery's [1970] study to the right. Even though Vickery's building has a broader face and the turbulence is different, the similarity of the results provide confidence in the validity of simulation studies

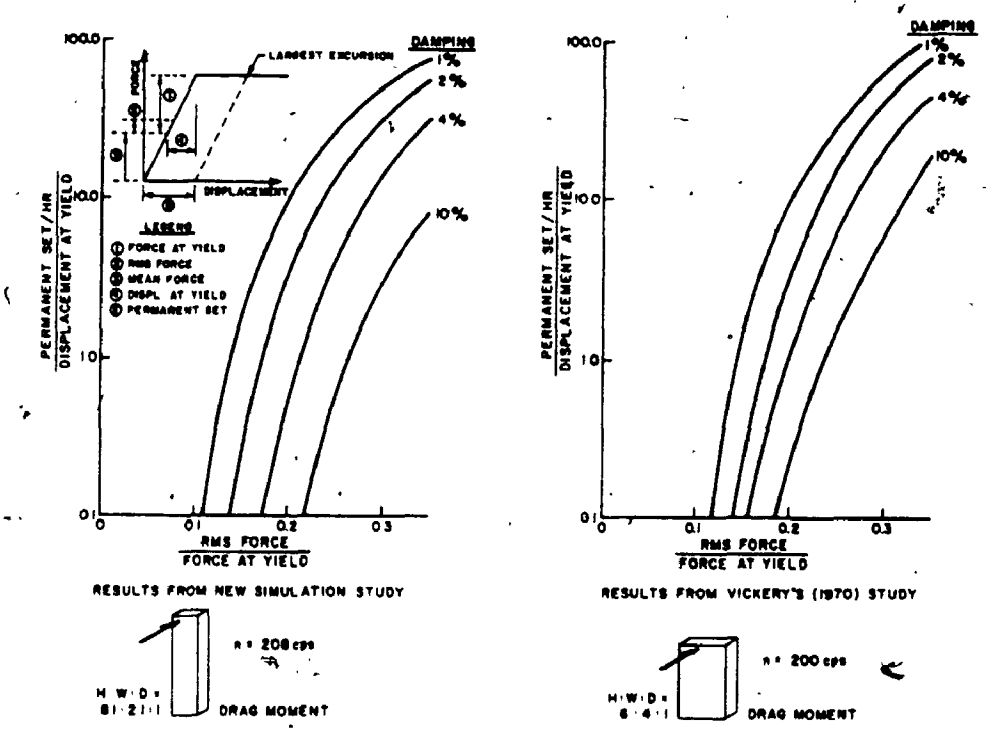

FIG. 4.8 COMPARISON OF VICKERY'S STUDY ON YIELDING STRUCTURE WITH NEW SIMULATIONS

The abscissas show the nondimensional ratio of the equivalent static response due to the RMS component to the remaining force above the mean force to the start of yielding in the structure. This value can easily be determined for a structure. The ordinates show the ratio of the permanent set per hour versus the displacement at yield, above the mean displacement. A value of less than 1.0 would probably be acceptable from a safety standpoint, a value of greater than 10 not. These criteria are approximate, for better values the ductility of the joints and location of yielding zones should be investigated.

Two important facts can be seen in Fig. 4.8:

i) the damping properties have a significant effect on the permanent set; and

ii) the curves are very steep, indicating that little reserve strength is present after a structure starts yielding due to wind loads.

Gravity loads, which were neglected for the above simulations, may decrease the safety factor even further. The curves for low damping values and large displacements are not of practical value, as the damping would increase, making the resulting curves somewhat less steep.

Similar observations as (i) and (ii) above are observed in all the drag simulation studies described below. Note, however, that the yielding-model chosen is simplistic, and should be regarded for comparative purposes only, and not in an absolute sense.

4.5.3 Basic Simulation Run for Various Wind Velocities

The results in Fig. 4.8 show that the damage increases rapidly with increasing forces. The effects from increasing the mean wind velocity is even more pronounced, the force being proportional to the velocity squared. Vickery [1970] suggested that the mean wind speed necessary to produce severe damage can be typically 20 percent greater than that necessary to just produce yielding. This is consistent with the results shown in Fig. 4.9, the abscissa showing the normalized velocity $\bar{V}_T/nD$, where $\bar{V}_T$ is the mean velocity at the top of the building, n the natural frequency of the structure and D the square root of the floor area. The ordinates are identical in all figures showing simulations for nonlinear drag response.

The structural parameters are in the simplest form: 1) a simple yielding force displacement curve, and 2) the damping is constant with the values shown for all displacement ranges. These are the same conditions as used in Section 4.5.2, and provide a basis to study effects of changing individual parameters (1) and (2).

Critical levels of damage would depend on the structural properties. In Fig. 49 it is indicated, as an initial guideline, that an ordinate value of 1.0 would cause little distress to a structure, but ratios in excess of 10 would be dangerous. The effect of the damping is to increase the velocity for the onset of damage, but the ratios with which the

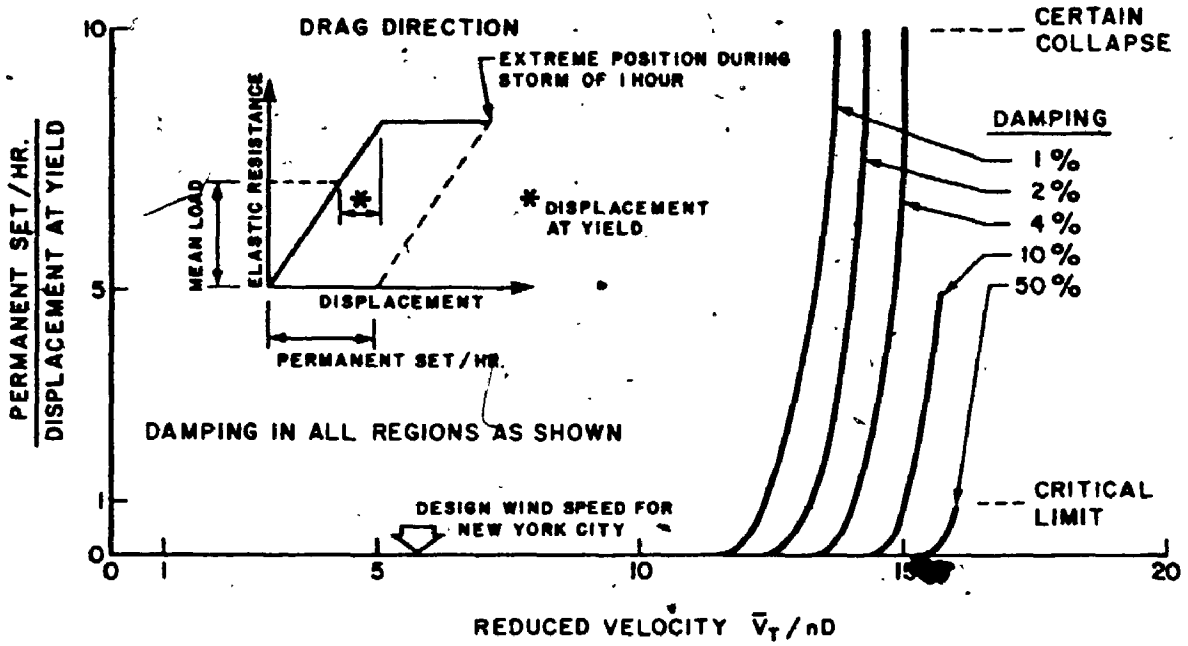

FIG. 4.9 BASIC SIMULATION IN DRAG DIRECTION OF SIMPLE YIELDING STRUCTURE FOR DIFFERENT DAMPING RATIOS

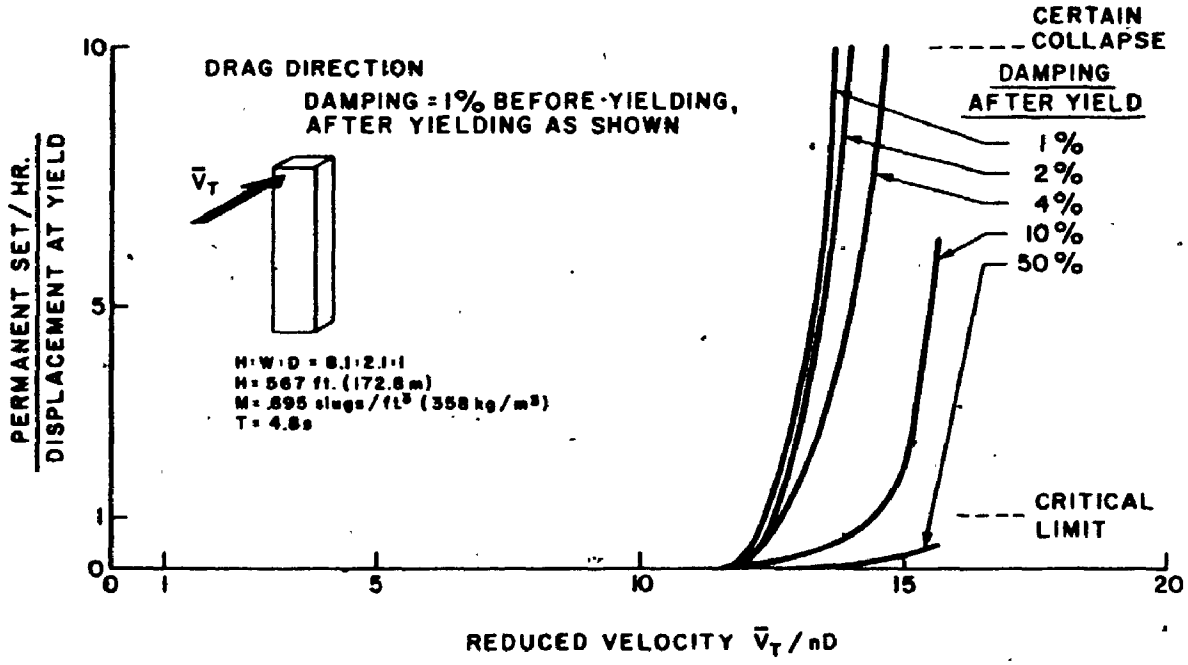

FIG. 4.10 SIMULATIONS WITH INCREASED DAMPING AFTER ONSET OF YIELDING

velocities are increased for significant damage remain largely the same. This too, is in agreement with Vickery's [1970]results.

The velocity increase for a set of 1.0 and 10.0 to the velocity of no damage in Fig. 4.9 are:

Damping	1%	2%	4%	10%
vel. ratio for set of 1.0	6%	6%	6%	6%
vel. ratio for set of 10	18%	15%	16%	

Note that the wind speeds causing damage in the above example with the chosen structural parameters are very high, roughly twice the wind speed that this structure would be designed for in a city, such as New York City, for a 100 year return period.

Wyatt and May [1971] described the ultimate load behaviour of structures from simulation studies with graphs for the expected yield per cycle. Their damage rate increases rapidly too for yield levels smaller than approximately 3 times the RMS values of the displacement greater than the mean. This is similar to the velocity required to just produce yielding.

For different ductility factors (the ratio of the largest displacement before collapse to the yield displacement) reduction coefficients could be calculated for the applied loads, similar to earthquake practise. A high ductility would reduce the design loads, but probably not as much as for earthquakes because of the long duration of the storms. This should be investigated with more extensive studies.

4.5.4 Effect of Increasing the Damping After Yielding Starts

The simulation method and step by step integration procedure described in this chapter are very flexible. Structural parameters, being numerical values, can easily be changed at each time step, depending on current displacement values, rate of deformation,

past time history, etc. As an illustration the damping is increased in Fig. 4.10 after yielding starts. From an initial value of 1.0 percent in all cases, the damping is increased to the values shown in the curves. This is an attempt to simulate a more realistic behaviour as damping is observed to increase due to cracks and slipping contact planes at large displacements. Fig. 4.10 is to be directly compared to Fig. 4.9, the only difference being that higher damping values in Fig. 4.10 only start after the system starts yielding. The 1 percent damping curve is identical in both figures. As can be expected, the onset of damage occurs at the same velocity, but the curves are flatter for higher damping values. The responses are primarily different at low damage rates. At large damage levels (or conversely at high wind speeds) the difference is small in comparison to when higher damping was present from the start.

This conclusion, that the structure has little "memory" of its initial state is important, as structures might be designed for constant damping values only, according to the conditions in the nonlinear range. This should be confirmed, however, by additional studies.

4.5.5 Trilinear Force-Displacement Relationship

The behaviour of an actual structure cannot be adequately represented by a simple yielding model as used in the examples above. In many buildings architectural finishes provide a significant source of stiffness, if not strength. This is on the whole not desirable, because the more rigid these finishes, the more resistance they "attract" and the earlier they will crack and crumble. A schematic representation of the load-drift curve is shown in Fig. 4.11.

It is difficult to estimate the degree of participation of the architectural finishes, but as an illustration of its effects, the responses are shown in Fig. 4.12 for a 10 percent reduction in stiffness at a deformation of $\Delta H/500$. The damping values indicated are used through all displacement ranges.

The permanent set can be compared with Fig. 4.9, where the conditions are identical, except that there is no reduction of stiffness assumed. The 1 percent curve from Fig. 4.9

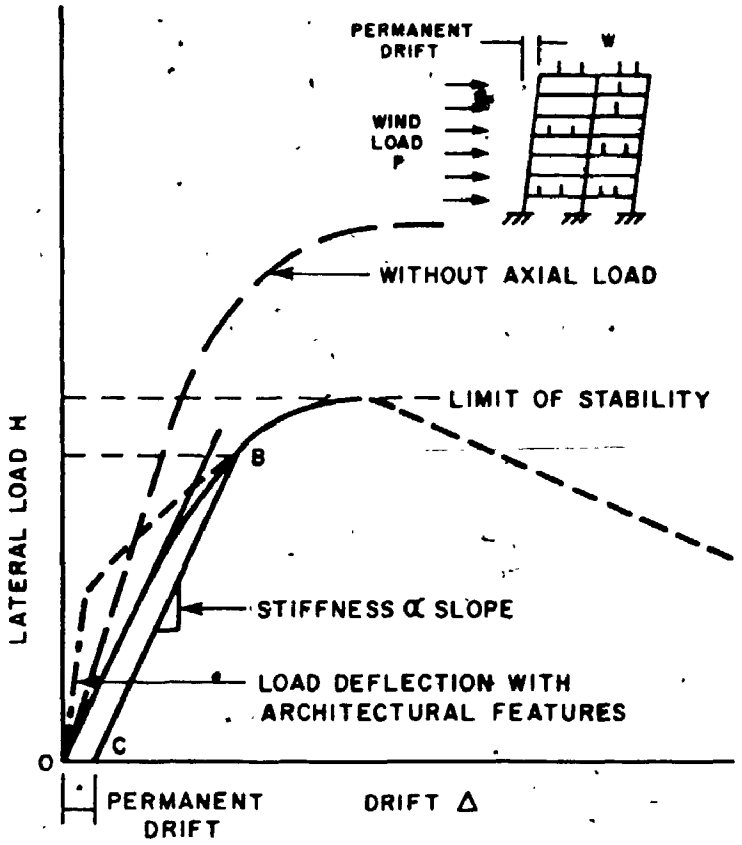

FIG. 4.11 SCHEMATIC REPRESENTATION OF FAILURE UNDER WIND ACTION [after Davenport, 1975]

is also superimposed in Fig. 4.12. The reduction in stiffness causes the curves to flatten out and the onset of damage occurs at a lower wind speed, as expected. At higher velocities, however, the effect becomes much less important, especially for higher damping values. This indicates that it may be sufficient to determine the permanent set for high velocities based on the initial conditions and the level of complete yielding. For different strain reversal curves than those shown in Fig. 46, these results might change, however, and further simulation studies are advised to confirm this simplified conclusion.

4.5.6 Stiffness Reduction Due to Gravity Effects

The resistance-displacement relationship in Fig. 4.12 can be modified to include a reduction of stiffness after serious yielding starts. This conforms to effects at large displacements due to axial dead loads. For Fig. 4.13 a reduction equivalent to 10 percent of the initial stiffness is assumed, with all the other properties identical to Fig. 4.12.

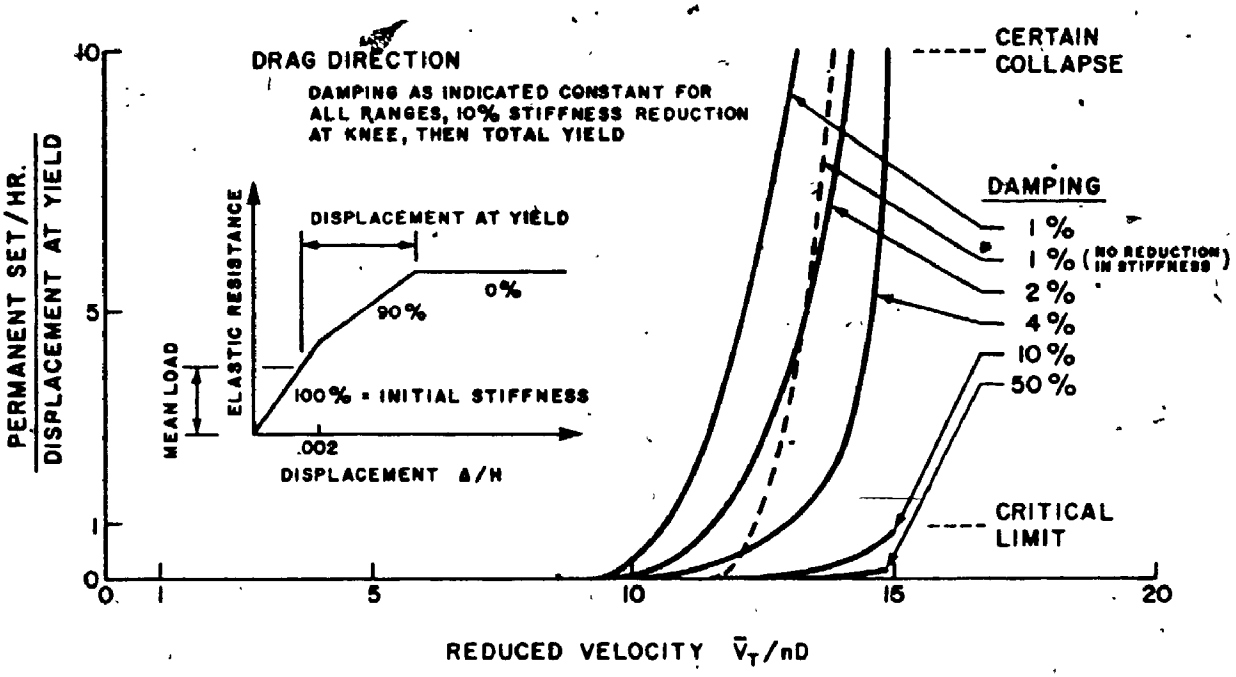

FIG. 4.12 SIMULATIONS WITH TRI–LINEAR ELASTIC RESISTANCE

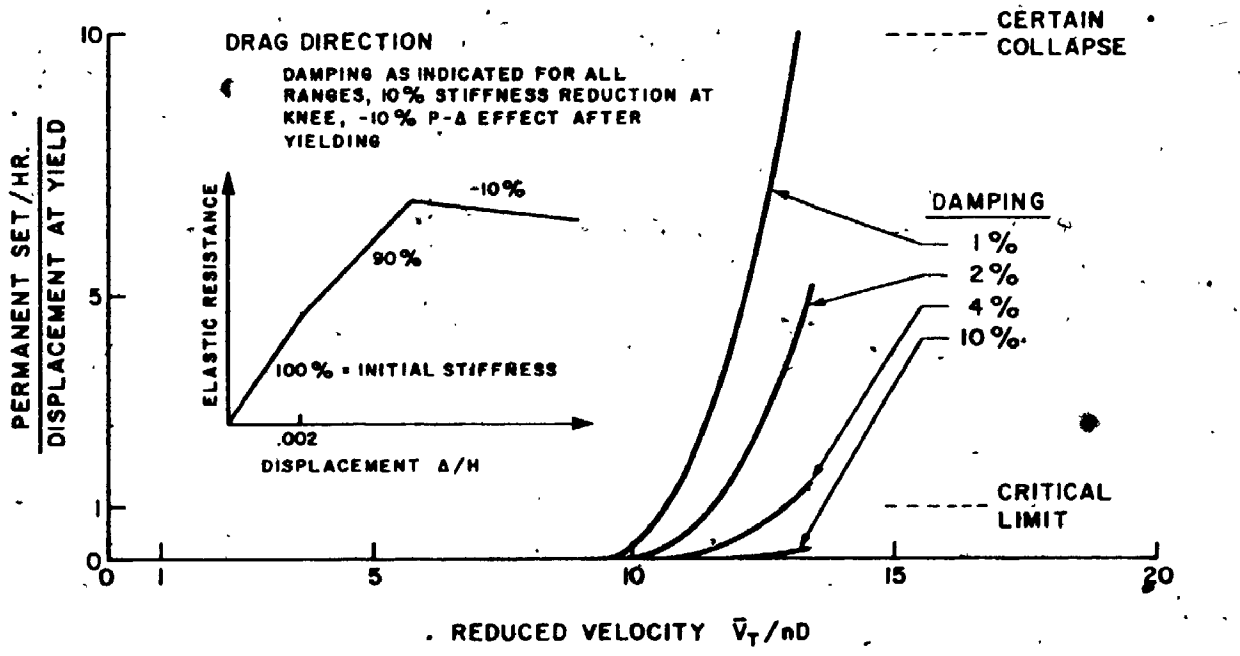

FIG. 4.13 SIMULATIONS WITH TRI–LINEAR ELASTIC RESISTANCE AND P–Δ EFFECT

The simulation shows almost exactly the same response as for a constant restoring force after yielding starts. Simulations to higher velocities would certainly show a change. The explanation for this unexpected result might be that the excursions in the reduced restoring-force range are so brief as to not affect the response at velocities corresponding to the start of critical yielding.

4.5.7 Discussion

The examples above illustrate the type of nonlinear problems which can be investigated using simulation studies for high wind speeds in the drag direction. For a realistic analysis, applied to a particular building, the elastic restoring force and changes of damping with different strain levels sho be accurately determined. This is not easily done, as discussed above, because little information is pu lished on this problem.

The most important effect is shown to be from the damping values. In addition to the structura damping is an aeroelastic damping term. This is neglected in the above simulations, but is expected t be a positive value, increasing for higher velocities. This has the effect of "flattening" the curves, i.e. to make the damage rate less sensitive to the wind speed.

The mean load in the drag loading has the effect that the yielding occurs virtually all in the same direction. Observing the steep curves in Fig. 4.8, indicates that only a small mean force is required to bias the permanent set towards one direction. Taking as an example a mean load of 20% of the load capacity of a simple yielding system, gives an abscissa value of 0.15 in Fig. 4.8 in positive direction, but a value of 0.09 towards the other direction. The former would cause significant permanent set, the latter only negligible damage.

Given that the true force-deformation behaviour and damping values for a structure for first mode normal forces is known, the techniques applied above can be expected to give much insight in the drag response of buildings at high velocities.

4.6 SIMULATION STUDIES ON A SIMPLE YIELDING STRUCTURE IN THE LIFT DIRECTION

The across wind response differs from the along wind response in having a zero, or a very small mean force component. The dynamic forcing function, however, is significant. The across wind pea response is often larger than the along wind peak response, depending on the geometric shape and terrain conditions.

Simulation studies can be carried out identically to the along wind examples described above, after the autoregressive parameters are determined by fitting the measured force spectra. The requirement of knowing the structural properties is the same as for along wind simulations, with the additional caution that the aerodynamic damping may become negative. The aerodynamic damping is discussed in Chapter II, where it is shown that the value switches from positive to negative as the wind speed is increased above the velocity where vortex shedding gives a dominant contribution to the lift force. Vortex shedding is indicated in the force spectra by bands of higher spectral energy than is present at neighbouring frequencies. If the values are known from theory or experiments, they can be incorporated in the simulation studies without difficulty by changing the numerical values for the damping parameter in the computer program.

The same building as used for the along wind simulations is used for the lift direction. The parameters for the *AR(4)* process used for simulating the load function are shown in Fig. 3.6c. The force-displacement relationship is assumed to be the simple bilinear initial stiffness to a constant value after yield, as used in the basic drag direction run, Section 4.5.3. The damping is taken to be 1% and aerodynamic effects are neglected.

The permanent set cannot be expected to occur in one direction only, as is the case for the drag response which contains a large mean force. A typical across wind simulation for a one hour storm is shown in Fig. 4.14. The top figure represents the time history of the response, which is a narrow band random process. Occassionally the response exceeds the proportional stiffness range, causing a permanent set and shifting the mean position. This shift is best noticeable in the last 10 minutes of the record.

The permanent set alone is shown in the centre figure. The ordinate is drawn at an expanded scale, the abscissa showing the time has the same scale as the figure above. This figure points out the important events and the severity of the damage. Important observations include: 1) damage accumulation occurs in both directions, 2) the pattern of excursions in the inelastic range is irregular, but does not appear to be statistically independent, i.e. two excursions in the same direction or complete strain reversal into the other direction can be observed; 3) the damage is not necessary largest at the end of a set period; and 4) the number of excursions in the inelastic range is low.

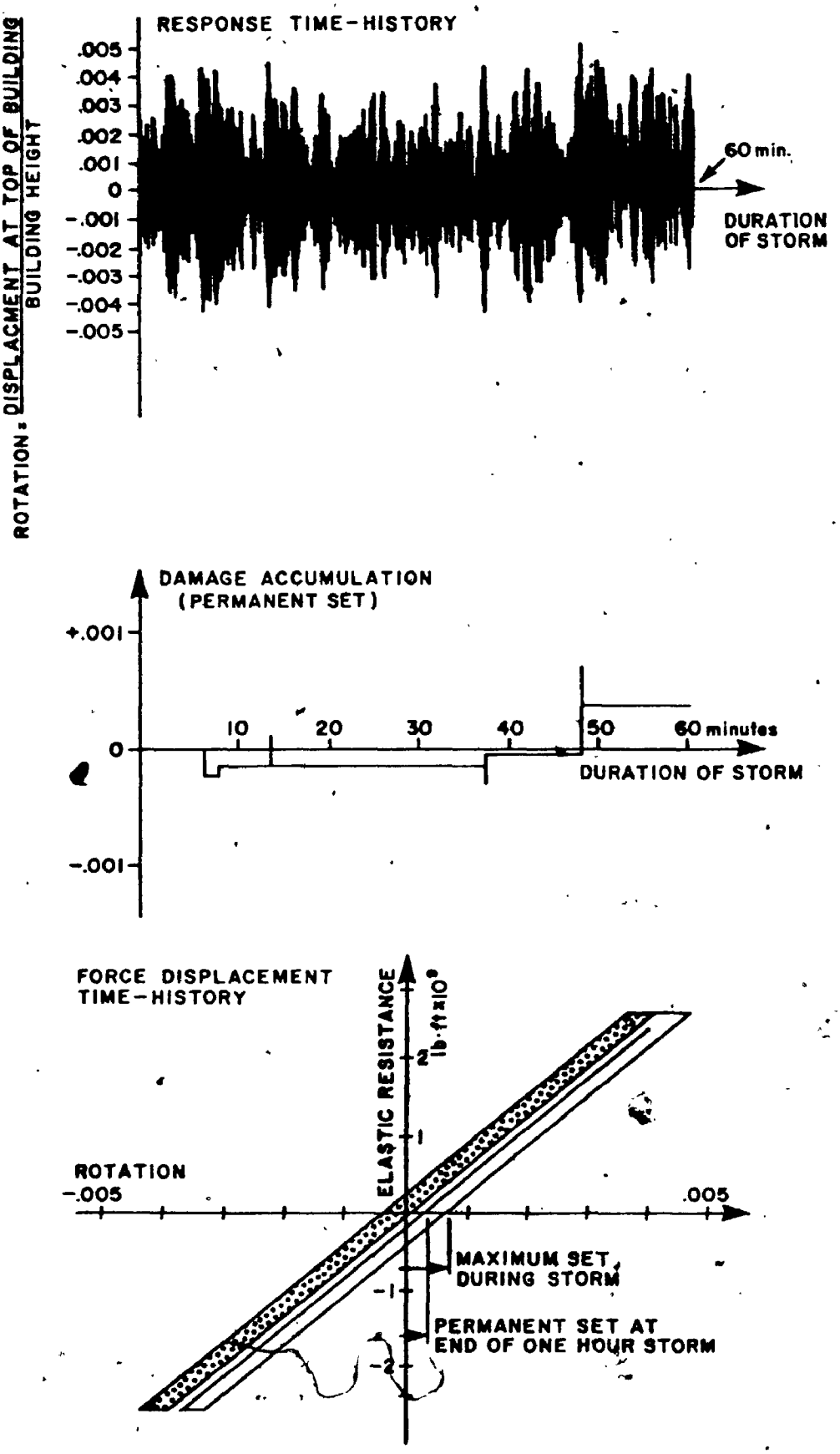

FIG. 4.14 TYPICAL ACROSS WIND SIMULATION FOR A ONE HOUR STORM

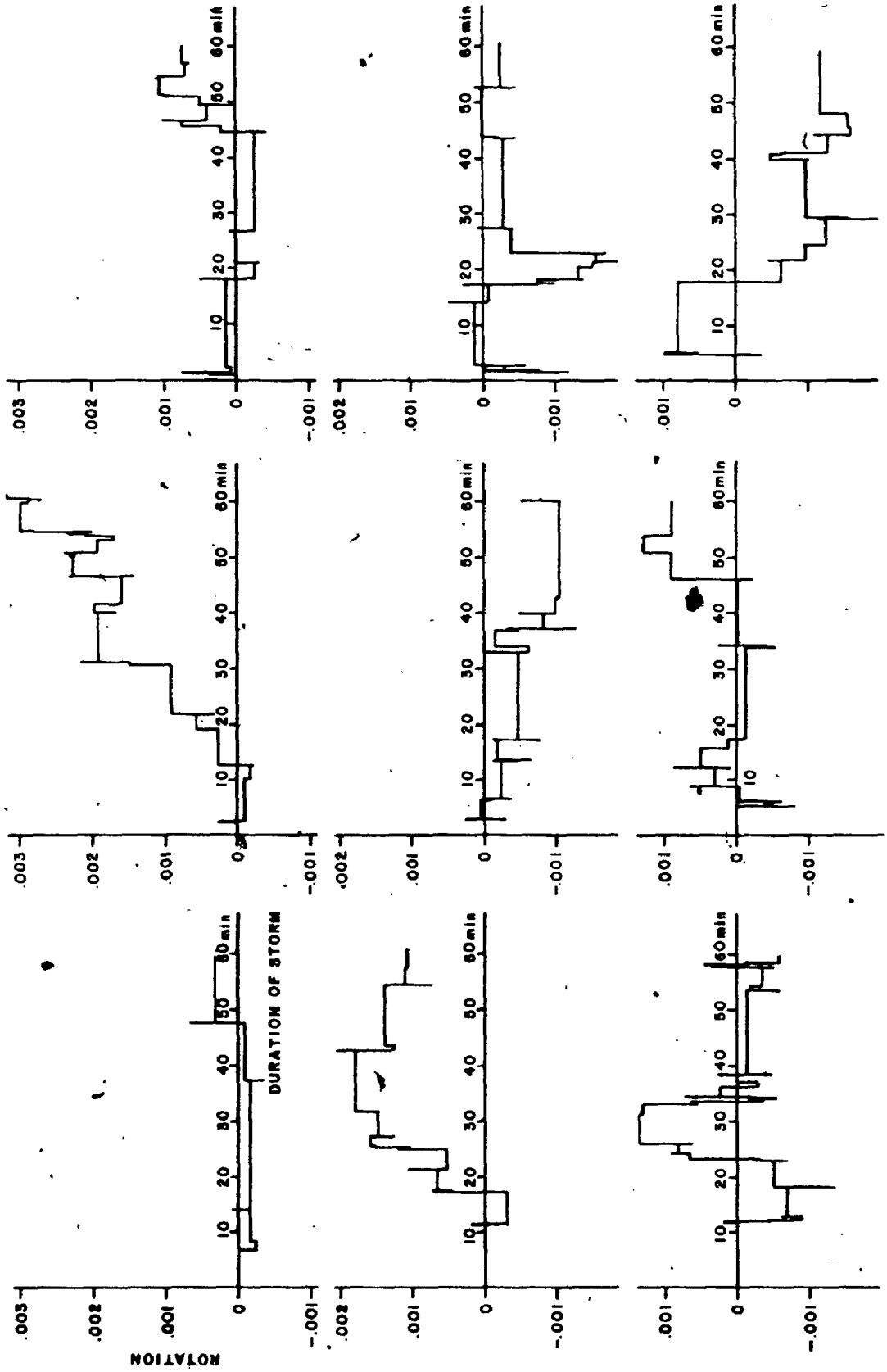

FIG. 4.15 PERMANENT SET ACCUMULATION IN THE LIFT DIRECTION FOR NINE ONE HOUR STORMS

The bottom of Fig. 4.14 shows the elastic restoring force versus the instantaneous deformation of the structure. Observations (1) to (4) from above can also be observed from this figure, but the centre figure is more generally useful. This force-displacement plot gives more insight during real time plotting than as a finished figure.

The irregular nature and small number of occurences of yielding makes statistical predictions in terms of a damage rate per time period more difficult than for along wind response predictions. Nine simulation studies with different forcing functions but with the same spectral distribution and statistical properties are shown in Fig. 4.15. The structural properties are all identical to the case use in the basic along wind simulations (Fig. 4.9). The irregular damage accumulation is clearly visible a there is no constant observable damage rate per time period. In contrast to these plots, damage rates were observed to occur at fairly constant rates in the drag direction. Perhaps a maximum set at any intermediate time during a number of one hour storms would be a more useful criteria, but as the centre figure on the top of Fig. 4.15 shows, it is possible to get a "runaway" situation or miss such a case altogether with a limited number of simulations. Another criterion might be to limit the allowa set to be a very small value only, and to consider the structure as failed if this small criterion is exce eded. Indications show that the wind speed can only marginally be increased to increase the damage significantly.

The mean and RMS absolute values of the damage rate for the nine storms are shown in Fig. 4.16. Although the sample is small, it shows a more defined trend. For small loading ranges where occasional excursions occur with equal probability in positive or negative direction, the expected damage trend is similar to a random walk problem. The distance from the original position, i.e. the permanent set, for a random walk problem grows as a square root function of time. The accumulat damage would hence grow initially fast, and grow at a lesser rate as time becomes large.

As the loading values are further increased, an excursion into the non-linear range causes severa dependent cycles of yielding and lessens the statistical independence. Furthermore, the $P-\Delta$ effects would become important and bias the permanent set towards one direction. The straight line in Fig. 4.16 is not intended to convey a linear rate of growth for a general case, but rather serve as an indication of the growth of damage for this particular example.

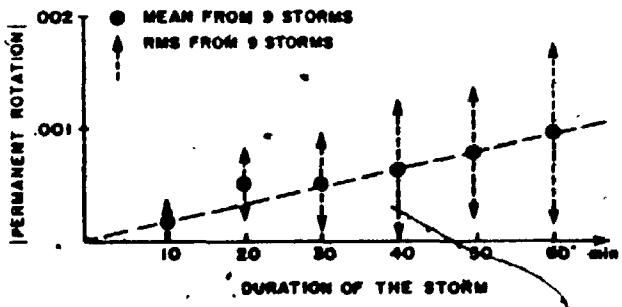

FIG. 4.16 AVERAGE DAMAGE ACCUMULATION FROM NINE STORMS IN LIFT DIRECTIO

Some of the force spectra which have sharply peaked narrow band frequency bands due to periodic forcing effects, such as vortex shedding, cannot be represented very accurately by low order autoregressive processes. For force spectra which show unacceptable fits by the AR parameters, other simulation methods may be more appropriate, such as the method by Shinozuka and Jan [1972] described in Section 3.4.2, or by superimposing a narrow band process upon a broad band process as done by Wyatt and May [1972] and described in Section 3.6.

Since the structural properties, such as the force-displacement curve, and structural and aerodynamic damping, should be well defined to make conclusive statements, across wind yielding of buildings was not pursued further here. The results in this section are presented primarily to illustrate the feasibility of the simulation studies.

4.7 SUGGESTED EXTENSIONS TO THE NONLINEAR BEHAVIOUR STUDIES

Some areas of the analysis presented in this chapter could be studied further, especially: (1) more realistic models of the force-displacement behaviour; (2) yielding occurring at selected levels only for multi-storey buildings, rather than more or less uniformly to preserve the mode shape as was assumed here; and (3) better fits for some of the force spectra exhibiting narrow band excitation.

To find models for yielding at intermediate storeys it would be necessary to know the load distribution. For this it might be necessary to use information from both moment and shear measurements, similar to the suggestion for estimating the contribution from higher mode shapes in Chapter II.

An important effect would probably be the multi-dimensional response of a building. All members, especially corner columns, are stressed from a combination of drag, lift and torsional forces. Partially correlated forcing functions can be simulated as described in Section 3.10, but correlations of the forces for different degrees-of-freedom at higher frequencies were measured to be extremely small. More correlation might be expected

between torsional and lift forces at the frequencies where vortex shedding is important. For most cases, however, it might be sufficient to generate the forcing functions independently for each direction.

Simple models are quired to study the response of three-dimensional response of a building. One approach is to determine the strength interaction surfaces as described by Zimmerli and Thurlimann [1979]. The strength surface encloses the "safe" values of the two lateral forces and of torsion, if these forces are shown as vectors in a three-dimensional spaee. Outside this surface the structure deforms rapidly without increasing the force, indicating collapse. According to the concept of nonlinear response discussed in this chapter, this surface could simply set the proportional limit for the restoring force. For short excursions outside this limit, the elastic restoring forces would not increase any further.

The actual shape of these strength interaction surfaces is complicated and laborious to compute but Zimmerli and Thürlimann [1979] described a simplified shape, such as shown in Fig. 4.17, which may be acceptable in many cases.

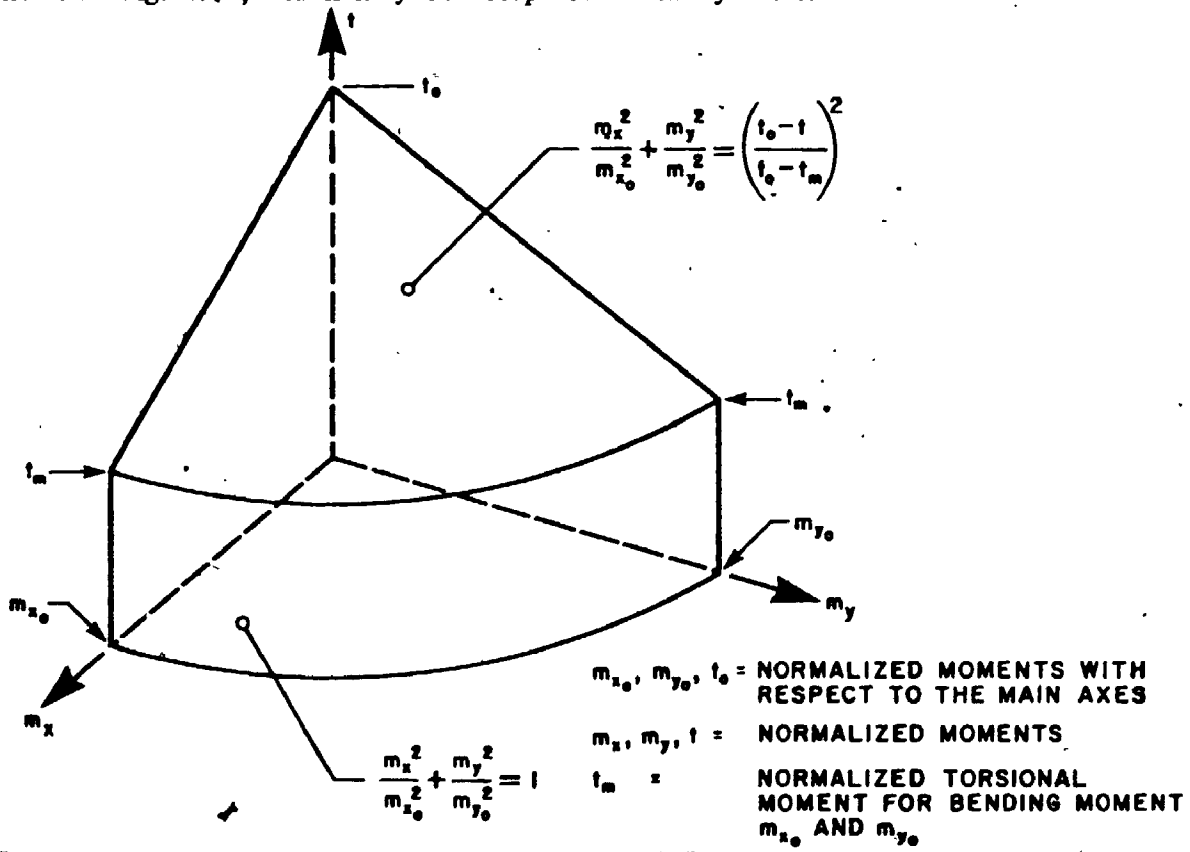

FIG. 4.17 APPROXIMATION OF STRENGTH SURFACE FOR COMBINED LOADING ACTION [after Zimmerli and Thürlimann, 1979]

4.8 SUMMARY OF NONLINEAR BUILDING RESPONSE SIMULATIONS

The nonlinear behaviour of structures is considered to be more difficult to solve than for linear systems. Methods based on superposition principles, i.e. normal mode analysis and frequency domain analysis are not applicable.

Step by step integration methods are compared to solve the dynamic equation of motion in the time domain. An efficient computer algorithm for the Runge-Kutta Method is presented. Because of the ease of its use and good accuracy, it is chosen to evaluate the response for all simulations in this chapter.

Implicit in the development of nonlinear vibration models are assumptions associated with the behaviour of the material. The need for more information on the force-displacement relationship and damping values is emphasized, but suitable assumptions are taken to analyse a typical tall building.

The yielding in the drag direction gives much insight in the behaviour of nonlinear structures. Most important is the damping value, which is shown to dominate the damage rate according to its value in the nonlinear range. The damage is shown to increase rapidly with increasing wind speed, after the onset of permanent displacements.

The yielding in the across wind direction is more difficult to categorize. It is much more irregular in direction and magnitude than for drag responses, and is often larger at intermediate times than at the end of a storm. Further investigations may clarify criteria to be used for yielding in the lift direction.

The feasibility of simulation studies is shown, and the information presented in this work enables other researchers to do more extensive studies, with only the aid of a fast digital computer. These can be applied to specific buildings or to general parameter studies. Suggestions to extend the study for combined loading cases are given.

CONCLUSIONS

This study described an approach to the direct measurement of total dynamic wind forces and applications in response predictions, wind force simulations, and nonlinear behaviour investigations of structures.

The proposed method to measure forces is based on a high frequency balance-model system, essentially having a "flat" frequency response for the range where the wind has sufficient energy to contribute significantly to the response. The models can be fabricated simply from dense lightweight foam by cutting it to the required shape. The balance, however, has to be well designed to optimize the contradictory requirements of high sensitivity and high rigidity for good frequency response. The five-component balance is believed to be the state of the art for the intended range of forces. (Higher loads allow for more flexibility in design because of larger physical sizes.) The final design and possible alternative solutions for different load ranges have been described in detail.

A practical application for dynamic force measurements is simplified response predictions for linear structures. Modal forces are dependent only on the structure shape and not on the dynamic structural properties. This is advantageous, as structural properties may change during the design, and revised response predictions can readily be made. The structural response is related to the modal force by a simple mechanical transfer function. Some attention has to be given to aerodynamic damping and the non-conservative torsion force measurements. These effects are also discussed. Comparisons of the proposed force method with conventional aeroelastic tests and the National Building Code of Canada confirmed that the direct measurement of dynamic forces is a

useful alternative to more expensive aeroelastic model tests. Approaches by other investigators in modal force measurements were shown to be less versatile than the balance-model combination of this study, once a high performance balance is available.

For nonlinear structures it is desirable to have the wind loads defined in the time domain. Of the possible methods, such as on-line evaluation or storage in analogue or digital form on tape, it was advantageous to regenerate the time series on a digital computer using simulations. Low order autoregressive processes provided good representations to most measured load functions. A large collection of modal forces were presented in Appendix A, suitable for frequency domain (power spectrum) and time domain (time series simulation) applications.

The applicability of time series simulations of dynamic forces was shown in studies on a nonlinear structure. No tools are required besides a digital computer after the simulation parameters were determined in an initial study in the wind tunnel. Parameter studies, such as different yielding models and damping properties, demonstrated that an increase in wind speed by typically 20 percent from that required to just produce yielding causes serious damage. The importance of the damping, the value of which is not well known for large displacements, was also demonstrated.

The direct force measurement approach has other potential applications, such as aiding the codification of other directions than drag response. The main benefits, however are the applications for simplified experimental response predictions over other presently available methods.

APPENDIX A

MEASURED FORCE SPECTRA, FITTED FOR TIME SERIES SIMULATION

This Appendix shows measured force spectra for a selection of tested building shapes, exposures, wind directions and degrees-of-freedom. The fitted curves show estimated spectra for time series simulations using autoregressive processes. Preference was given to low order processes, permitting efficient time series generation, as well as expressing the dynamic forces in the frequency domain with few parameters.

A legend and typical description of the figures in Appendix A is given in Section 3.8 and Fig. 3.5. Autoregressive processes in general are treated in Chapter III.

Some of the spectra having energy concentrated at specific vortex shedding frequencies were not fitted well with low order processes, but they are presented with their best fit and the user can judge if the fit is acceptable for the intended application.

In proving the performance of the balance, a large number of building shapes were studied. Only some of these are specifically used in examples throughout the thesis. The remaining data are provided in this appendix for general information.

The data presented can serve as a basis for analytical studies and codification. Comparing variations of the modal load spectra for different angles, for instance, shows little variation of the shape. This is perhaps unexpected, but the collection of modal force spectra is believed to be unique and of good quality.

6:4:1	Building, Suburban
6:4:1	Building, Open Country
4:4:1	Building, Suburban
4:4;1	Building, Open Country
3.75:5.65:1	Building, Suburban
3.75:5.65:1	Building, Open Country
7:1:1	Building, Suburban
7:1:1	Building, Open Country
7:1:1	Medium Tall Building, Surburban
7:1:1	Medium Tall Building, Open Country
3:1:1	Building, Suburban
3:1:1	Building, Open Country Exposure
8.1:1.8:1	Building, Surburban .
	Empire State Building, Suburban
	Empire State Building, Suburban with Neighbouring Tall Buildings

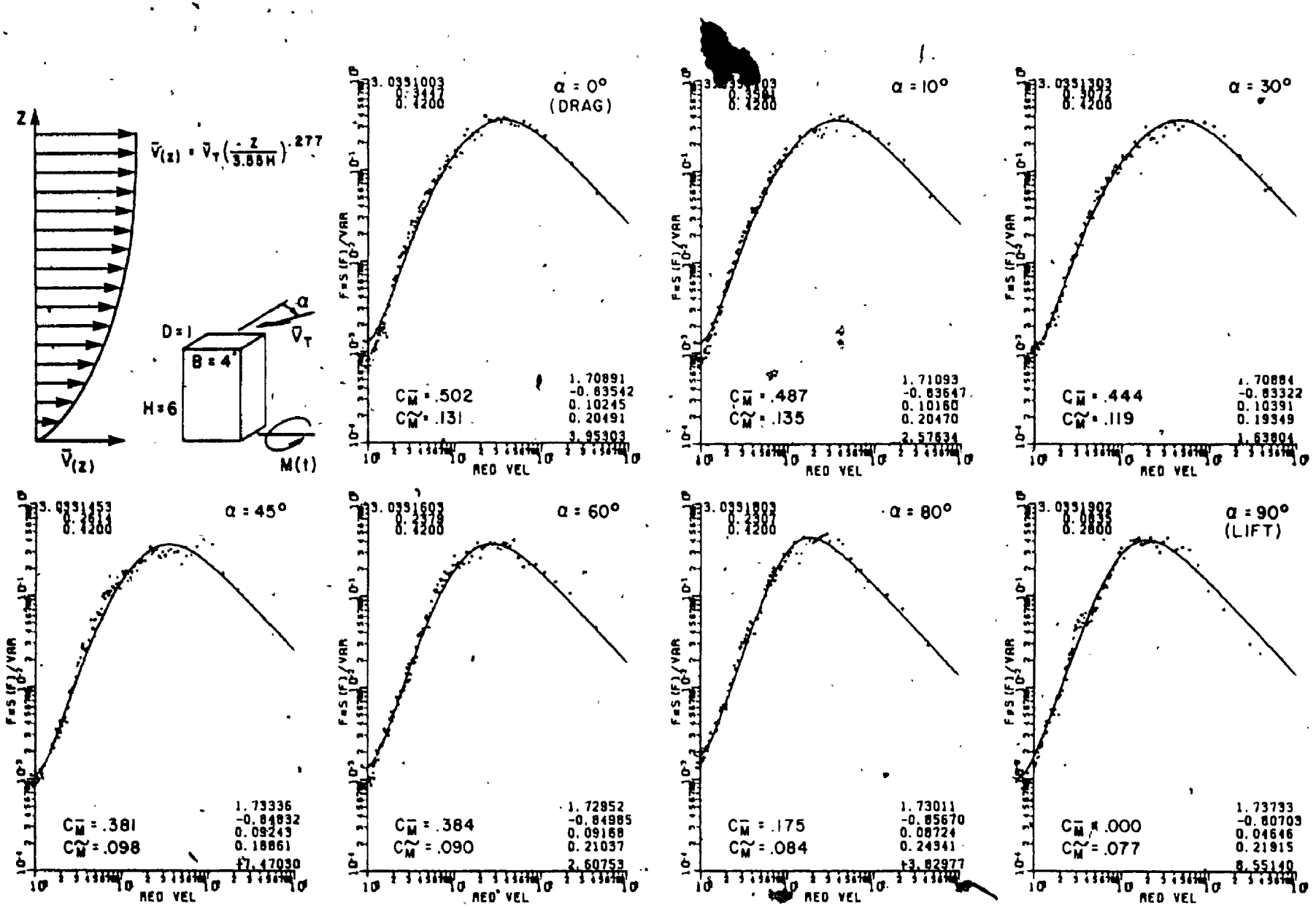

FIG. A.1 MOMENTS ON BROAD SIDE OF 6:4:1 BUILDING, SUBURBAN EXPOSURE

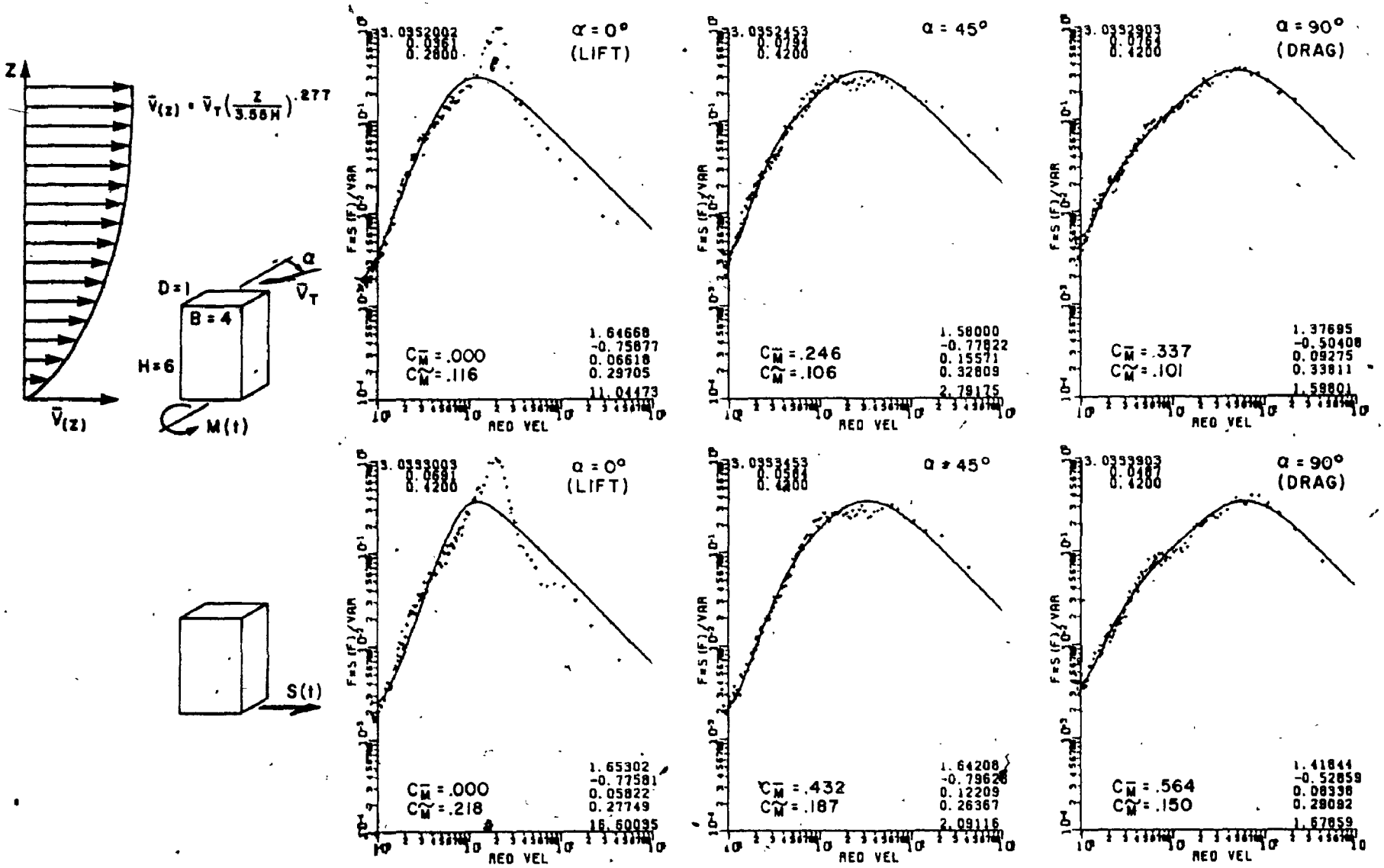

FIG. A.2 MOMENTS AND SHEARS ON NARROW SIDE OF A 6:4:1 BUILDING, SUBURBAN EXPOSURE

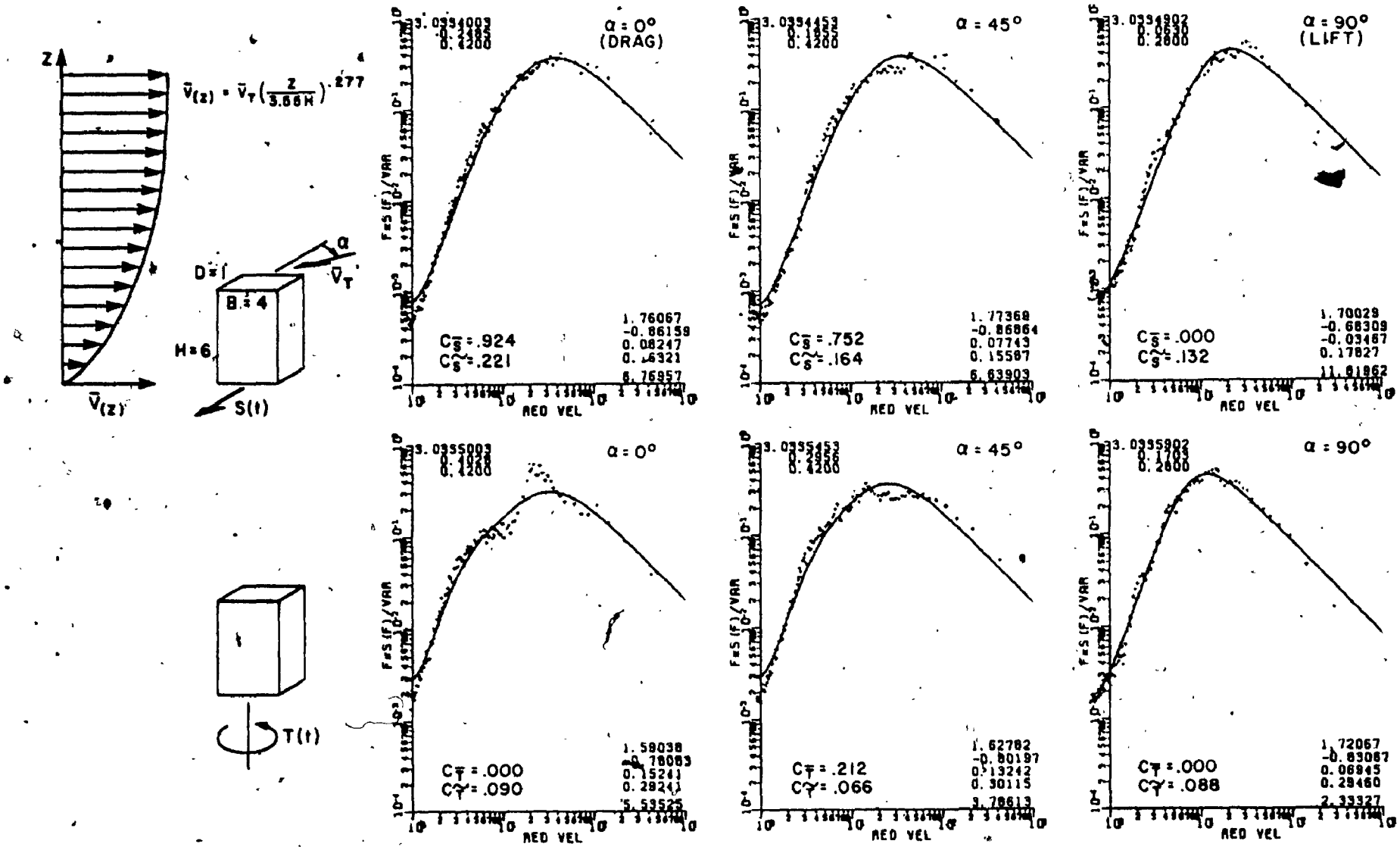

FIG. A.3 SHEARS ON A BROAD SIDE AND TORSION OF A 6:4:1 BUILDING, SUBURBAN EXPOSURE

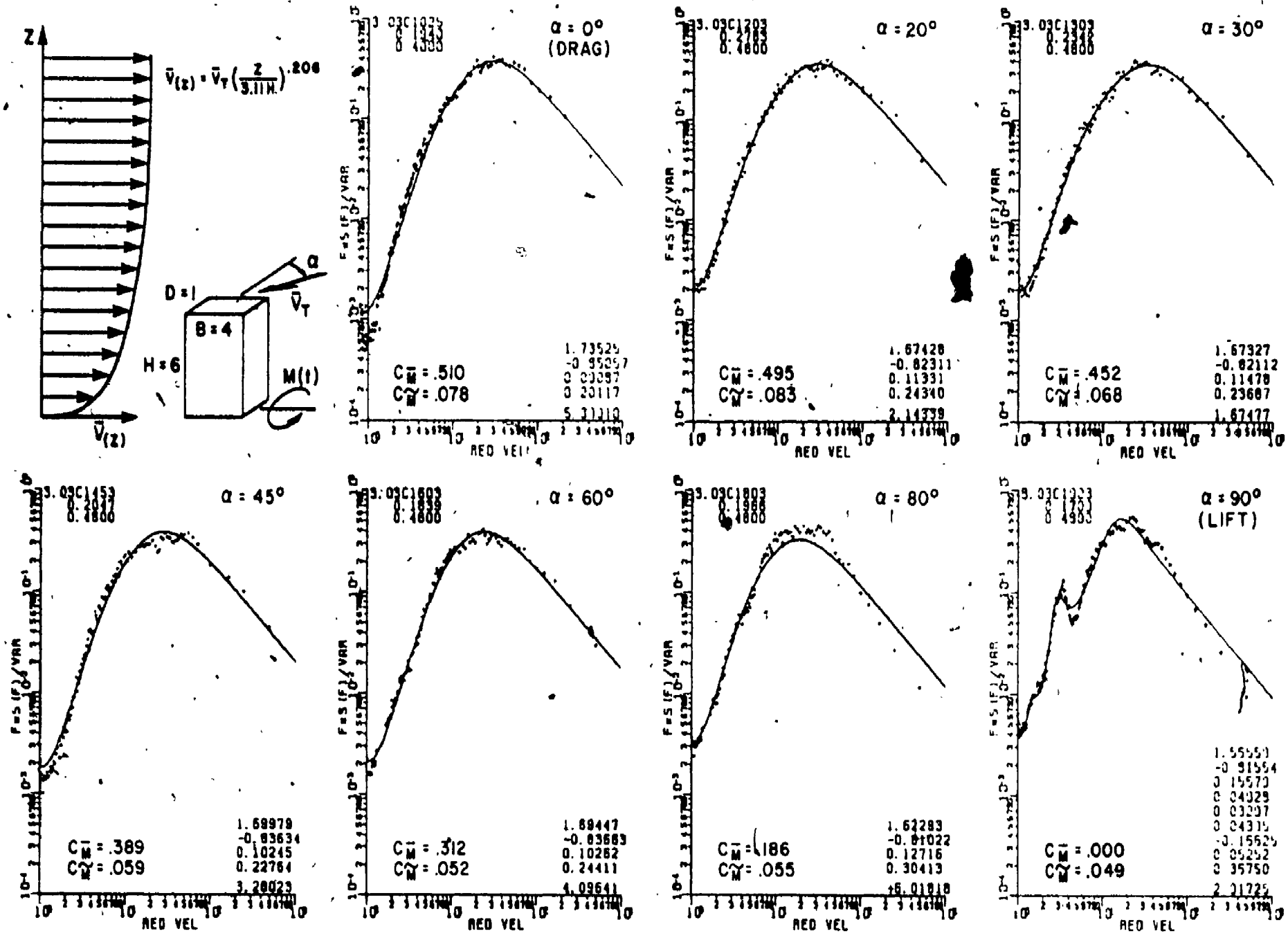

FIG. A.4 MOMENTS ON BROAD SIDE OF A 6:4:1 BUILDING, OPEN COUNTRY EXPOSURE

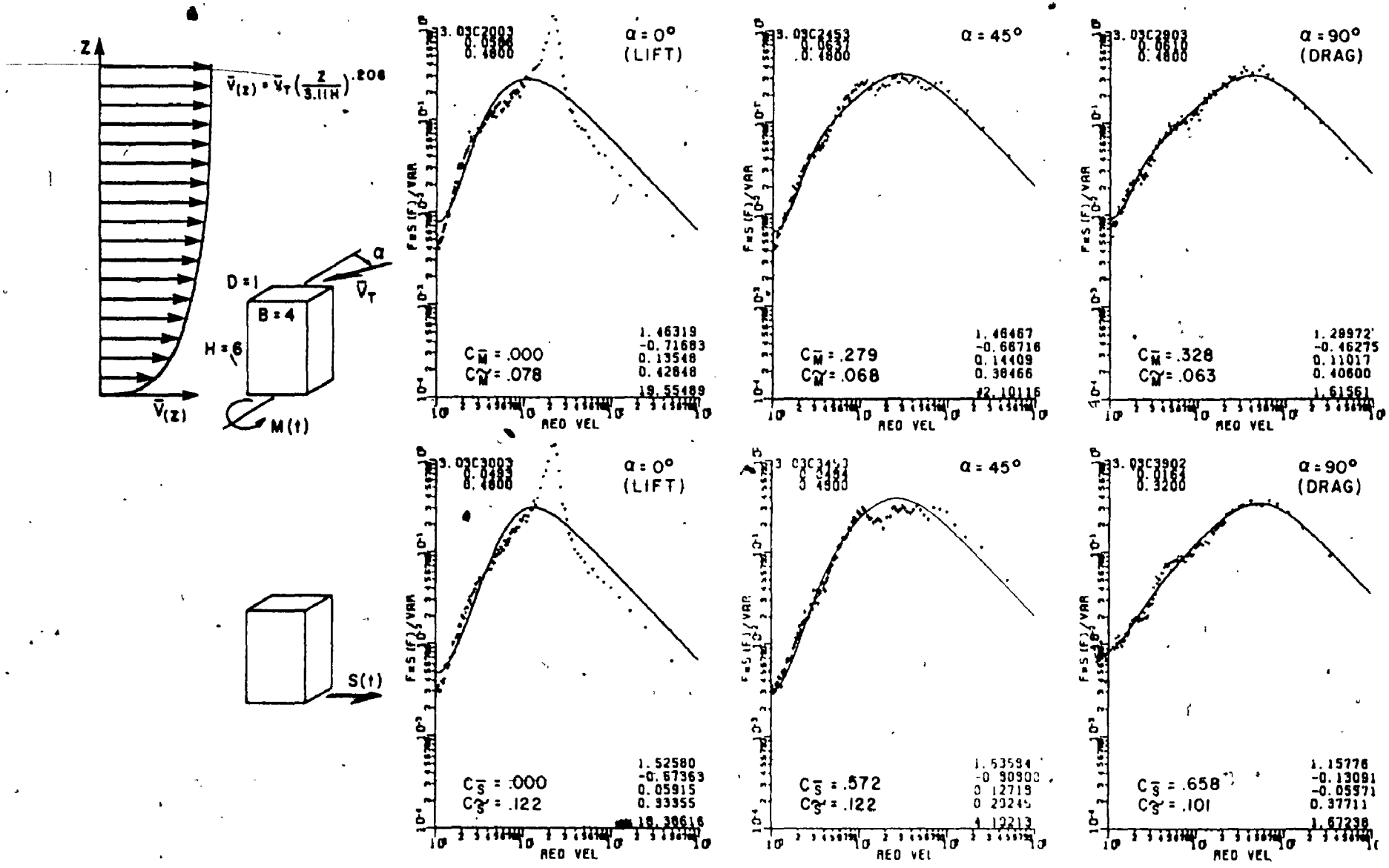

FIG. A.5 MOMENTS AND SHEARS ON NARROW SIDE OF A 6:4:1 BUILDING, OPEN COUNTRY EXPOSURE

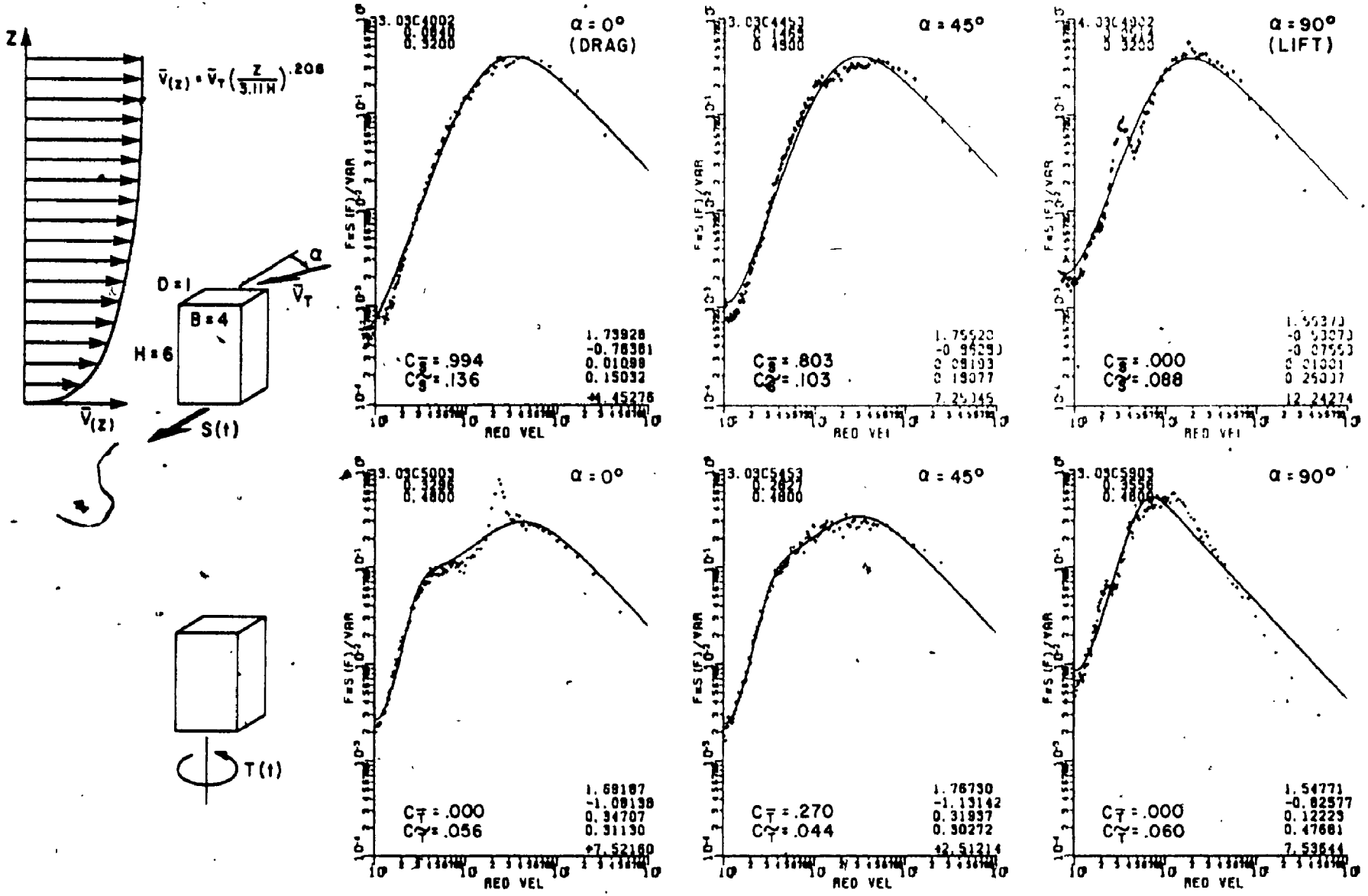

FIG. A.6 SHEARS ON A BROAD SIDE AND TORSIONS OF A 6:4:1 BUILDING OPEN COUNTRY EXPOSURE

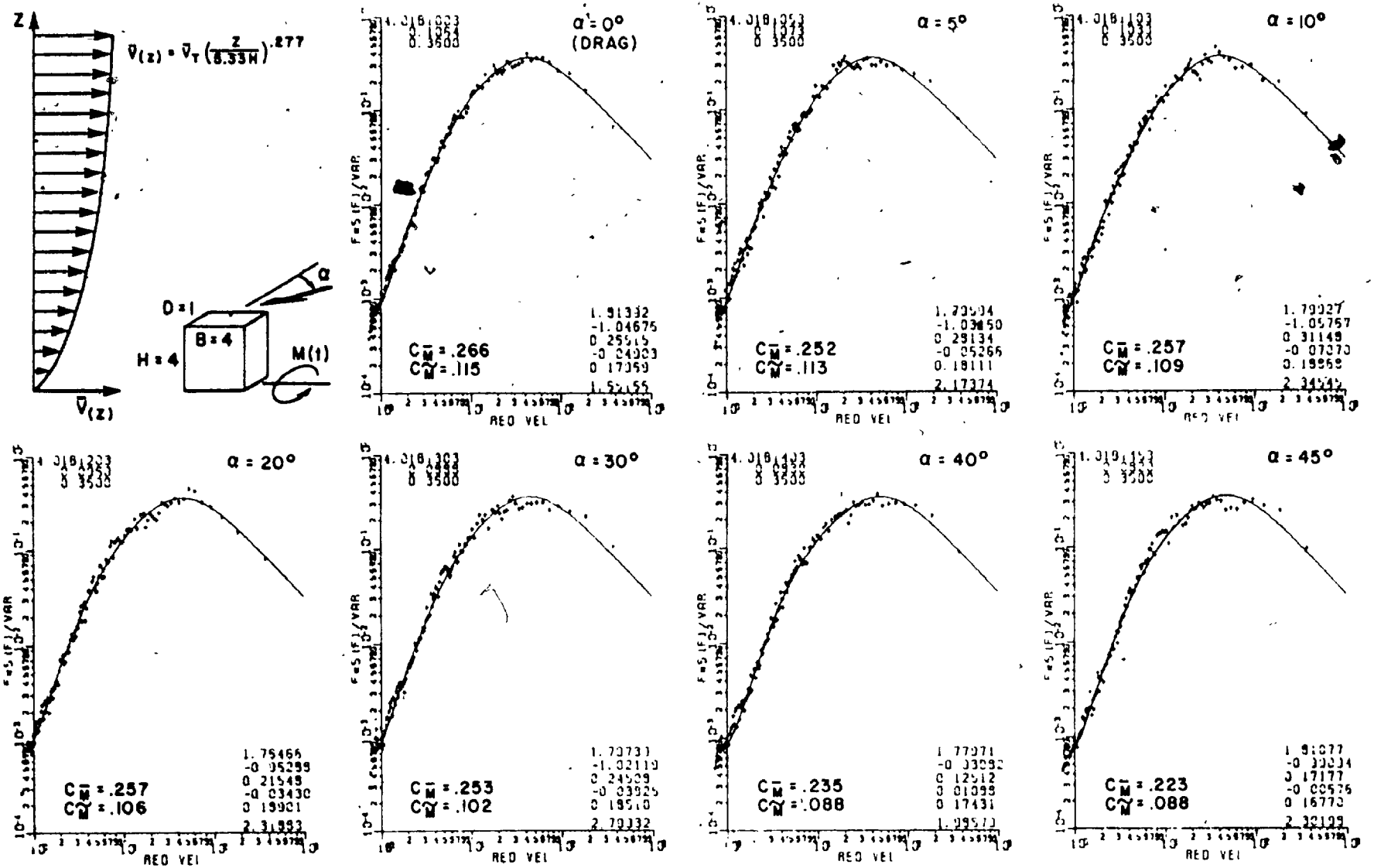

FIG. A.7a , MOMENTS ON BROAD SIDE OF A 4:4:1 BUILDING, SUBURBAN EXPOSURE

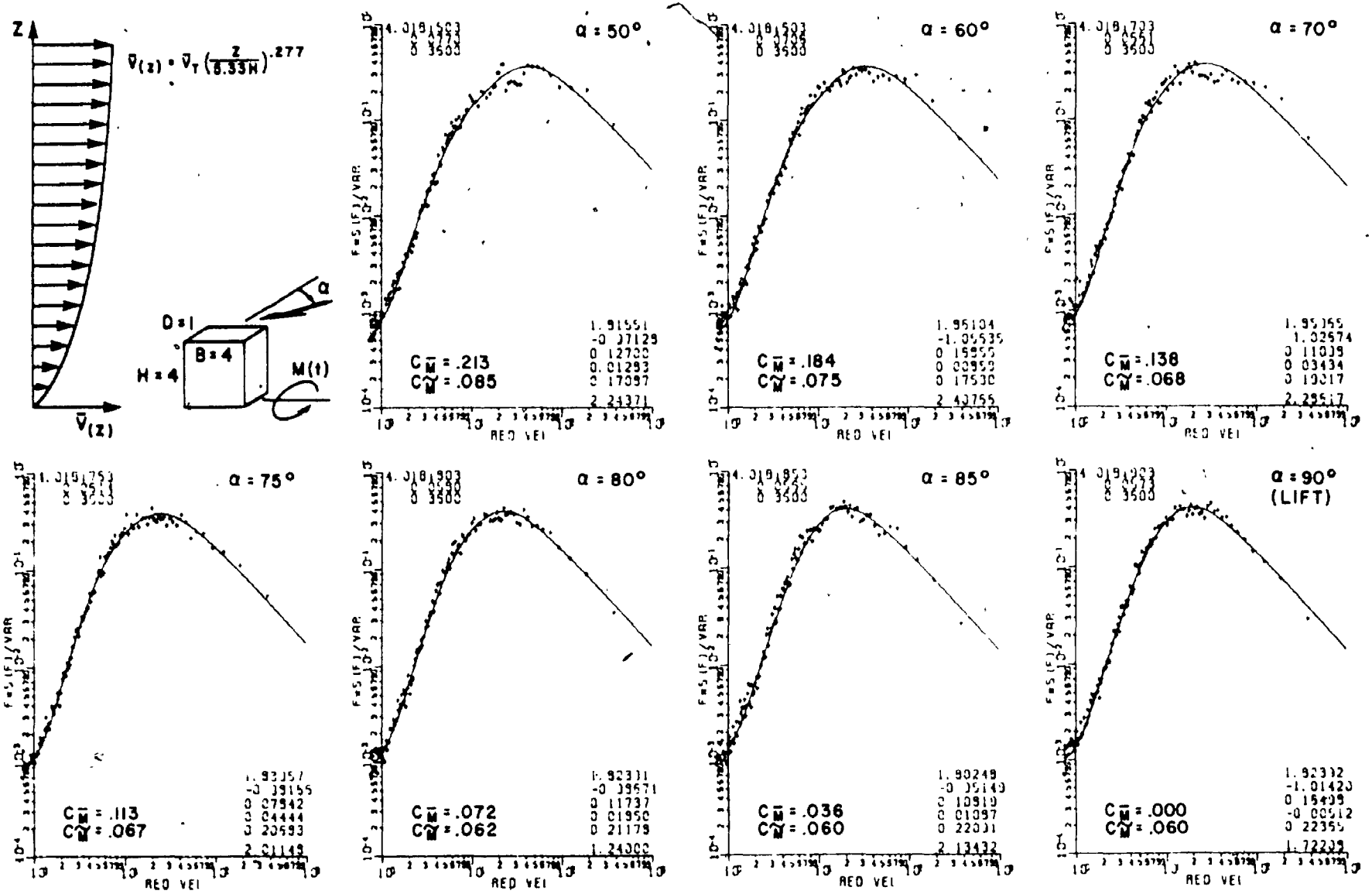

FIG. A.7b MOMENTS ON BROAD SIDE OF A 4:4:1 BUILDING, SUBURBAN EXPOSURE

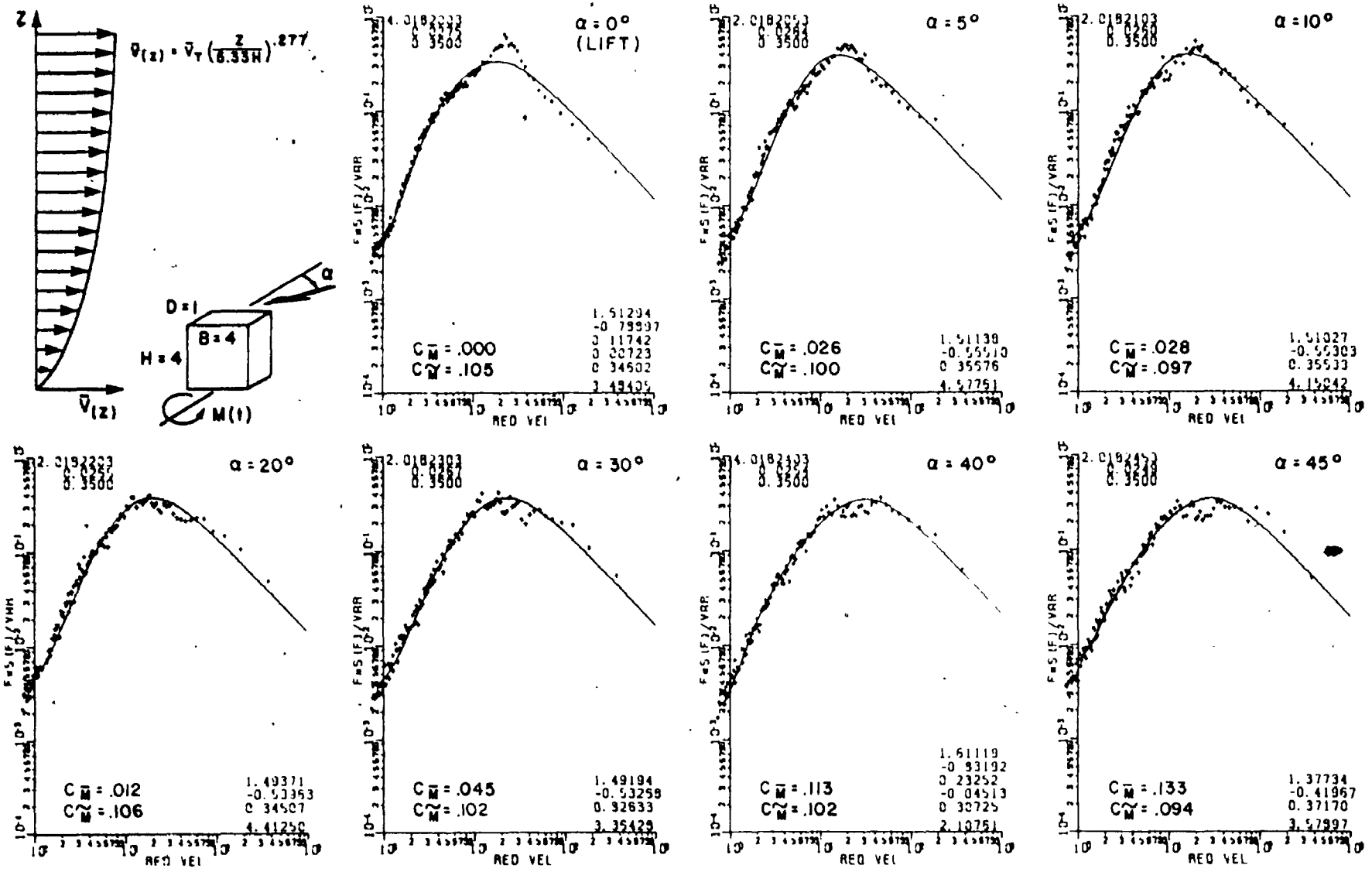

FIG. A.8a MOMENTS ON NARROW SIDE OF A 4:4:1 BUILDING, SUBURBAN EXPOSURE

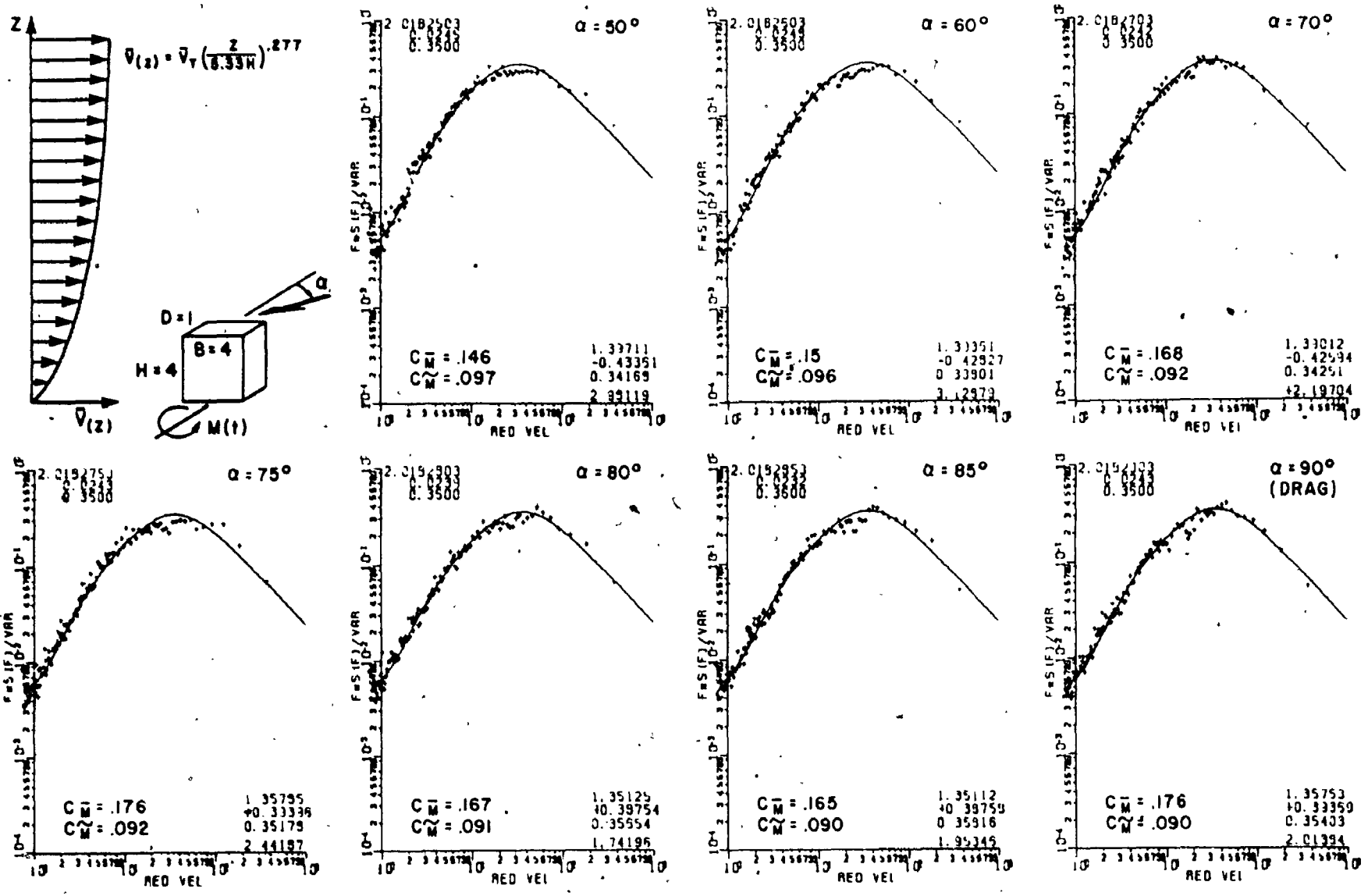

FIG. A.8b MOMENTS ON NARROW SIDE OF A 4:4:1 BUILDING, SUBURBAN EXPOSURE

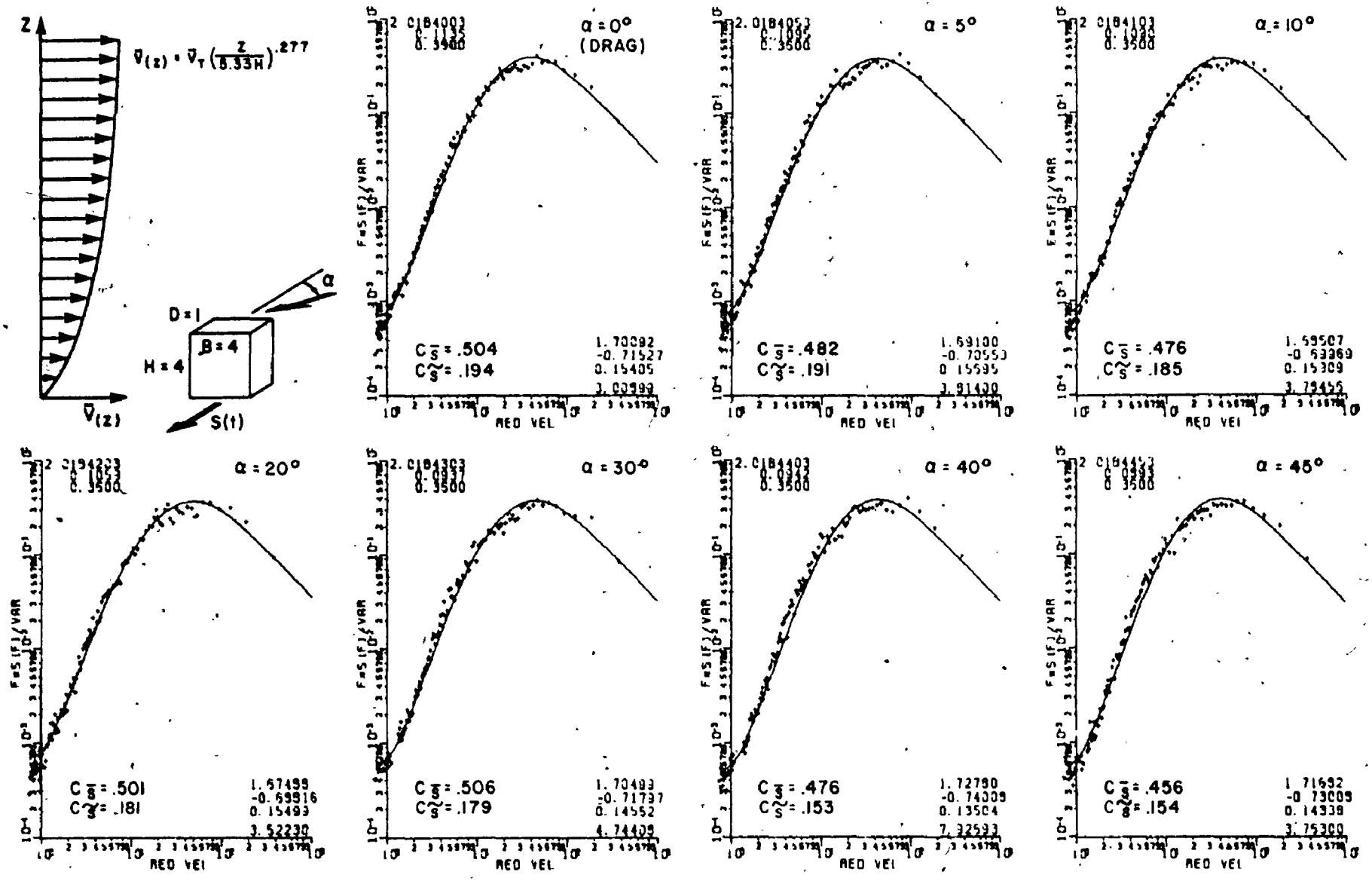

FIG. A9a SHEARS ON BROAD SIDE OF A 4:4:1 BUILDING, SUBURBAN EXPOSURE

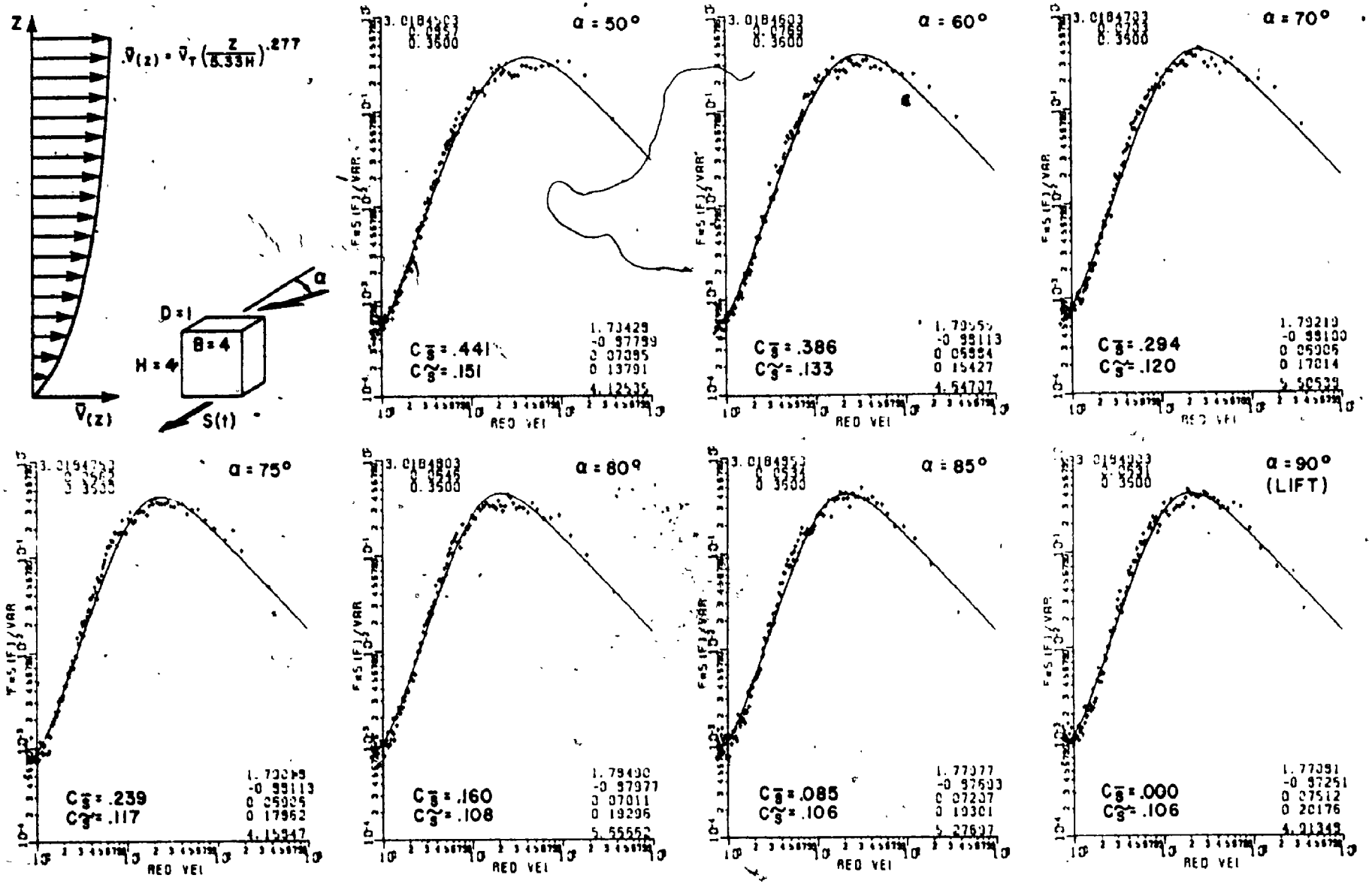

FIG. A.9b SHEARS ON THE BROAD SIDE OF A 4:4:1 BUILDING, SUBURBAN EXPOSURE

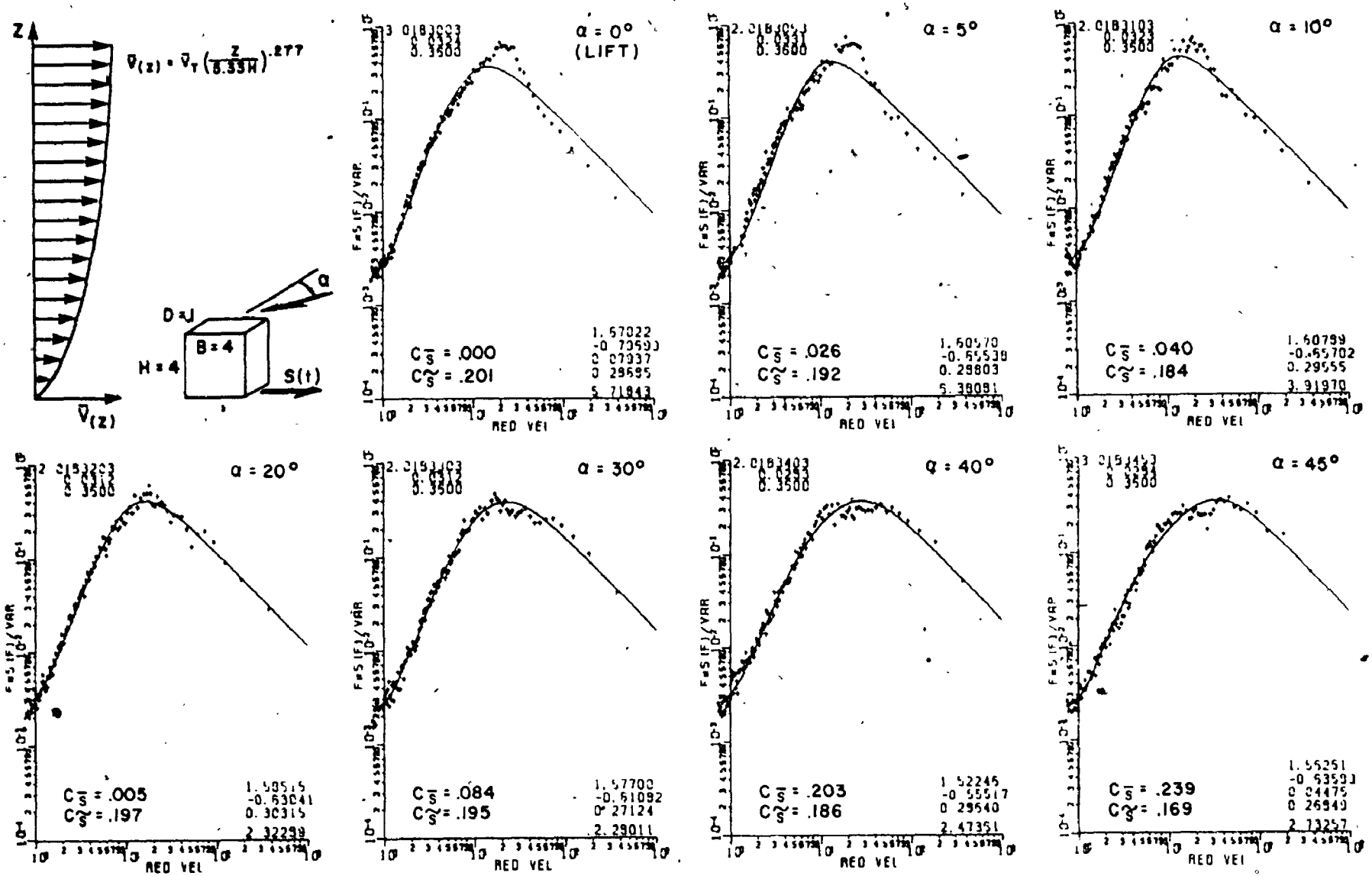

FIG. A10.a SHEARS ON NARROW SIDE OF A 4:4:1 BUILDING, SUBURBAN EXPOSURE

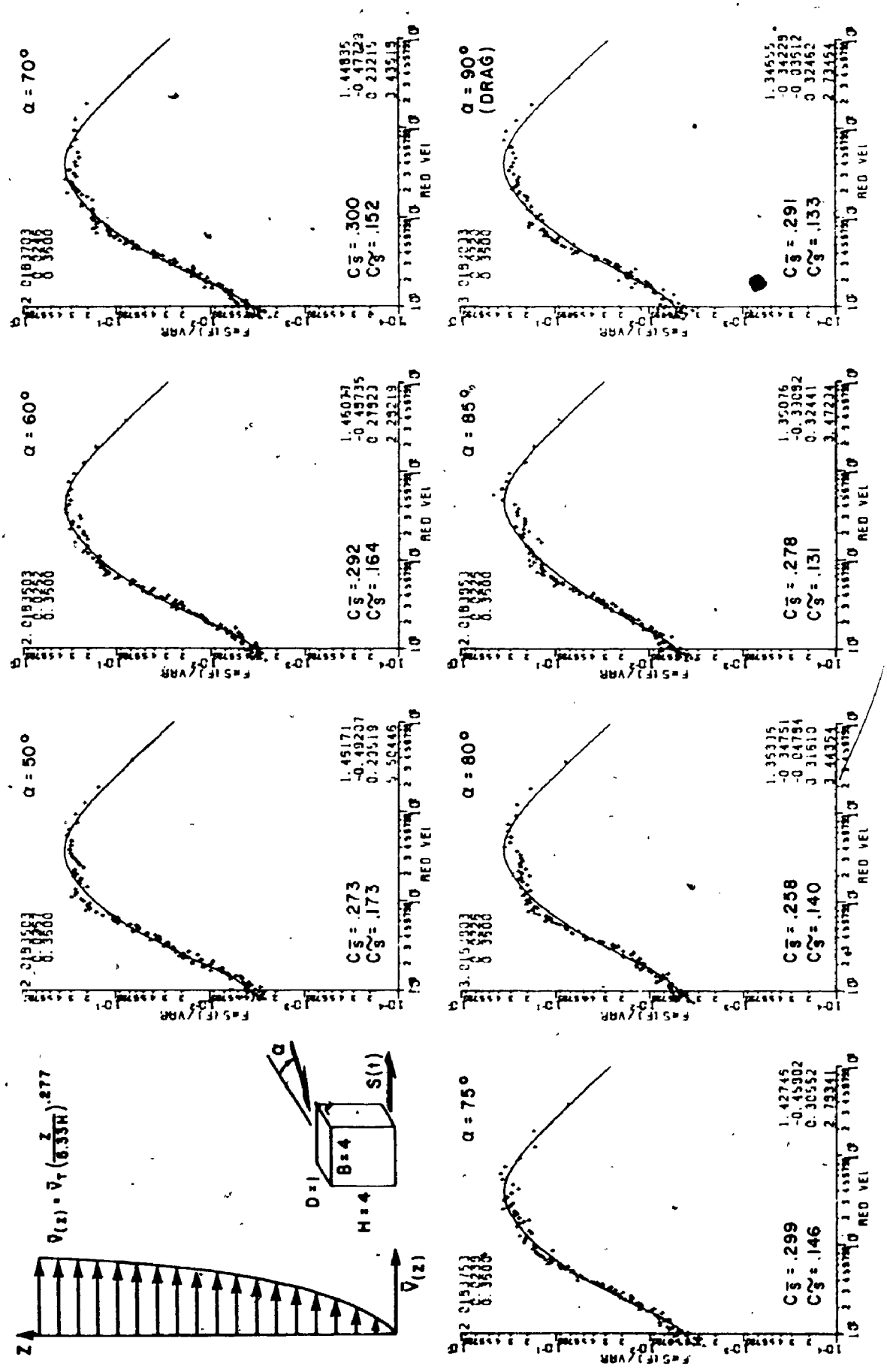

FIG. A.10.b SHEARS ON NARROW SIDE OF A 4:4:1 BUILDING, SUBURBAN EXPOSURE

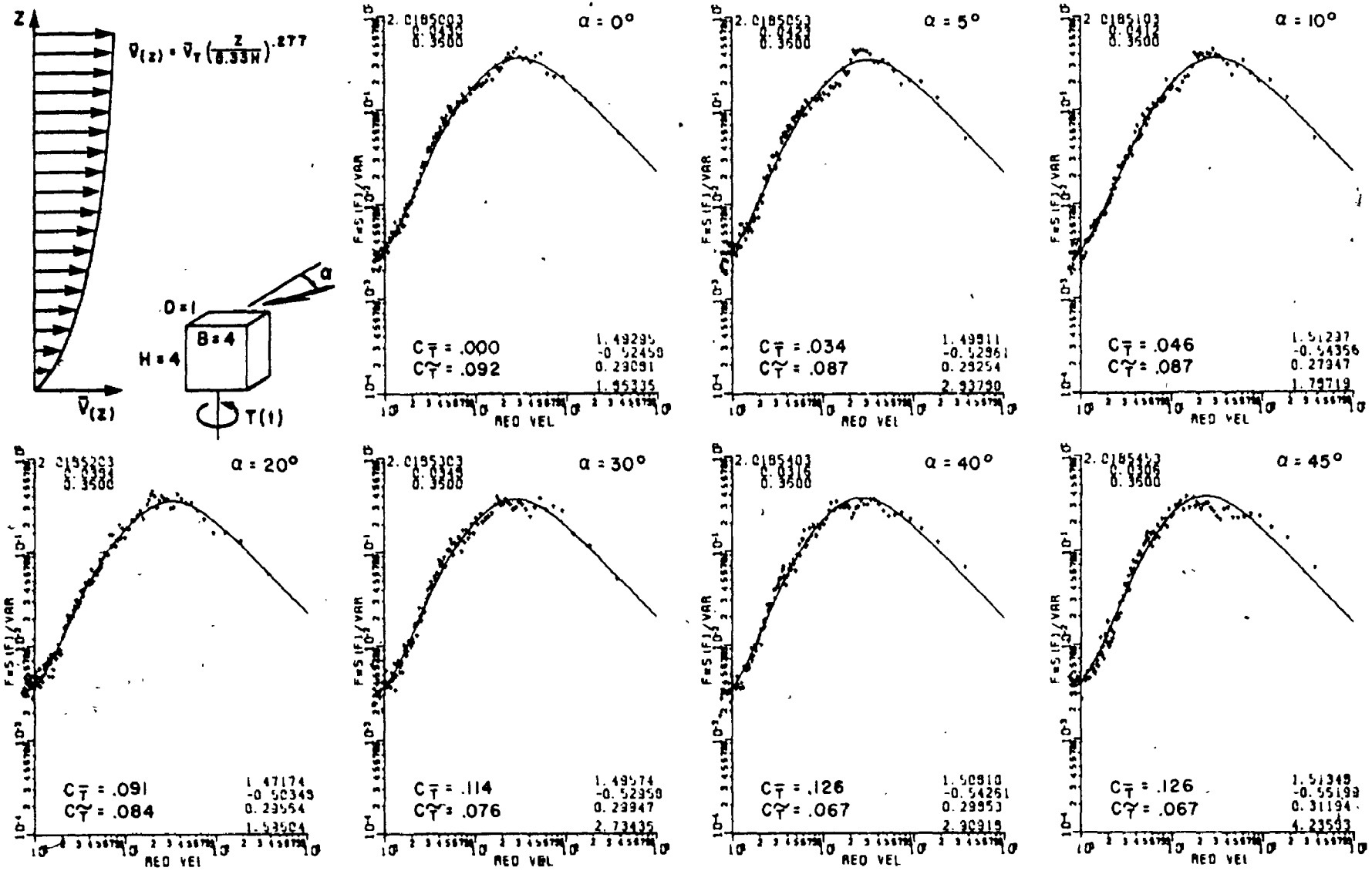

FIG. A.11.a TORSIONS ON A 4:4:1 BUILDING, SUBURBAN EXPOSURE

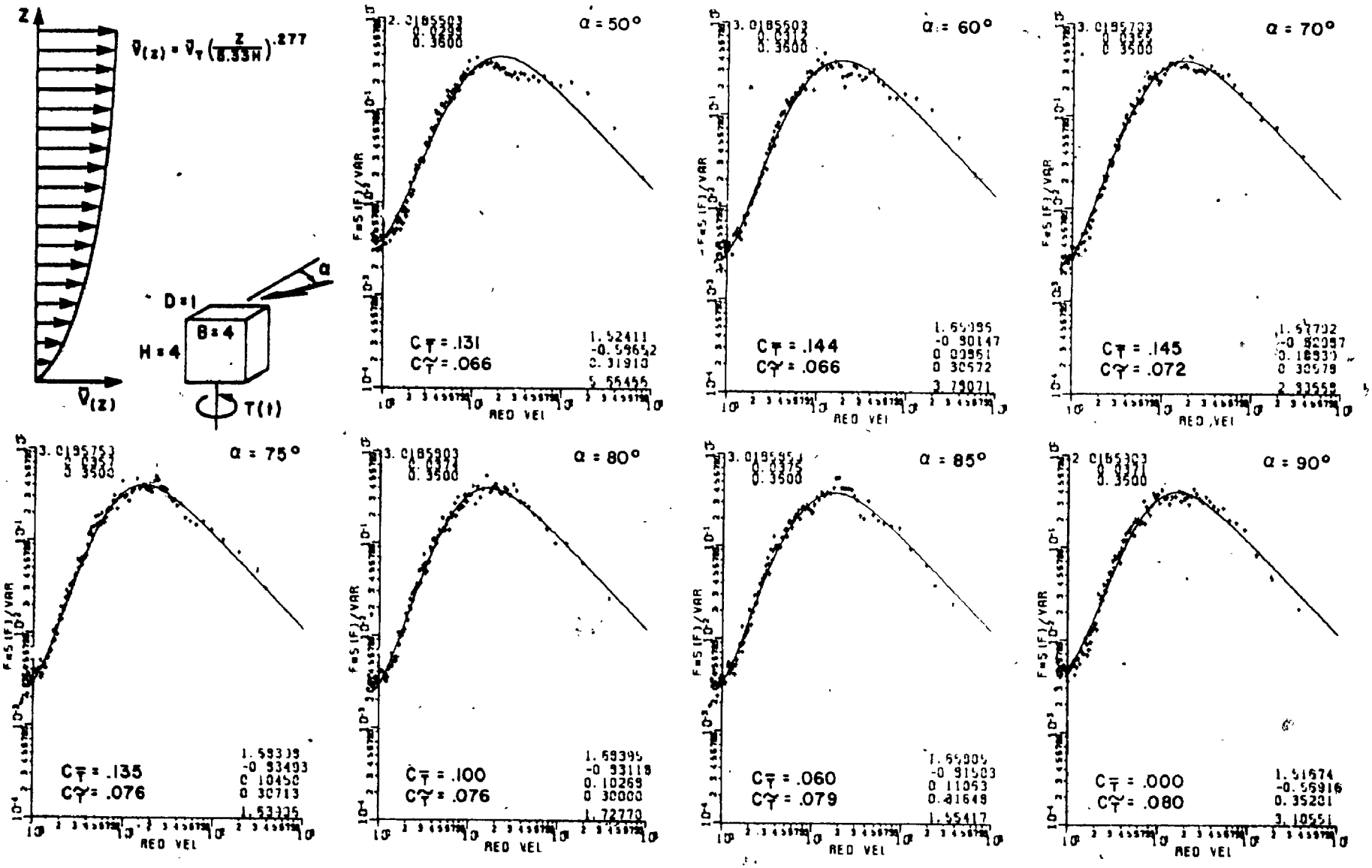

FIG. A.11.b TORSIONS ON A 4:4:1 BUILDING, SUBURBAN EXPOSURE

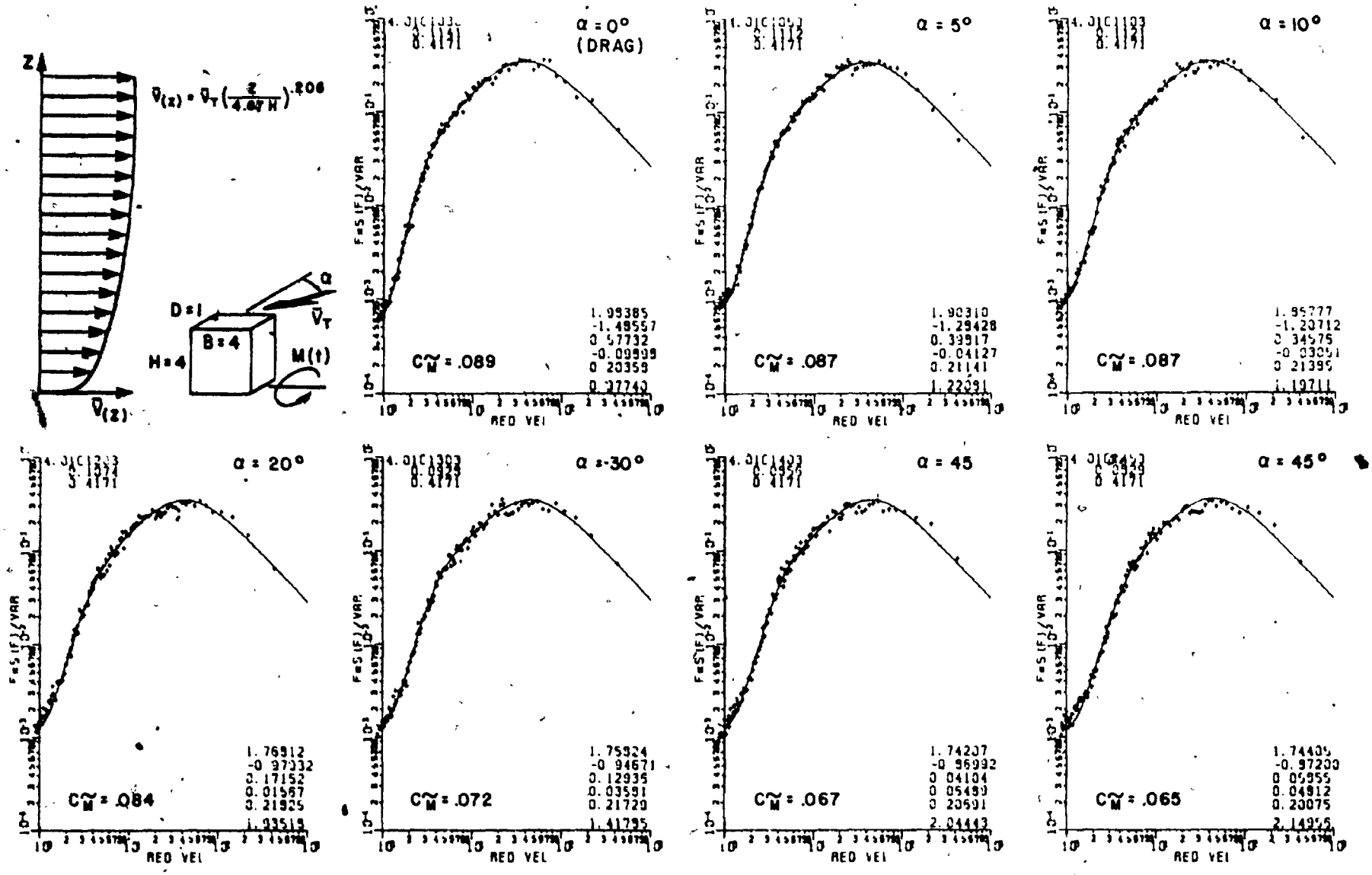

FIG. A.12.a MOMENTS ON BROAD SIDE OF A 4:4:1 BUILDING, OPEN COUNTRY EXPOSURE

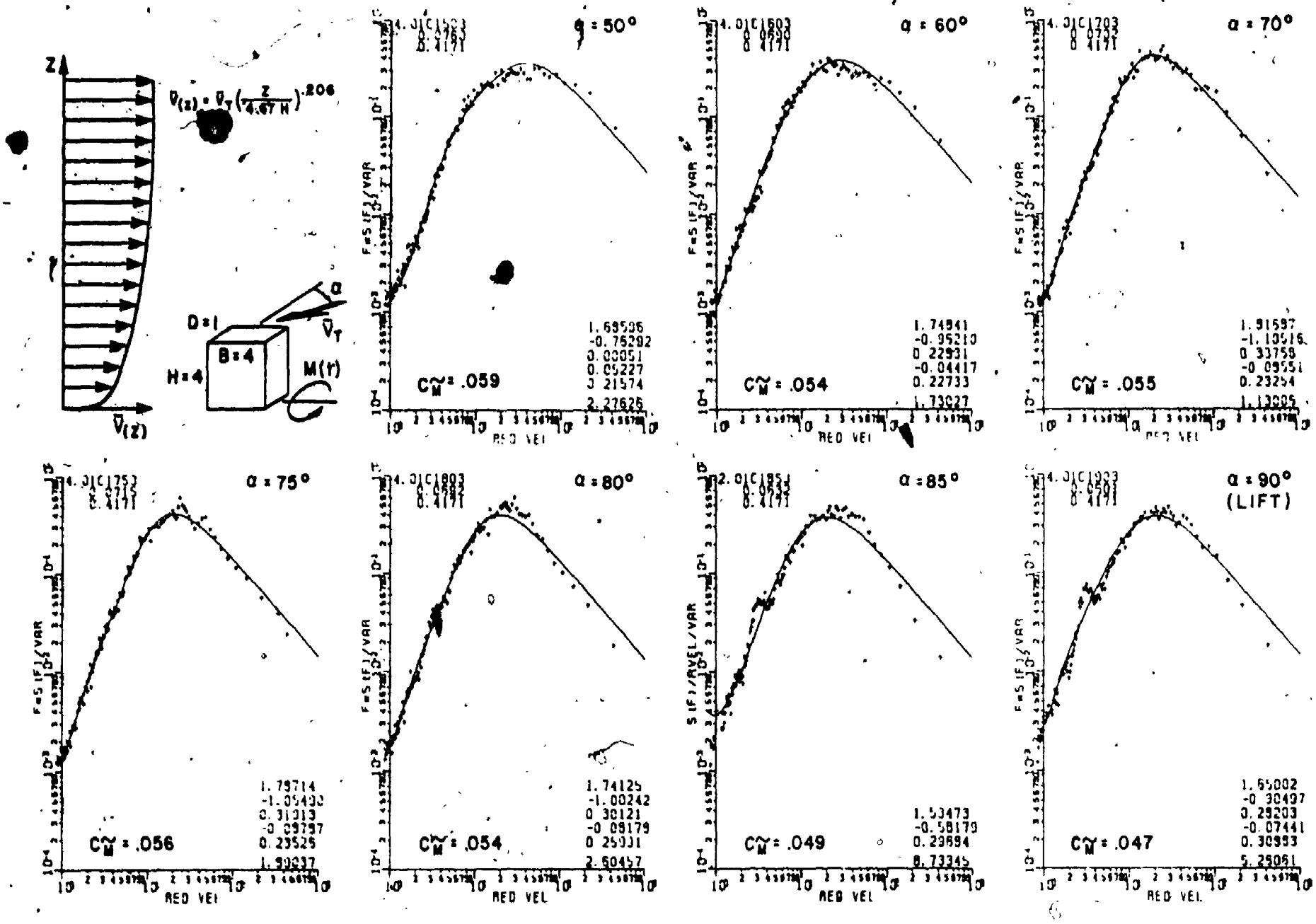

FIG. A.12.b MOMENTS ON BROAD SIDE OF A 4:4:1 BUILDING, OPEN COUNTRY EXPOSURE

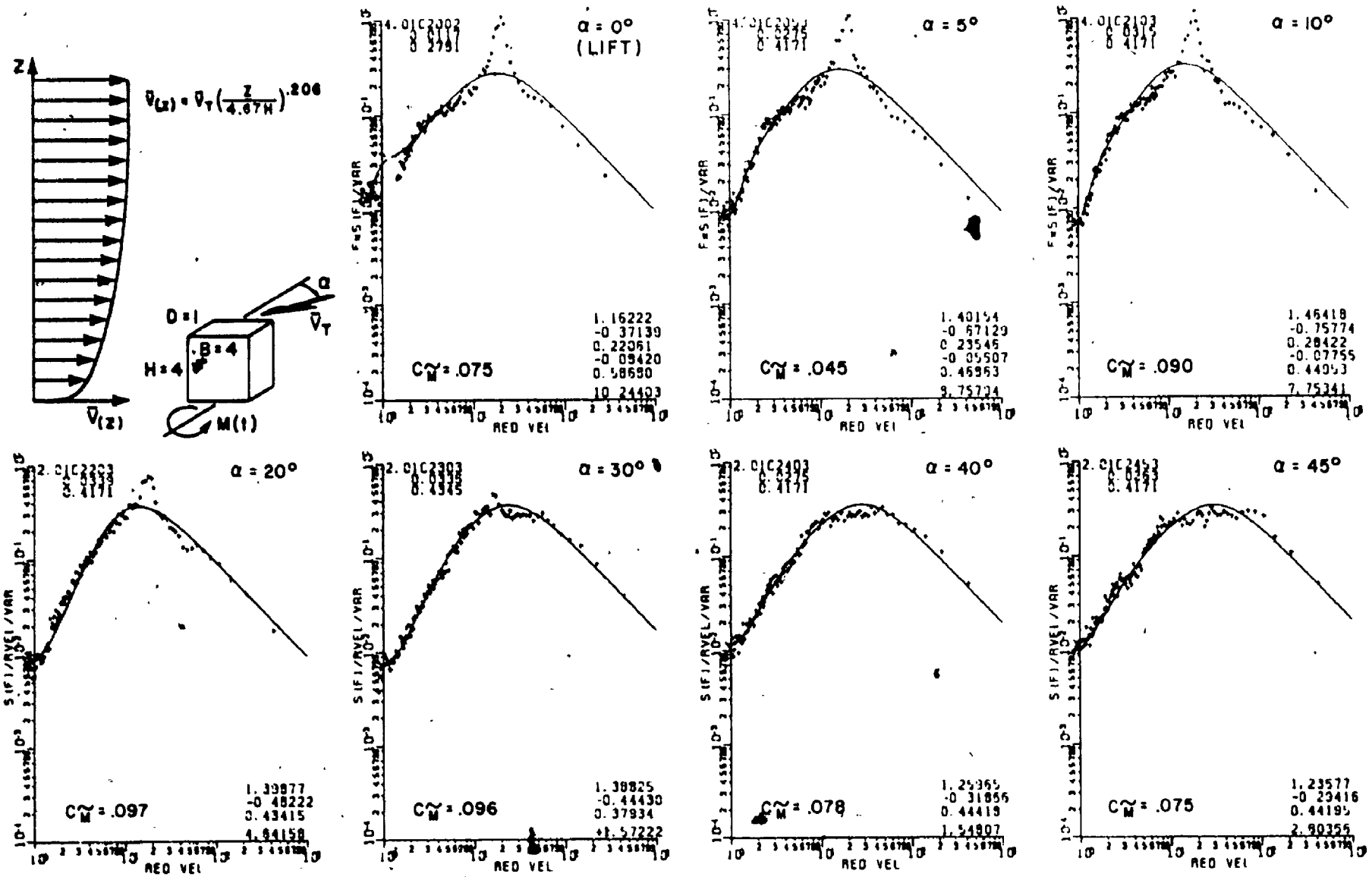

FIG. A.13.a MOMENTS ON NARROW SIDE OF A 4:4:1 BUILDING, OPEN COUNTRY EXPOSURE

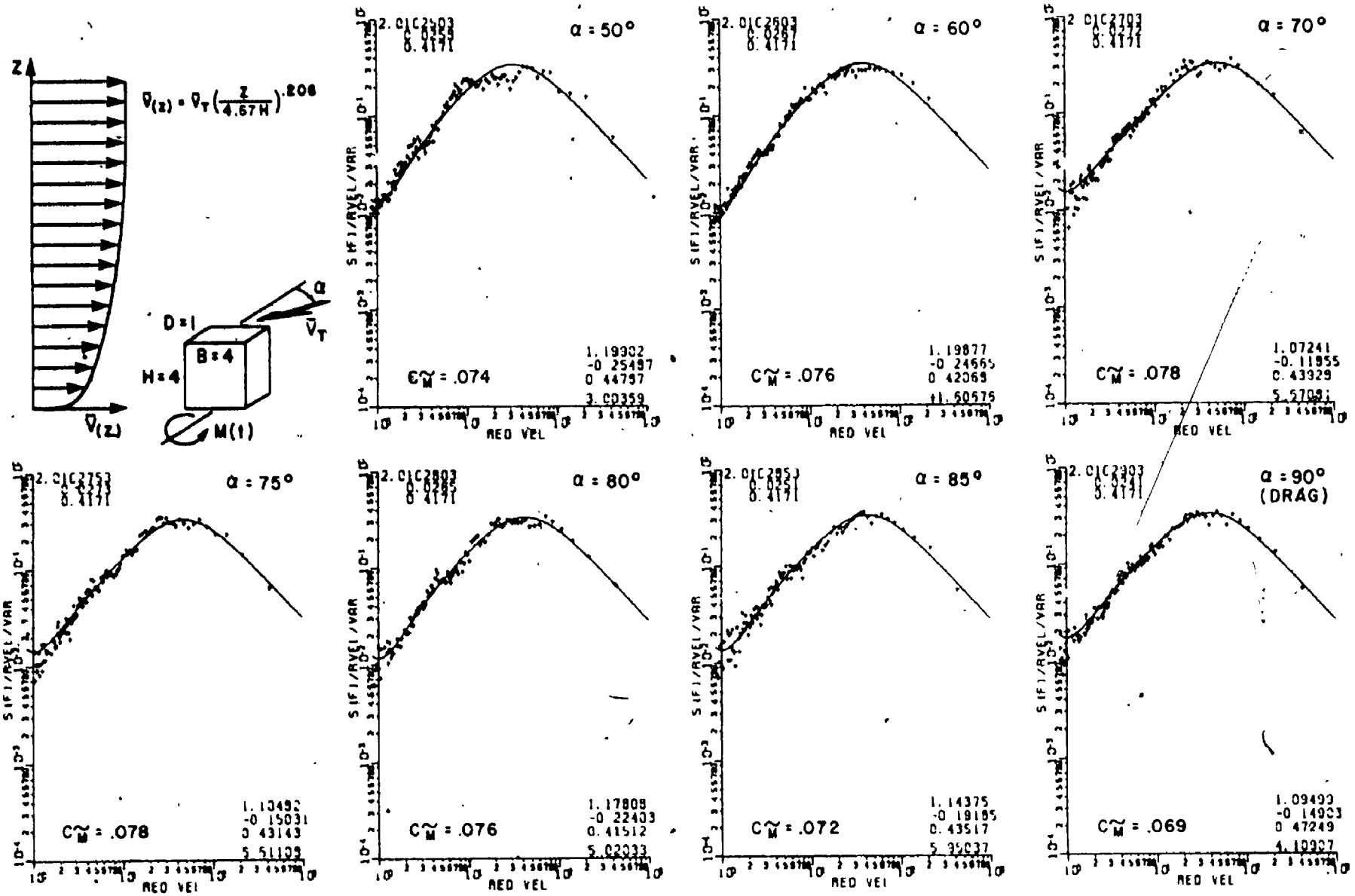

FIG. A.13.b MOMENTS ON NARROW SIDE OF A 4:4:1 BUILDING, OPEN COUNTRY EXPOSURE

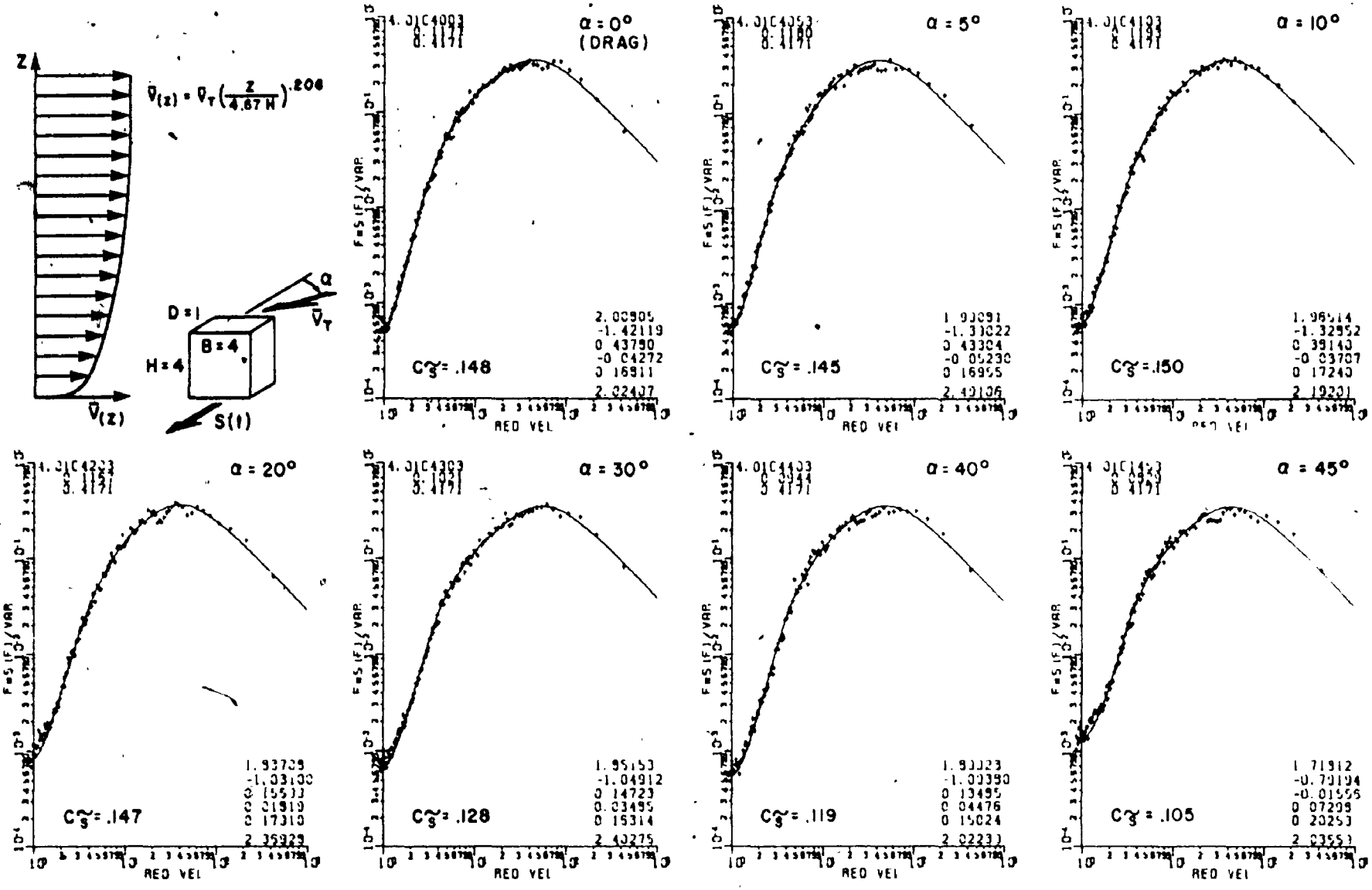

FIG. A14.a SHEARS ON BROAD SIDE OF A 4:4:1 BUILDING, OPEN COUNTRY EXPOSURE

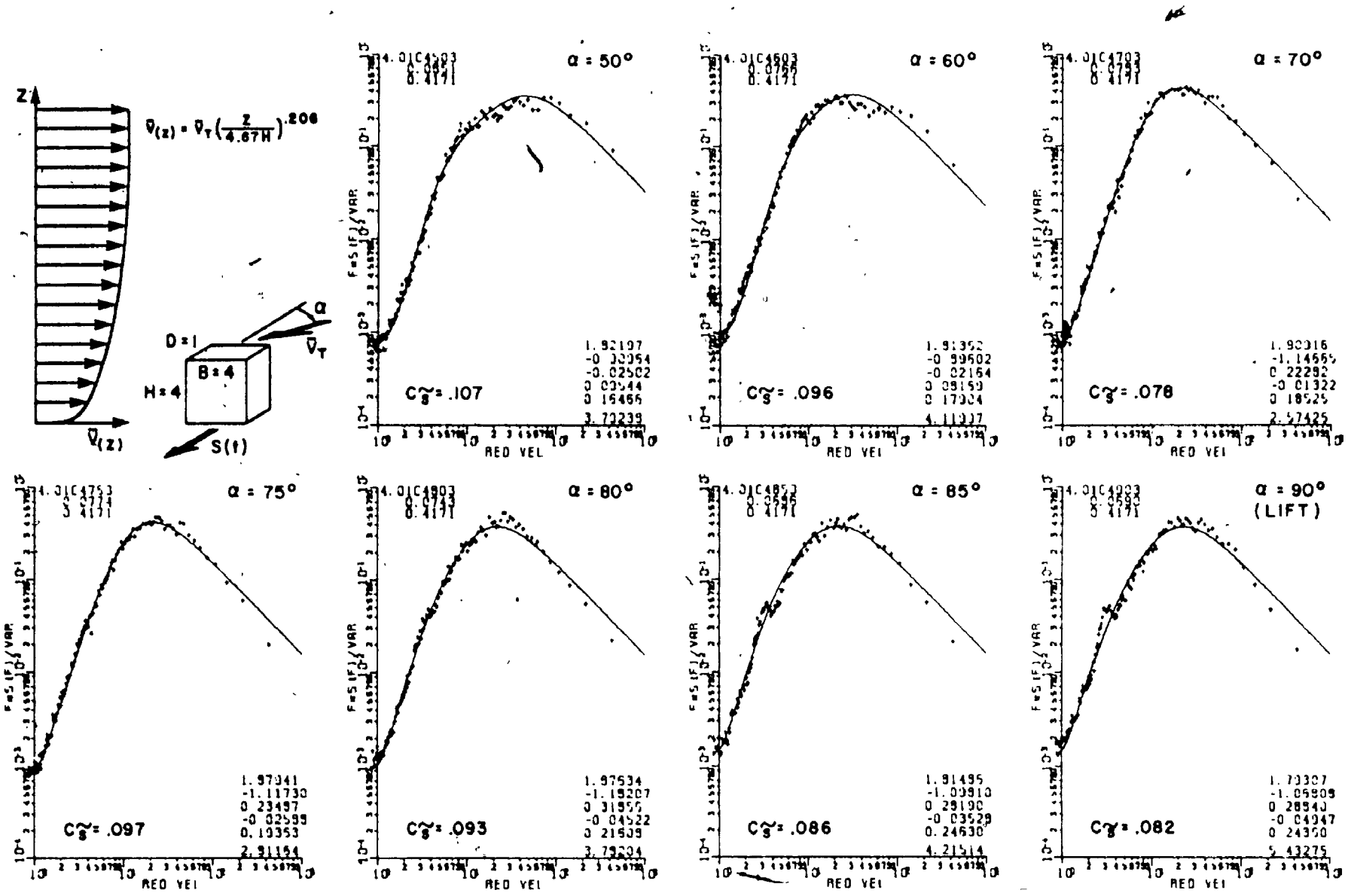

FIG. A.14.b SHEARS ON BROAD SIDE OF A 4:4:1 BUILDING, OPEN COUNTRY EXPOSURE

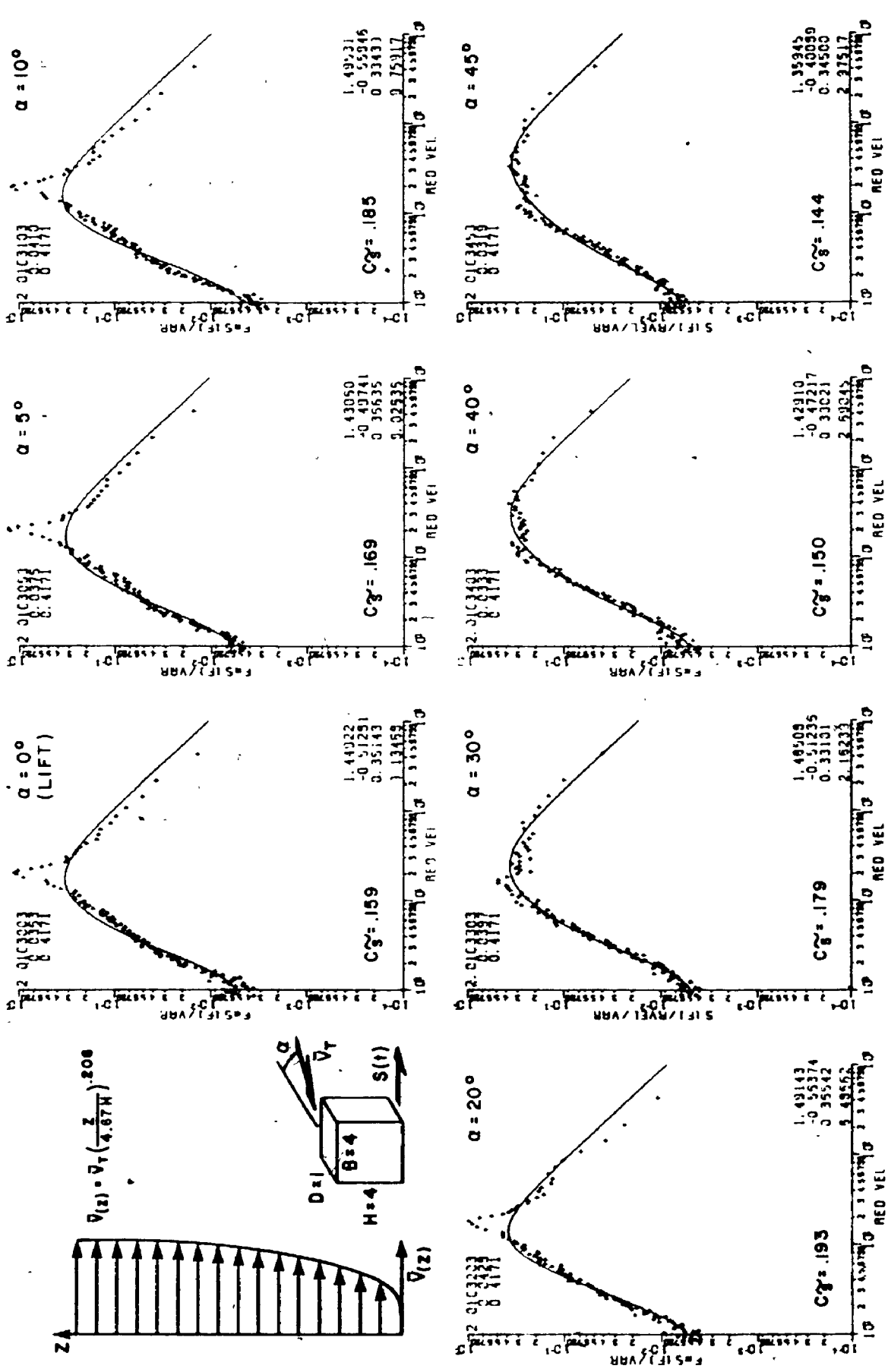

FIG. A.15.a SHEARS ON NARROW SIDE OF A 4:4:1 BUILDING, OPEN COUNTRY EXPOSURE

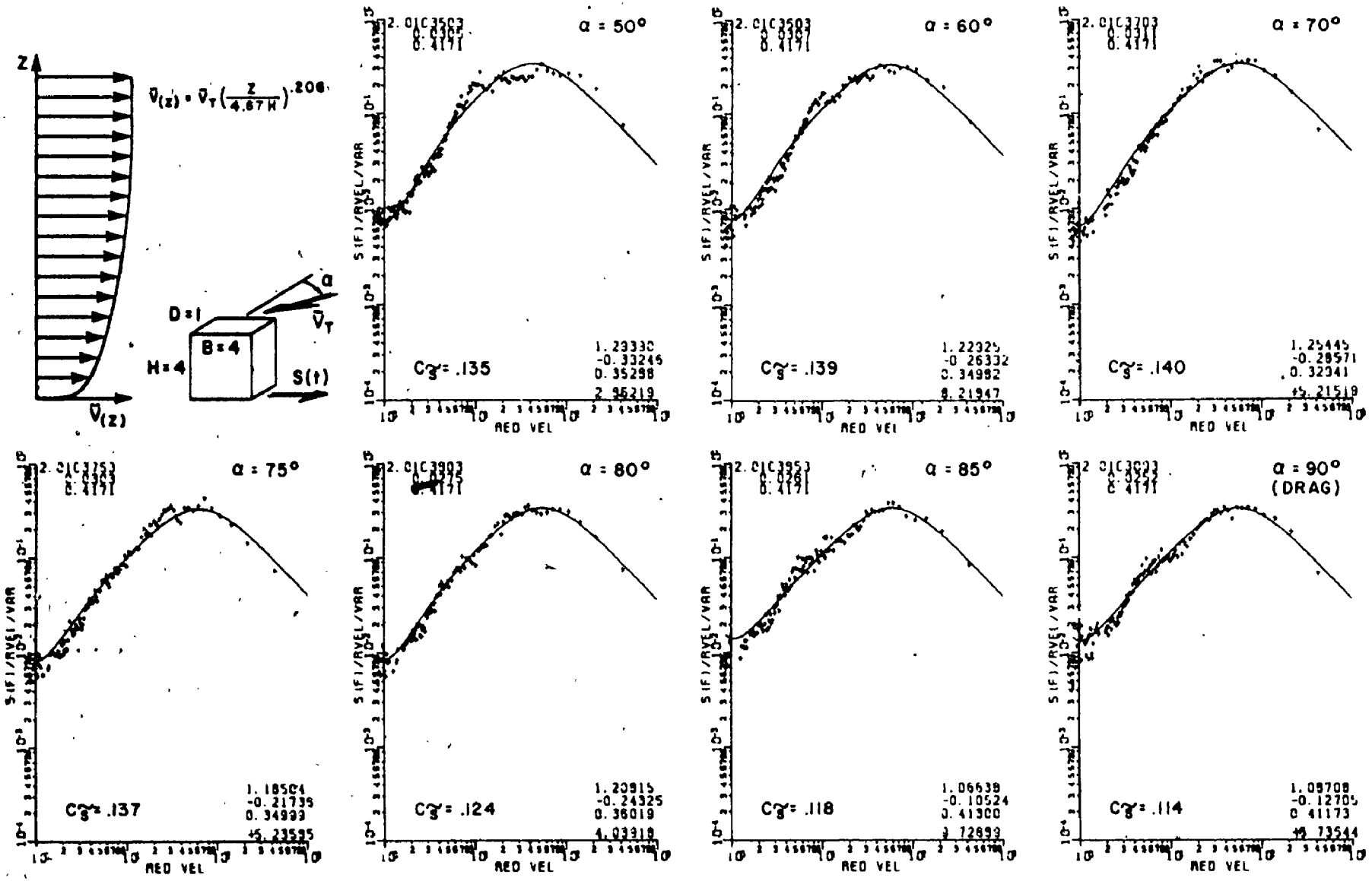

FIG. A.15.b SHEARS ON NARROW SIDE OF A 4:4:1 BUILDING, OPEN COUNTRY EXPOSURE

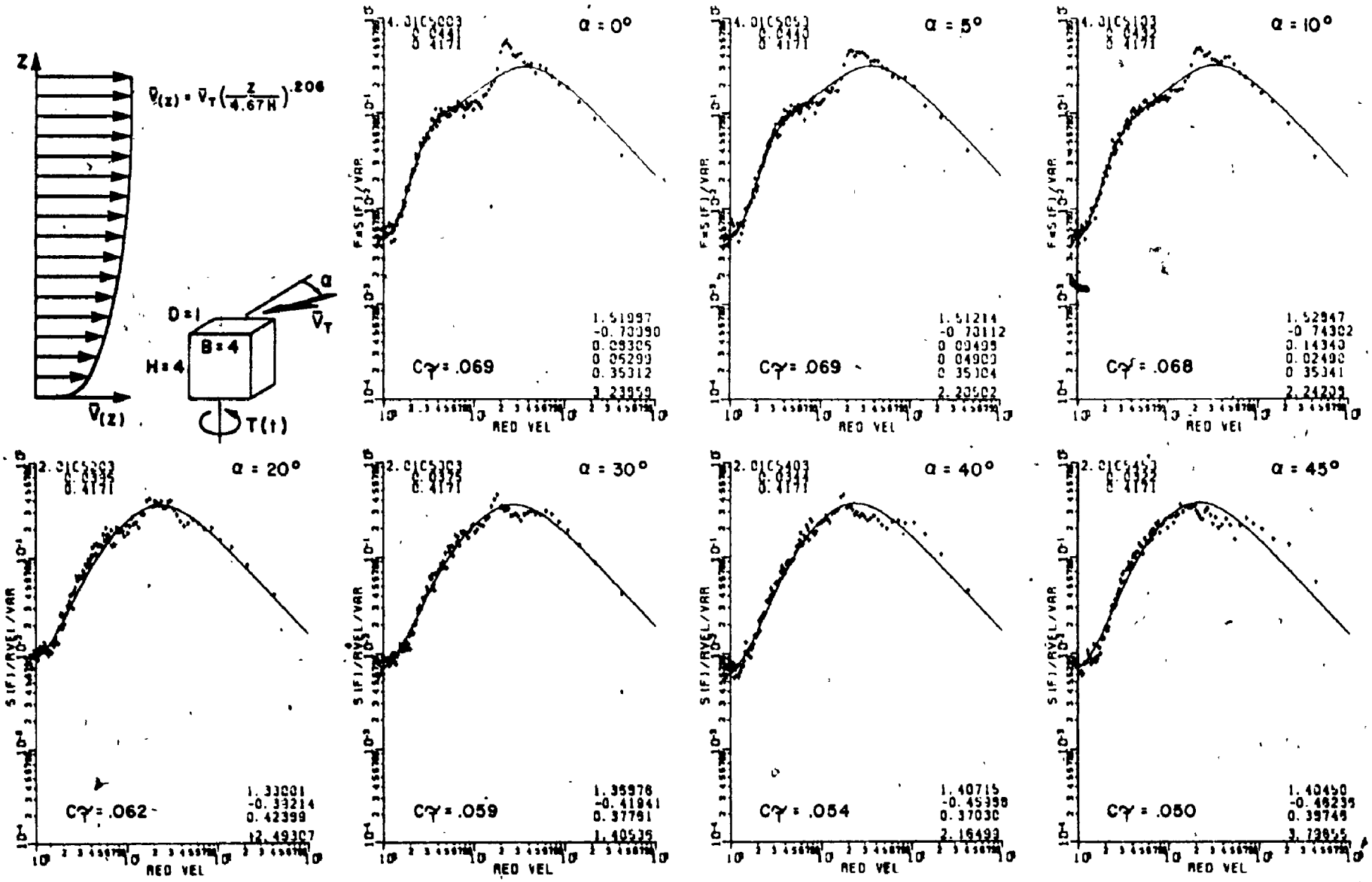

FIG. A.16.a TORSIONS ON A 4:4:1 BUILDING, OPEN COUNTRY EXPOSURE

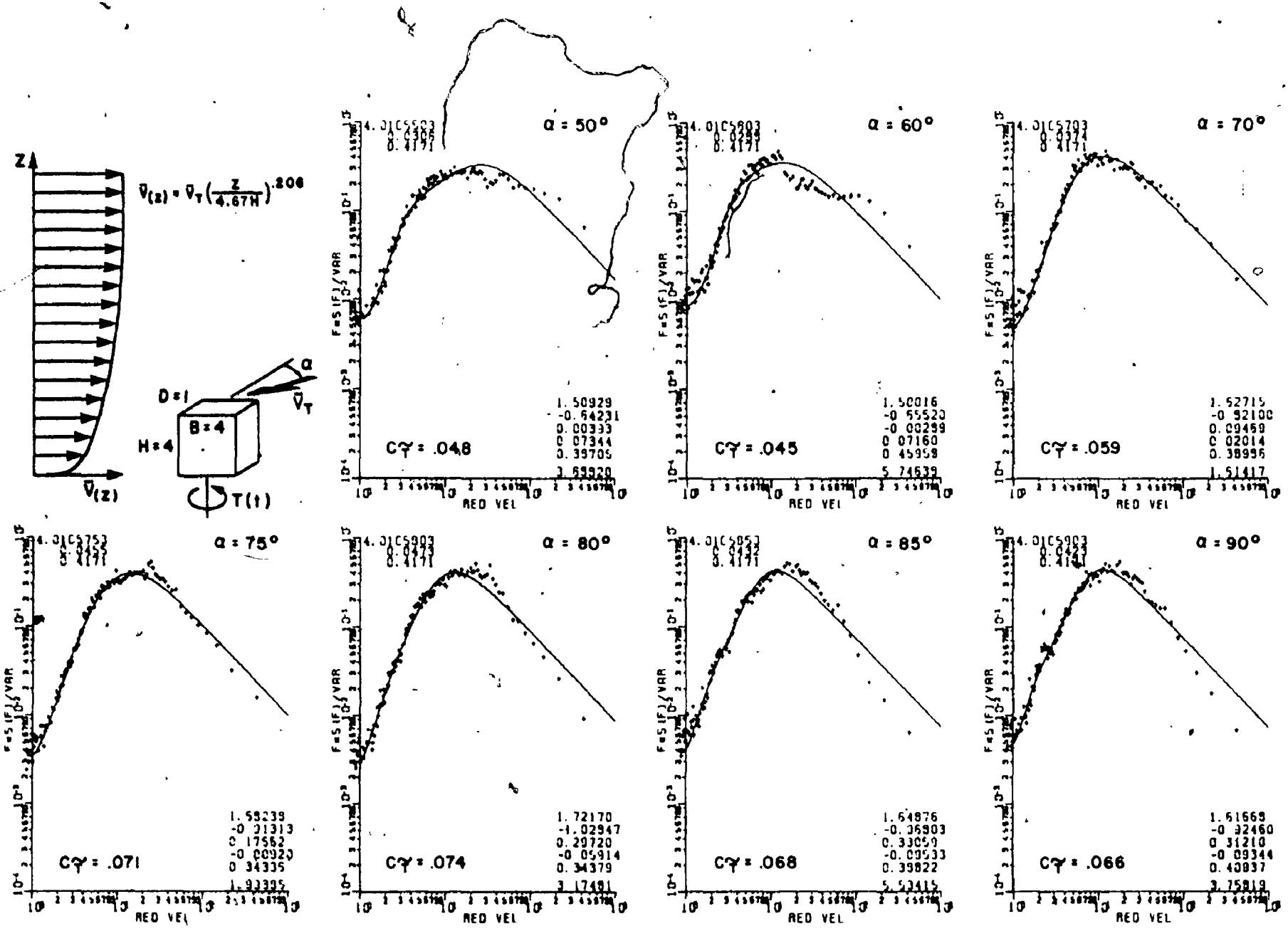

FIG. A.16.b TORSIONS ON A 4:4:1 BUILDING, OPEN COUNTRY EXPOSURE

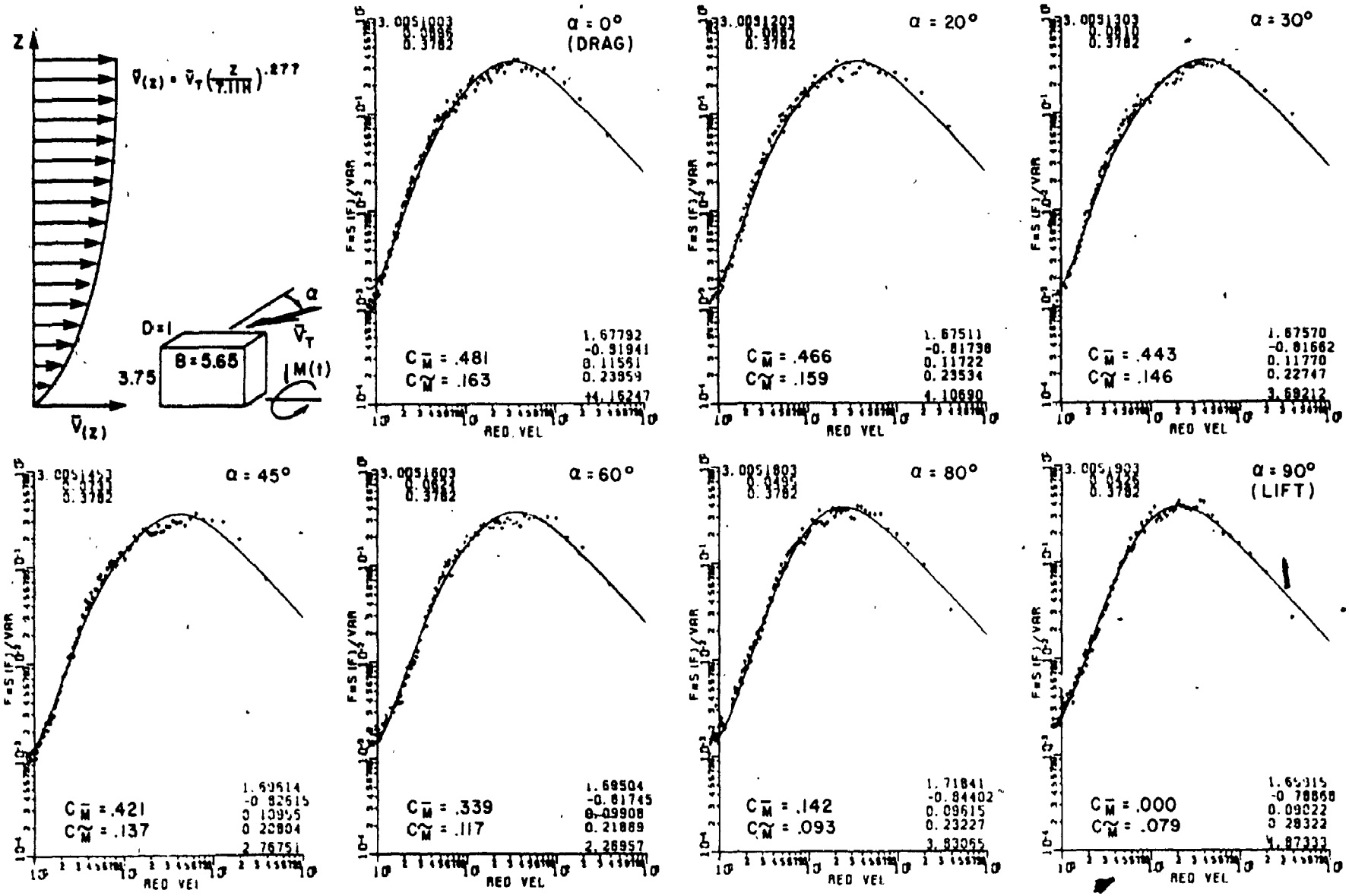

FIG. A.17 MOMENTS ON BROAD SIDE OF A 3.75:5.65:1 BUILDING, SUBURBAN EXPOSURE

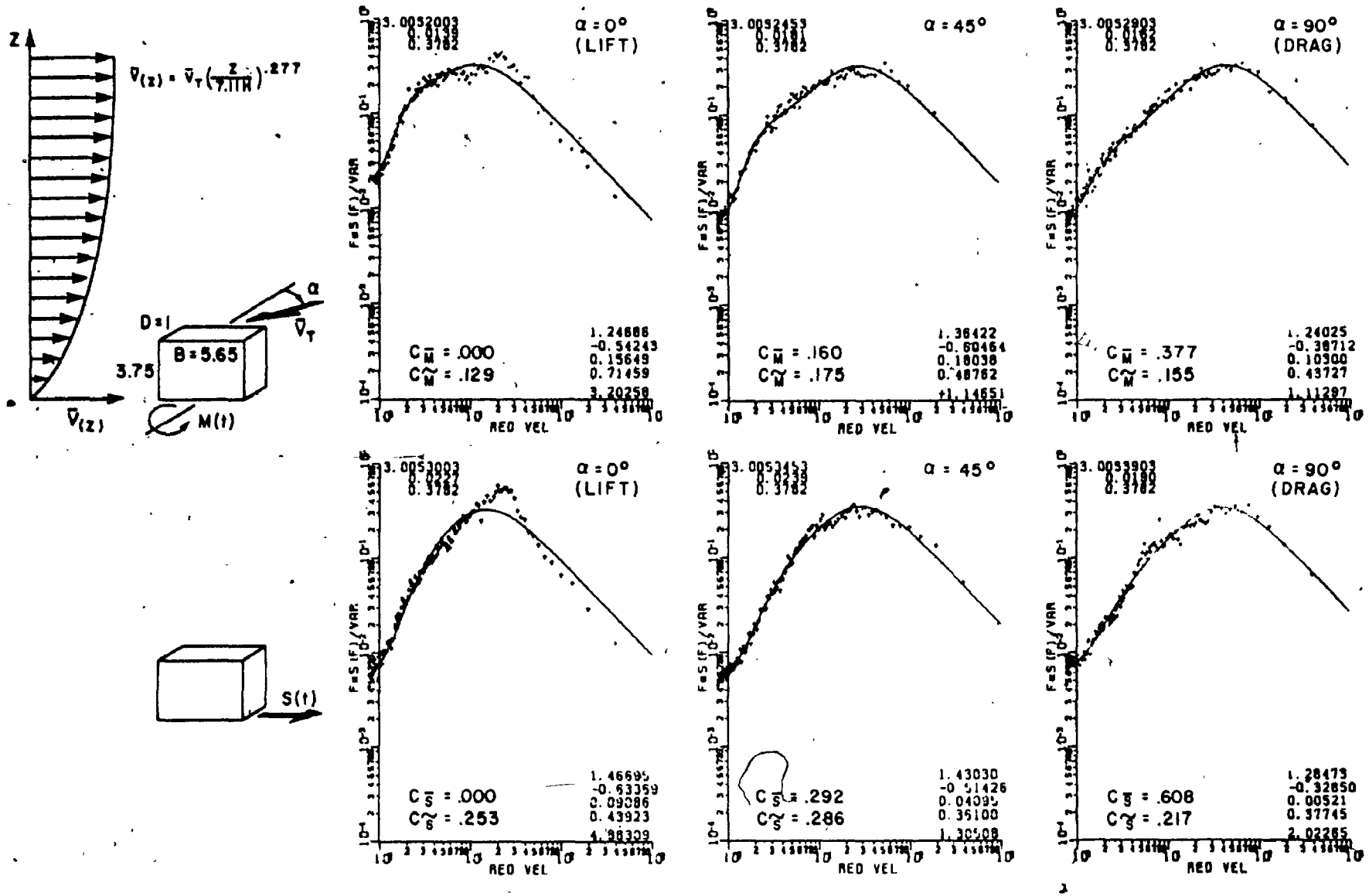

FIG. A.18 MOMENTS AND SHEARS ON NARROW SIDE OF A 3.75:5.65:1 BUILDING, SUBURBAN EXPOSURE

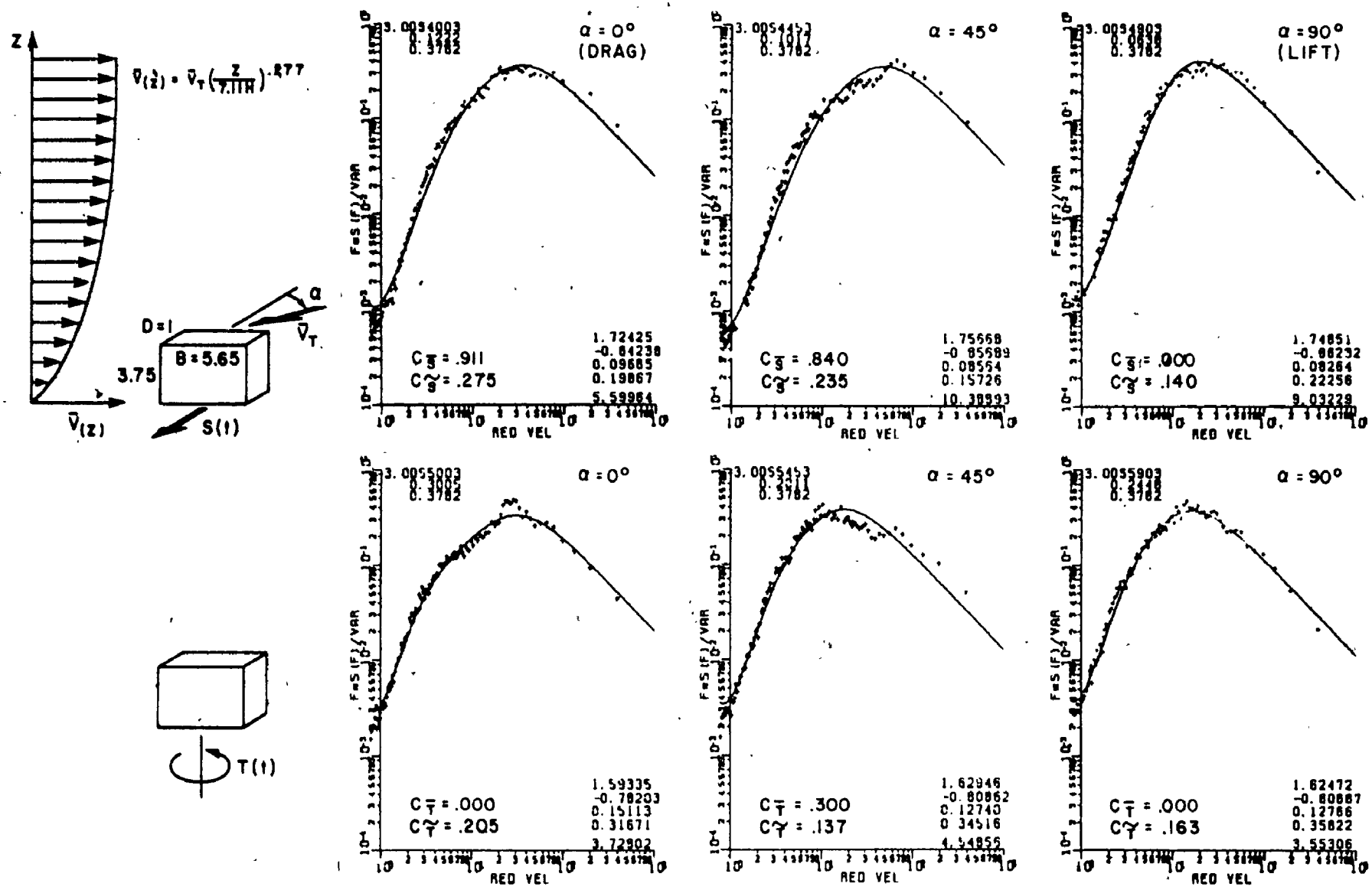

FIG. A.19 SHEARS ON BROAD SIDE AND TORSIONS OF A 3.75:5.65:1 BUILDING, SUBURBAN EXPOSURE

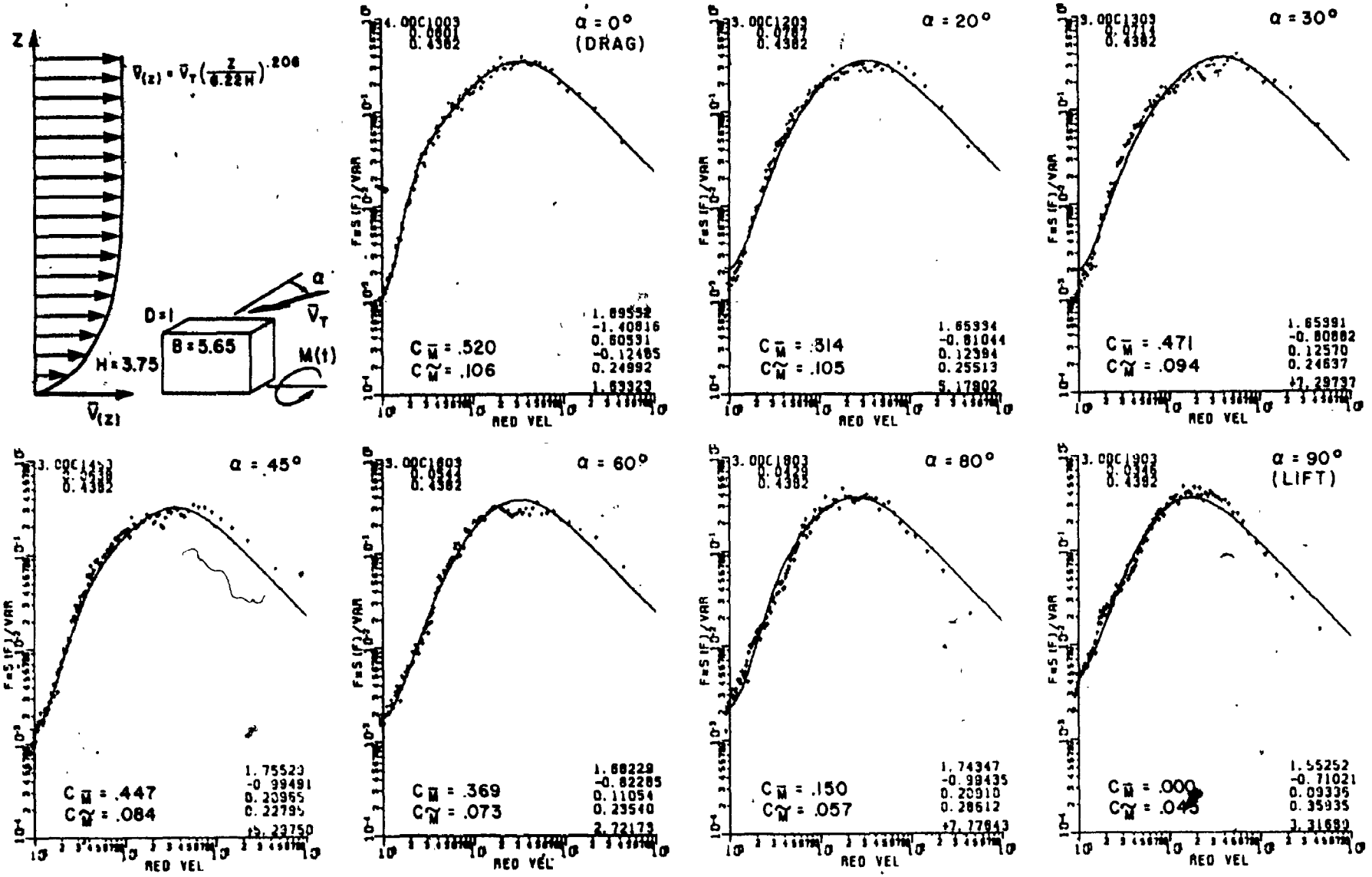

FIG. A.20 MOMENTS ON BROAD SIDE OF A 3:75:5.65:1 BUILDING, OPEN COUNTRY EXPOSURE

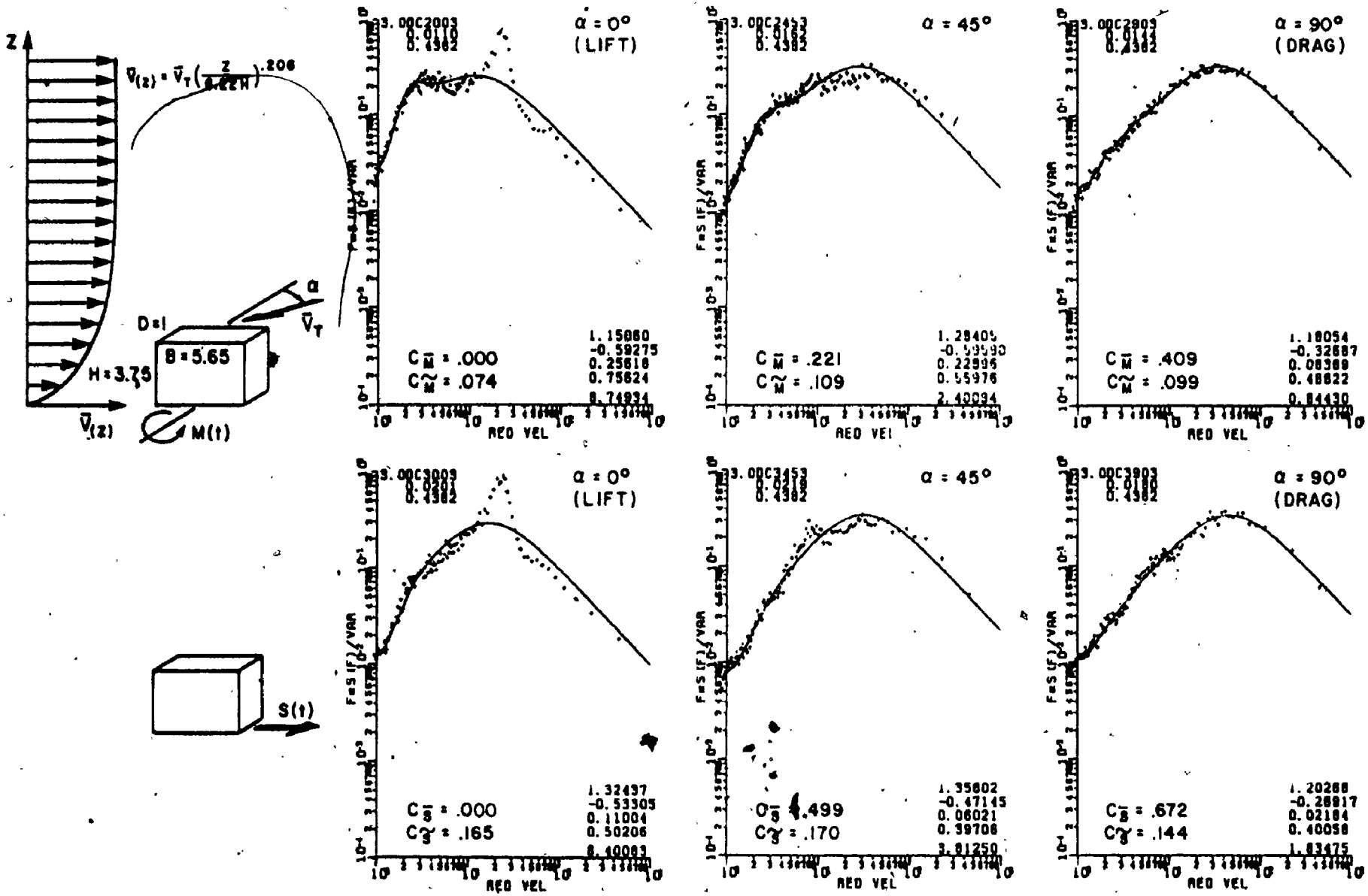

FIG. A.21 MOMENTS AND SHEARS ON NARROW SIDE OF A 3.75:5.65:1 BUILDING, OPEN COUNTRY EXPOSURE

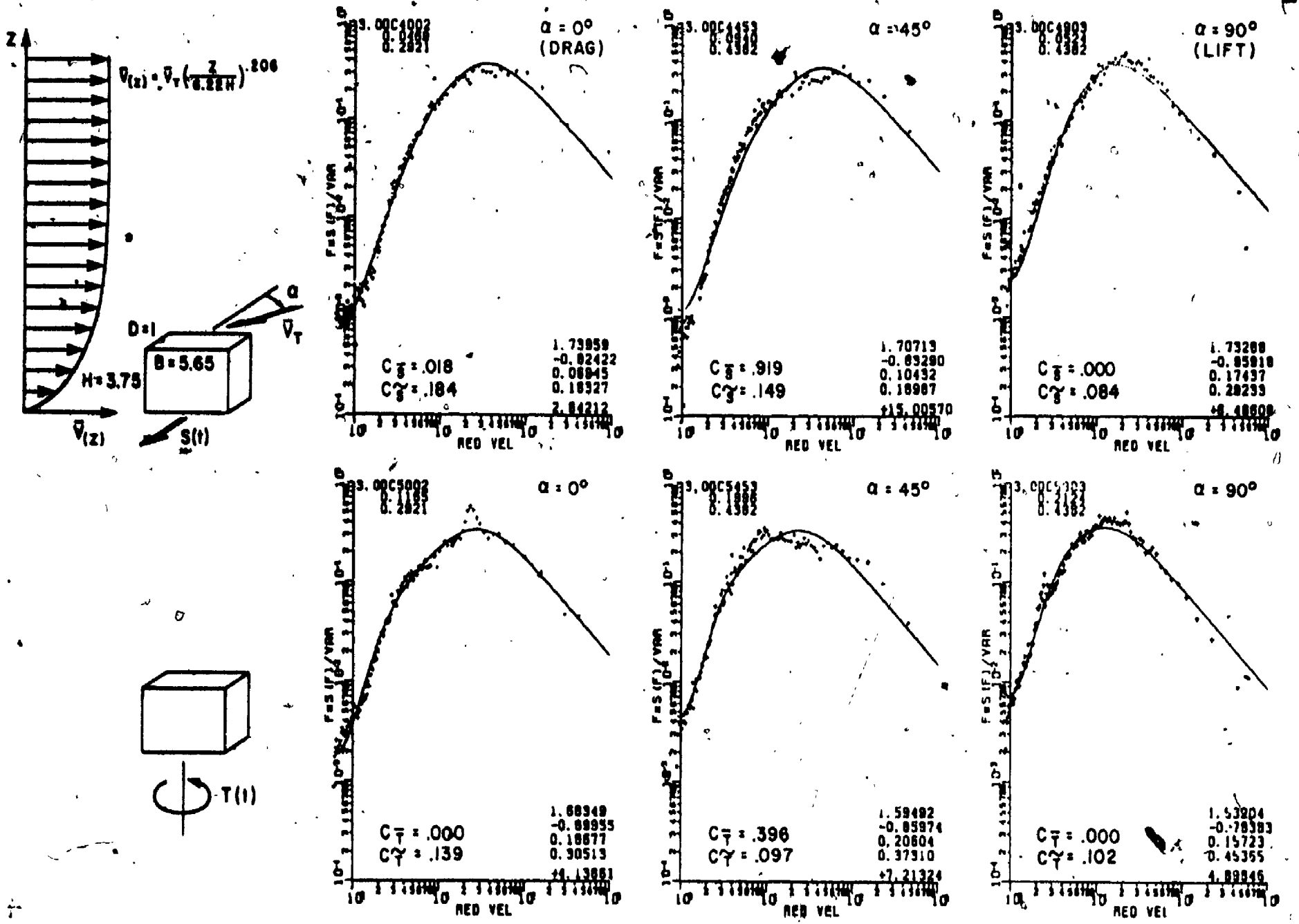

FIG. A22 SHEARS ON BROAD SIDE AND TORSIONS OF A 3.75:5.65:1 BUILDING, OPEN COUNTRY EXPOSURE

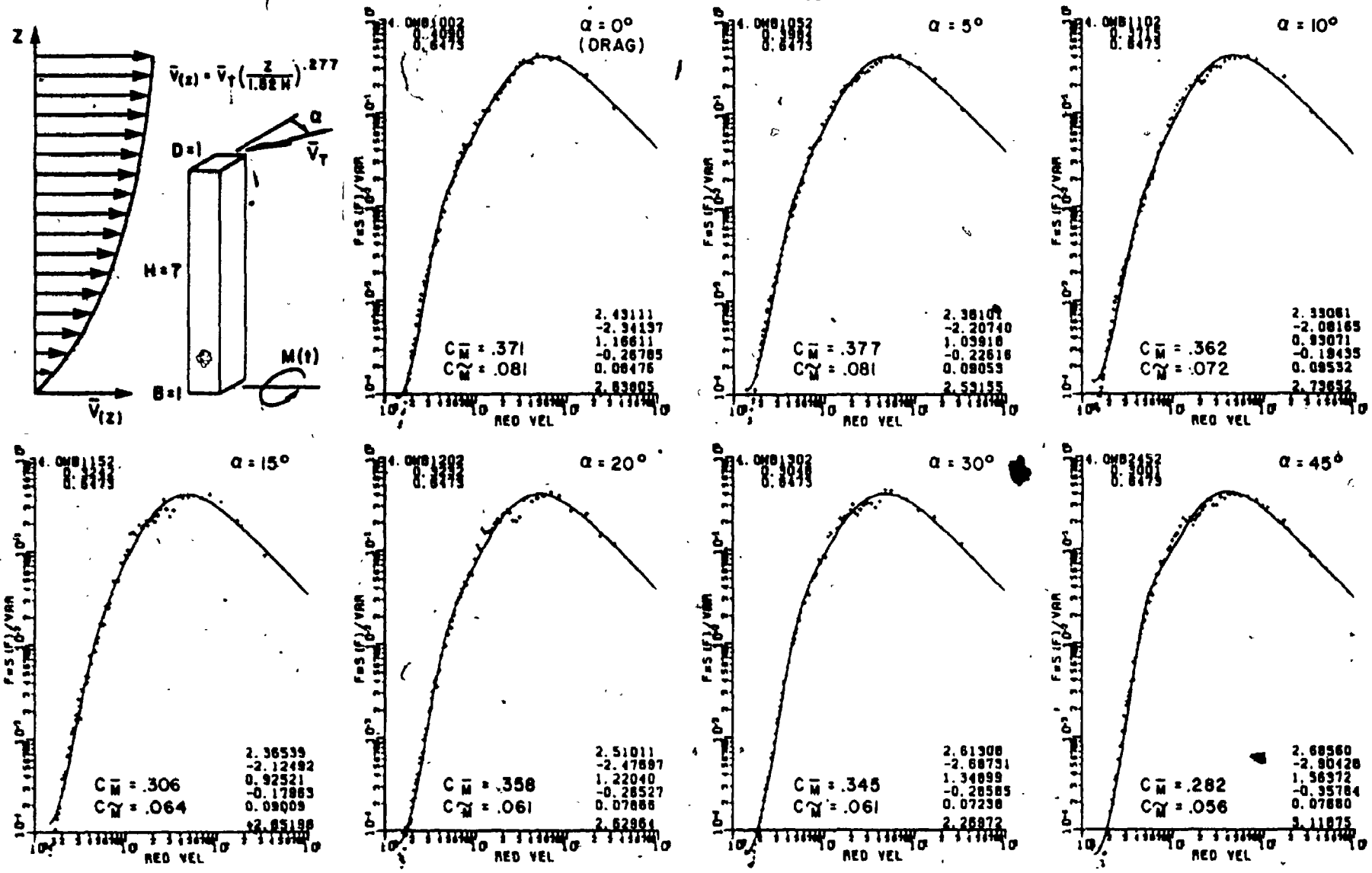

FIG. A.23.a MOMENTS ON A TALL 7:1:1 BUILDING, SUBURBAN EXPOSURE

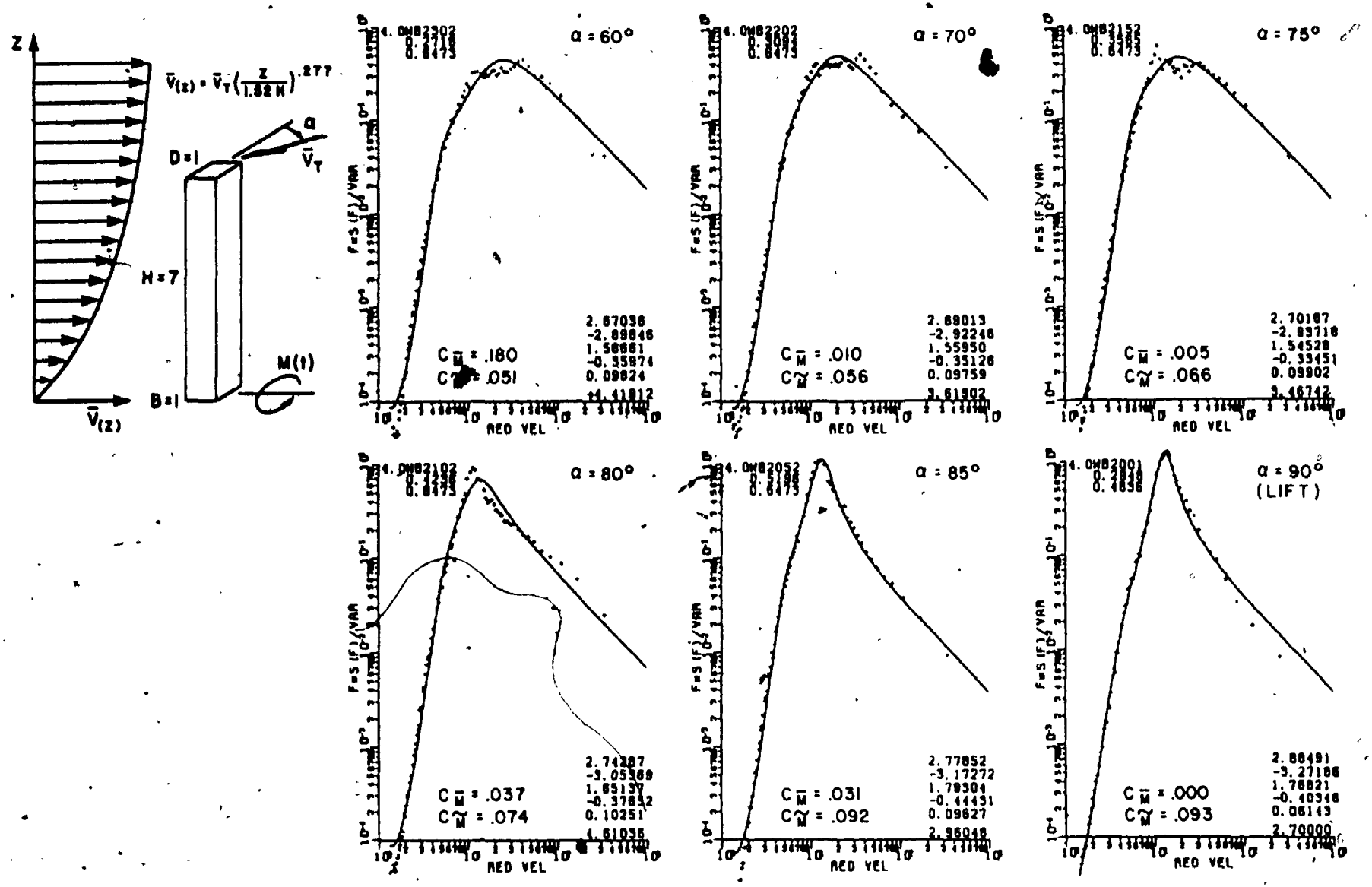

FIG. A.23.b MOMENTS ON A TALL 7:1:1 BUILDING, SUBURBAN EXPOSURE

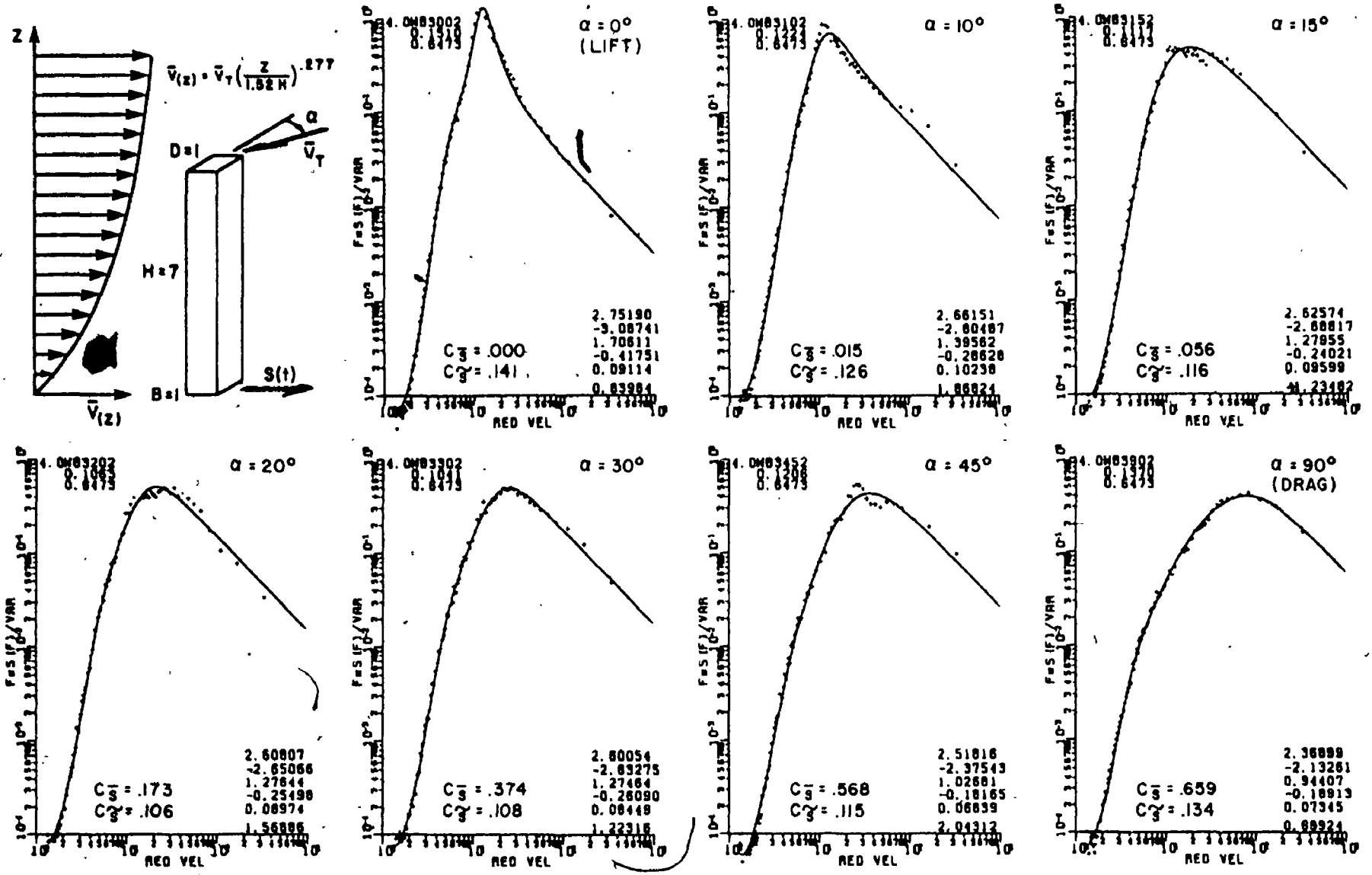

FIG. A.24 SHEARS ON A TALL 7:1:1 BUILDING, SUBURBAN EXPOSURE

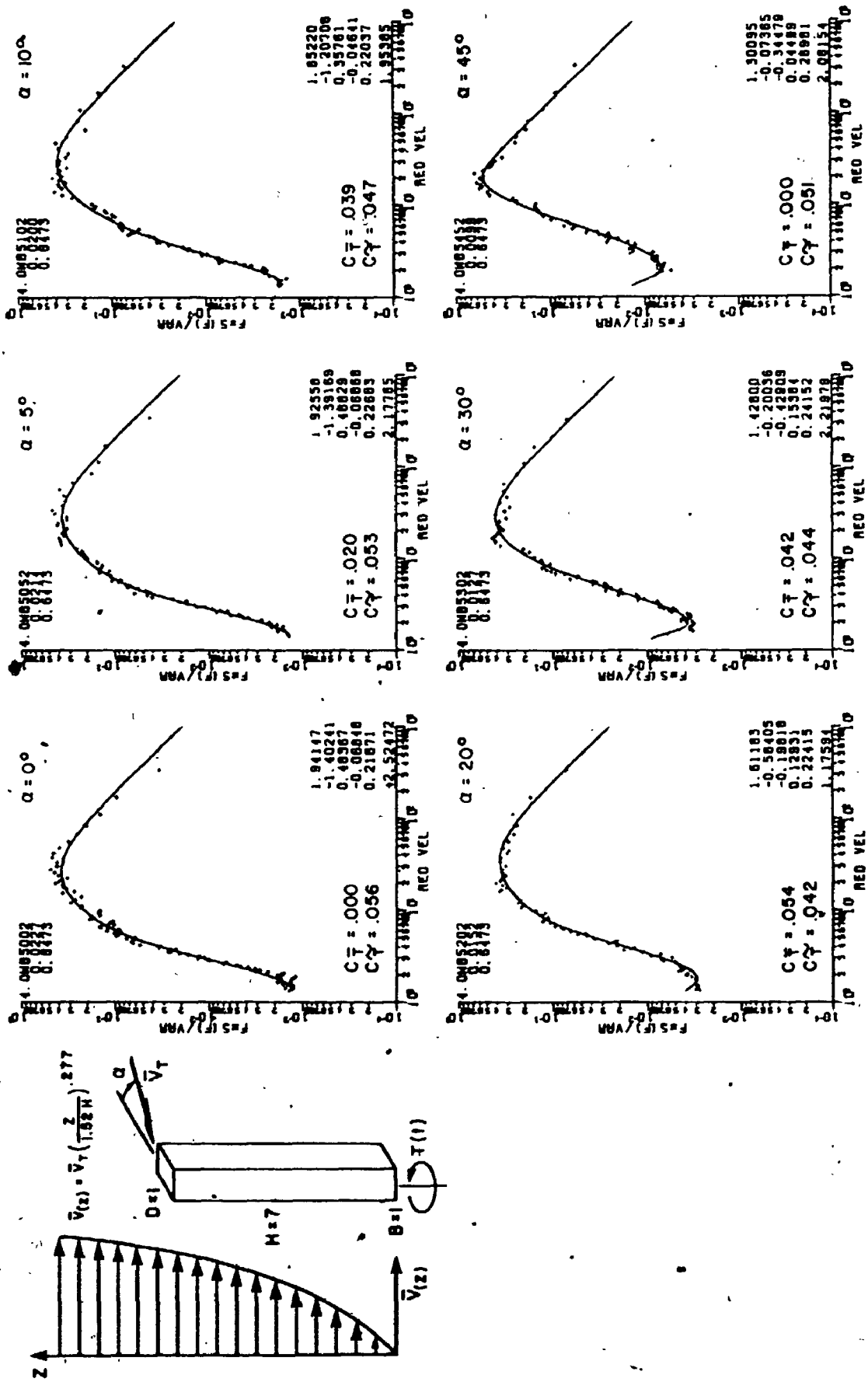

FIG. A.25 TORSIONS ON A TALL 7:1:1 BUILDING, SUBURBAN EXPOSURE

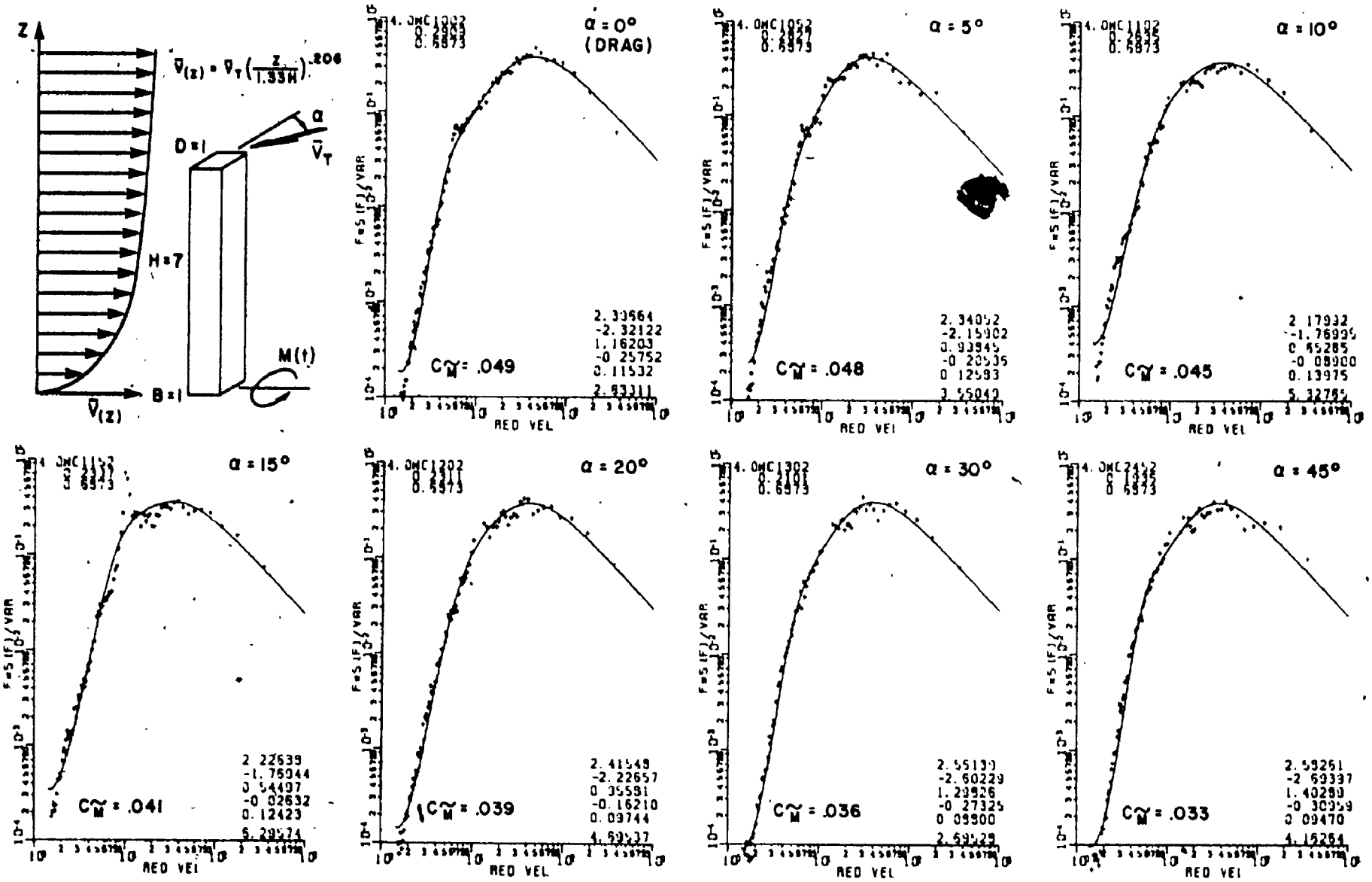

FIG. A.26.a MOMENTS ON A TALL 7:1:1 BUILDING, OPEN COUNTRY EXPOSURE

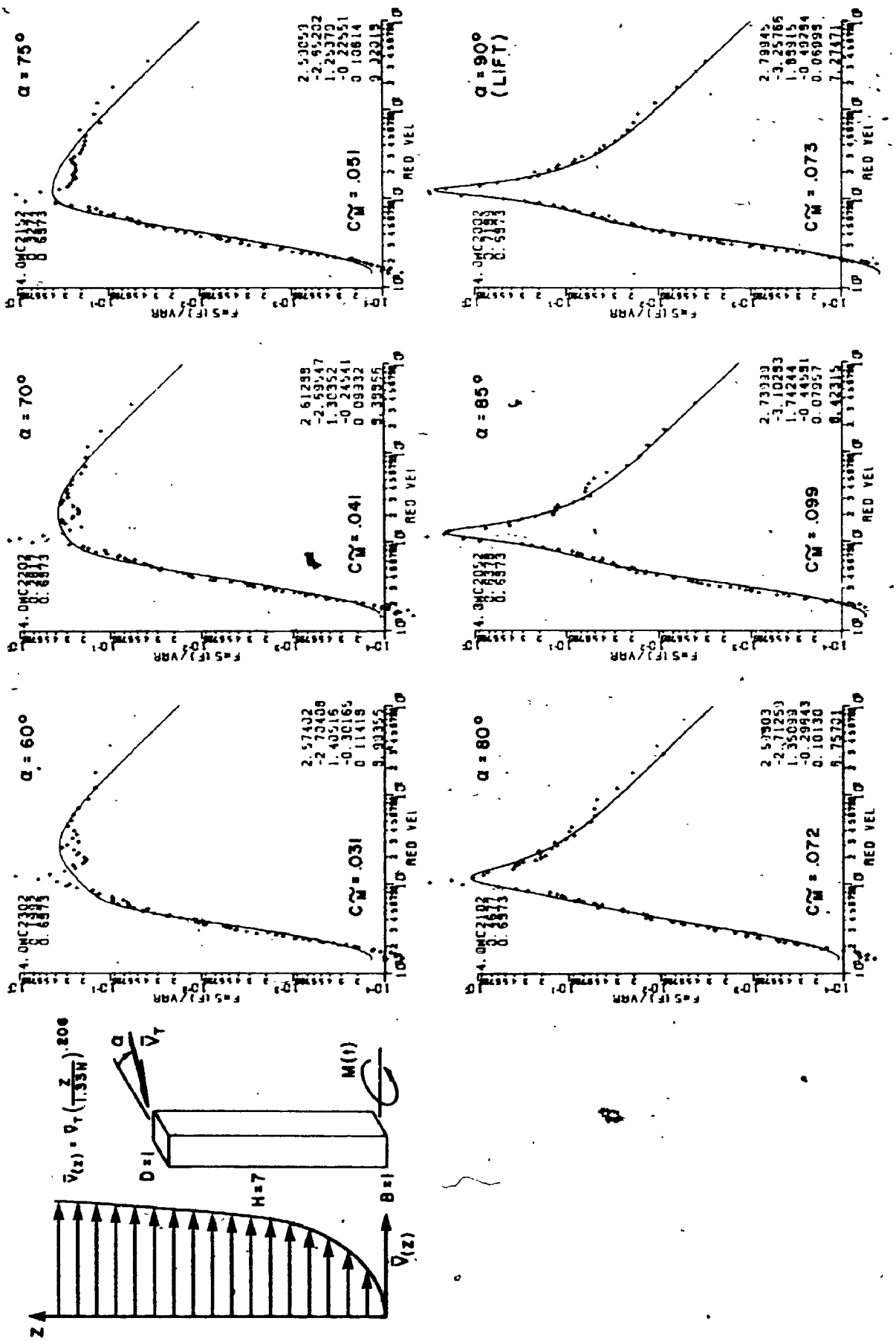

FIG. A.26.b MOMENTS ON A TALL 7:1:1 BUILDING, OPEN COUNTRY EXPOSURE

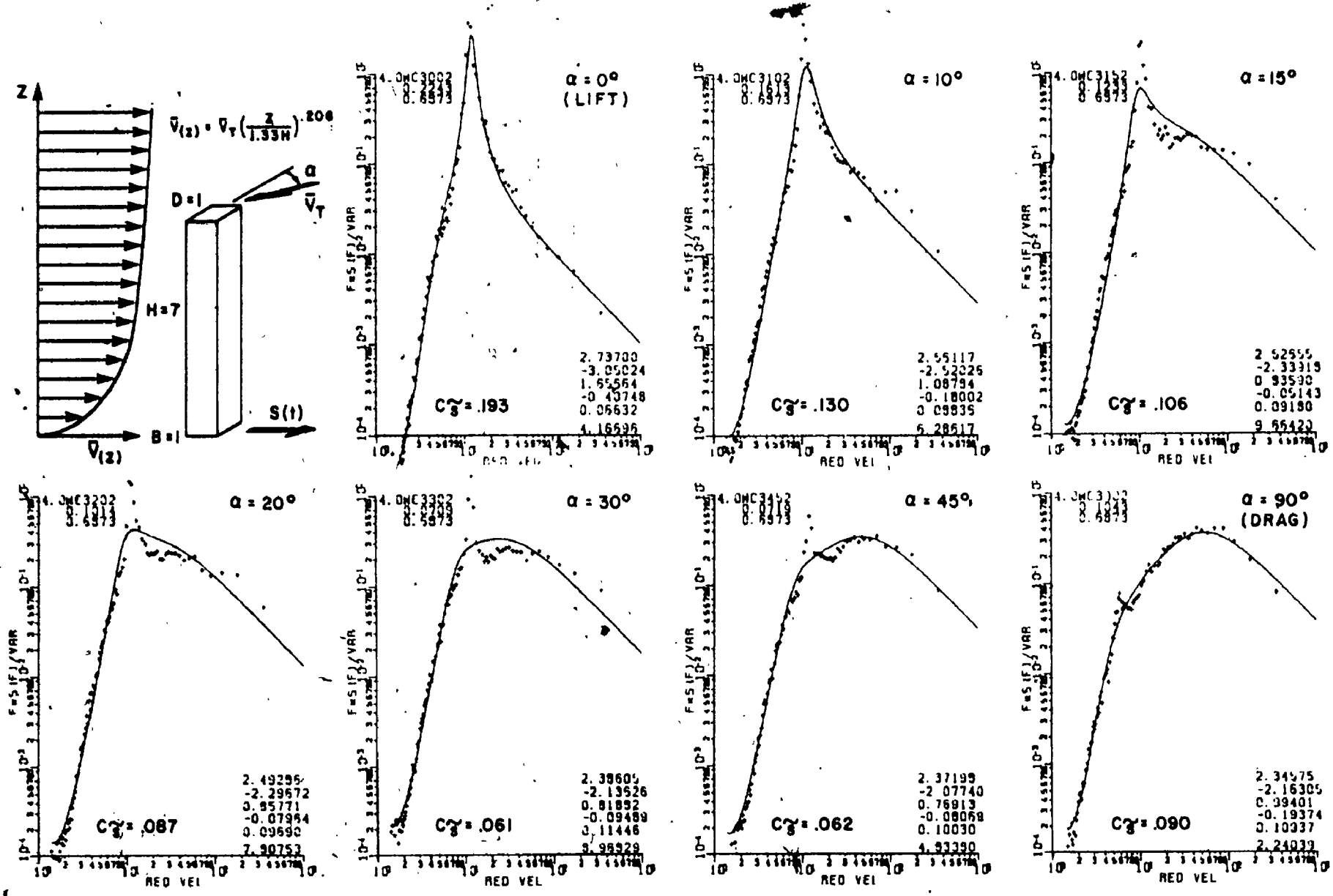

FIG. A.27 SHEARS ON A TALL 7:1:1 BUILDING, OPEN COUNTRY EXPOSURE

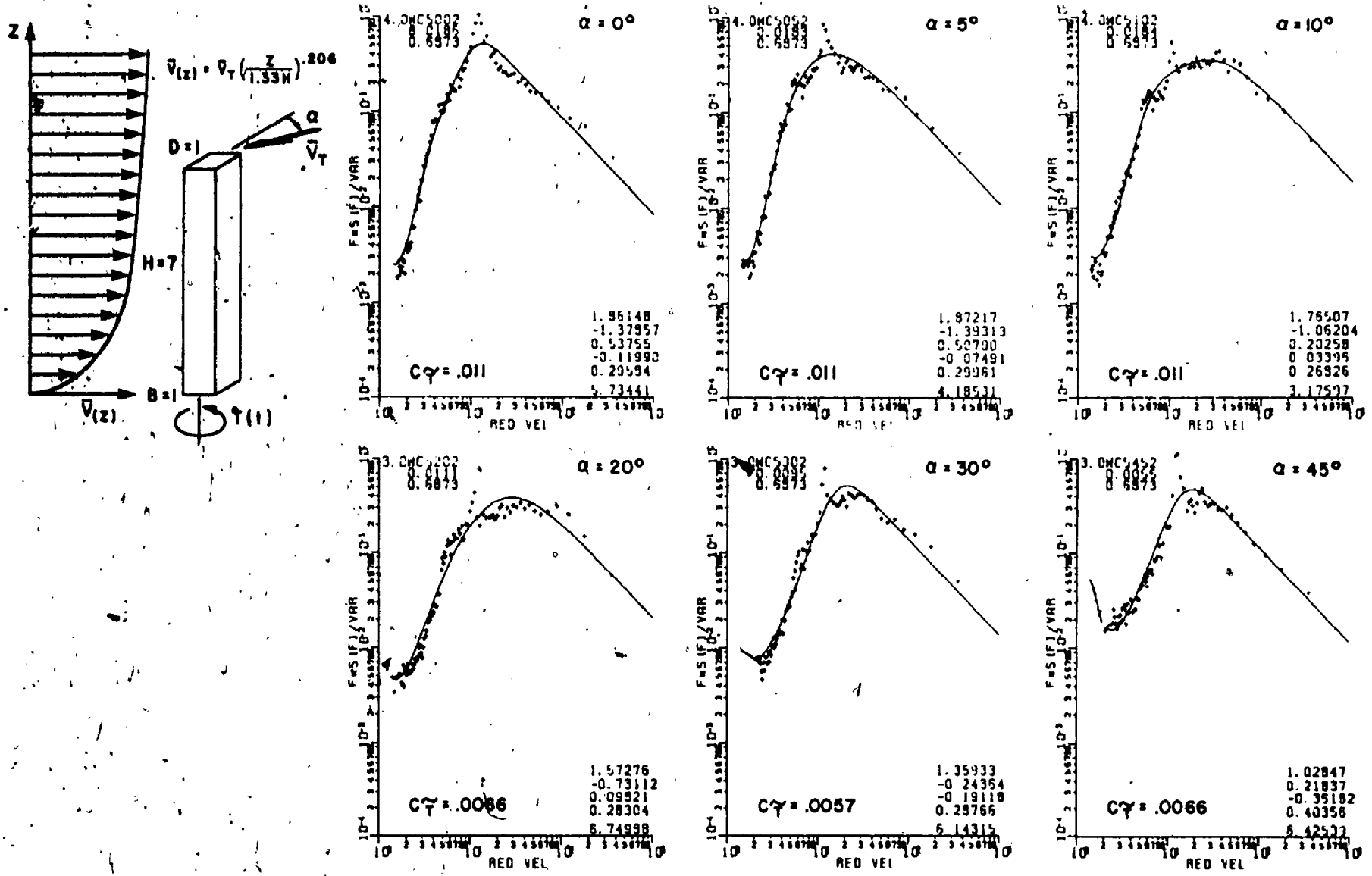

FIG. A.28 TORSIONS ON A TALL 7:1:1 BUILDING, OPEN COUNTRY EXPOSURE

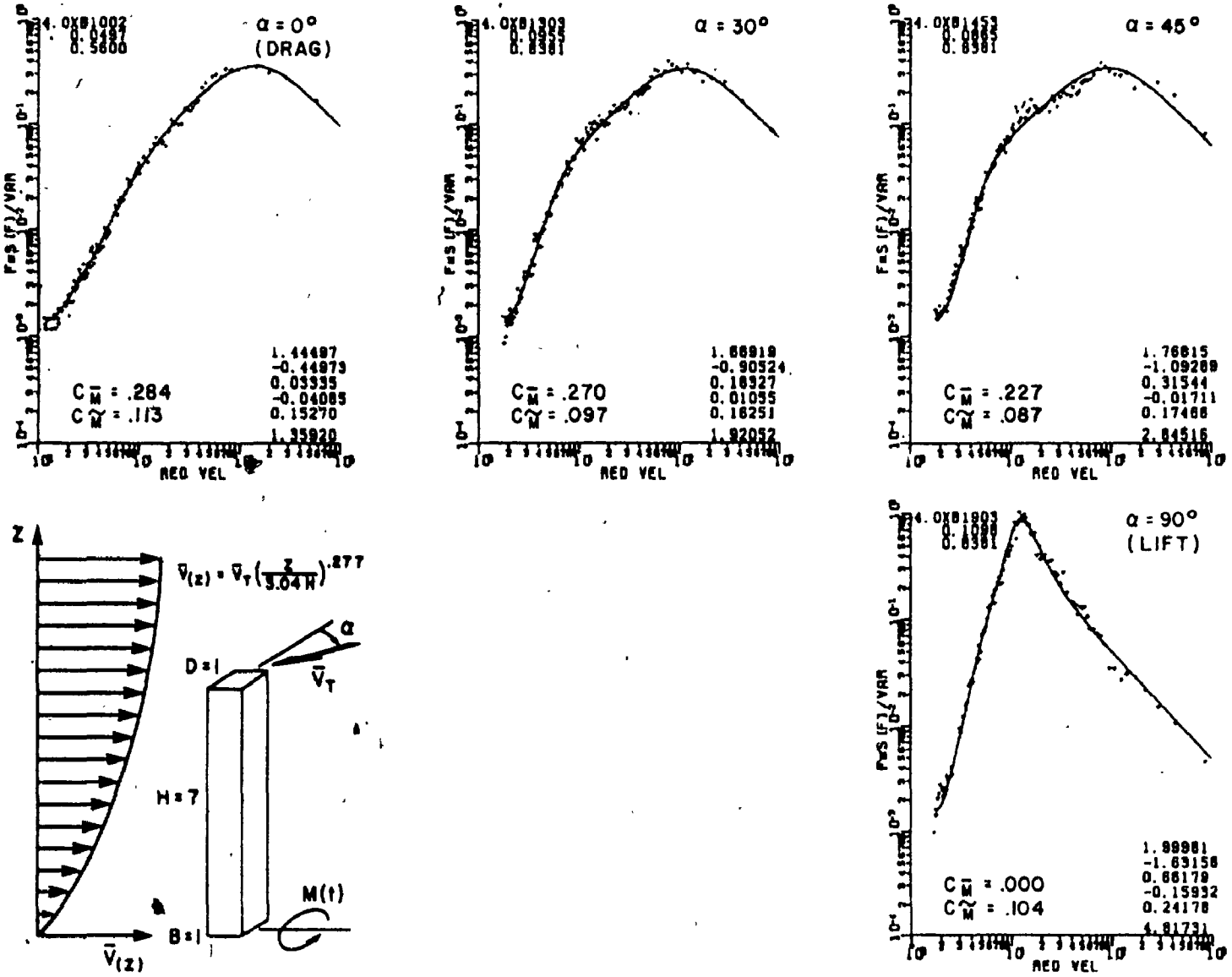

FIG. A.29 MOMENTS ON A MEDIUM TALL 7:1:1 BUILDING, SUBURBAN EXPOSURE

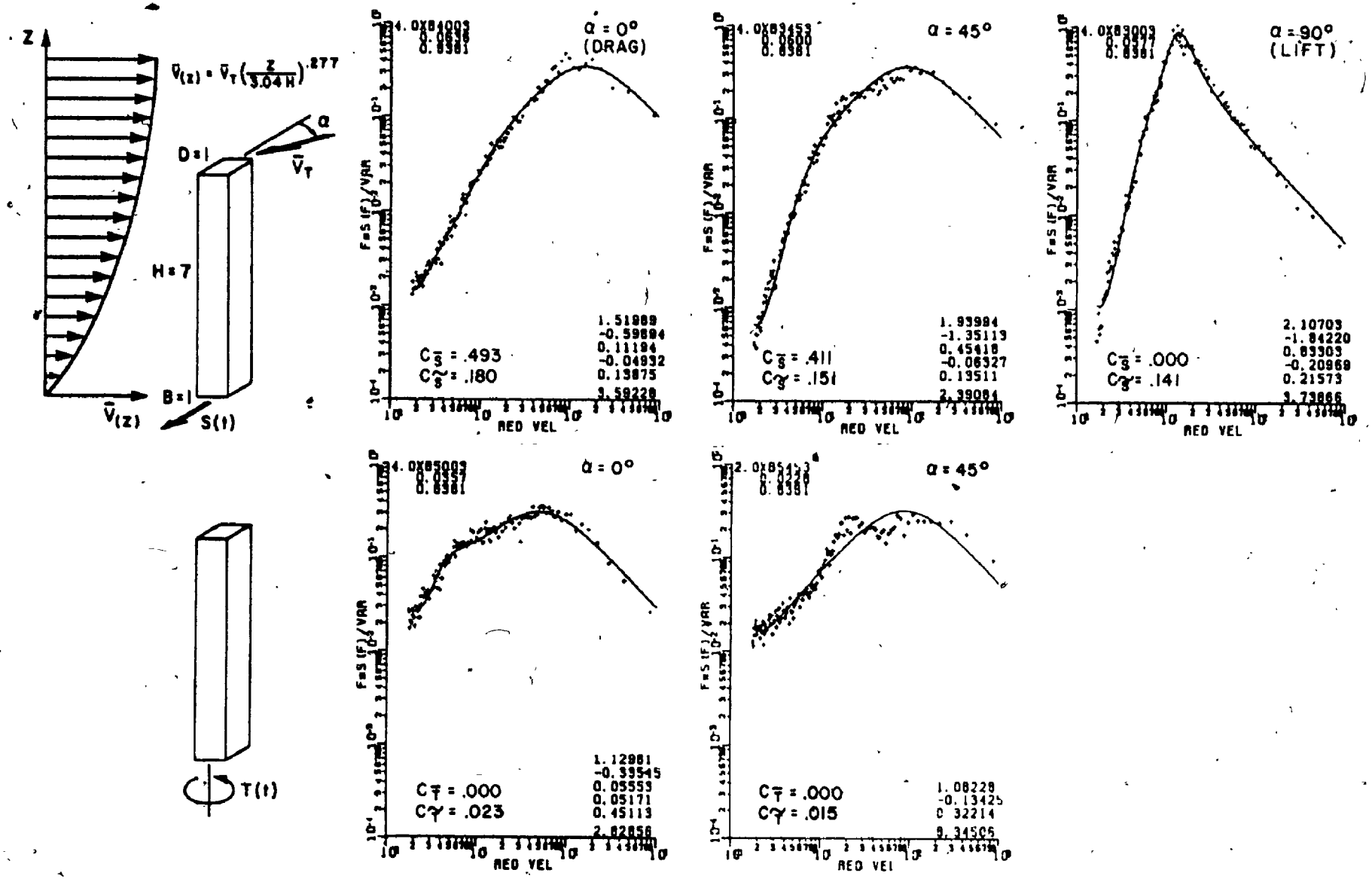

FIG. A.30 SHEARS AND TORSIONS ON A MEDIUM TALL 7:1:1 BUILDING, SUBURBAN EXPOSURE

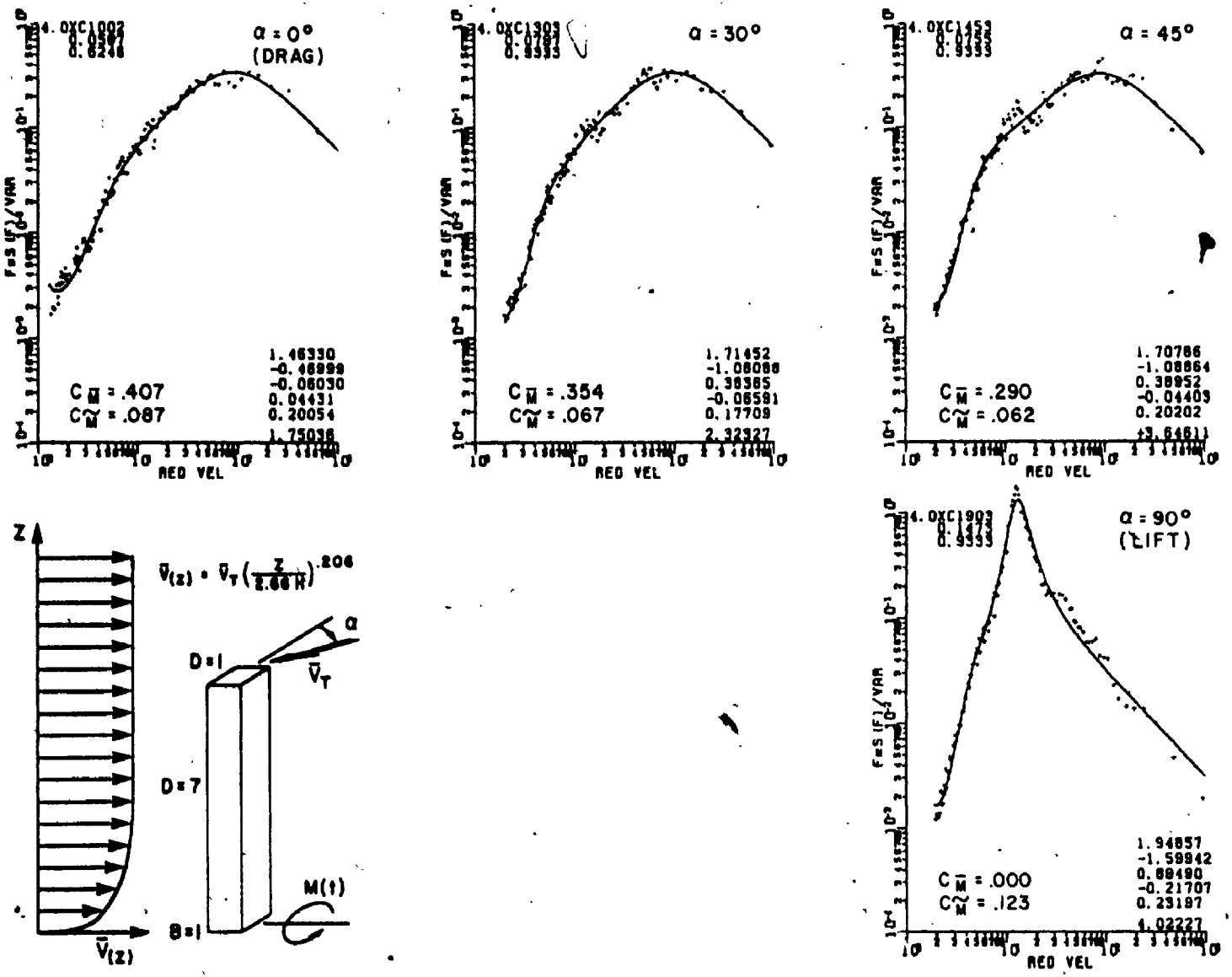

FIG. A.31 MOMENTS ON A MEDIUM TALL 7:1:1 BUILDING, OPEN COUNTRY EXPOSURE

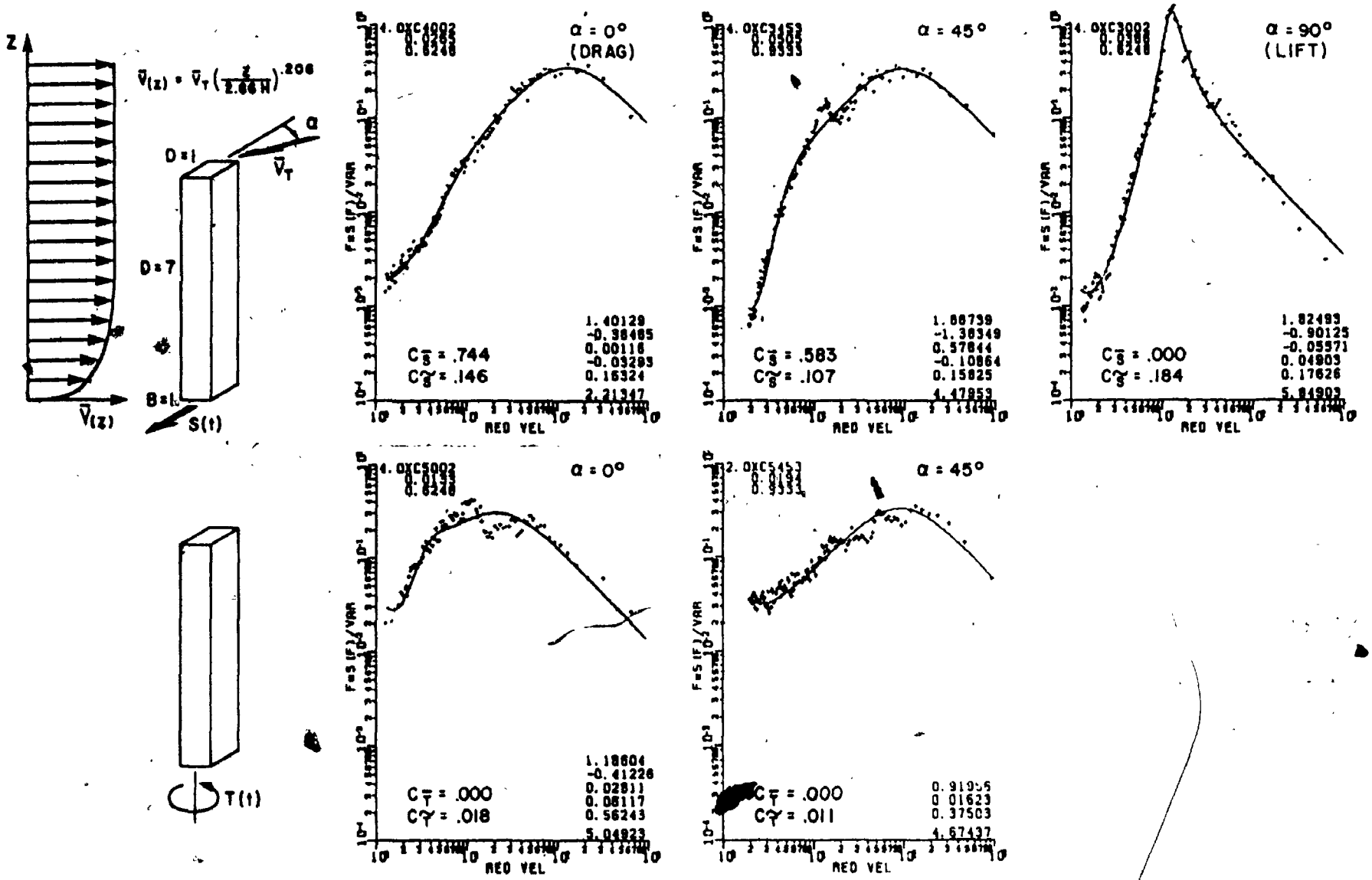

FIG. A.32 SHEARS AND TORSIONS ON A MEDIUM TALL 7:1:1 BUILDING, OPEN COUNTRY EXPOSURE

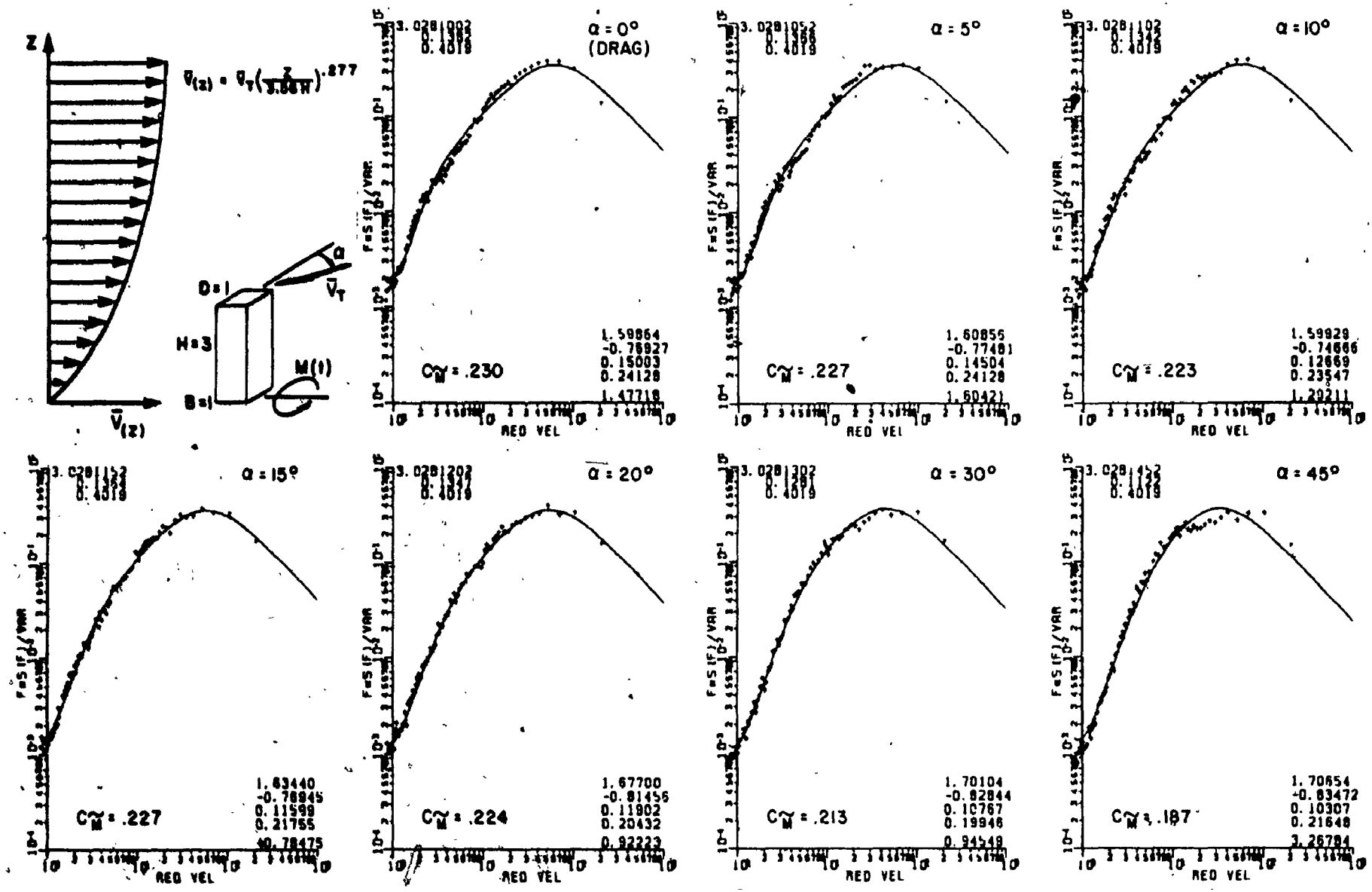

FIG. A.33.a MOMENTS ON A 3:1:1 BUILDING, SUBURBAN EXPOSURE

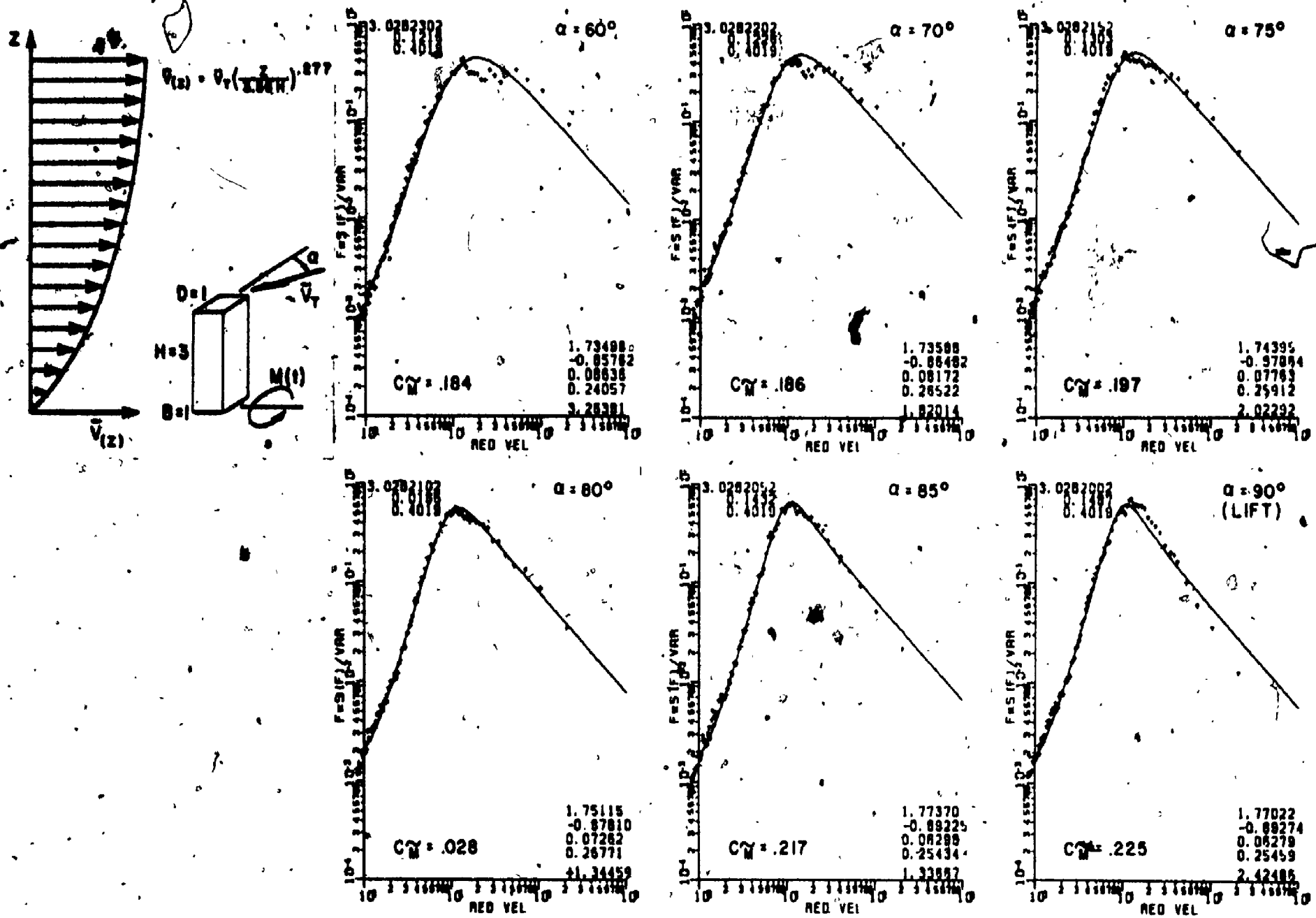

FIG. A.33.b MOMENTS ON A 3:1:1 BUILDING, SUBURBAN EXPOSURE

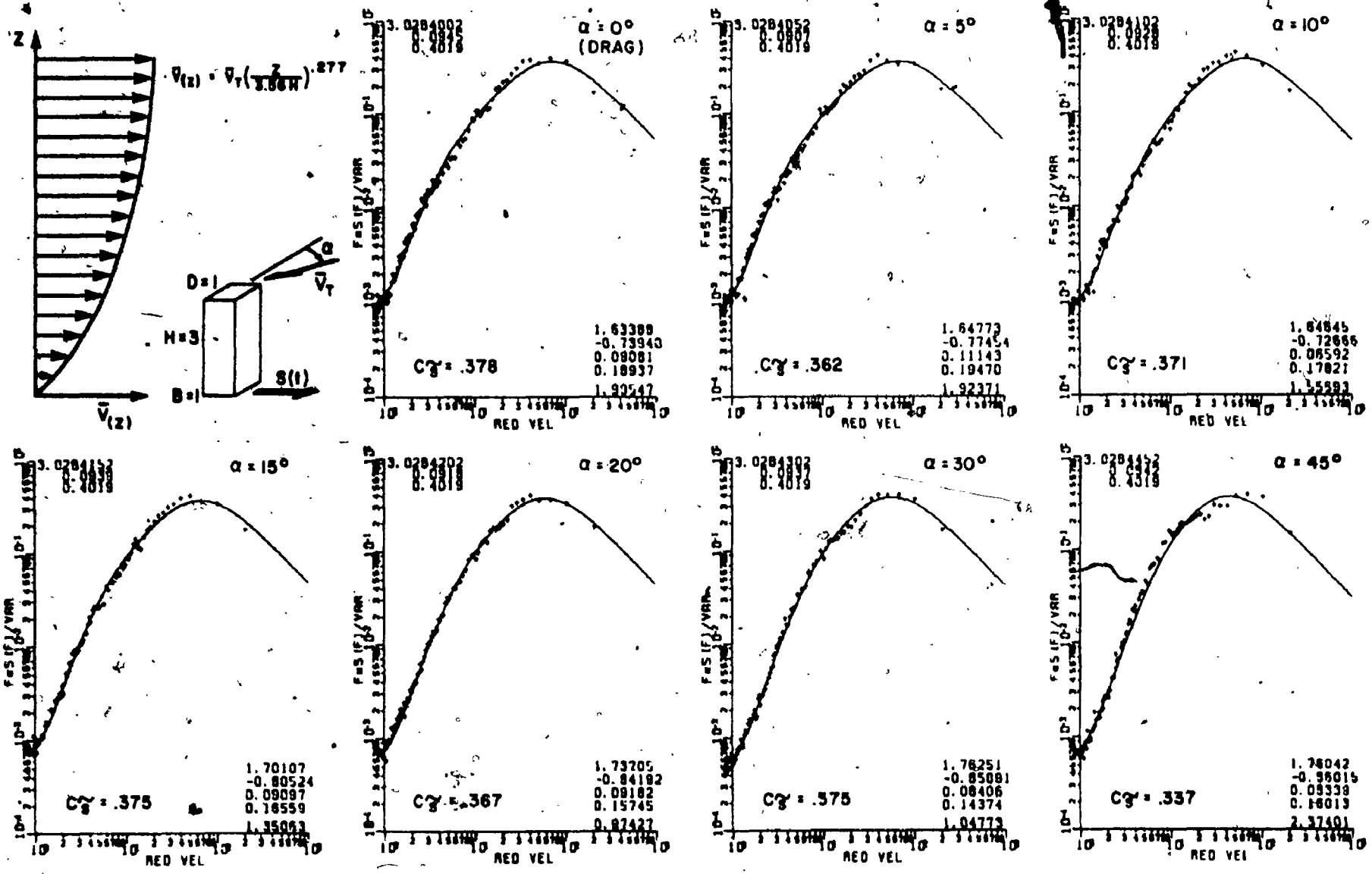

FIG. A.34.a . SHEARS ON A 3:1:1 BUILDING, SUBURBAN EXPOSURE

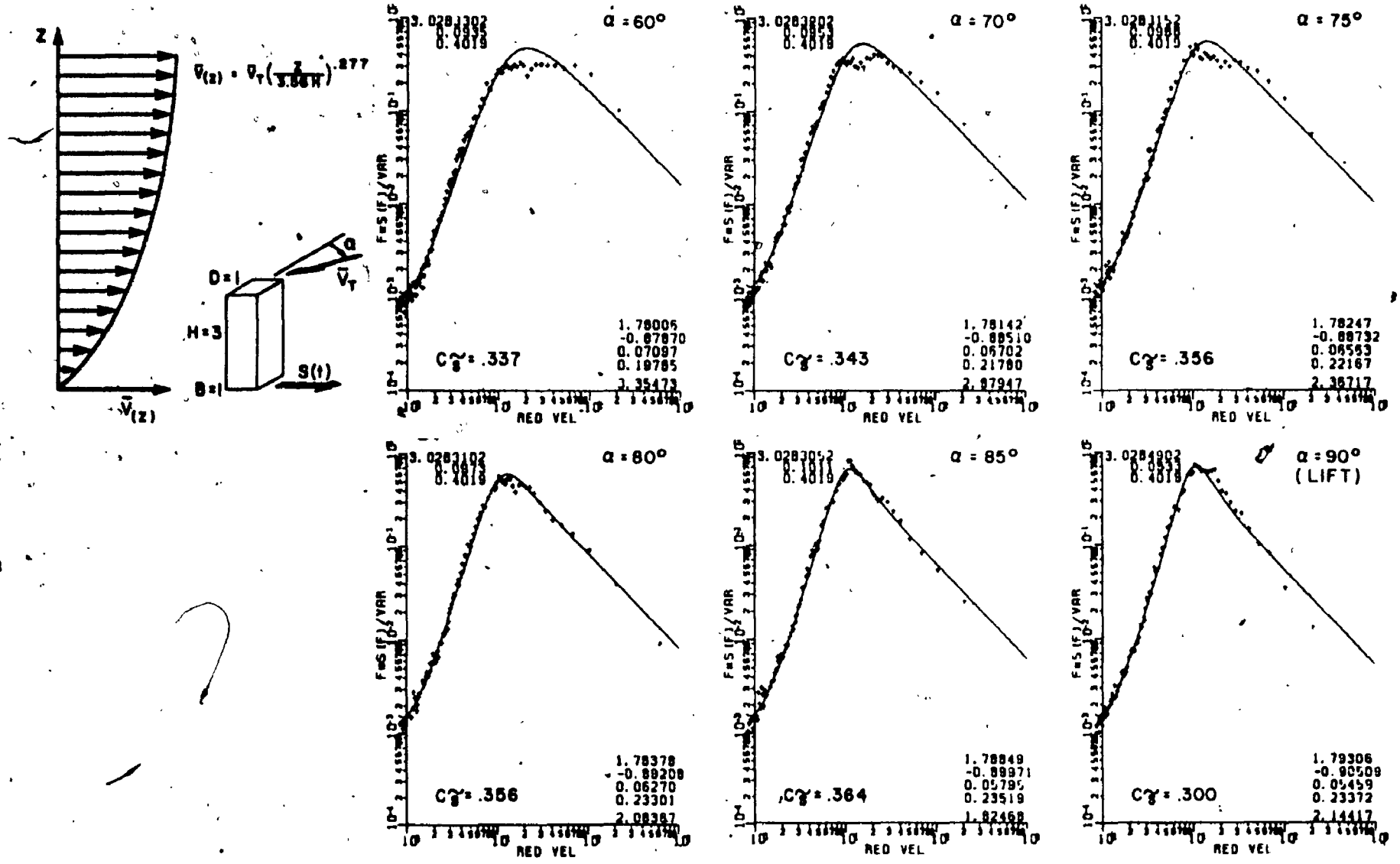

FIG. A34.b SHEARS ON A 3:1:1 BUILDING, SUBURBAN EXPOSURE

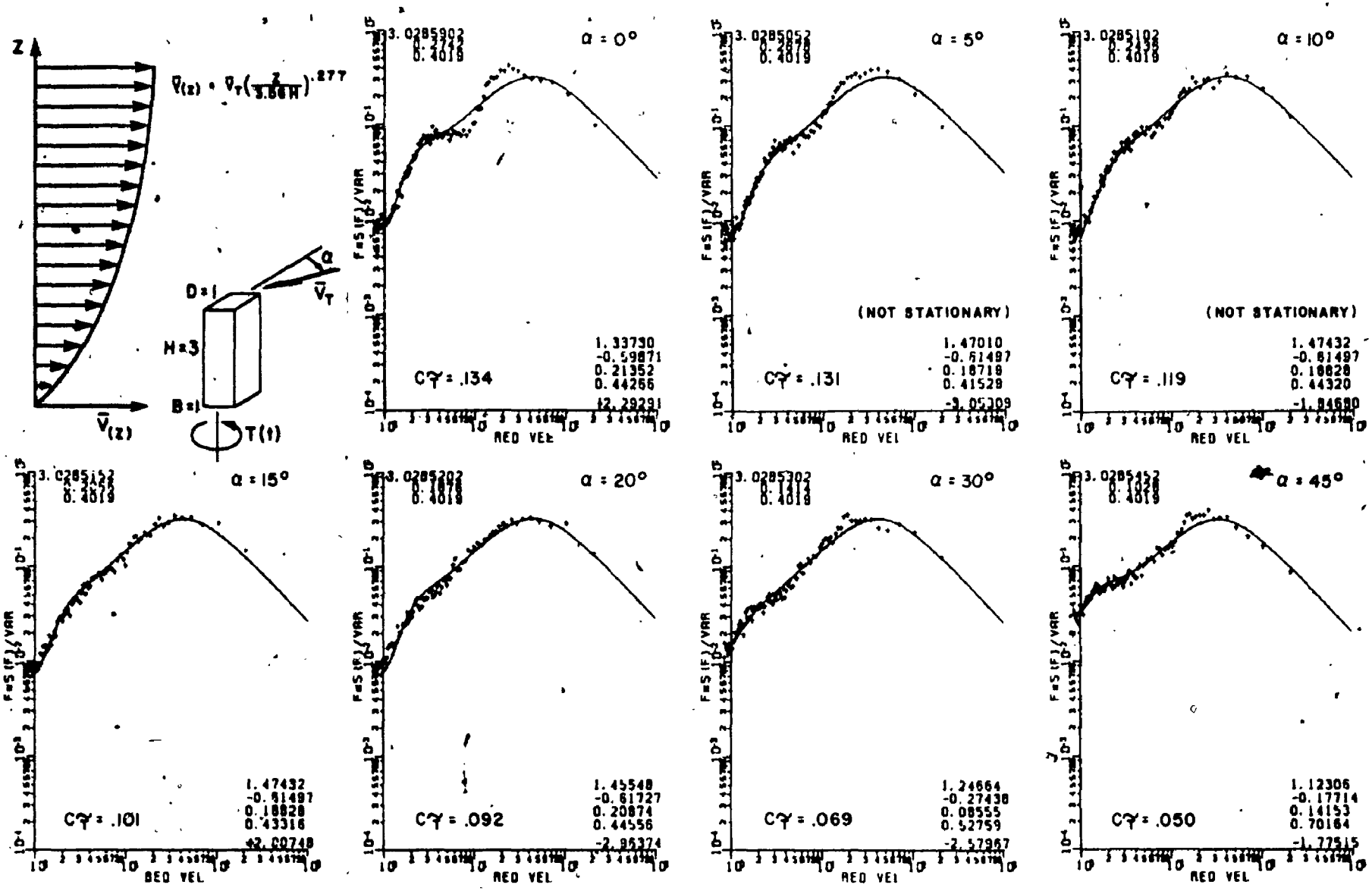

FIG. A35 TORSIONS ON A 3:1:1 BUILDING, SUBURBAN EXPOSURE

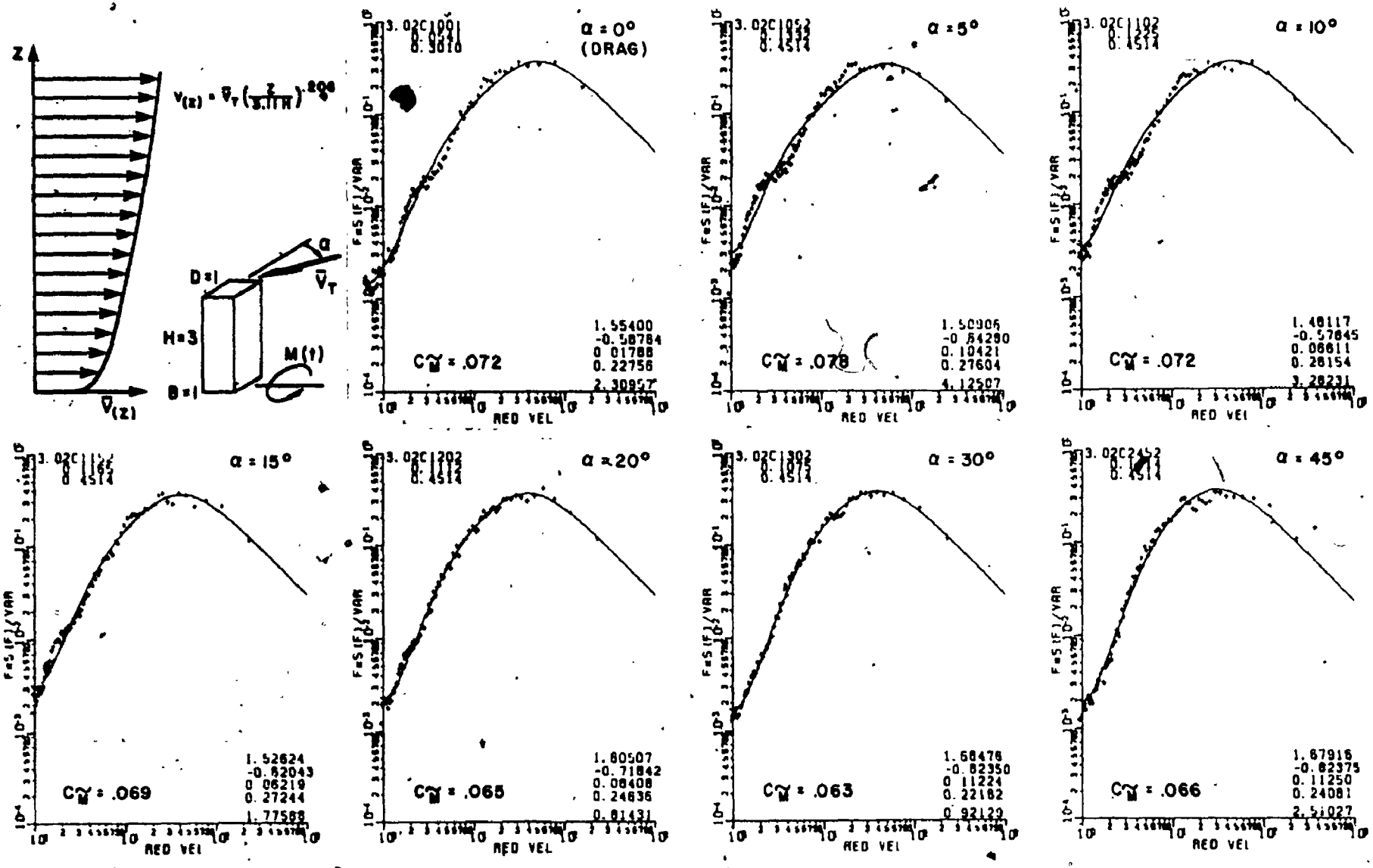

FIG. A.36.a MOMENTS ON A 3:1:1 BUILDING, OPEN COUNTRY EXPOSURE

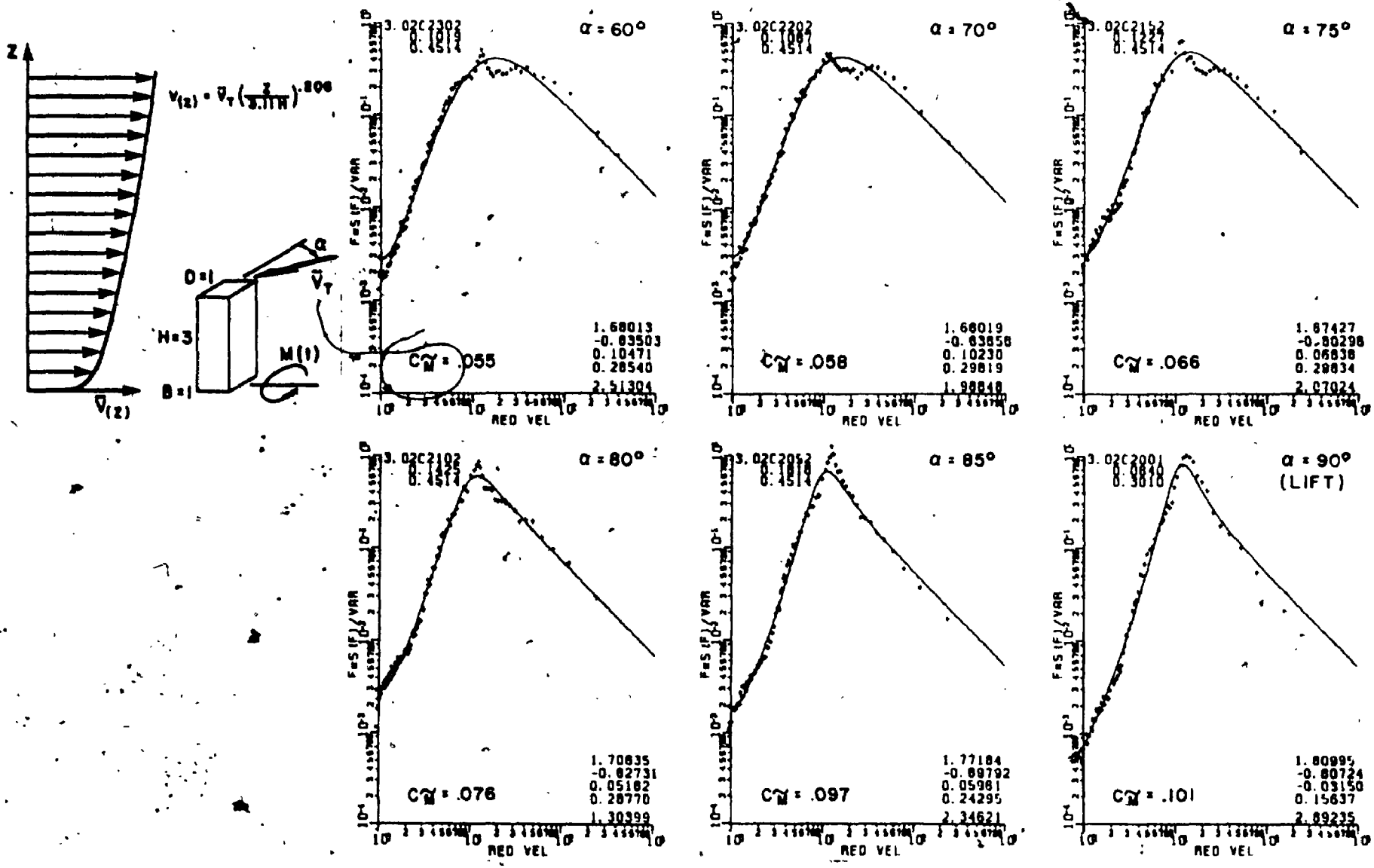

FIG. A.36.b MOMENTS ON A 3:1:1 BUILDING, OPEN COUNTRY EXPOSURE

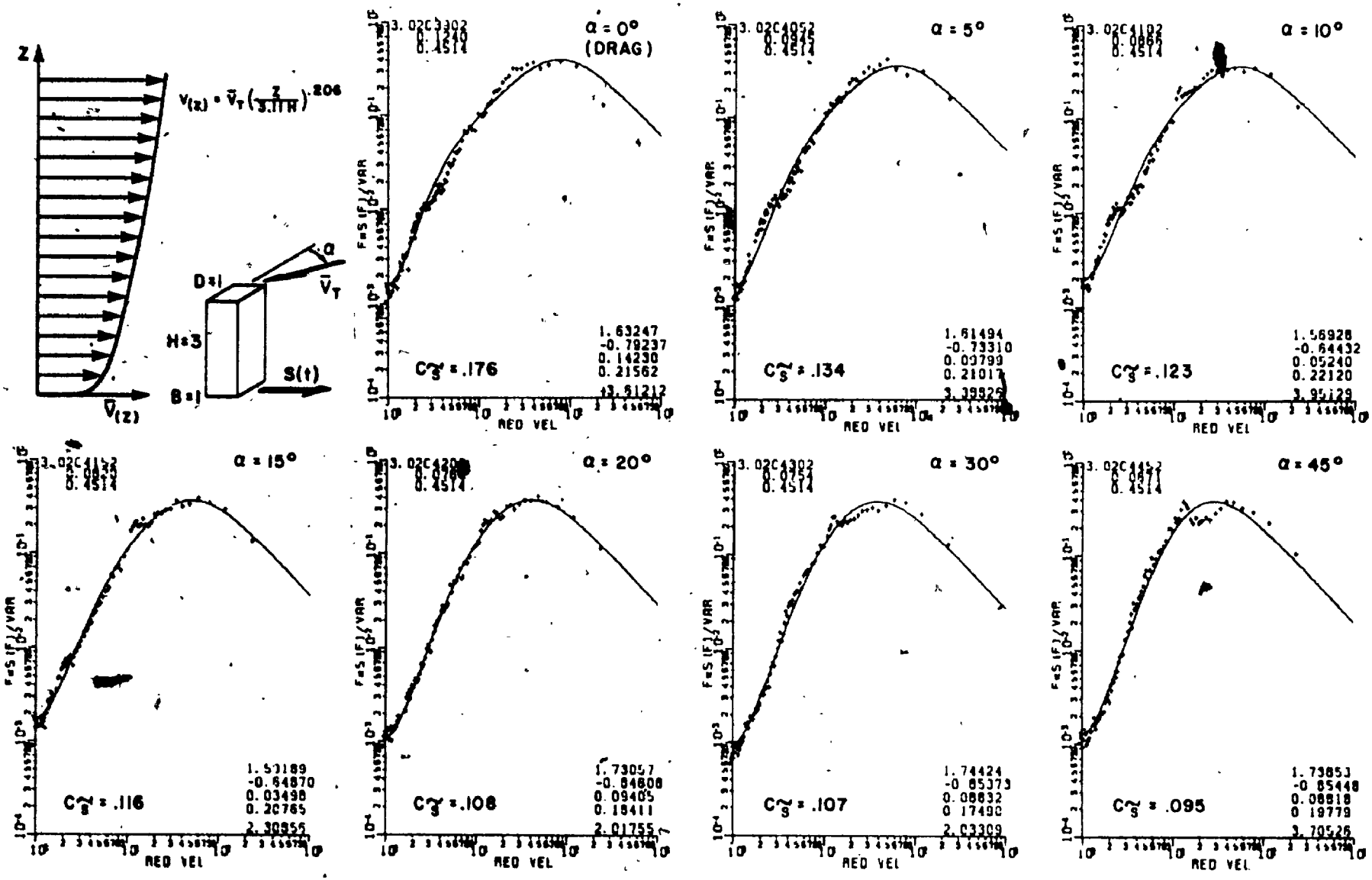

FIG. A.37.a SHEARS ON A 3:1:1 BUILDING, OPEN COUNTRY EXPOSURE

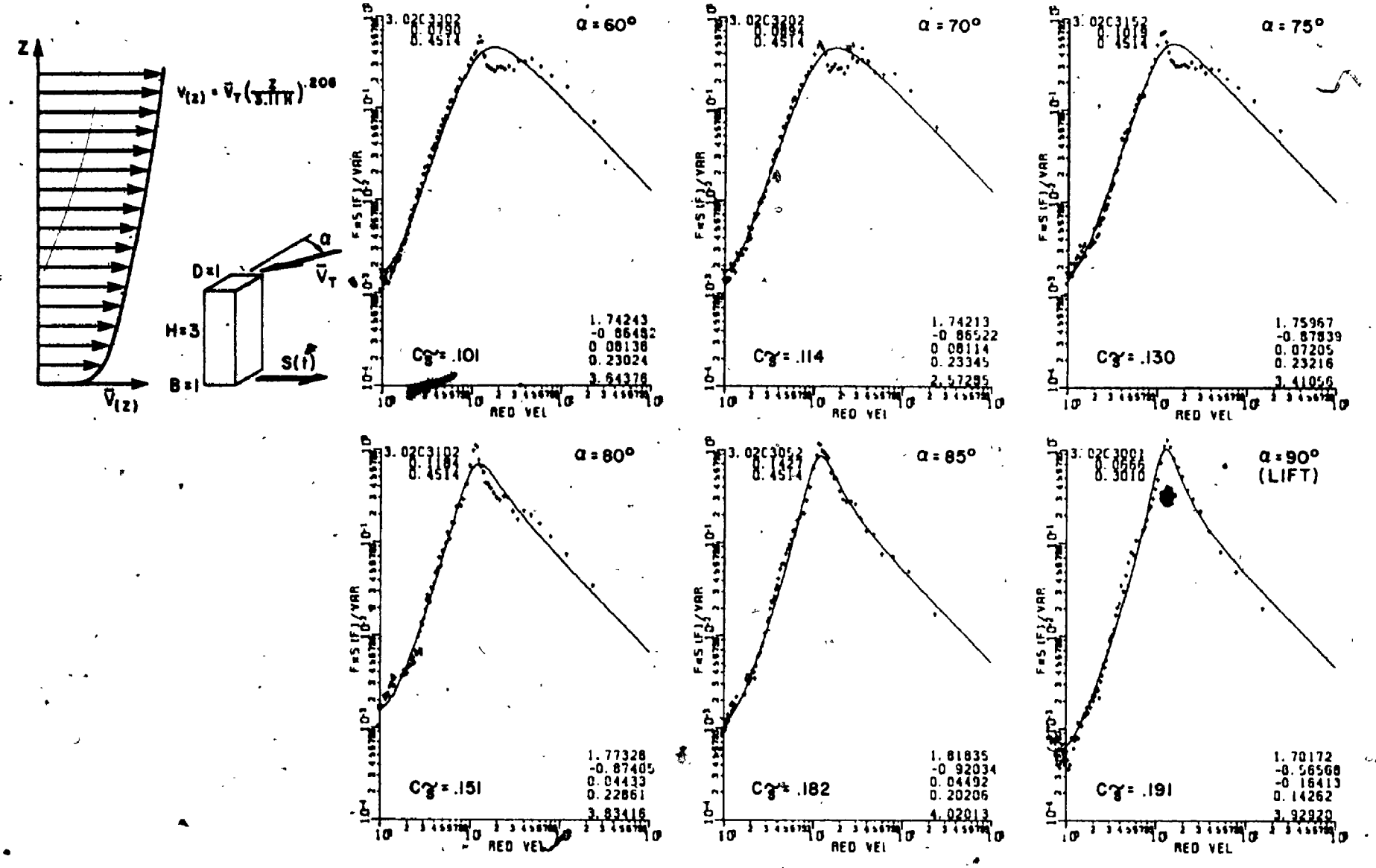

FIG. A37.b SHEARS ON A 3:1:1 BUILDING, OPEN COUNTRY EXPOSURE

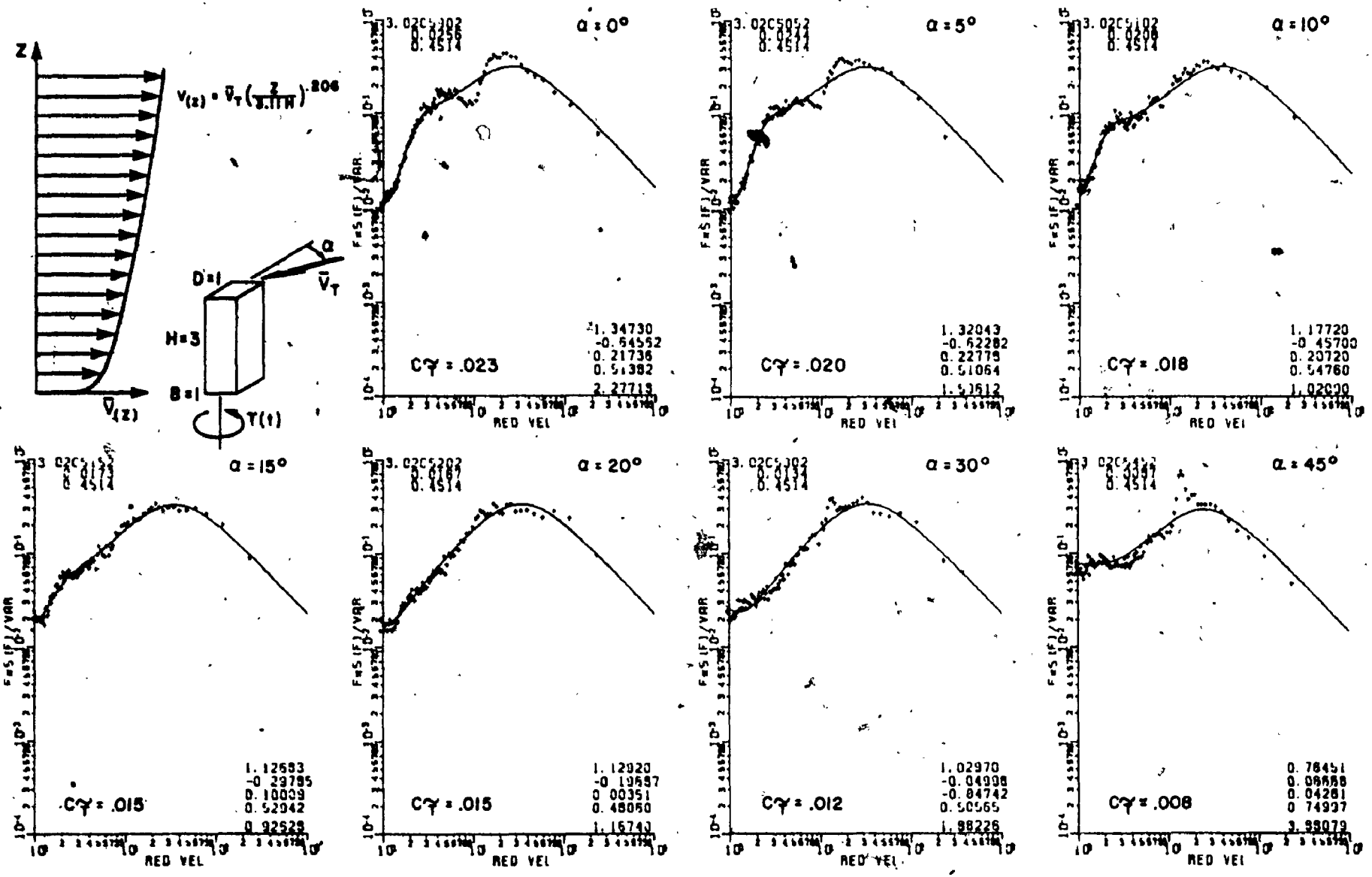

FIG. A.38 TORSIONS ON A 3:1:1 BUILDING, OPEN COUNTRY EXPOSURE

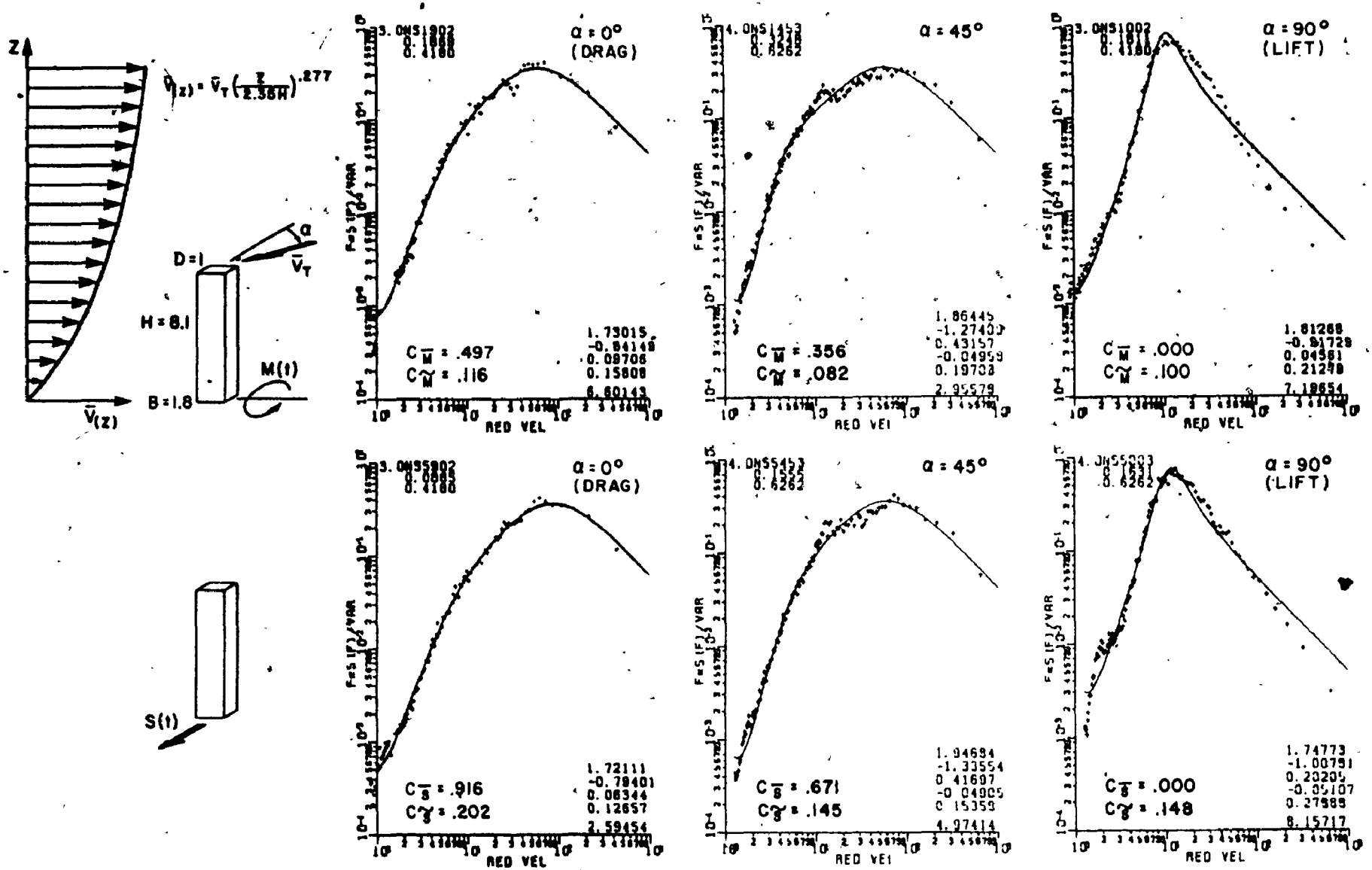

FIG. A39 MOMENTS AND SHEARS ON BROAD SIDE OF AN 8.1:1.8:1 BUILDING, SUBURBAN EXPOSURE

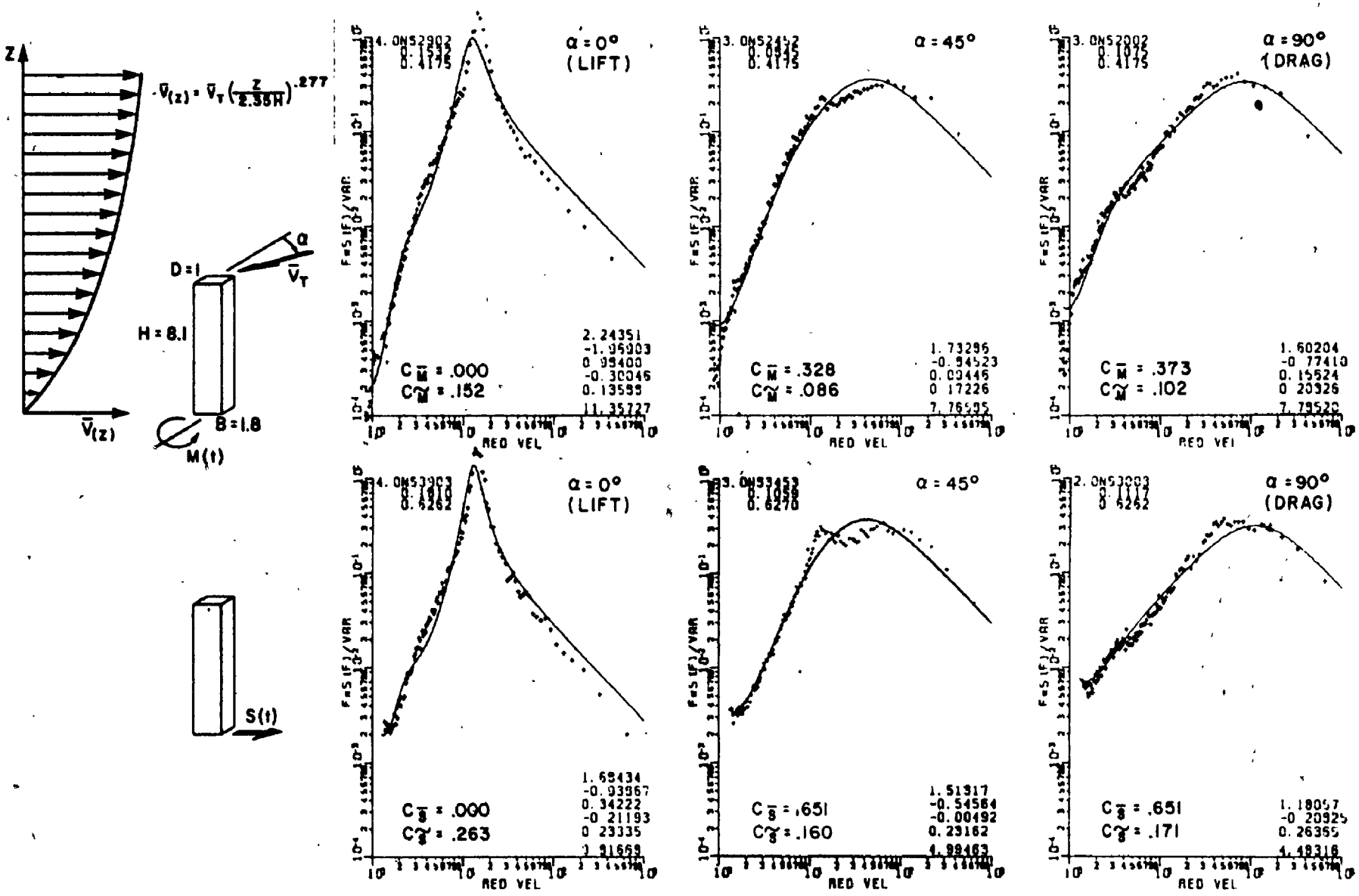

FIG. A.40 MOMENTS OF SHEARS ON NARROW SIDE OF AN 8.1:1.8:1 BUILDING, SUBURBAN EXPOSURE

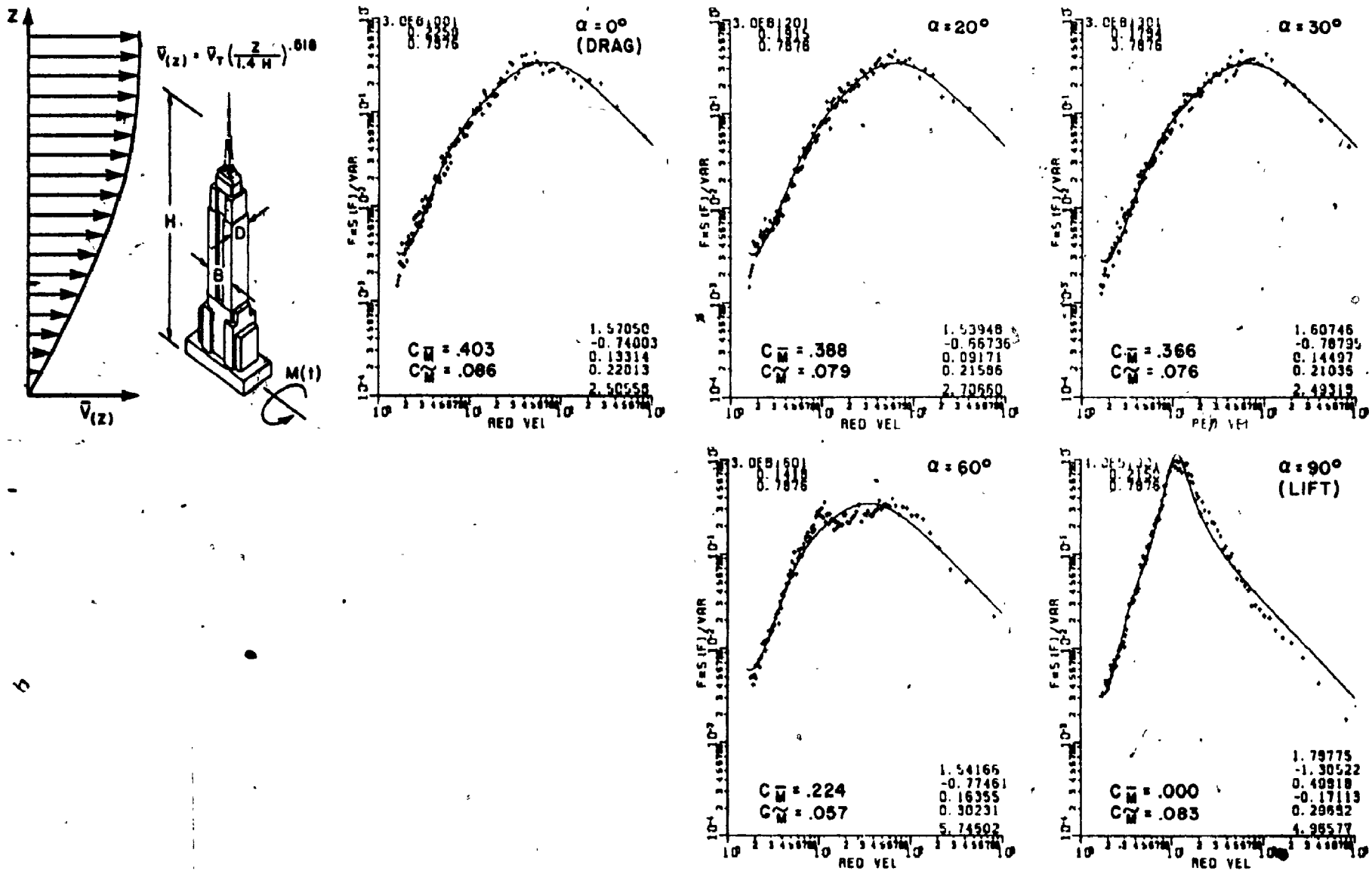

FIG. A.41 MOMENTS ON THE BROAD SIDE OF THE EMPIRE STATE BUILDING, SUBURBAN EXPOSURE

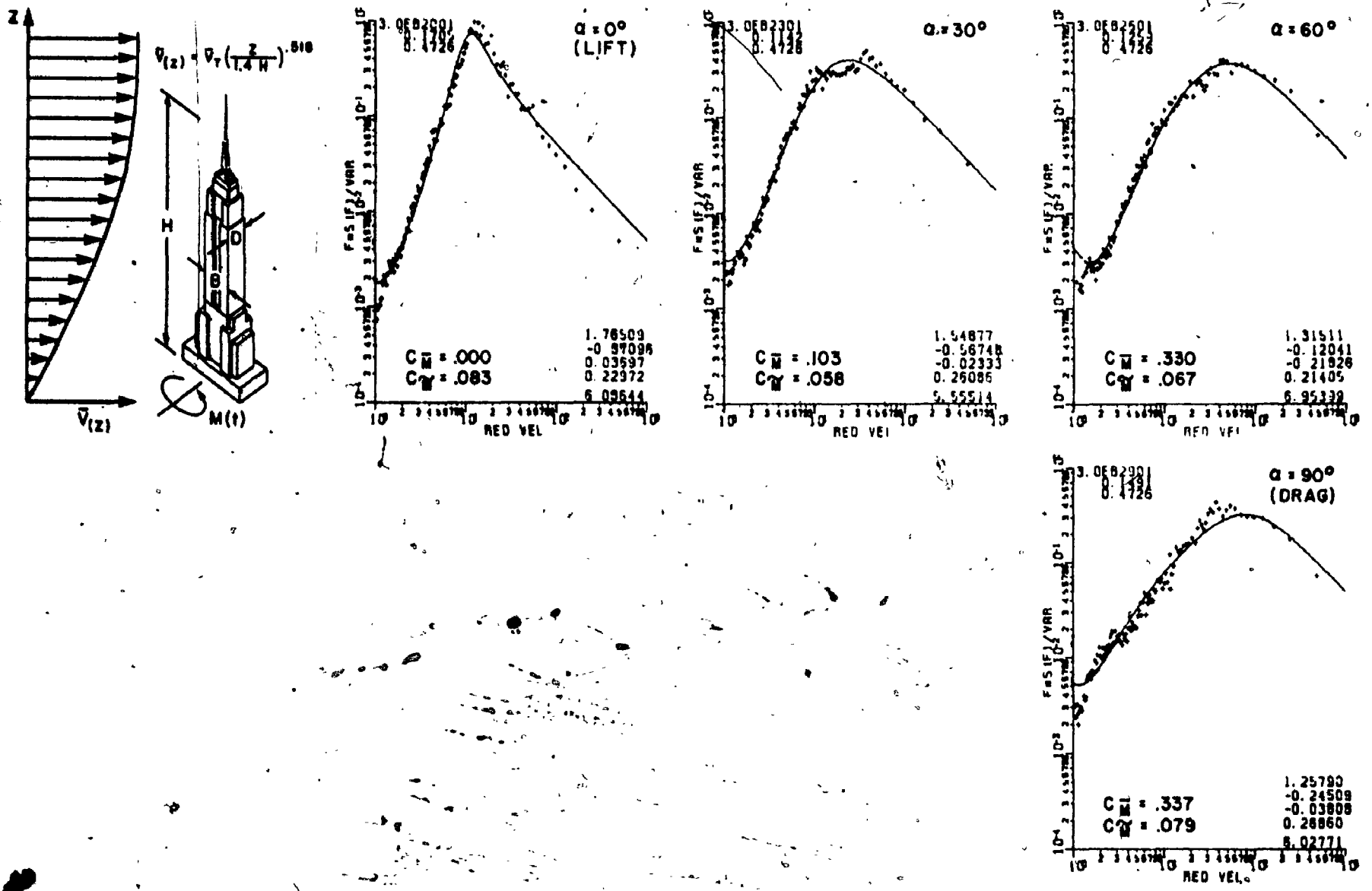

FIG. A.42 MOMENTS ON NARROW SIDE OF THE EMPIRE STATE BUILDING, SUBURBAN EXPOSURE

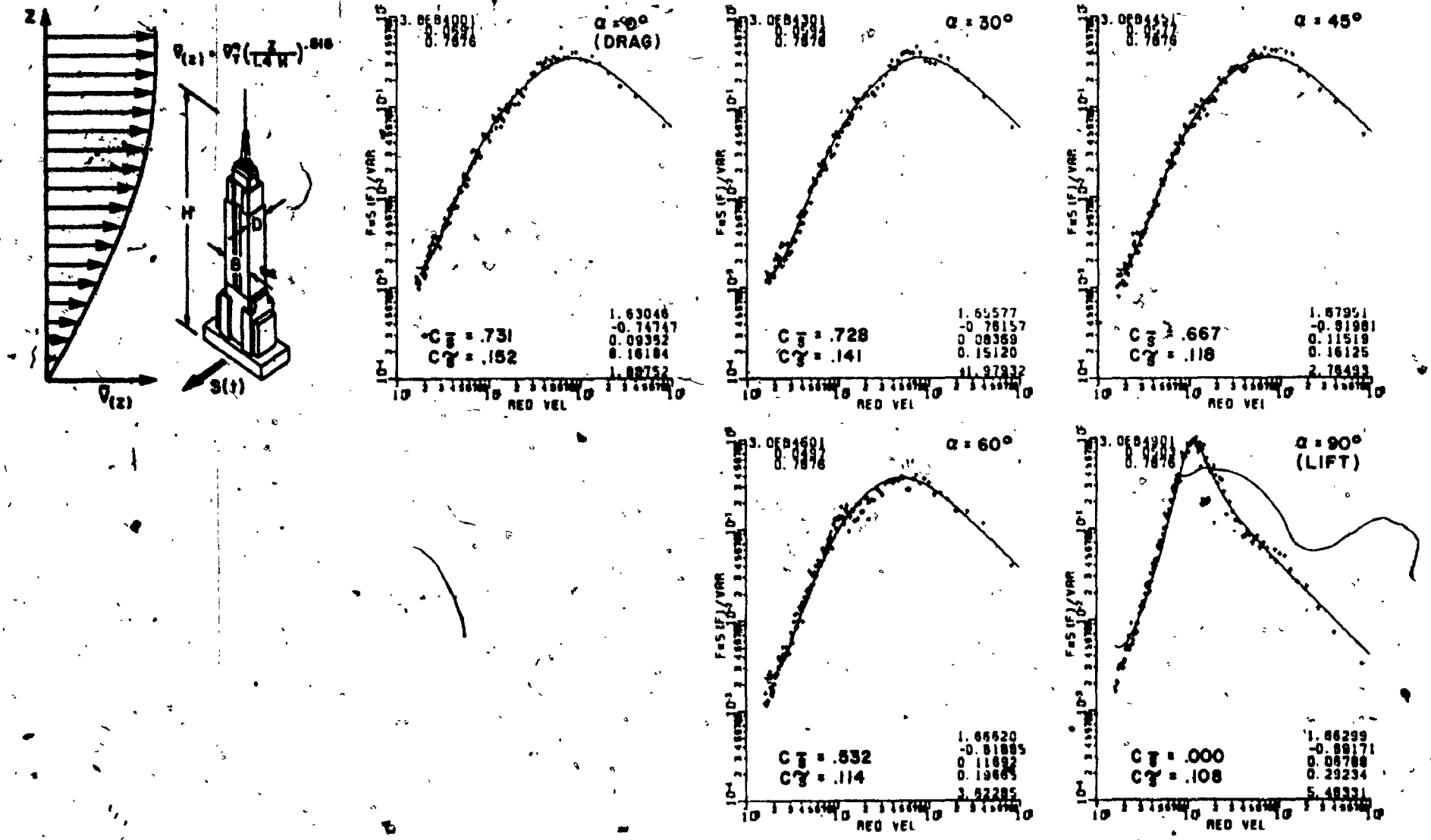

FIG. A.43 SHEARS ON BROAD SIDE OF EMPIRE STATE BUILDING, SUBURBAN EXPOSURE

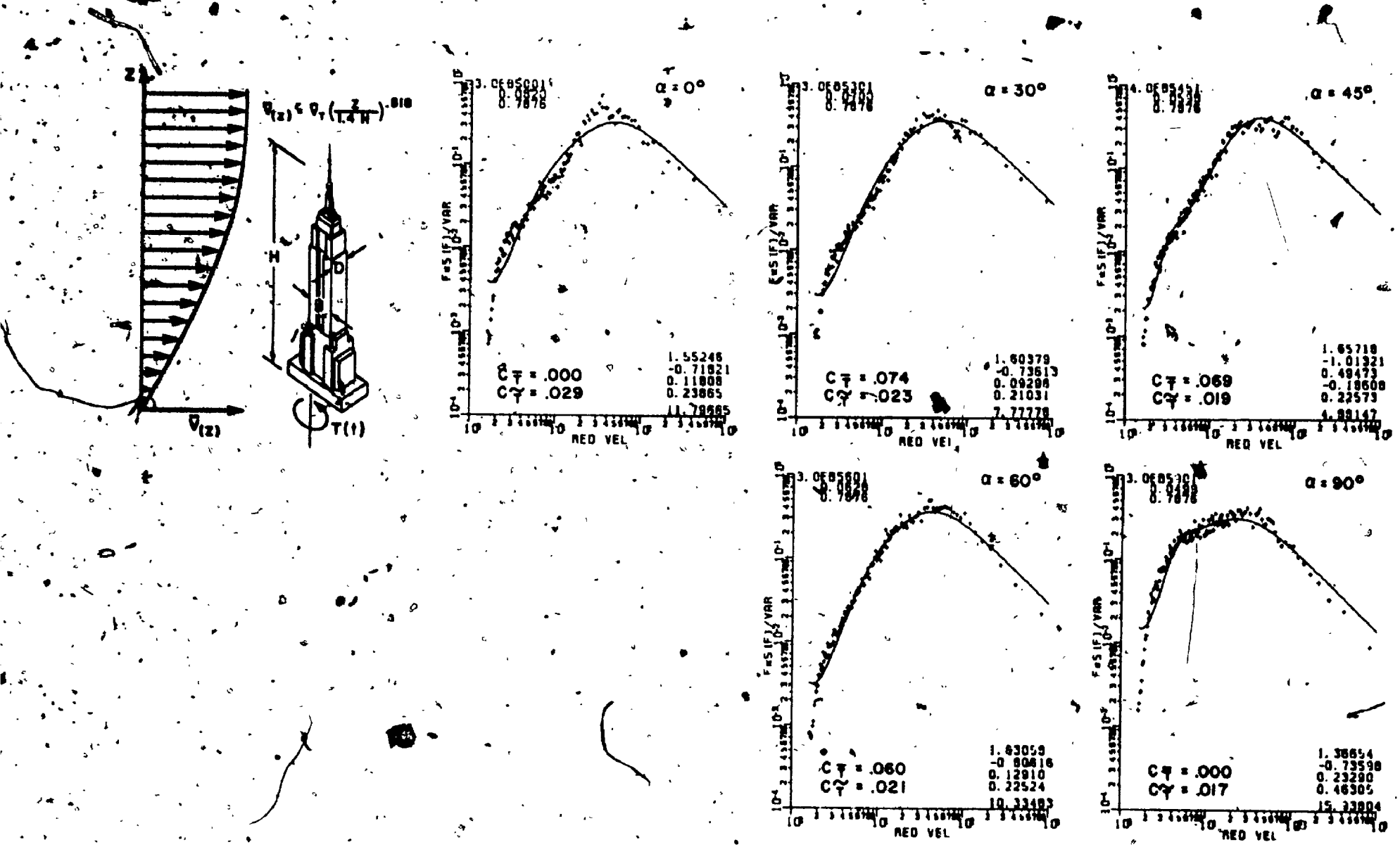

FIG. A.44 TORSIONS ON EMPIRE STATE BUILDING, SUBURBAN EXPOSURE

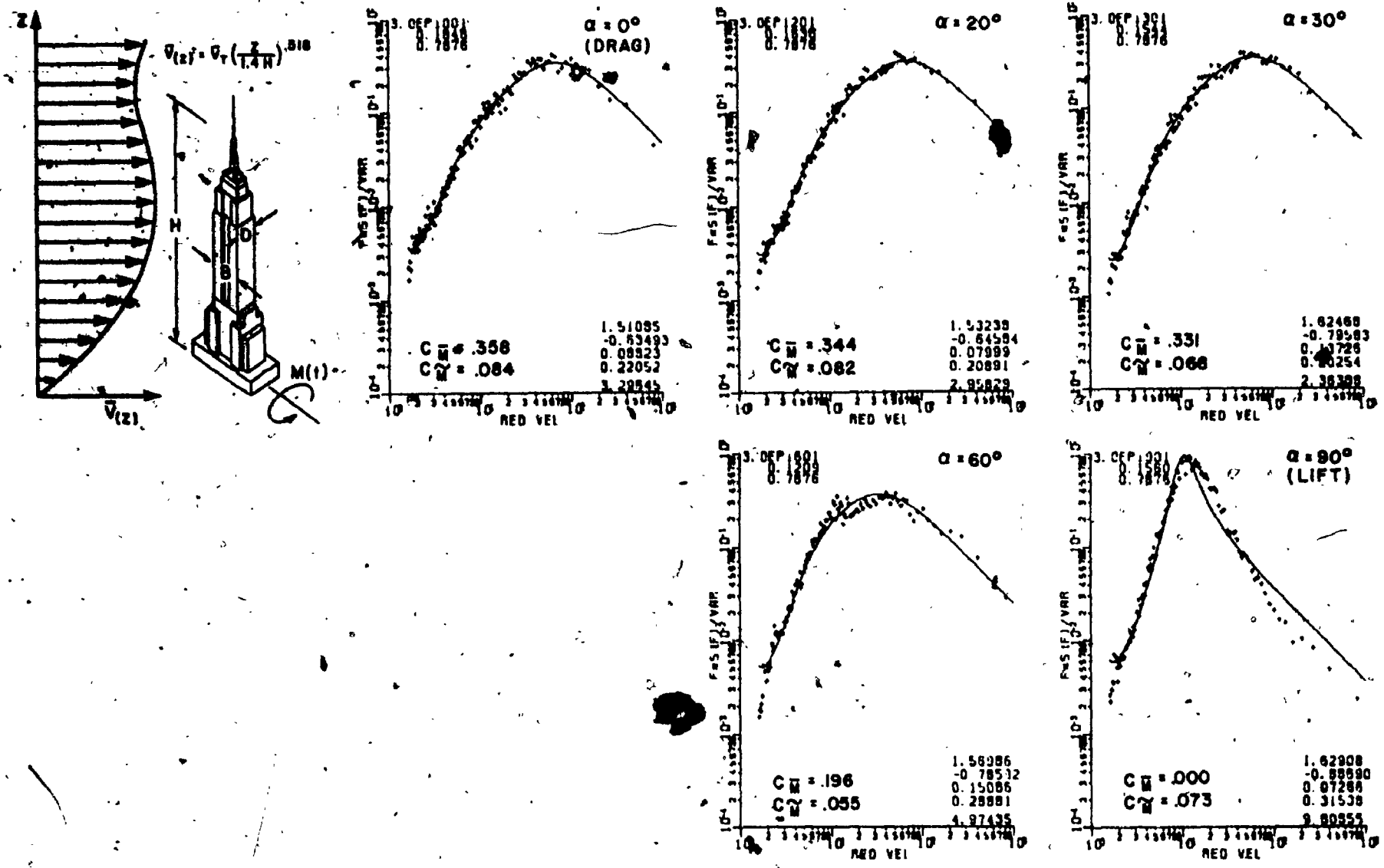

FIG. A45 MOMENTS ON BROAD SIDE OF THE EMPIRE STATE BUILDING, SUBURBAN (WITH NEIGHBOURING TALL BUILDINGS), EXPOSURE

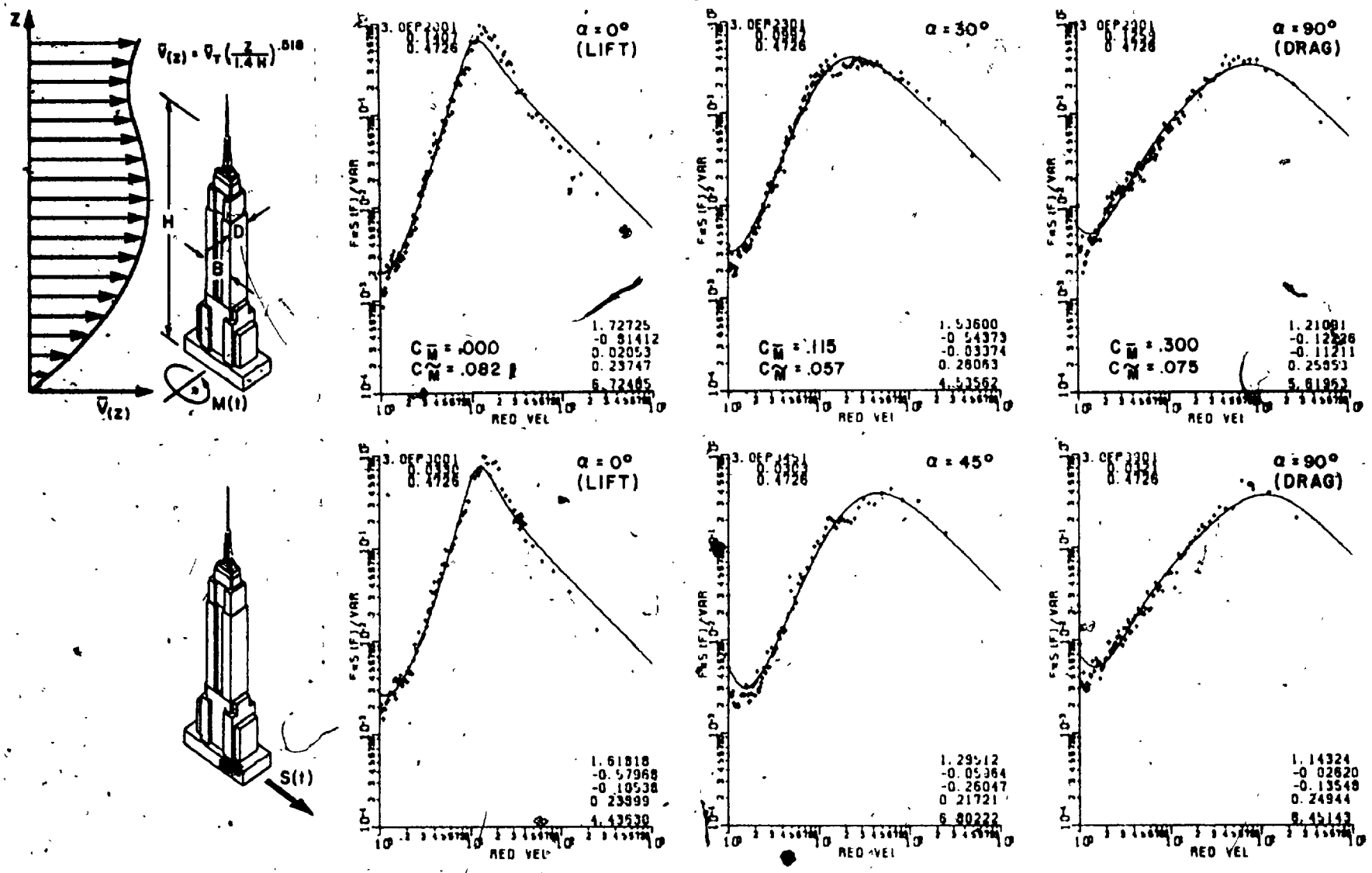

FIG. A.46 MOMENTS AND SHEARS ON NARROW SIDE OF THE EMPIRE STATE BUILDING, SUBURBAN (WITH NEIGHBOURING TALL BUILDINGS) EXPOSURE

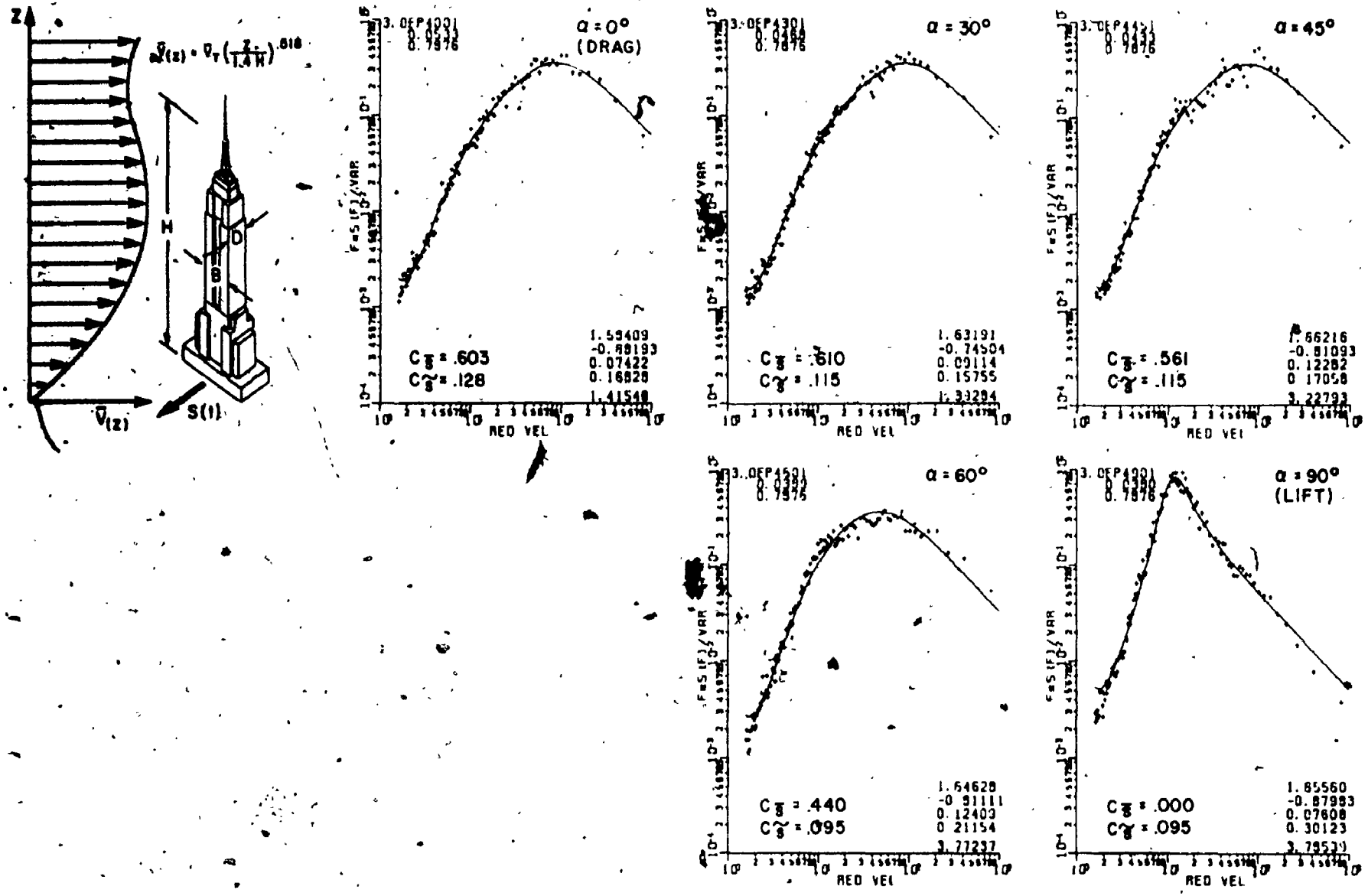

FIG. A.47 SHEARS ON BROAD SIDE OF EMPIRE STATE BUILDING, SUBURBAN (WITH NEIGHBOURING TALL BUILDINGS) EXPOSURE

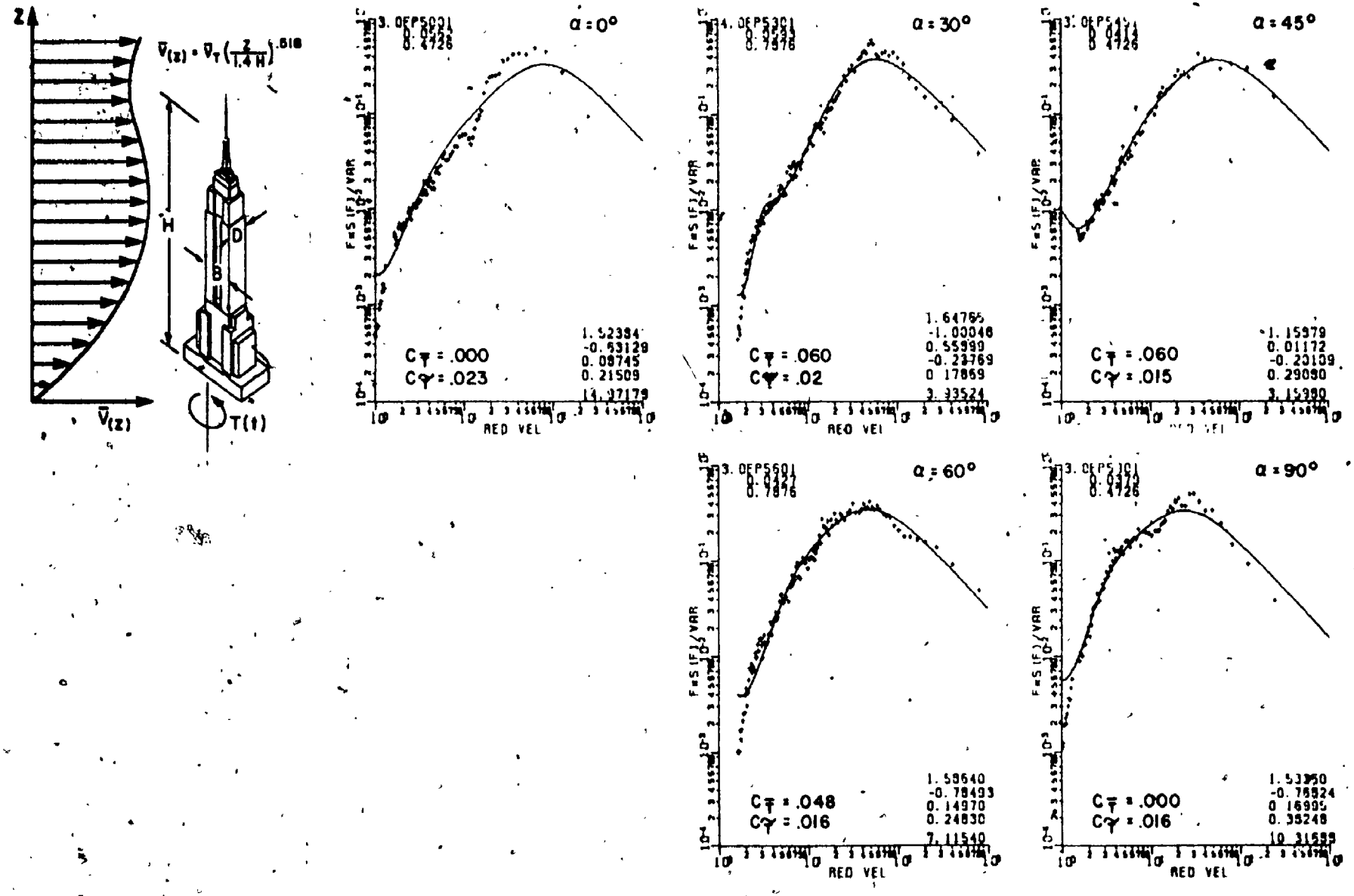

FIG. A.48 TORSIONS ON EMPIRE STATE BUILDING, SUBURBAN (WITH NEIGHBOURING TALL BUILDINGS) EXPOSURE

APPENDIX B

MODAL FORCE COEFFICIENTS FOR SELECTED BUILDING SHAPES

The force coefficients are described in Section 2.12. Non-dimensional coefficients relate the wind induced forces to the wind speed and are required to make response predictions as outlined in Section 2.5. Numerical values for mean and rms coefficients are also given with the force spectra in the Appendix A.

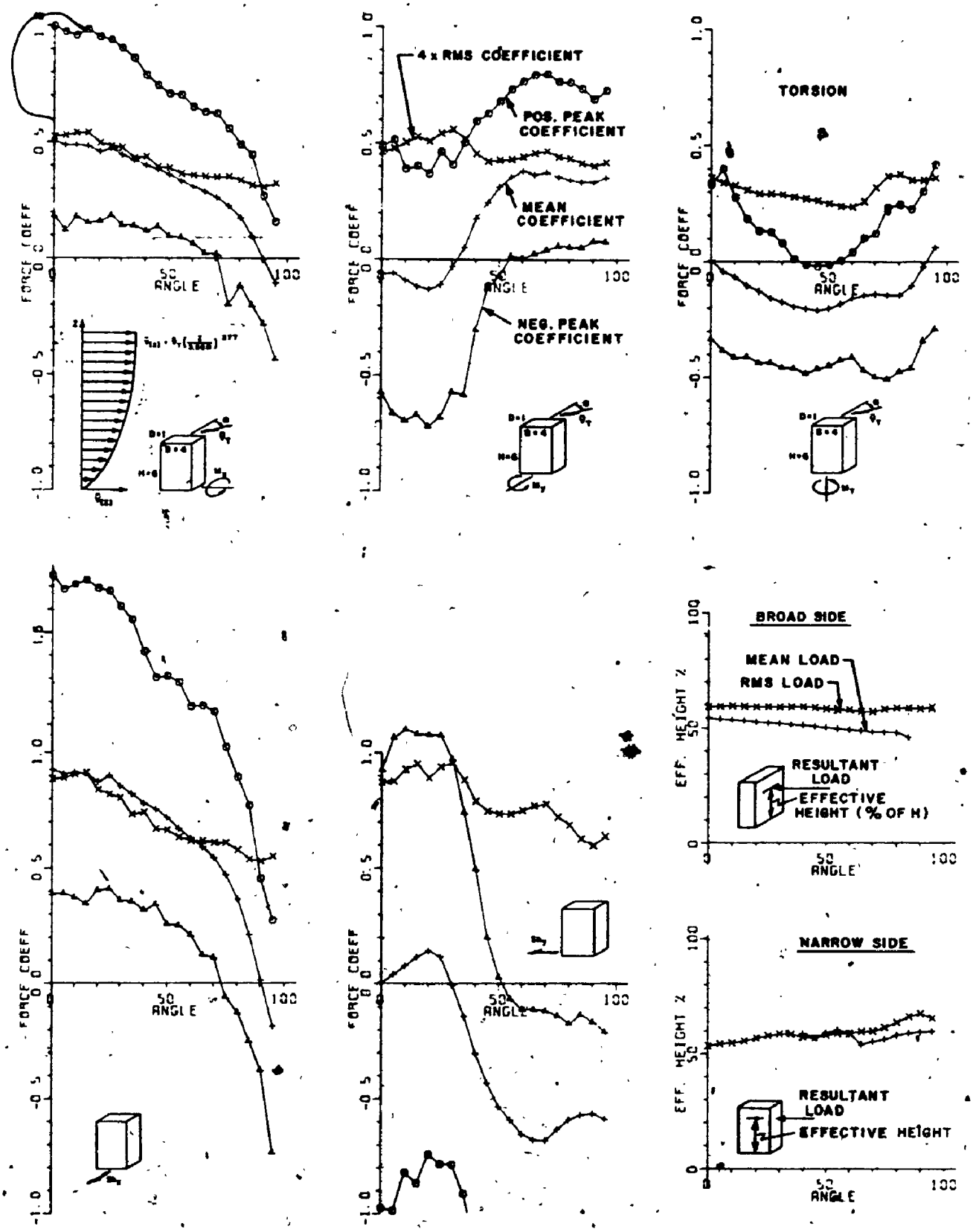

FIG. B.1 FORCE COEFFICIENTS FOR A 6:4:1 BUILDING, SUBURBAN EXPOSURE

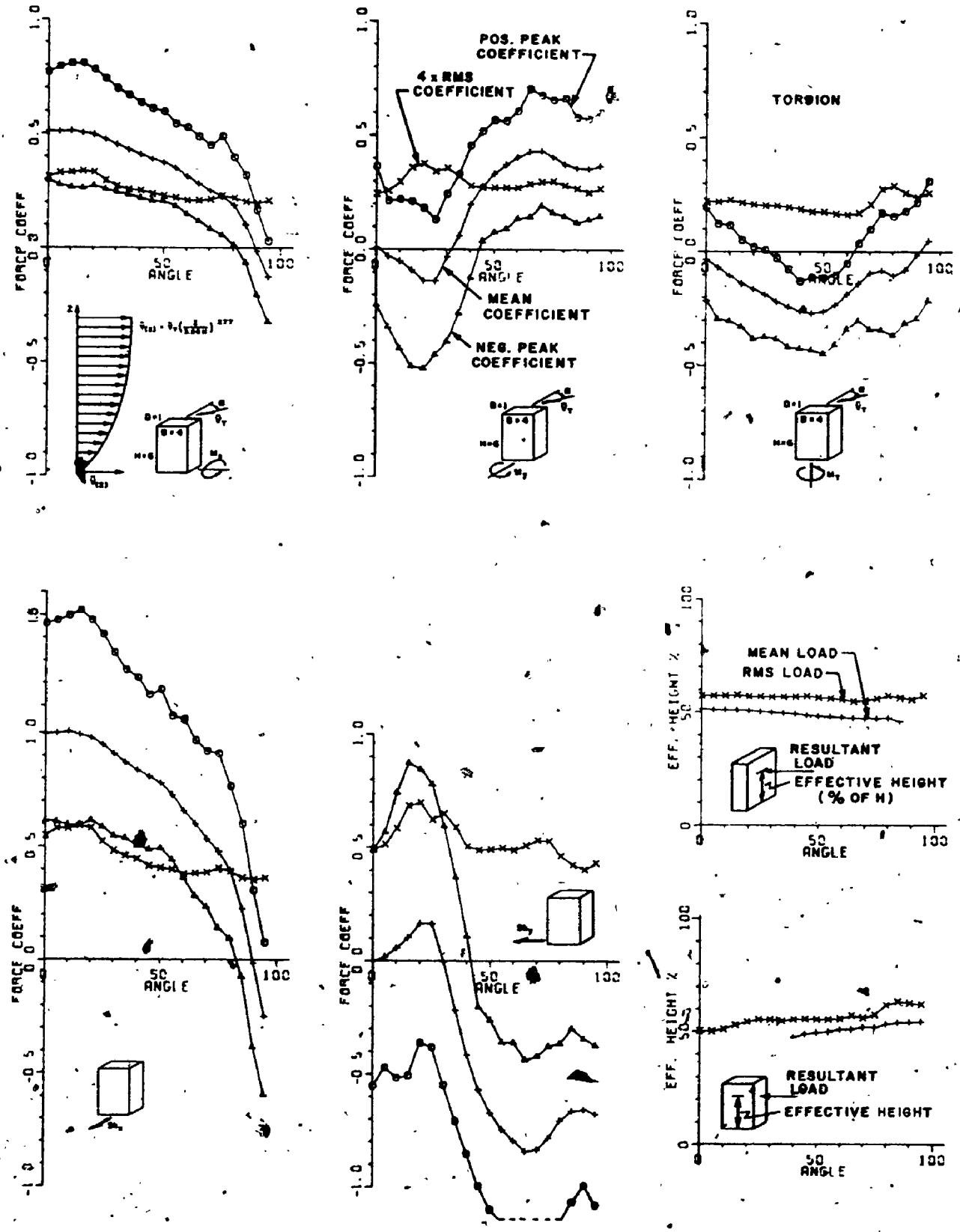

FIG. B.2 FORCE COEFFICIENTS FOR A 6:4:1 BUILDING, OPEN COUNTRY EXPOSURE

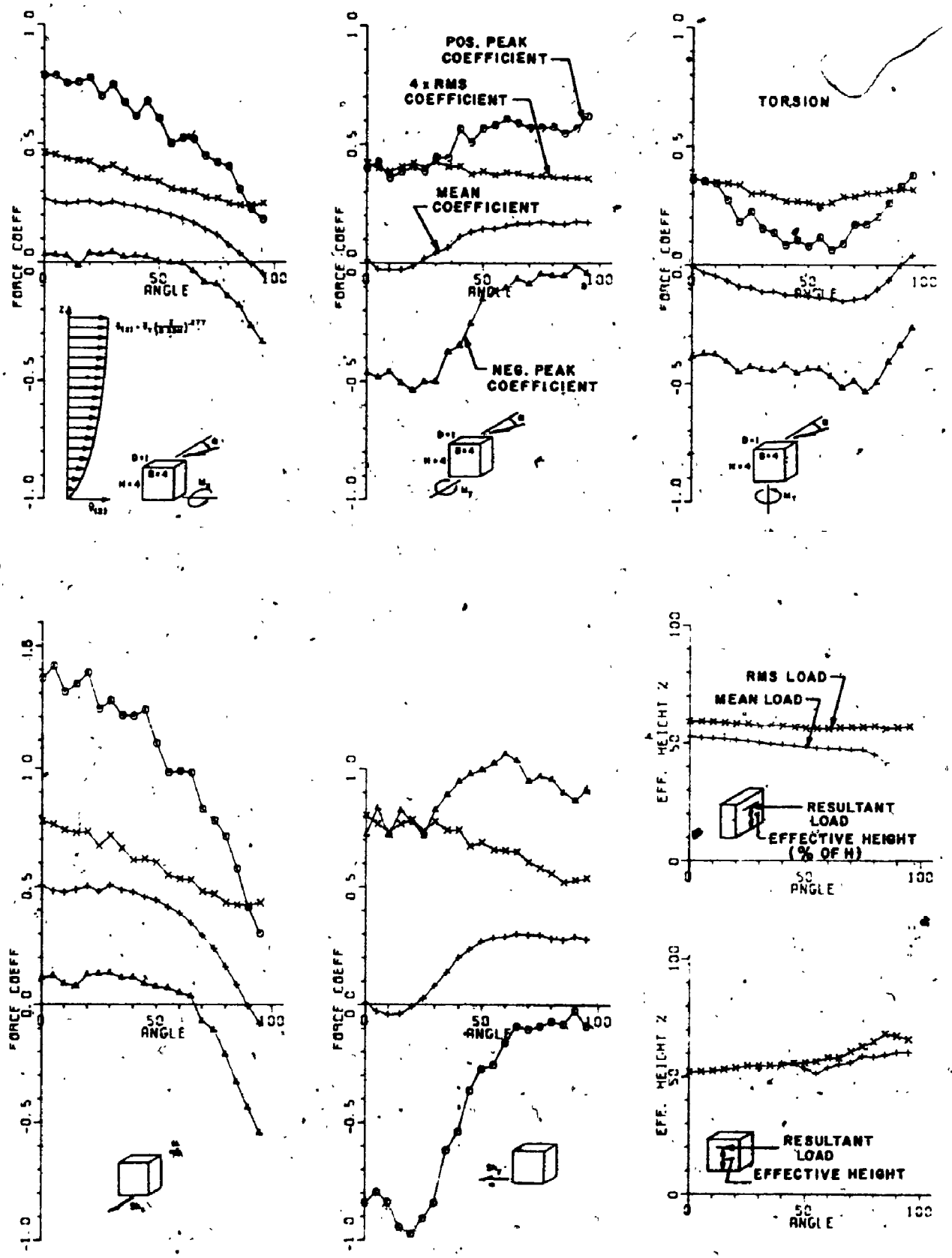

FIG. B.3 FORCE COEFFICIENTS FOR A 4:4:1 BUILDING, SUBURBAN EXPOSURE

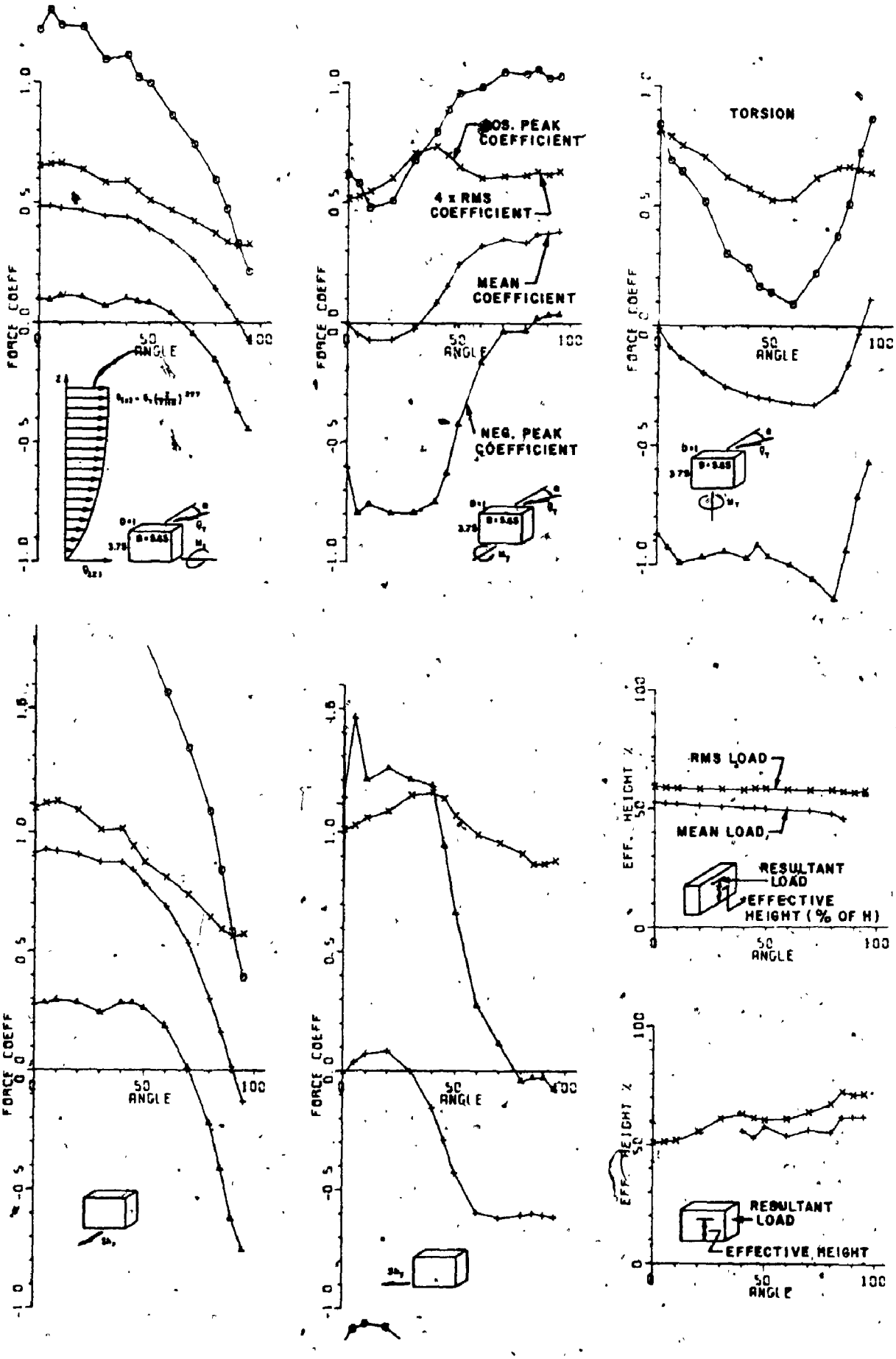

FIG. B.4 FORCE COEFFICIENTS FOR A 3.75:5.65:1 BUILDING, SUBURBAN EXPOSURE

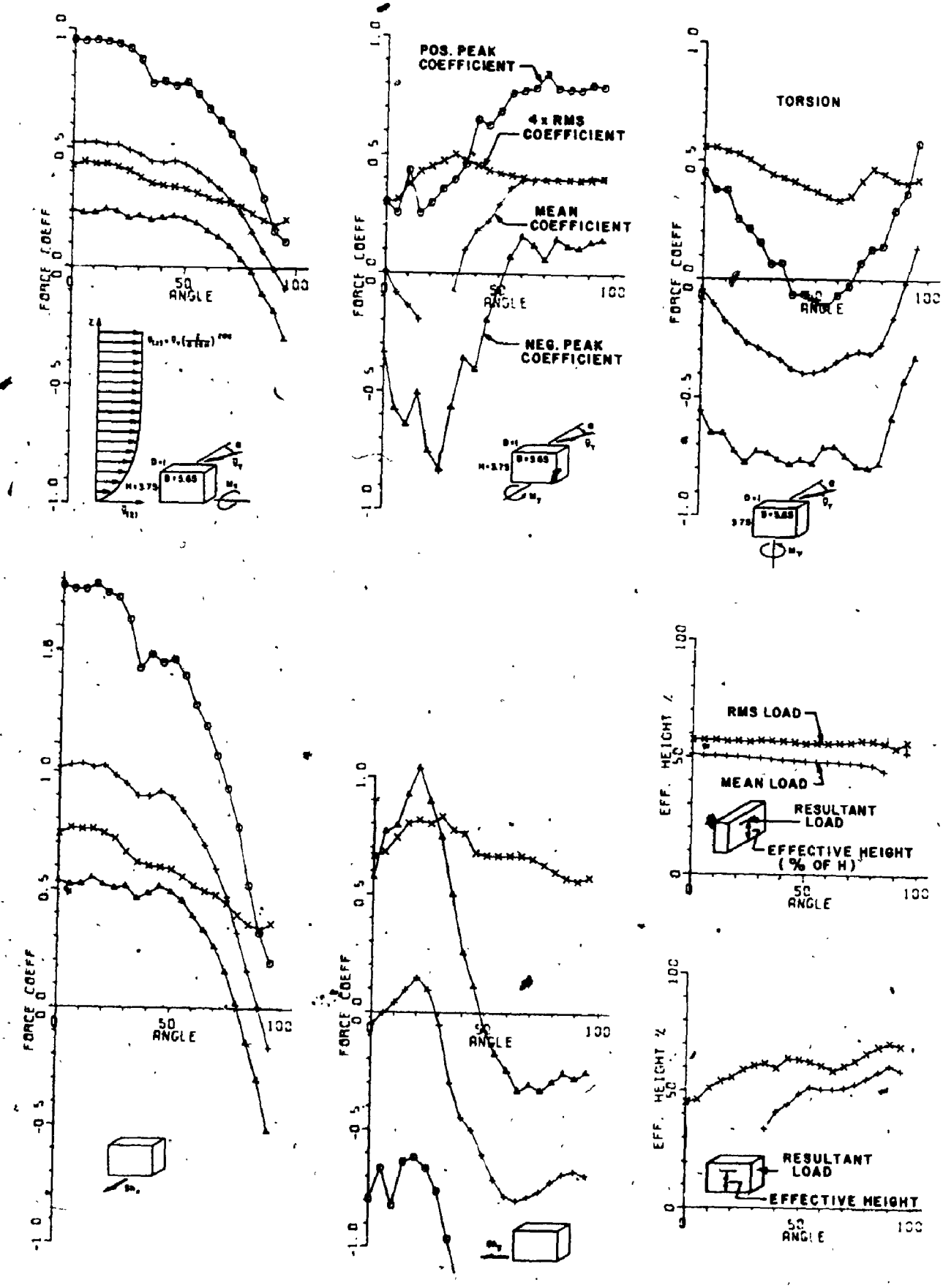

FIG. B.5 FORCE COEFFICIENTS FOR A 3.75:5.65:1 BUILDING, OPEN COUNTRY EXPOSURE

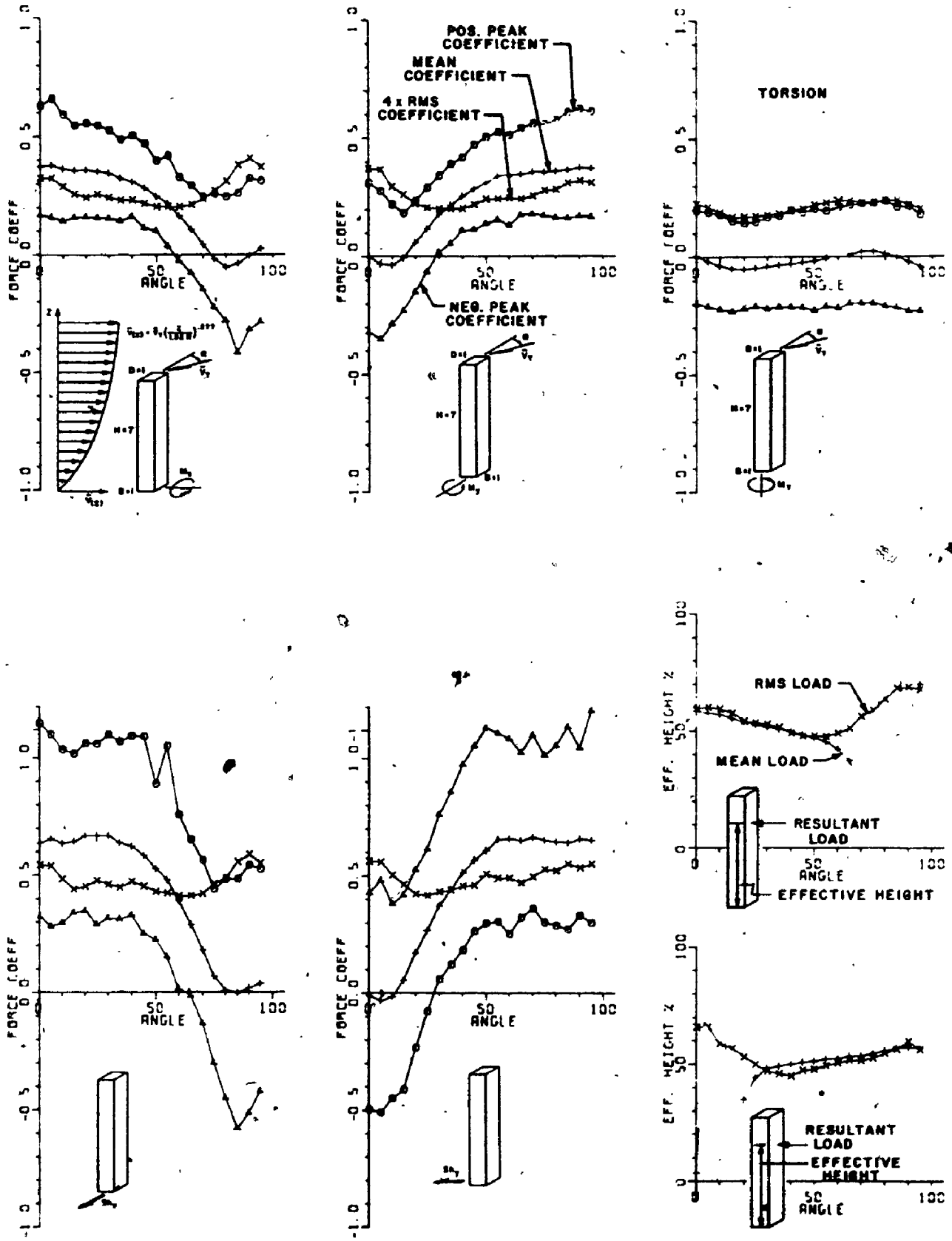

FIG. B.6 FORCE COEFFICIENTS FOR A TALL 7:1:1 BUILDING, SUBURBAN EXPOSURE

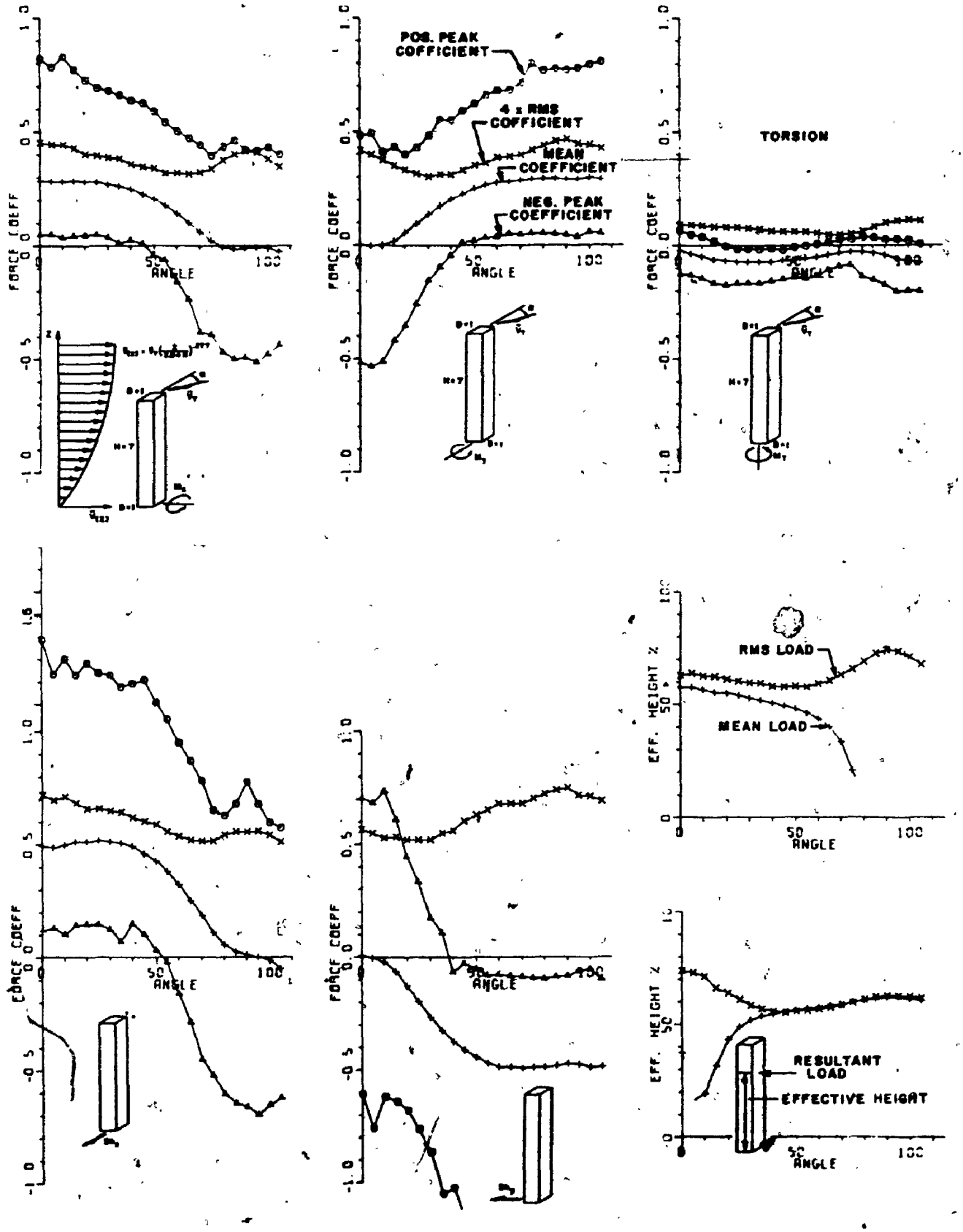

FIG. B.7 FORCE COEFFICIENTS FOR A MEDIUM TALL 7:1:1 BUILDING, SUBURBAN EXPOSURE

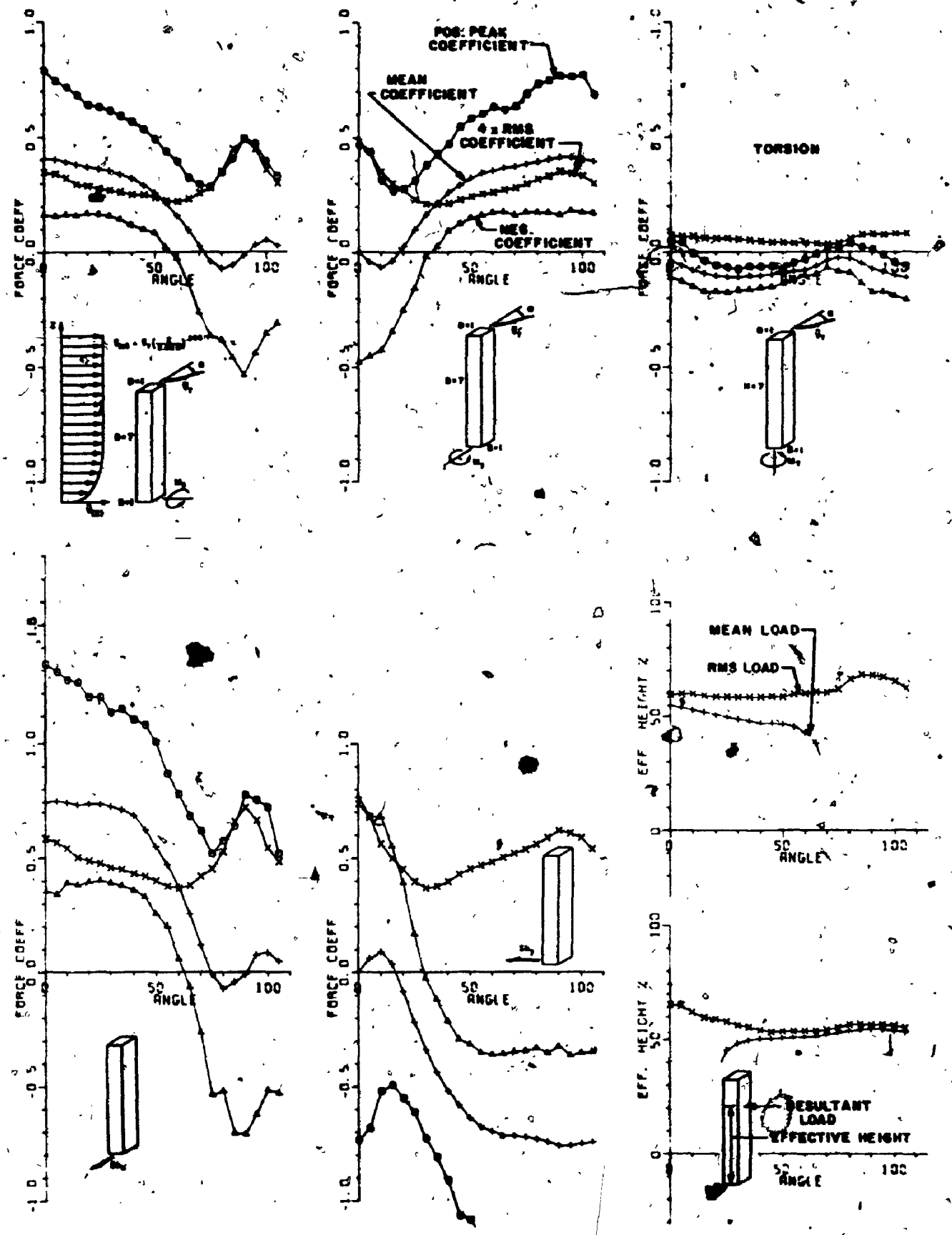

FIG. B.8 FORCE COEFFICIENTS FOR A MEDIUM TALL 7:1:1 BUILDING, OPEN COUNTRY EXPOSURE

4 4

OF / DE

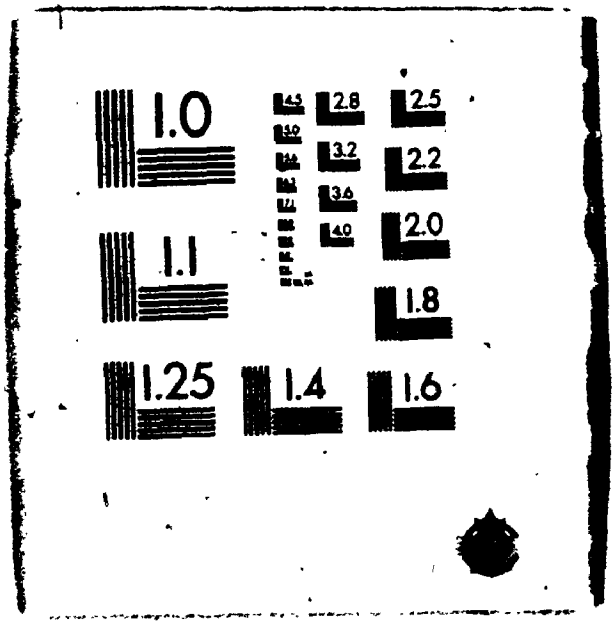

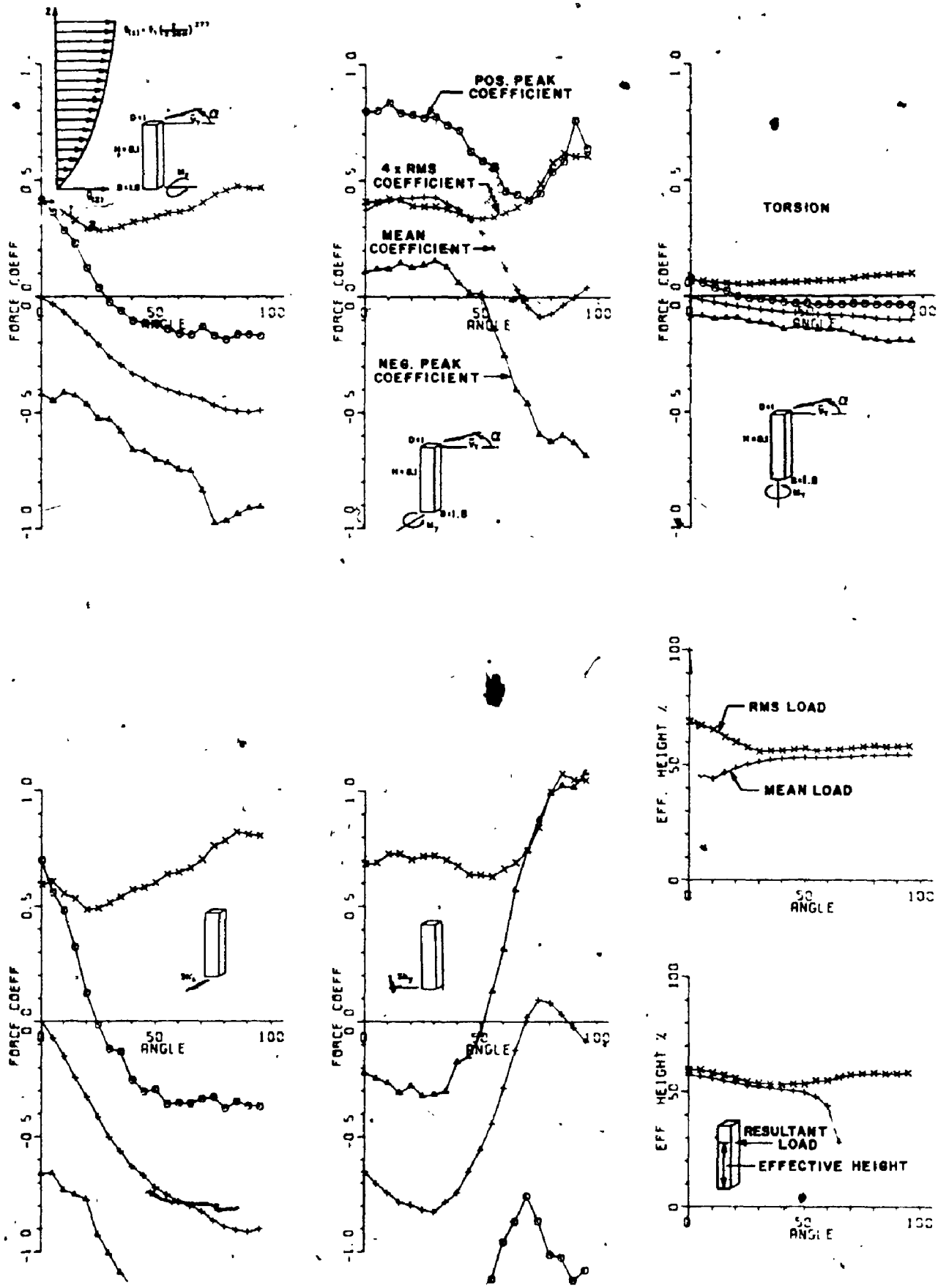

FIG. B.9 FORCE COEFFICIENTS FOR AN 8.1:1.8:1 BUILDING, SUBURBAN EXPOSURE

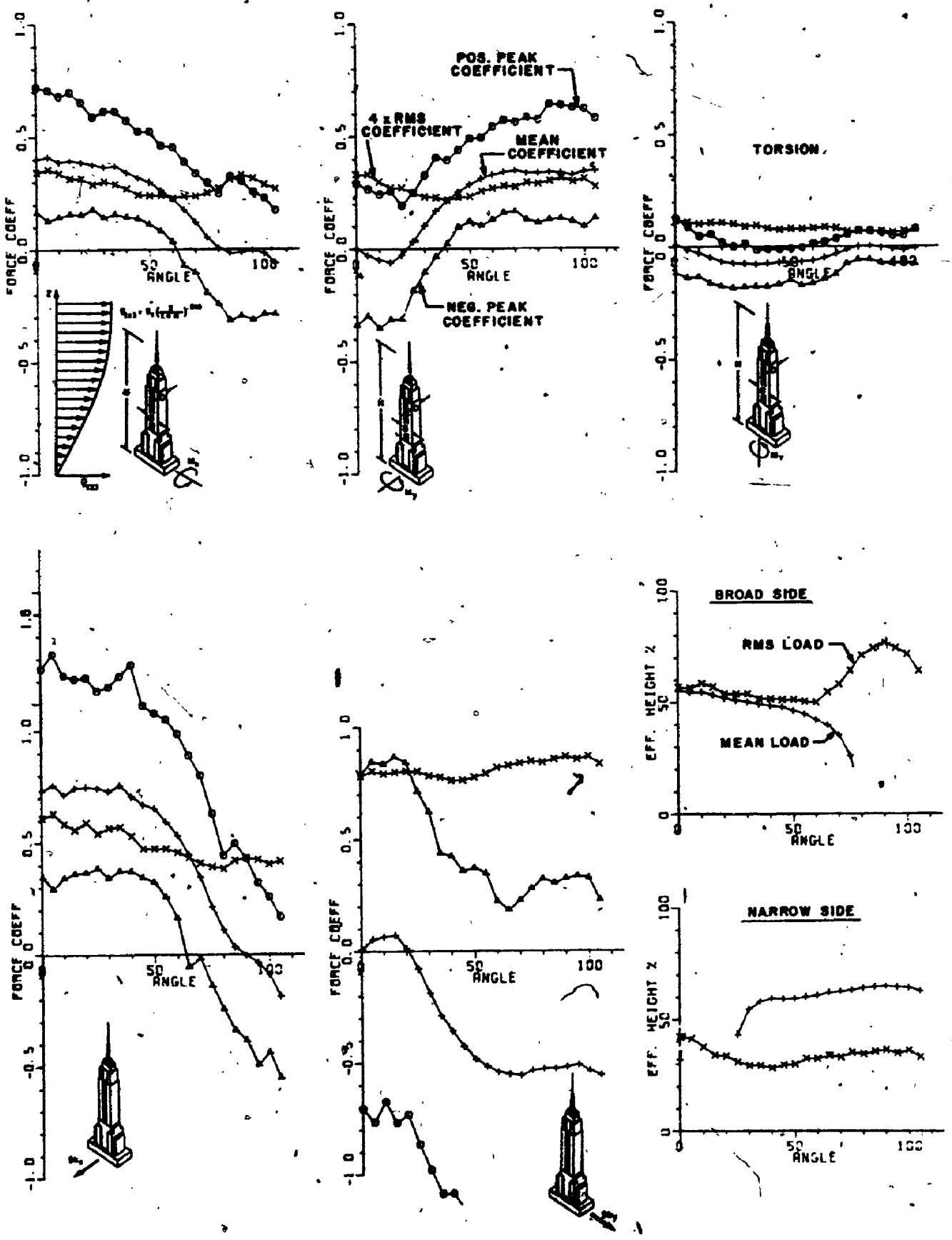

FIG. B.10 FORCE COEFFICIENTS FOR THE EMPIRE STATE BUILDING, SUBURBAN EXPOSURE

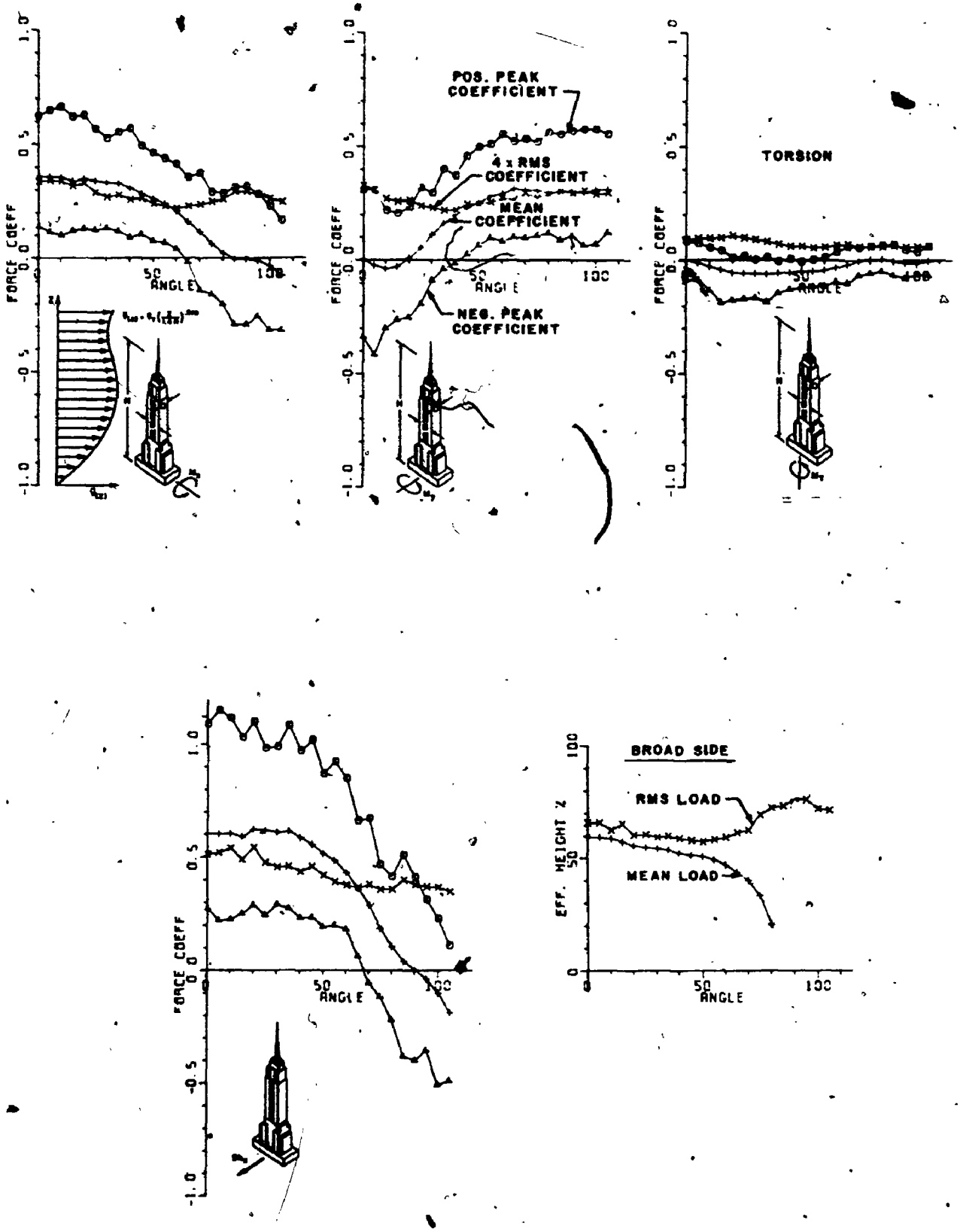

FIG. B.11 FORCE COEFFICIENTS FOR THE EMPIRE STATE BUILDING, SUBURBAN EXPOSURE WITH SOME NEIGHBOURING TALL BUILDINGS

REFERENCES

1. Adby, P.R. and Dempster, M.A.H., "Introduction to Optimization Methods," Chapman and Hall Mathematics Series, Wiley & Sons, New York, N.Y., 1974.

2. Akaike, H., "Statistical Prediction Identification," Annals of the Institute for Mathematical Statistics, Vol. 22, 1970, pp. 203–217.

3. Anderson, J.R., "Strain Gauge Balances for Wind Tunnels: An Outline of Practice in the United Kingdom," RAE Techn. Note, Aero 2434, Jan. 1956. (Also available as AGARD Report 5, 1956.)

4. Best, D.J., "Some Easily Programmed Pseudo-Random Normal Generators," The Australian Computer Journal, Vol 11, No. 2, May 1979, pp. 60–62.

5. Box, G.E.P. and Jenkins, G.M., "Time Series Analysis : Forecasting and Control," Revised Edition 1976, Holden-Day, San Francisco.

6. Bridel, G., "Strömungsuntersuchungen an 2 rotierenden Zylindern mit einer neuen Mehrkomponenten–Waage," Thesis presented at the Eidgenossischen Technischen Hochschule Zürich, Switzerland in 1978 in partial fulfillment of the requirements for the degree of Doctor of technical science.

7. Bulirsch, R. and Stoer, J., "Numerical Treatment of Ordinary Differential Equations by Extrapolation Methods," Numerische Mathematik, Band 8, 1966, pp. 1–13.

8. Cermak, J.E., Sadeh, W.Z. and Hsi, G., "Fluctuating Moments on Tall Buildings Produced by Wind Loading," Proc. Technical Meeting Concerning Wind Loads on Buildings and Structures, Nat. Bureau of Standards, Building Sci. Series 30, Nov. 1970, pp. 45–59.

9. Chan, S.P., and Newmark, N.M., "Comparison of Numerical Methods for Analysing the Dynamic Response of Structures," Civ. Eng. Stud. Struct. Res. Ser. No. 36,

1952, Univ. Illinois, Urbana, Ill.

10. Chevallier, J.P. and Cabot, L., "Dynamomètres à Strain-Gauges à Faible Course et à Grande Sensibilité," La Recherche Aéronautique, No. 40, 1954.

11. Davenport, A.G., "Spectrum of Horizontal Gustiness Near the Ground in Strong Winds," Quart. J. R. Met. Soc., Vol. 87, April 1961a, pp 194–211.

12. Davenport, A.G., "The Application of Statistical Concepts to the Wind Loading of Structures," Proceedings of the Institute of Civil Engineering, London, paper No. 6480, Vol. 19, Aug. 1961b, pp. 449–472.

13. Davenport, A.G., "The Distribution of Largest Values of a Random Function with Application to Gust Loading," Proceedings of the Institute of Civil Engineering, Vol. 28, 1964, pp. 187–196.

14. Davenport, A.G., "The Treatment of Wind Loading on Tall Buildings," Symp. on Tall Buildings at the University of Southampton, 13–15 April 1966, Pergamon Press, pp. 3–44.

15. Davenport, A.G., "Gust Loading Factors," Journal of the Structural Division, ASCE, Vol. 93, No. ST3, Proc. Paper 5255, June 1967, pp. 11–34.

16. Davenport, A.G., and Isyumov, N., "The Application of the Boundary Layer Wind Tunnel to the Prediction of Wind Loading," Proc. Int. Sem. on Wind Effects on Buildings and Structures, Ottawa, 1967, Vol. I, pp. 201–230.

17. Davenport, A.G., "An Approach to Human Comfort Criteria for Environmental Wind Conditions," Teaching the Teachers Colloquium on Bldg. Climatology, Stockholm, Sweden, Sept. 1972.

18. Davenport, A.G., "The Design of Tall Buildings for Wind Forces: International Developments and the Present State of the Art," South African Conf. on Tall

Buildings, Carlton Hotel, November 18–20, 1975, paper No. 13.

19. Davenport, A.G., "The Prediction of the Response of Structures to Gusty Wind," International Seminar of the Safety of Structures Under Dynamic Loading," Vol. 1, Norwegian Institute of Technology, June 1977, pp. 257–283 (published by Tapir 1978).

20. Davenport, A.G., "The Influence of Turbulence on the Aeroelastic Responses of Tall Structures to Wind," IAHR/IUTAM Pratical Experiences with Flow-Induced Vibrations Symposium, Karlsruhe, Sept. 3–6, 1979 (Published by Springer Verlag, Berlin 1980), G1, pp. 681–695.

21. Davenport, A.G., Mackey, S. and Melbourne, W.H., Council on Tall Buildings, Committee 9, 1980, "Wind Loading and Wind Effects," Chapter CL–3, Vol. CL of Monograph on Planning and Design of Tall Buildings, ASCE, New York, N.Y., pp. 143–248.

22. Davenport, A.G. and Tschanz, T., "The Response of Tall Buildings to Wind : Effects of Wind Direction and the Direct Measurement of Dynamic Force," Proceedings, The Fourth U.S. National Conference on Wind Engineering Research, Seattle, Wa., July 27–29, 1981, pp. 205–223.

23. Dean, M., "Semiconductor and Conventional Strain Gauges," Academic Press, 1962.

24. Dorsey, J., "Homegrown Strain Gauge Transducers," Experimental Mechanics, July 1977, pp. 255–260.

25. Duong, Q.P., "On the Choice of the Order of Autoregressive Models: A Ranking and Selection Approach," Dept. of Statistical and Actuarial Sciences, The University of Western Ontario, TR–81–08, August 1981.

26. Durbin, P.A. and Hunt, J.C.R., "Fluctuating Surface Pressures on Bluff Structures in Turbulent Winds : Further Theory and Comparison with Experiment," Proc.

of the Fifth Int. Conf. on Wind Engineering, Colorado, U.S.A., 8–14 July 1979, Pergamon Press, Oxford, pp. 491–507.

27. English, E. and Durgin, F.H., "A Wind Tunnel Study of Shielding Effects on Rectangular Structures," Proceedings, Fourth U.S. National Conference on Wind Engineering Research, July 27–29, 1981, Seattle, Wa., pp. 178–185.

28. Evans, R.A. and Lee, B.E., "The Assessment of Dynamic Wind Loads on a Tall Building: A Comparison of Model and Full Scale Results," Preprints, Fourth U.S. National Conference on Wind Engineering Research, July 27–29, 1981, Seattle, Wa., pp. 214–221.

29. Fintel, M. and Khan, F.R., "Shock Absorbing Soft Storey Concept for Multi-Storey Earthquake Structures," 64th Annual ACI Convention, Los Angeles, March 1968.

30. Fortier, L.J. and Scanlan, R.H., "A Cooling Tower Wind Loading Model Based on Full-Scale Data," Proceedings, 5th International Conference on Wind Engineering, 8–14 July 1979, Colorado State University, Fort Collins, pp. 1217–1226.

31. Foutch, D.A., and Safak, E., "Torsional Vibrations of Along-Wind Excited Structures," Journal of the Engineering Mechanics Division ASCE, Vol. 107, No. EM2, Proc. paper 16192, April 1981, pp. 323–337.

32. Gear, C.W., "The Automatic Integration of Ordinary Differential Equations," Comm. of the ACM, March 1971a, Vol. 14, No. 3, pp. 176–179.

33. Gear, C.W., "DIFSUB for Solution for Ordinary Differential Equations," Alogrithm 407, Comm. of the ACM, March 1971b, Vol. 14, No. 3, pp. 185–190.

34. Goldenblat, I.I. and Sizov, A.M., "Stabilita a Kmitání Stavebních Konstrukcí: Preklad Sovětské Příručky pro Stavební Inženýry," Státní Nakladatelství Technické Literatury, Prag, 1955. (Originally published in Russian Spravochnik po Rischetu Stroitel'nikh Konstriktsii na ustroichevost' i Komebaniia. Moscow, 1952.

35. Gommers, C.M.J., "Construction of Strain Gauge Measurement Elements," de Constructeur, Jan. 1978, Nr. 1, Translated by E.R. Funke and G.R. Mogridge. Internal Report, HY218, National Research Council of Canada, 1981.

36. Granger, C.W.J. and Morris, M.J., "Time Series Modelling and Interpretation," J.R. Statist. Soc. A (1976), 139, Part 2, pp. 246–257.

37. Hamming, R.W., 1962, "Numerical Methods for Scientists and Engineers," McGraw-Hill, N.Y.

38. Hudspeth, R.T., and Borgman, L.E., "Efficient FFT Simulation of Digital Time Sequences," Journal of the Engineering Mechanics Division, ASCE, Vol. 105 No. EM2, Proc. Paper 14517, April 1979, pp. 223–235.

39. Hull, T. E., Enright, W.H., Fellen, B.M. and Sedgwick, A.E., "Comparing Numerical Methods for Ordinary Differential Equations," SIAM Journ. Num. Anal. Vol. 9, No. 4, December 1972, pp. 603–637.

40. Humar, J.L. and Wright, E.W., "Numerical Methods in Structural Dynamics," Canadian Journal of Civil Engineering, 1, 1974, pp. 179–193.

41. Hunt, J.C.R., "A Theory of Turbulent Flow Around Two-Dimensional Bluff Bodies," J. Fluid Mech., 65, 1973, pp. 625–706.

42. International Mathematical and Statistical Library I, 1977, Reference Manual, Houston, Texas.

43. Jenkins, G.M. and Watts, D.G., "Spectral Analysis and its Applications," Holden-Day, San Francisco, Cal., 1968.

44. Kinderman, A.J. and Monahan, J.F., "Computer Generation of Random Variables Using the Ratio of Uniform Deviates," ACM Trans. Math. Software, 3 (1977) pp. 257–260.

45. Kutta, W., "Beitrag zur näherungsweisen Integration totaler Differentialgleichungen," Zeitschrift für Math. und Phys. Leipzig, Vol. 46, 1901, pp. 435–453.

46. Lee, L.H.N., "Dynamic Plasticity," Nucl. Engr. Design, 27, 1974, pp. 386–397.

47. Lidstone, R.B., "Mechanical Property Data for Alcan Alloys CA–26S and CA–75S," ALCAN Research Report K–TM–339–70–15–04, 1970.

48. Lyman, Taylor, Editor, Metals Handbook, 8th Edition. Vol. I. Properties and Selection of Metals, American Society for Metals, Metals Park, Ohio, 1961.

49. Lyness, J.N., "SQUANK (Simpson Quadrature Used Adaptively – Noise Killed)," Algorithm 379, Communications of the ACM, Vol. 13, Number 4, April 1970, pp. 260–263.

50. McFarland, K.H. and Dimeff, J., "Problems Involved in Precision Measurements with Resistance Strain Gauges," AGARD Report No. 12, 1966.

51. Marsaglia, G. and Bray, T.A., "A Convenient Method for Generating Normal Variables," SIAM Review, Vol. 6, No. 3, 1964, pp. 260–264.

52. Merluzzi, P. and Brosilow, C., "Runge Kutta Integration Algorithms with Built-In Estimates of the Accumulated Truncation Error," Computing, 20, 1978, pp. 1–16.

53. Mulheru, M.R. and Moley, R.O., "Building Period Measurements Before, During and After the San Fernando Earthquake," N.O.A.A., Report on San Fernando Earthquake, 1973.

54. Murphy, L.M., "San Fernando, California Earthquake of February 9, 1971," Vo. I, U.S. Dept. of Commerce, U.S. Government Printing Office, Washington, D.C., 1973.

55. National Research Council of Canada, "Commentaries on Part 4 of the National Building Code of Canada 1980," The Supplement to the National Building Code

of Canada, NRCC No. 17724, Ottawa, 1980.

56. Newmark, N.M., "A Method of Computation for Structural Dynamics," J. Eng. Mech. Div., Am. Soc. Civil Eng., 85, 1959, pp. 67–94.

57. Nielsen, N.N., "Damping in Multi-Storey Buildings Determined from Steady-State Vibration Tests," ASCE Structural Eng. Conference, Miami, Fla., Jan. 31 – Feb. 4, 1966, Conference Preprint 296, pp. 1–24.

58. Norris, C., Hansen, R.J., Holley, M.J., Biggs, J.M., Namyet, S. and Minami, J.K., "Structural Design for Dynamic Loads," McGraw-Hill Book Co., Inc., N.Y., 1959.

59. Novak, M., "A Statistical Solution of the Lateral Vibrations of Cylindrical Structures in Air Flow," Acta Technica CSAV, No. 4, 1967, pp. 375–404.

60. O'Donnel, W.J., "The Additional Deflection of a Cantilever Due to the Elasticity of the Support," Transactions of the ASME Journal of Applied Mechanics, September 1960, pp. 461–464.

61. Otsuki, Y., Washizu, K., Tomizawa, H. and Ohya, A., "A Note on the Aeroelastic Instability of a Prismatic Bar with Square Section," Journal of Sound and Vibration, Vol. 34, 1974, pp. 233–248.

62. Pardoen, G.C., Hart, G.C., and Bunce, B.T., "Damage Assessment of the Imperial Co. Services Building," ASCE Fall Convention and Exhibition, Hollywood, Fla., October 1980.

63. Paros, J.M., "Digital Pressure Transducers," Measurements & Data, Issue 56, Vol. 10, No. 2, March–April 1976.

64. Perry, C.C. and Lissner, H.R., "The Strain Gauge Primer," McGraw-Hill, 1962.

65. Pierre, D.A., "Optimization Theory with Applications," Wiley & Sons Inc., New York, N.Y., 1969.

66. Powell, M.J.D., "An Efficient Method for Finding the Minimum of a Function of Several Variables without Calculating Derivatives," The Computer Journal, Vol. 7, July 1964, pp. 155–162.

67. Rebuffet, P., "Some Strain Gauge Balances Used in French Wind Tunnels," AGARD Report 6-T 1956.

68. Reinhold, T.A. and Sparks, P.R., "The Influence of Wind Direction on the Response of a Square-Section Tall Building," Proceedings of the Fifth Int. Conf. on Wind Engineering, Colorado, U.S.A., July 1979, Pergamon Press, Oxford, pp. 685–698.

69. Rice, S.O., In "Selected Papers on Noise and Stochastic Processes," (Editor: N. Wax) Mathematical Analysis of Random Noise, New York : Dover Publications Inc., pp. 180–181.

70. Robinson, I., "An Algorithm for Automatic Integration Using the Adaptive Gaussian Technique," The Australian Computer Journal, Vol. 8, No. 3, November 1976, pp. 106–115.

71. Rosati, P.A., "The Response of a Square Prism to Wind Load," Research Report BLWT–II–68, March 1968, M.E.Sc., Thesis supervised by A.G. Davenport.

72. Runge, C., "Ueber die numerische Auflosung von Differentialgleichungen," Mathematische Annalen, Vol. 46, 1895, pp. 167–178.

73. Saunders, J.W. and Melbourne, W.H., "Tall Rectangular Building Response to Cross-Wind Excitation," Proceedings of the Fourth Int. Conference on Wind Effects on Buildings and Structures, Heathrow 1975, Cambridge University Press, London, pp. 369–379.

74. Shinozuka, M. and Jan C.-M., "Digital Simulation of Random Processes and its Applications," Journal of Sound and Vibration, Vol. 25, 1972, pp. 111–128.

75. Simiu, E., "Gust Factors and Alongwind Pressure Correlations," Journal of the Structural Division, ASCE, Vol. 99, No. ST4, Proc. Paper 9686, April 1973, pp. 773–783.

76. Spescha, G. and Volle, E.; "Piezoelectric Measuring Instruments," Report Nr. 20.054e of the Kistler Instrumente AG, Winterthur, Switzerland (no date).

77. Surry, D. and Isyumov, N., "Model Studies of Wind Effects – A Perspective of Experimental Technique and Instrumentation," 6th Int. Congress on Instrumentation in Aerospace Simulation Facilities, ICIASF '75 Record, pp. 76–91.

78. Thompson, K.J., and Park, R., "Seismic Response of Partially Prestressed Concrete," Journal of the Structural Division, ASCE, Vol. 106, No. ST8, Proc. Paper 15598, August 1980, pp. 1755–1775.

79. Timoshenko, S., "Strength of Materials," D. Van Nostrand Company Inc., New York, N.Y., Part 1, Third Edition, 1955, p. 175.

80. Troxel, G.E. and Davis, H.E., "Composition and Properties of Concrete," McGraw Hill, New York, N.Y., 1956.

81. Tung, T.P. and Newmark, N.M., "A Review of Numerical Integration Methods for Dynamic Response of Structures," Civ. Eng. Stud. Struct. Res. Ser. No. 69, Univ. Illinois, Urbana, Ill, 1954.

82. Unvala, B.A. and Green, A.K., "An Inexpensive Voltage-Stablized Power Supply for Strain-Gauge Applications," Journal of Strain Analysis, Vol. 9, No. 2, 1974, pp. 88–89.

83. Velozzi, J. and Cohen, E., "Gust Response Factors," Journal of the Structural Division, ASCE, Vol. 97, No. ST6, Proc. Paper 5980, June 1968, pp. 1295–1313.

84. Vickery, B.J., "On the Assessment of Wind Effects on Elastic Structures," C.E. Trans. Inst. Aust., 1966, pp. 183–192.

85. Vickery, B.J., "On the Reliability of Gust Loading Factors," in Proceedings of the Technical Meeting Concerning Wind Loads on Buildings and Structures, Building Science Series 30, National Bureau of Standards, Washington, D.C., 1970.

86. Vickery, B.J., "Wind Action on Simple Yielding Structures," J. Eng. Mech. Div. ASCE, Vol 66, 1970, pp. 107–120.

87. Vickery, B.J. and Davenport, A.G., "A Comparison of Theoretical and Experimental Determination of Elastic Structures to Turbulent Flow," Wind Effects on Buildings and Structures, Ottawa, Canada, 1968, pp. 705–738.

88. Wang, P.C., "Numerical and Matrix Methods in Structural Mechanics," John Wiley and Sons, Inc., New York, 1966.

89. Wardlaw, R.L. and Moss, G.F., "A Standard Building Model for the Comparison of Simulated Natural Winds in Wind Tunnels," Commonwealth Advisory Aeronautical Research Council, cc 662, Tech 25, 1970.

90. Whitbread, R.E., "The Measurement of Non-Steady Wind Forces on Small-Scale Building Models," Fourth International Conference on Wind Engineering, Heathrow 1975, Cambridge University Press, pp. 567–574.

91. Wilde, D.J. and Beightler, C.S., "Foundations of Optimization," Prentice-Hall, Englewood Cliffs, N.J., 1967.

92. Wyatt, T.A. and May, H.I., "The Ultimate Behaviour of Structures Under Wind Loading," Proceedings of the 3rd International Conference on Wind Effects and

Structures, Tokyo, 1971, pp. 501–510.

93. Wyatt, T.A. and May, H.I., "The Generation of Stochastic Load Functions to Simulate Wind Loading on Structures," Earthquake Engineering and Structural Dynamics, Vol. 1, 1973, pp. 217–224.

94. Zangwill, W.I., "Nonlinear Programming : A Unified Approach," Prentice-Hall, Englewood Cliffs, N.J., 1969.

95. Zimmerli, B. and Thürlimann, B., "Strength Interaction Surfaces for Tall Buildings," Journal of the Structural Division, ASCE, Vol 105, No. ST3, Paper 14426, March 1979, pp. 481–492.

Additional References

96. Box, G.E.P. and Muller, E., "A Note on the Generation of Random Normal Deviates," Ann. Math. Stat. 28, 1958, pp. 610–611.

97. Jeary, A.P. and Sparks, P.R., "Some Observations on the Dynamic Sway Characteristics of Concrete Structures," ACI Symposium on Vibrations in Concrete Structures, New Orleans, 18–21 October, 1977.

END

26H01H83

FIN